Modeling familial Alzheimer's disease utilizing gene targeted human induced pluripotent stem cells

Inaugural-Dissertation

to obtain the academic degree

Doctor rerum naturalium (Dr. rer. nat.)

submitted to the Department of Biology, Chemistry and Pharmacy

of Freie Universität Berlin

by

Tobias Graß

2018

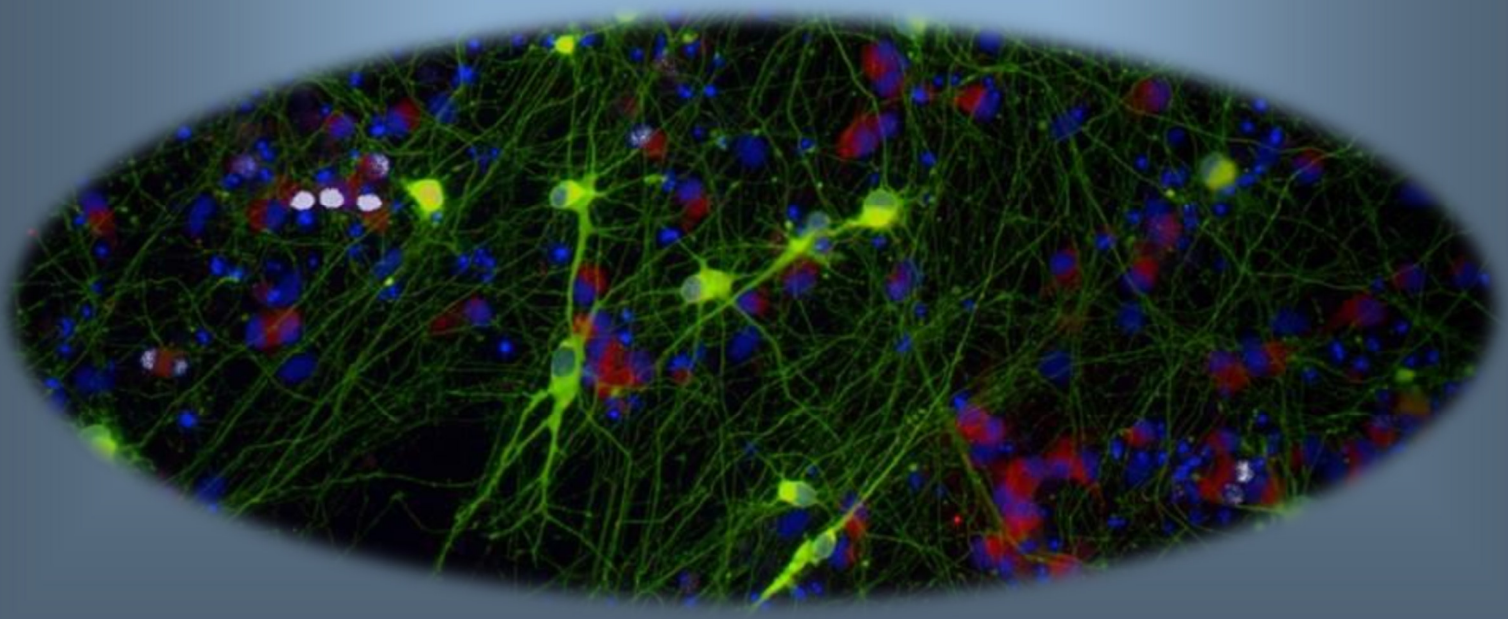

This work has been carried out from 14.08.2014 – 01.11.2018 under the supervision of Prof. Dr. Lee Rubin at the Department of Stem Cell and Regenerative Biology (SCRB), Harvard University, Cambridge, Massachusetts, USA,

1. Gutachter:	Prof. Dr. Lee Rubin_____
2. Gutachter:	Prof. Dr. Rupert Mutzel_____
Disputation am:	19.03.2019_____

Acknowledgements

I would like to thank my advisor Prof. Dr. Lee Rubin for the support and mentorship throughout my time in Boston. I am very grateful for the opportunity to work on such an interesting, exciting and challenging project as well as for all the resources that he provided for me and the fruitful collaborations I became of.

Further, I would like to thank Prof. Dr. Rupert Mutzel. His help and support made it possible to work on my thesis abroad in collaboration with the Harvard University and I am grateful for his commitment to be my second dissertation advisor.

I would like to thank Dr. Natalia Rodriguez-Muela for her supervision, her great feedback, her ideas and endless support, all of which made this thesis possible.

I would like to thank Michelle Watts and Soumyaa Mazumder for critical reading of this thesis and for their valuable feedback.

Finally, I would like to thank my family, Matthias, Cornelia, Christian and Sina for their unlimited support, their help and their advice during the time.

Contents

Abbreviations

AB	Antibody
AD	Alzheimer's disease
AICD	Amyloid precursor protein intracellular domain
APP	Amyloid precursor protein
AT	Protective "Icelandic mutation" at position 673 of the gene APP
AV	Pathogenic "Italian mutation" at position 673 of the gene APP
Aβ	Amyloid-beta
Aβ40	Amyloid-beta 40
Aβ42	Amyloid-beta 42
BACE-1	Beta-site APP cleaving enzyme
BDNF	Brain Derived Neurotrophic Factor
BSA	Bovine Serum Albumin
Cas	CRISPR associated genes
CAS9	CRISPR associated protein 9
CNS	Central Nervous System
Comp E	Compound E, γ-secretase inhibitor
CNTF	Ciliary Derived Neurotrophic Factor
CRISPR	Clustered Regularly Interspaced Short Palindromic Repeats
CTF	C-terminal fragment
CSF	Cerebrospinal Fluid
Cx	Cortical
DAPI	1,4-diamino-2-fenilindol
DAPT	γ-secretase inhibitor, also known as GSI-IX or LY-374973
DMSO	Dimetil-sulfóxido
DNA	Deoxyribonucleic Acid
DSB	Double-Strand-Break
ELISA	Enzyme-Linked ImmunoSorbent Assay
ER	Endoplasmic Reticulum
FACS	Fluorescence-Activated Cell Sorting
fAD	Familial Alzheimer's disease
GDNF	Glial Derived Neurotrophic Factor
gRNA	Guide RNA
HDR	Homologous-directed repair
HR	Homologous Recombination
hESCs	Human embryonic stem cells
hiPSCs	Human induced pluripotent stem cells
ICH	Immunohstochemistry
IF	Immunofluoresence
iPSCs	Induced pluripotent stem cells
Indel	Insertion or deletion of bases in the genome
KO	knock-out
LON	Pathogenic "London mutation" at position 717 of the gene APP
LTD	Long Term Depression

LTP	Long term Potentiation
MAPT	Microtubule associated protein tau
MNs	Motor neurons
MG132	Cell-permeable proteasome inhibitor (carbobenzoxy-Leu-Leu-leucinal)
mESCs	Mouse embryonic stem cells
NFTs	Neurofibrilar tangles
NHEJ	Non-Homologous-End-Joining
PCR	Polymerase chain reaction
PD	Parkinson's disease
PS1	Presenilin 1
PS2	Presenilin 2
pTAU	Phosphorylated microtubule associated protein tau
sAD	Sporadic Alzheimer's disease
sAPP	Soluble APP
sgRNA	Single-guide RNA
scRNAseq	Single cell RNA sequencing
SorL1	Endocytic sortilin-receptor-1
SWE	Pathogenic "Swedish mutation" at position 670/671 of the gene APP
TALENs	Transcription Activator-Like-Effector Nucleases
TAU	Microtubule associated protein tau
TG	Thapsigargin
tSNE	t-Distributed Stochastic Neighbor Embedding
Tun	Tunicamycin
Wt	Wild type
ZFNs	Zinc Finger Nucleases

Introduction

Improvements in modern medicines as well as healthy lifestyle changes have led to a dramatic increase in life expectancy over the past several decades. Unfortunately, with this increased lifestyle, the prevalence of age-related disorders like dementia, cancer, and other malignances have increased as well (Oeppen and Vaupel, 2002). While various options are available to treat the ladder, ranging from radiotherapy and surgery to individual and specialized pharmacological treatments (incl. growing "precision medicine"), the treatment of dementia is still symptomatic. In fact, not a single drug has been approved for dementia, despite enormous efforts from researchers and costly clinical trials. This lack in effective therapeutics is due in part to the complex nature underlying dementia as well as our lack of precise neurodegenerative models that recapitulate disease pathology and phenotypes seen in humans.

In recent years, two major discoveries were made that revolutionized the fields of molecular biology and regenerative medicine. First, the generation of induced pluripotent stem cells (iPSCs) (Takahashi and Yamanaka, 2006) allowed researchers access to patient derived cells carrying specific disease causing mutations, opening up new avenues for studying and modeling human diseases and providing an excellent source to complement current animal and overexpressing cellular models. By being able to differentiate iPSCs *in vitro* into the cell type most affected by a disease, new options emerged to provide researchers with cell types that are typically lost by end-stage of the disease, like dopaminergic neurons in Parkinson's disease (PD) or motor neurons in Spinal muscular atrophy (SMA). hiPSCs may have the potential to recapitulate the disease *in vitro* on a very specific level, leading to new insights, new potential drug targets and revealing new pathways involved. A second discovery was the recent invention of precise and flexible genome-editing tools, specifically the CRISPR-CAS9 system. Programmable endonucleases are able to target and modify almost any gene in the human genome, carrying huge hopes to further improve disease modelling and precision medicine. By either correcting a disease-causing mutation and turning a disease cell line into a healthy control line or, alternatively inserting a disease-causing mutation into a healthy cell line, we can now model diseases in an isogenic context. This minimizes interfering "line to line" background mutations and phenotypes, providing

ideal experimental controls and ensuring that whatever phenotype is observed *in vitro* is caused solely by the mutation of interest.

Cumulatively, these groundbreaking discoveries have revolutionized disease modeling, allowing advances in our understanding of regenerative biology and dementia such that one day there may be effective therapeutic options.

1.1 Alzheimer's disease

1.1.1 Relevance and impact of Dementia and Alzheimer's disease

Dementia is a general term for conditions involving memory loss and cognitive impairments severe enough to interfere with a person's ability to perform every day activities (Scott and Barrett, 2007). In 2018, nearly 50 million people were affected worldwide (Figure 1) (Freudenberg-Hua et al., 2018), a number that is expected to triple by the year 2050, with an estimated 45% of affected people needing high intensity care. A variety of aging related, neurodegenerative disorders contribute to and involve dementia, including frontotemporal dementia (FTD), dementia with Lewy Bodies (DLB) and vascular dementia (VD). However, the most common cause is Alzheimer's disease (AD), accounting for as much as 60-80% of all dementia cases (Figure 2) (Hebert et al., 2003; Scott and Barrett, 2007).

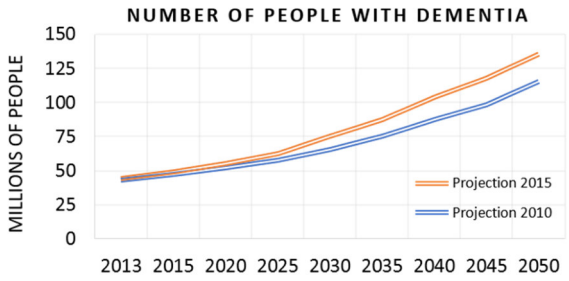

Figure 1. The number of people affected by Alzheimer's disease and dementia worldwide is supposed to double every 20 years according to latest forecasts.

AD is not only the most common form of dementia, but also the most prevalent neurodegenerative disease worldwide. It is the 5th leading cause of death worldwide, and the only disease in the top ten leading causes of death that cannot be cured, prevented, or even slowed down. Additionally, the rate of death for AD and dementia has more than doubled from 2000 – 2016 (World Health Organization, 2018). AD is characterized by an insidious onset and progressive deterioration of cognitive abilities, ultimately leading to death 4 to 8 years after onset of symptoms (Barnes et al., 2018). Despite the devastating distress it causes for people who suffer from this disease as well as their

beloved ones, their families and caregivers, AD has also become a huge economic burden. The global combined costs for treating dementia, with AD the main contributor, reached an estimated $818 billion in 2016, indicating that it will become a trillion-dollar disease in 2018 (Jia et al., 2018).

1.1.2 History of Alzheimer's disease

AD was first described by the German physician Dr. Alois Alzheimer in 1906, when he reported the results of the autopsy of Auguste Deter, a 55-year-old woman, who had died from a very progressive and behavioral disorder. Dr. Alzheimer noticed two distinctive pathologies in Auguste Deter's brain: neurofibrillary tangles and military foci or neuritic plagues, which he described as dystrophic neuronal processes surrounding a "special substance in the cortex" and which he thought represented a special case of dementia. It was not until the late 1960's that a connection between the amount of these neuritic plagues and a risk for dementia was established (Blessed et al., 1968). In the 1980's, Glenner and Wong purified that "special substance" Alzheimer had described and showed that it was a ~4kDa peptide, mostly ranging from 40 to 42 amino acids in lengths (Glenner and Wong, 1984). It was assumed that it was product of a larger, cleaved precursor protein, which was confirmed in 1987 when Kang et al. cloned the amyloid precursor protein (APP) (Kang et al., 1987). The short peptide isolated by Glenner and Wong thereafter became known as amyloid-beta (Aβ)-peptide. Then, it was not until the late 1980's and early 1990's that it was found that the discovered neurofibrillary tangles were made of different hyperphosphorylated isoforms of the microtubule-associated protein tau and a causal connection between abnormal filaments (assembled to inclusions) and neurodegeneration and dementia

Type of dementia	Characteristics	% of all dementia cases
Alzheimer's disease	**Impaired memory, apathy & depression, gradual onset**	**60-80**
Vascular dementia	Similar to AD, but memory less affected, mood fluctuations more prominent, Physical frailty, Steepwise onset	10
Dementia with Lewy Bodies (DLB)	Marked fluctuations in cognitive ability Visual hallucinations Parkinonism (tremor & rigidity)	<5
Frontotemporal Lobar degeneration (FTLD)	Personality changes, Mood changes, Disinhibition, Language difficulties	5-10
Parkinson's disease dementia	Problems with movement (slowness, rigidity, tremor & changes in gait)	6-8
Creutzfeld-Jakob disease	Impaired memory and coordination, causes behavior changes	<0,0001
Normal pressure hydrocephalus	Difficulty walking, inability to control urination, memory problems	<0,1
Mixed Dementia	Mixed symptoms	50

Figure 2. Different types of dementia. AD accounts for the majority of the dementia cases. The so-called mixed dementia consists of at least two different types being AD always one of them.

was established (Goedert et al., 1992; Greenberg et al., 1992).

1.1.3 Hallmarks of AD & amyloid-beta-hypothesis

Nowadays and after years of research, these two distinctive pathologies that Alois Alzheimer noticed have been further characterized and have become the two pathological hallmarks of AD. In detail, these are- 1) abnormal amounts of intracellular neurofibrillary tangles, composed of hyperphosphorylated microtubule associated protein tau (MAPT, TAU) and 2) extracellular located senile plagues, consisting of aggregated Aβ-peptides found in postmortem brain of affected individuals. Genetic, biochemical and behavioral research suggests that the physiologic generation of the neurotoxic Aβ peptide by sequential cleavage of APP is the crucial step in AD pathology. This theory, known as the amyloid-beta-hypothesis or amyloid-beta-cascade (Aβ-hypothesis) (Figure 3) (Beyreuther and Masters, 1991; Hardy and Allsop, 1991; Hardy and Higgins, 1992; Selkoe, 1991) has dominated and guided the pharmaceutical and academic research of AD for more than 25 years now (Selkoe and Hardy, 2016). According to the hypothesis, the accumulation of Aβ, especially of its most toxic form Aβ 42, caused by either increased overall production of the toxic peptide or by an imbalance in Aβ production and clearance, starts a cascade that leads to synaptic and neuritic injury, microglial and astrocytic activation (as part of the inflammatory response), altered neuronal ionic homeostasis, oxidative damages, changes of kinases/phosphatases activities and the formation of NFTs. These circumstances lead to progressive and substantial neuronal cell death, affecting vulnerable brain regions including the entorhinal cortex, the nucleus basalis (Meynert, Ch4) and the hippocampus first, before affecting other parts within the whole cortex (Gomez-Isla et al., 1996, Whitehouse et al., 1981, Simic et al., 1997).

While the majority of researchers in the AD field agree with the Aβ-hypothesis, there are significant objections that undercut this hypothesis. These objections are mostly based on the fact that the number of amyloid deposits in the brain of people with AD does not correlate as well with the degree of cognitive impairment as neurofibrillary tangles do. However, it can be argued that Aβ deposits appear very early in AD pathology and are therefore further away from clinical dementia, potentially explaining why more downstream effects like microgliosis or tangles etc. are much closer to and causative of observed cognitive impairment and neuronal dysfunction than the initial Aβ deposits (Selkoe and Hardy, 2016). Additionally, other researches question the AB hypothesis due to the fact that some people have Aβ-deposits in their cortex but effectively lack any sign of AD or even mild cognitive impairment. A counterargument here is that at least some of

these deposits are diffuse amyloid plaques, with less abnormal neurites and a lower number of Aβ oligomers per plaque than those of AD patients (Esparza et al., 2013). Moreover, other hypotheses for the cause of AD include the cholinergic-hypothesis, which postulates that loss of cholinergic neurons is the main cause and initiator of AD (Bartus et al., 1982) as well as the tau-hypothesis, which proposes that abnormal levels of hyperphosphorylated protein tau lead to conformational changes of normal tau into paired helical filaments (PHF) and neurofibrillary tangles (Goedert, 1993). These then become the main trigger for AD. Thus, while there is a large amount of evidence to support the Aβ -hypothesis and the claim that Aβ is the primary pathogenic driver in AD (Jonsson et al., 2012; Kero et al., 2013; Rovelet-Lecrux et al., 2006; Selkoe and Hardy, 2016) the debate is still ongoing.

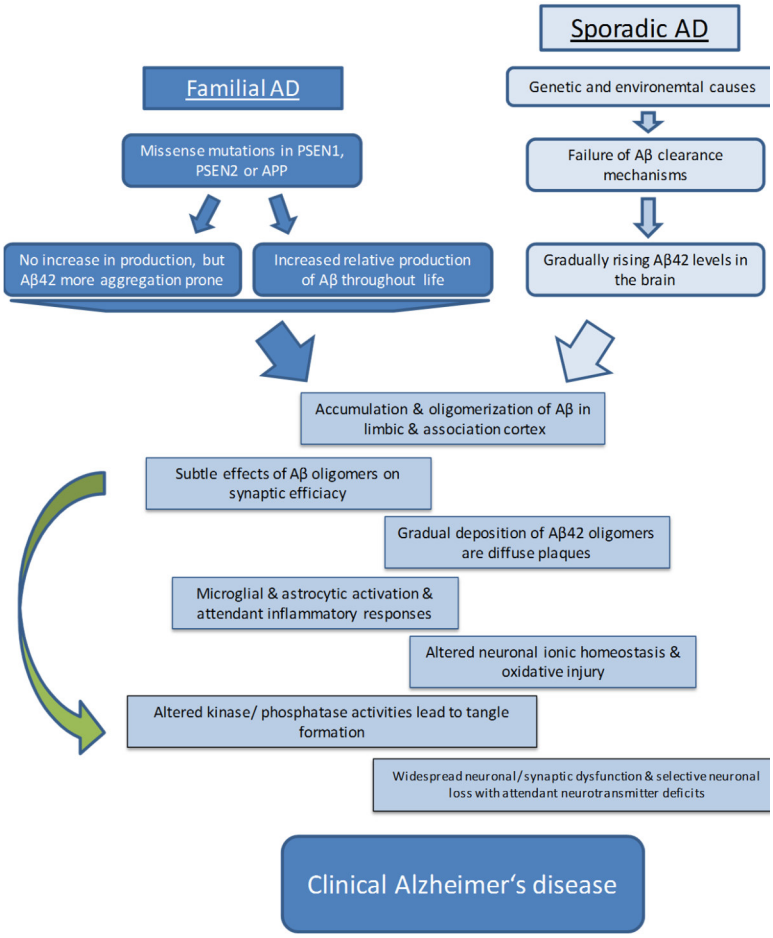

Figure 3. The amyloid beta hypothesis postulates that Aβ is the main driver of pathogenic events that ultimately lead to Alzheimer's disease. Green arrow indicates that Aβ oligomers besides activating microglia and astrocytes, might cause neuronal injuries directly as well.

1.1.4 Genetics of AD: fAD vs sAD

Two major types of AD can be distinguished: an early onset form, called early onset AD (eoAD) or familial AD (fAD), which accounts for only 1-5% of all cases and is caused by fully penetrant mutations in the genes APP, Presenilin 1 (PS1) or Presenilin 2 (PS2) (encoding for the

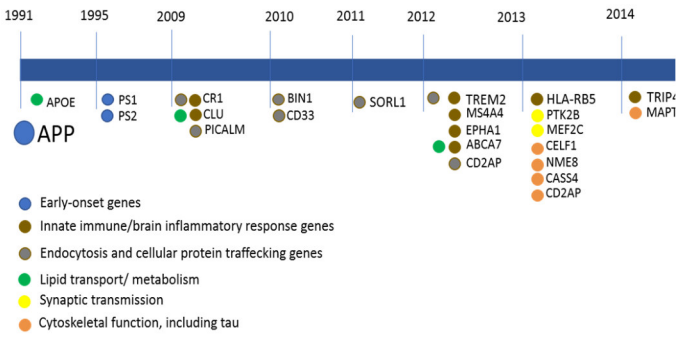

Figure 4. Risk factors and involved pathways for familial and sporadic AD by year of discovery.

proteins Presenilin 1 and 2, respectively). To date a total of 32 APP, 179 PS1 and 14 PS2 gene mutations have been discovered that result in early onset Alzheimer's disease, the majority of which are inherited autosomal dominant. A second, late onset form, called sporadic AD (sAD) or late onset AD (loAD), accounts for the majority of cases and is most likely caused by the interaction of genetic susceptibilities and environmental risk factors. Besides age, the main risk factors for sAD, one prominent genetic risk factor is the e4 allele of the apolipoprotein E gene, that regulates cholesterol metabolism but also directly binds to Aβ as well. Recent genome wide association studies have revealed several other genes like Triggering receptor expressed on myeloid cells 2 (TREM2) or sortilin-related receptor 1 (SORL1), that are considered to increase the risk for the late onset form of the disease (Figure 4) (Jonsson et al., 2012; T Cuenco K et al., 2008; Dodson et al., 2008). Even though there are differences in pathological causes, fAD and sAD do not differ histologically or clinically, despite for the earlier age of onset in fAD (Shepherd et al., 2009, Bateman et al., 2011). Both forms show similar patterns of senile Aβ plagues, neurofibrillary tangles and microglial infiltration. Furthermore, both forms have hippocampal and media-temporal lobe atrophy and similar levels of biochemical markers measuring Aβ, TAU as well as phosphorylated TAU taken from cerebrospinal-fluid (CSF). Given the convergence in pathological and clinical features between fAD and sAD, it is likely that therapeutic strategy to treat fAD may also prove beneficial to sAD patients.

1.1.5 Amyloid precursor protein and its function

One of the most important proteins involved in AD pathogenesis is the amyloid precursor protein. It belongs to a family that includes the amyloid-precursor-like proteins 1 and 2 (APLP1 and APLP2, respectively). All of them are single-pass type-1-transmembrane proteins with large ectodomains and short cytoplasmic tails. They are processed in a similar manner and they share some conserved domains like the E1 and E2 domain in the extracellular sequence, but the Aβ domain is unique to APP and therefore only APP generates an amyloidogenic fragment (Figure 5).

The APP gene is located on chromosome 21 in humans, encoding 8 different isoforms, of which 3 are most common: APP695, APP751 and APP770, containing 695, 751 and 770 amino acids respectively. APP695 is predominantly expressed in neurons, whereas the latter two isoforms contain a 56 amino acid long Kunitz Protease Inhibitor (KPI) domain and are expressed ubiquitously (Bayer et al., 1999). Studies with mice have shown that APP knockout (KO) mice are viable and show few abnormal phenotypes (Zheng et al., 1995) as well as APLP1 or APLP2 KO mice (Dawson et al., 1999). APP triple KO mice as well as APP/APLP2 and APLP1/APLP2 double null mice show early postnatal lethality (Herms et al., 2004). Interestingly APP/APLP1 mice are viable, pointing into a direction that APLP2 seems to be sufficient for mice when APP and/or APLP1 are missing (Heber et al., 2000). Although APP has been the subject of several studies and investigations, its precise function still remains elusive.

APP and its cleavage products have been associated with important roles in neurogenesis, synaptic function and plasticity, neurite outgrowth, neuronal protein trafficking along the axon, cell adhesion and calcium metabolism. Additional functions for cell survival or motility or in response to cellular stress have been mentioned, but most of them still require *in vivo* evidence (Zheng and Koo, 2006). During its intracellular trafficking, APP is cleaved by different secretases resulting in generation of a variety of different metabolites, each having distinct functions and impacts on cell health and homeostasis. That is why the full net benefit of full-length APP is to be considered not only full-length APP's function, but also all metabolites (adverse) effects on a cellular level.

The site most active in the APP ectodomain are its two heparin-binding domains, with one of them being the binding-site for F-spondin and nectrin-1, the only ligands for APP identified so far. (Ho and Sudhof, 2004; Mok et al., 1997). Even though F-spondin has been associated with neuronal repair and development, APP's (Yamazaki et al., 1997) function in these processes remains elusive. Among other potential ligands are Notch, a molecule similar in structure to APP and an important signaling development molecule, as well as laminin and the Aβ peptide itself. Binding of these ligands influences the way APP is processed downstream, but the precise and signaling events are unknown and therefore APP's function as a membrane receptor remains elusive. However, there has been some evidence linking APP to cell adhesion. One study found that APP colocalizes with β-1 integrins in neural cells (Yamazaki et al., 1997) and others demonstrated that APP can form homodimers and heterodimers with other APP family members in a trans-dimerization manner, promoting intercellular adhesion (Soba et al., 2005). Another

study discovered antiparallel dimer formation via x-ray analysis (Wang and Ha, 2004). APP's intracellular C-terminus is a critical domain that serves two different functions: first, as a transcriptional regulator, and second, as a regulator of its own intracellular sorting. The YENPTY amino acid domain is responsible for internalization of APP into clathrin-coated pits, which is initiated through a series of different binding partners. To interact with the YENPTY domain, proteins must have a phosphotyrosine binding domains (PTBs). Two of these potential binding partners are X11 and Fe65, the first containing one PTB, the latter containing two PTBs. Both proteins are highly expressed in the brain and both are associated with initiating the binding of APP to the endocytic sortilin-receptor-1 (SorL1), a receptor belonging to the vacuolar protein sorting 10 (VPS10) domain receptor family.

This receptor has recently gained a lot of attention in the AD field and is already considered to be one of the top 6 AD risk genes (Holstege et al., 2017; Louwersheimer et al., 2017; Raghavan et al., 2018). SorL1, a type-1 transmembrane protein, is part of the retromer, a protein sorting complex, that helps direct APP from the endosomes back to the trans/Golgi network. By binding and interacting with APP and shuttling it back to the trans-Golgi, it limits the interaction of APP with APP-processing secretases, thereby limiting the production of toxic Aβ.

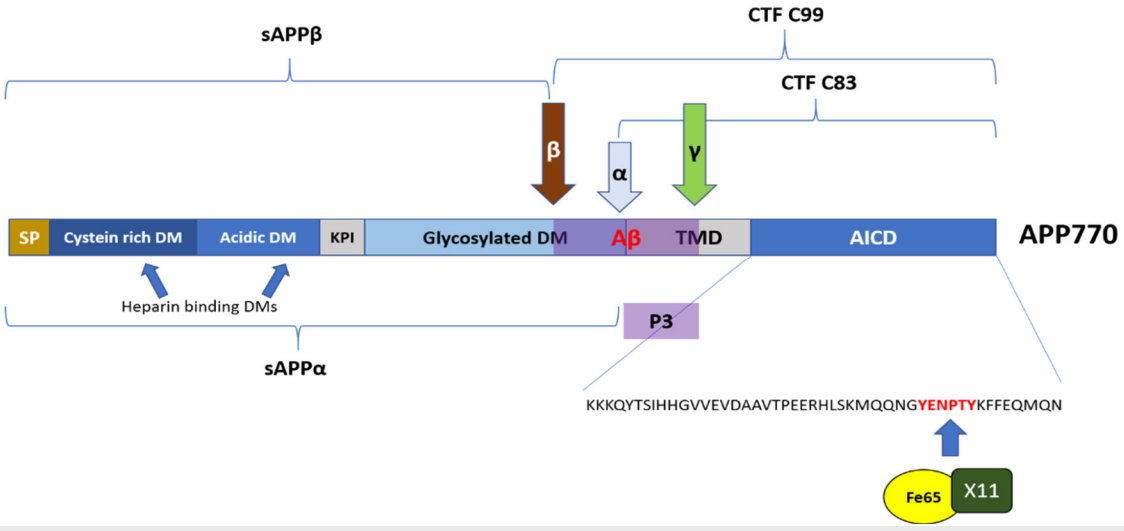

Figure 5. Amyloid precursor protein isoform 770, one of three pre-dominant APP isoforms. APP770 and APP751 are ubiquitously expressed, whereas APP695, lacking the KPI domain, is primarily expressed in neurons. KPI: kunitz-protease inhibitor region, TMD: trans-membrane domain; AICD: APP intracellular domain; arrows mark the cleavage sites for α-, β- and γ-secretase.

It is also believed that SorL1 routes Aβ peptides to the lysosome for degradation. Fe65 and X11 knock-out mice crossed with APP overexpressing mice show increased Aβ production and

accumulation, whereas mice overexpressing Fe65 and X11 show significantly lower Aβ levels (Lee et al., 2003), highlighting the importance of the APP-Fe65-X11-SorLA binding series.

This *in vivo* data is supported by data generated from genome wide association studies (GWAS). Recently, 17 rare pathogenic loss-of-function variants of SorL1 were found to segregate with AD in families and carriers developed the disease 7 years earlier than non-carriers (Raghavan et al., 2018). Further, a protective single nucleotide polymorphism (SNP) that leads to elevated SorL1 levels results in lowered Aβ in cell culture (Young et al., 2015).

1.1.5.1 Proteolytic processing of APP in neuronal cells

Processing of APP occurs in many different neuronal compartments, including dendrites, axons and nerve terminals. Full length APP is synthesized and undergoes folding in the endoplasmic reticulum (ER), followed by post-translational modification in the ER and later in the Golgi apparatus. Through secretory vesicles, APP is then transported anterograde into pre- and postsynaptic compartments. APP can be processed in two different pathways (Figure 6).

(a) In the non-amyloidogenic pathway, which is stimulated by synaptic activity (Hoey et al., 2009), APP reaches the plasma membrane and is cleaved first by the α-secretase ADAM10, a disintegrin and metalloprotease domain-containing protein (Corbett et al., 2015). Cleavage by ADAM10 results in release of a large n-terminal fragment called soluble APPα (sAPPα), which is released into the extracellular milieu, while a c-terminal fragment, α-CTF or C83 remains inserted in the membrane. This c terminal fragment is then processed by gamma-secretase (γ-secretase), an aspartyl intramembrane protease, which cleaves a wide spectrum of different type 1 integral membrane proteins and which resides in late recycling endosomes, the plasma membrane, lysosomes and the trans-Golgi network, its main active site. γ-secretase performs an endopeptidase like cleavage (ε-cleavage), which results in the release of the APP intracellular domain (AICD), followed by carboxypeptidase-like-cleavage (γ-cleavage), which generates the P3 fragment that is released into the extracellular space. Since ADAM10 cleaves APP right in the Aβ domain of APP at Leu^{17}, the P3 fragment corresponds to Aβ17-40 or Aβ14-42, and Aβ production is thus precluded in this pathway.

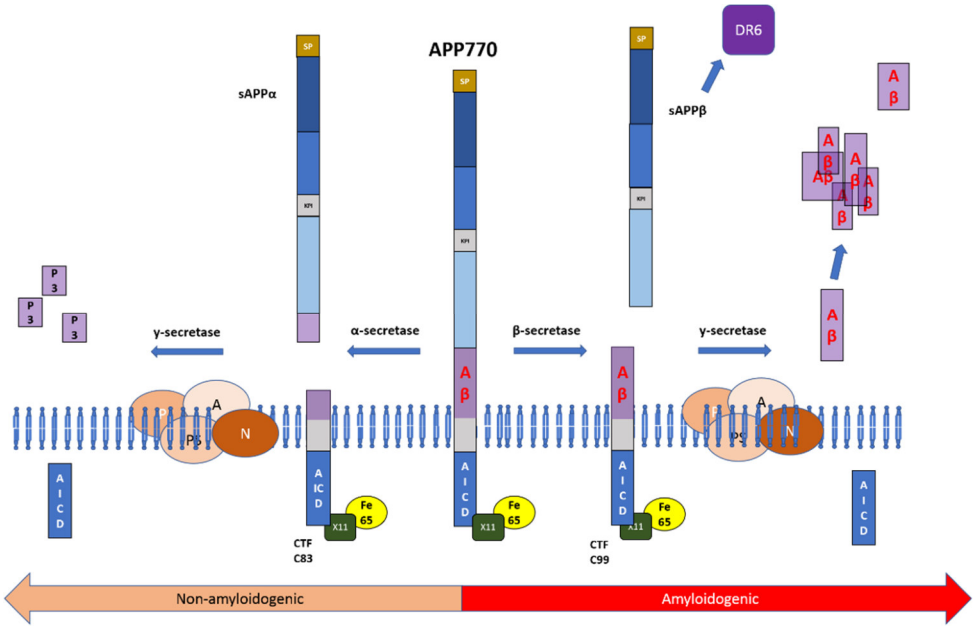

Figure 6. Proteolytic processing of APP: in the non-amyloidogenic pathway, membrane-bound APP is cleaved within the Aβ-domain by α-secretase at Leu[17], resulting in sAPPα and a CTF-83, which is then further processed by γ-secretase, releasing the P3 fragment and the AICD. In the amyloidogenic pathway, APP is processed by β-secretase first, resulting in sAPPβ and CTF-99, which is then cleaved by γ-secretase, releasing the AICD and Aβ, mostly 40 or 42 amino-acids long.

(b) In the canonical amyloidogenic pathway non-α-secretase-processed surface full-length APP (as well as non-processed sAPPα) is internalized via clathrin-dependent endocytosis, whereas the lipid-raft resident β-secretases 1 and 2 (BACE-1 and BACE-2, respectively) are internalized via clathrin-independent endocytosis. Both, full-length APP and BACE-1 and BACE-2 converge in early endosomes. The low, acidic pH of these compartments lead to activation of the ß-secretases and APP is cleaved at a site that becomes the n-terminal part of Aβ, resulting in soluble APPβ (sAPPβ) and β-secretase C-terminal fragment (CTF), which remains tethered to the membrane, while sAPPβ is released.

Through recycling endosomes, non-processed full-length APP and sAPPβ can be re-inserted into the plasma membrane again. Via the endocytic pathway, the β-CTF is then transported to the ER, the trans-Golgi network, as well as to late endosomes, lysosomes and multivesicular bodies (MVBs). The final cleavage of sAPPβ takes places in MVBs, lysosomes and mitochondria associated membranes of the ER (MAMs) (Area-Gomez et al., 2009). In these

compartments β-CTF is recognized by γ-secretase, whose cleavage results in generation of Aβ peptide and APP intracellular domain (AICD).

Under physiological normal conditions, BACE-1 predominantly cleaves the APP at the Glu^{11} site (at position 11 of Aβ), which is its major cleavage site. Cleavage at that site generates a soluble ectodomain and CTF C89, which, when processed by γ-secretase, results in a truncated Aβ' production that is non-amyloidogenic and immediately degraded (Deng et al., 2013). However, if APP is cleaved by BACE-1 at the minor Asp^{1} site, sAPPβ and a longer C-terminal fragment, C99, is produced, which is further processed and leads to Aβ generation. In detail, γ-secretase cleaves the β-CTF/C99 via endopeptidase like ε-cleavage, generating AICD and Aβ48 as well as Aβ49. These two Aβ peptides are then further processed via γ-cleavage every 3 or 4 residues within the hydrophobic sequence generating shorter Aβ peptides: Aβ48 is processed to Aβ45, Aβ42 and Aβ38, whereas Aβ49 is processed to Aβ46, Aβ43 and Aβ40. Aβ can be secreted post- or pre-synaptically (DeBoer et al., 2014), but the majority of secreted fragments in the axon are endocytosed and processed in the soma and then transported to the pre-synapse. γ-secretase itself is a multi-subunit-protein-complex, consisting of the four proteins, presenilin (either presenilin-1 or presenilin-2 respectively), anterior pharynx-defective 1 (APH-1), nicastrin and presenilin enhancer 2 (PEN2). PS1/PS2 is the catalytic subunit of γ-secretase consisting of 9 transmembrane domains (TM). APH-1, consisting of 7 TMs, appears to stabilize the complex, whereas nicastrin, consisting of only 1 TM is supposed to be the substrate recruiting component. PEN-2 is important for activation of presenilin and also maturation of the whole complex (Figure 7). γ-secretase catalyzes cleavage not only of APP, but also of other type 1 integral membrane proteins like Notch, N-Cadherin and CD44 (Edbauer et al., 2003; Lammich et al., 2002; Sato et al., 2007). Overall, APP intra-neuronal processing is regulated very strictly and APP as well as the secretases are transported together through the secretory pathway along axons to dendrites and synaptic terminal into boutons. α-secretase resides and cleaves primarily at the plasma membrane, whereas β- and γ -secretase undergo exocytosis first to reach the plasma membrane, followed by endocytosis and retrograde trafficking to reach their final active compartments.

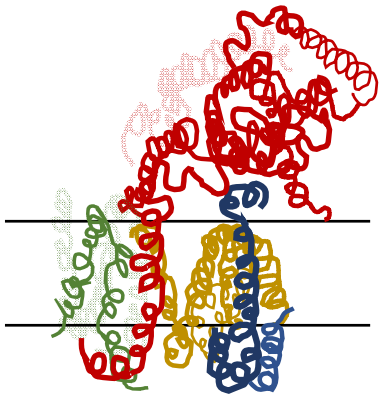

Figure 7. Schematic overview of γ-secretase complex in its typical „horse-shoe" conformation consisting of PS1/S2 (yellow), Nicastrin (red), APH-1 (green) and PEN-2 (blue).

1.1.5.2 Impact of Aβ and other proteolytic fragments of processed APP

Amyloid beta

Cleavage of APP by β-secretase followed by proteolytic processing by γ-secretase produces Aβ peptides, mostly ranging in size from 38-49 amino acids. The most common forms are Aβ42 and Aβ40 with the former being more neurotoxic than the latter. While Aβ40 is a soluble variant of the peptide, which only very slowly converts into the insoluble β-sheet conformation, Aβ42 is highly fibrillogenic (Zhang et al., 2002) and has a stronger tendency to aggregate (Haass and Selkoe, 2007; Jarrett et al., 1993; Klein et al., 1999). Aβ monomers exist in equilibrium with dimers, trimers, oligomers, multimers and they also form fibril rich assemblies known as senile plaques, which are the end stage lesions of AD (Polanco et al., 2018). Originally it was thought that senile plaques correlate mostly with memory and cognitive impairment, but recent studies have shown that plague burden does so poorly, unless it has progressed to involve the striatum.

How exactly Aβ is aggregating, once it is secreted into the extracellular space, and how it forms the senile plaques is still poorly understood. It is known however that insoluble Aβ fibrils can also be formed inside the cell, a toxic process caused by internalization of Aβ, that ultimately leads to disturbance of MVBs and cell death (Friedrich et al., 2010). Emerging evidence suggests that soluble Aβ oligomers are the most toxic species, driving neurotoxicity and neurodegeneration (Figure 9) (Catalano et al., 2006; Cleary et al., 2005; Shankar et al., 2008; Yang et al., 2017). The oligomers formed by Aβ can be categorized into two different classes, type 1 and type 2 oligomers. Type 1 oligomers, including the recently described Aβ*56 dodecamers -based on their 56 kDa size- do not grow into larger assemblies (Lesne et al., 2006). They appear early in AD, they can travel through the brain and they are likely to interfere with synaptic function and cause cognitive impairment as shown with Aβ*56 oligomers in human samples and mouse models (Lesne et al., 2013). Type 2 oligomers are visible only after plaques have formed, always in very close proximity to them, where they form stable structures. They are of high molecular weight, show little cytotoxic activity in *in vitro* bioassays (Yang et al., 2017) and are most likely sequestered by the plaques. However, under certain conditions, they are able to dissociate from the plaques and into smaller, very high bioactive oligomers and they might be the reason that neurons surrounding plaques show clear symptoms of toxicity like dystrophic neurites, synaptic loss and elevated calcium levels (Bezprozvanny, 2009). Given the fact that the plaques sequester these high molecule weight oligomers, they might be considered as neurotoxic, but mainly inactive reservoirs of inert fibrils that coexist with mostly high molecular weight oligomers (Polanco et al., 2018).

Recent studies suggest that under certain conditions these HMW species can dissociate into smaller, low molecular weight oligomers, who are more bioactive and therefore do show more disease relevant activity (Yang et al., 2017) leading to the typical symptoms like neuritic dystrophy, astrocytosis and microglioses and neurofibrillary tangle formation.

Aβ Impact on Synaptic Toxicity

Aβ oligomers cause loss and dysfunction of synapses by acting on different synaptic receptors like N-methyl-D-aspartat (NMDA), α7-nicotinic acetylcholine (α7-nACh) and α-amino-3-hydroxy-5-methyl-4-isoxazolepropionic acid (AMPA) receptors, which are needed for synaptic plasticity. NMDA receptors are important, because they are required for long term potentiation (LTP) as well as for long term depression (LTD). While the former is a process involved in memory encoding in the hippocampus, the latter is involved in memory decay (Kandel et al., 2014). It is widely accepted that Aβ oligomers can directly bind to NMDA as well as AMPA receptors, and that AB oligomers decrease levels of the NMDA adaptor protein postsynaptic density protein 95 (PSD95), further negatively regulating these receptors through endocytosis and causing a reduction in the expression of receptor subunits. This leads to disruption of LTP and dendritic spine loss. Additionally, Aβ oligomers also cause enhanced LTD by interfering with glutamate uptake at the synapses (Li et al., 2009).

Effects on Microglia

It is accepted that senile plaques as well as Aβ oligomers activate the brain's immune system due to their toxicity, including activation of astrocytes and microglial response (Heneka et al., 2015). However, different activation pathways are likely involved for each process. For microglial activation, Aβ oligomers are thought to increase microglial chemokine and cytokine production, while at the same time diminishing their ability of phagocytosing the Aβ deposits (Pan et al., 2011; Sondag et al., 2009).

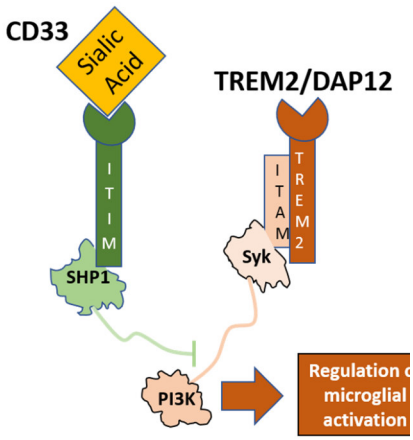

Figure 8. Two main regulators of microglial activation: by blocking or activating phosphatidylinositol-3 kinase (PI3K), Trem2 and CD33 have opposing actions on activation of microglia and phagocytosis of Aβ. Mutations in both genes can impair Aβ clearance.

Additionally, Aβ oligomers and plaques have been reported to involve the classical complement cascade and several elements of

this cascade can be found in close proximity especially to the plaques (McGeer et al., 1989). In recent years, genetic variability in that system has been discovered pointing to at least three AD risk genes and therefore implicating components of innate immunity and the well-known complement cascade as risk factor in AD (Jones et al., 2010). These newly discovered risk genes include CD33 (Bertram et al., 2008; Hollingworth et al., 2011), Complement Receptor 1 (CR1)(Lambert et al., 2009) and triggering receptor expressed on myeloid cell 2 (TREM2), all of them involved in microglial response. CD33 is a transmembrane protein and a sialic acid-binding immunoglobulin-like lectin that regulates innate immunity but has no known functions in the brain. It is, however, highly expressed in the AD brain and CD33-immunoreactive microglia are positively correlated with insoluble Aβ42 levels and plaque burden. Inactivation due to a rare loss-of-function mutation potentiates microglial uptake of Aβ (Figure 8) (Griciuc et al., 2013; Wang et al., 2015). CR1 is a transmembrane glycoprotein, highly expressed on blood cells and microglia. If CR1 is blocked, the complement cascade and resulting microglial activation is inhibited, and microglial phagocytosis is modulated. While it is increased for molecules like Dextran, a complex branched glucan, it is reduced for Aβ, illustrating that loss-of-function mutations in CR1 correlate with decreased Aβ clearance and accelerated AD pathogenesis (Crehan et al., 2013). The third risk gene, TREM2, is a member of the immunoglobulin superfamily and a Type 1 single-transmembrane receptor, which is primarily expressed in microglia, but also in osteoclasts and macrophages. TREM2 is processed like APP in the non-amyloidogenic pathway by a member of the disintegrin and metalloprotease domain-containing protein family followed by γ-secretase cleavage (Kleinberger et al., 2014; Wunderlich et al., 2013). While its biology is not fully understood yet, TREM2 has recently emerged to be one of the crucial players in CNS response to Aβ accumulation (Forabosco et al., 2013; Matarin et al., 2015). Preliminary data suggest that TREM2 may affect AD pathogenesis via phagocytosis of Aβ and via Aβ-related neuroinflammation. Patients with certain genetic variants of TREM2, the best known one being R47H, incur a higher risk of developing sAD, similar to the risk that APOE4 carriers face (Guerreiro et al., 2013; Jonsson et al., 2013; Rayaprolu et al., 2013). Expression levels of these three recently identified risk genes go up whenever plaque prevalence increases (Griciuc et al., 2013) and TREM2 levels in the cerebrospinal fluid also increase, possibly qualifying it as potential biomarker for AD (Suarez-Calvet et al., 2016).

Mitochondrial dysfunction

Neurons are highly dependent on mitochondrial energy production due to their limited glycolytic capacity. Mitochondria are present in all cellular compartments of neurons but are at the highest abundance in synapses (Reddy, 2007). Mitochondria serve as the master regulators of energy production, and their main functions include: (a) oxidative phosphorylation, (b) removal of damaged mitochondria by autophagy (Mitophagy), (c) mitochondrial dynamics (d) bioenergetics and (e) apoptosis. All these functions are impacted in AD in large part due to Aβ toxicity (oligomeric Aβ and also Aβ fibrils can cause these mitochondrial defects, whereas Aβ monomers do not seem as toxic (Eckert et al., 2008)). AB mediated mitochondrial dysfunction thus ultimately leads to neurodegeneration via disrupted synaptic transmission, impaired synaptic plasticity, and widespread apoptosis.

Cholesterol/sterol metabolism

Various forms of Aβ have been associated with controlling the cholesterol *de novo* synthesis and sphingomyelin levels (Grimm et al., 2016; Puglielli et al., 2003). The main enzymes which control the cholesterol synthesis and sphingomyelin levels (SM) are Hydroxymethylglutaryl-CoA reductase (HMGR) and sphingomyelinases (SMases), respectively, and Abeta42 directly activates neutral SMase and downregulates SM levels, whereas Abeta40 reduces cholesterol *de novo* synthesis by inhibition of HMGR activity (Grimm et al., 2016).

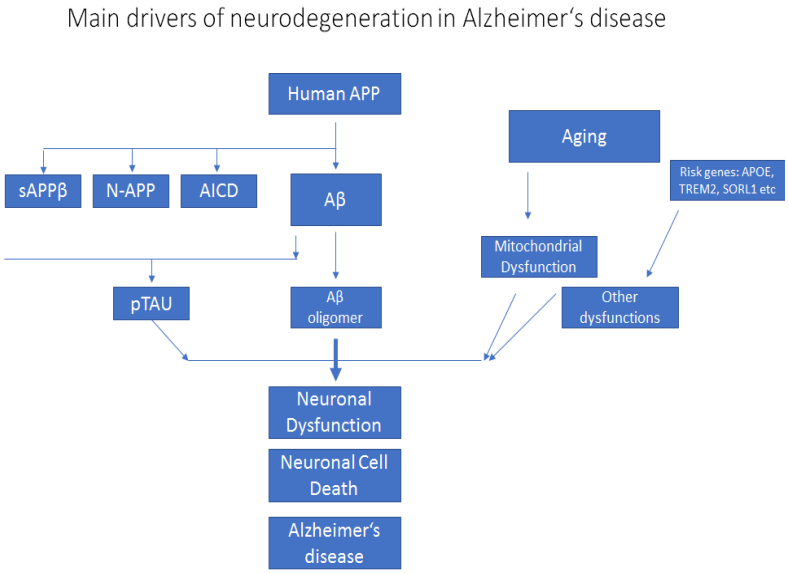

Post translational modifications

Aβ can also undergo a variety of post-translational modifications at the N-terminus, including phosphorylation, nitration, oxidation and pyroglutamylation, all of which can impact its fibril-forming and oligomerization properties (Kummer and Heneka,

Figure 9. Schematic view of main drivers of neurodegeneration in AD. Although the Aβ-hypothesis postulates that Aβ induces TAU pathology, other proteolytic fragments also appear to contribute to TAU pathology and other neuronal dysfunctions.

2014). Pyroglutamate modifications at specific residues have been associated with a tendency to aggregate *in vitro* (Nussbaum et al., 2012), whereas phosphorylation triggers the formation of Aβ oligomers that are more resistant towards degradation (Kumar et al., 2012). Nitrated Aβ, usually present in the center of senile plaques and therefore associated with plaque initiation, can inhibit LTP longer than non-nitrated peptides (Al-Hilaly et al., 2013; Kummer et al., 2011) and oxidation leads to the formation of ion-like-channel complexes in lipid membranes (Barnham et al., 2003).

However, besides its neurotoxic effects, it is important to mention that production of Aβ is a normal physiological process, that is even enhanced by synaptic activation(Kim et al., 2013; Li et al., 2013). Aβ is also associated with beneficial processes: It is associated with regulating synaptic scaling, synaptic physiology and synaptic vesicle transport (Abramov et al., 2009; Chen et al., 2006; Kamenetz et al., 2003). As long as there is balance between production and clearance from the brain, neurotoxicity and later cognitive decline is not dramatic. With increased age however, the clearance mechanism of Aβ is not as efficient, and Aβ subsequently accumulates in aggregates to cause the toxic cascade of neurodegenerative events.

C99 and β-CTF

C99 is linked to defective degradation pathways, which are involved in AD pathogenesis-endolysosomal and autophagic anomalies are specific early features of AD pathology (Nixon, 2007; Nixon et al., 2000; Shacka et al., 2008). Accumulation of C99 is both the cause of and result of impaired lysosomal-autophagic function (Lauritzen et al., 2016), linked to its aggregation within endosomal-autophagic-lysosomal-vesicle membranes and therefore in an Aβ independent manner. C99 has additionally been associated with mitochondrial dysfunction. In cellular models, C99 concentration in mitochondria-associated-membranes (MAM) of the endoplasmic reticulum was elevated, resulting in increased sphingolipid turnover and changes in lipid compositions of both membrane types that perturbed mitochondrial and bioenergetic functions. Cellular models have shown that C99 is directly or indirectly linked to levels of tau. Accumulation of C99 in cellular models by using γ-secretase inhibitors led to increased intracellular tau protein levels, whereas decreased C99 levels from β-secretase inhibitors showed the decreased intracellular tau (Moore et al., 2015).

Despite being a cleavage product generated in the amyloidogenic processing of APP, sAPPβ has been associated with neurotrophic functions (Furukawa et al., 1996). It is supposed to decrease cell adhesion and increase axonal outgrowth *in vitro* (Chasseigneaux et al., 2011). It also

induces rapid neural differentiation of human embryonic stem cells in a more efficient manner than sAPPα (Freude et al., 2011). Besides that, neurotoxic functions for sAPPβ have also been reported. Triggered by neurotrophic factor depletion sAPPβ production increases, but its proteolytic cleavage is also induced and a small 35kDa N-terminal fragment called N-APP is released. N-APP then binds to death receptor 6 and further downstream processes activate caspase 6 and caspase 3, causing axonal pruning and apoptosis (Nikolaev et al., 2009).

sAPPα and P3

Little is known about the P3 peptide (corresponding to Aβ 17-40 or Aβ 17-42), derived by α- and γ-secretase cleavage of APP, and its potential toxic or beneficial properties are not clear. P3 peptides have been reported as being a major constituent of diffuse plaques in Alzheimer's disease and cerebellar pre-amyloid in Down's syndrome. However, while it has been reported that P3 is unable to assemble into stable oligomers to cause synaptotoxic effects (Dulin et al., 2008), studies have also linked P3 neuronal cell death. Human neuroblastoma cell lines treated with P3 fragments showed activation of c-Jun N-terminal kinase, caspase-3 and caspase-8, suggesting that it induces apoptosis via a Fas-like/caspase-8 activation pathway (Wei et al., 2002).

Like sAPPb, sAPPα is also associated with neuroprotective functions, even though many details of its function remain elusive. sAPPa is approximately 100-fold more potent than sAPPβ in protecting hippocampal neurons against excitotoxicity, Aβ toxicity and glucose deprivation (Furukawa et al., 1996). Additionally, sAPPa may play an important role in neuronal plasticity and cell survival, may increase long-term potentiation (Ishida et al., 1997) and may serve as a proliferation factor of adult neural precursor cells (NPCs) (Demars et al., 2011; Demars et al., 2013)

AICD

The APP intracellular domain, corresponding to the amino acids 49/50-99 of the C-terminal fragment of APP, is mainly produced by the amyloidogenic pathway (Goodger et al., 2009), since it is not released from plasma-membrane bound APP (where cleavage by α-secretase occurs during the non-amyloidogenic pathway). AICD is difficult to detect *in vivo* and in cellular models because it is quickly inactivated and degraded, either by caspases (Lu et al., 2000) yielding a fragment call C31, or by cytosolic and endosomal insulin-degrading-enzymes (Edbauer et al., 2002), which cleaves AICD at multiple sites (Venugopal et al., 2007). AICD is mainly associated with transcriptional regulation, as it is known to form a complex with Fe65 and TIP60 histone acetyl transferase (AFT complex), which trans-locates to the nucleus (von Rotz et al., 2004). However, the

net effect of AICD on transcriptional function remains blurry (Slomnicki and Lesniak, 2008) and needs further investigation.

1.1.6 AD pathogenesis: a crosstalk between brain and peripheral tissues

Traditionally, AD is considered to be a disorder of the CNS. There is, however, new evidence emerging that AD's manifestations extend beyond the brain. Clinical, experimental and also epidemiological data suggest that systemic and peripheral alterations could reflect underlying processes linked to progression of the disease, rather than simply being secondary effects of cerebral degeneration.

Indeed, maintaining the homeostatic balance between beta-amyloid metabolism/production and clearance is essential for normal and healthy brain function (which when imbalanced, can cause AD (Selkoe and Hardy, 2016). However, amyloid-beta metabolism does not only occur in the brain, it also occurs in the periphery. This fact, as well as the regulatory feedback loops connecting peripheral tissues with the CNS, highlights the importance of a crosstalk between amyloid-beta biogenesis and metabolism in different regions of the body.

In the brain, APP is expressed by astrocytes, neurons and microglia, and Aβ is subsequently produced in these cells by the sequential cleavage of APP by beta-secretase and gamma-secretase. APP is also expressed in the periphery by a variety of different tissues and organs including the kidney, liver, pancreas, heart, various endothelial and blood cells, and muscle cells (Roher et al., 2009)**,** all of which serve as a large potential source of peripheral beta-amyloid production. Given that skeletal muscle accounts for almost 25% of human body weight highlights the importance that peripheral produced beta-amyloid might have on AD pathogenesis. However, there are important differences between peripheral and brain produced beta-amyloid. Aβ40 is the most dominant form produced by peripheral tissues and organs, whereas Aβ42 is more abundant in the brain. This could be explained by differential expression of the several different isoforms of APP. The main isoform produced in the brain is APP695, which lacks the KPI-domain (Kang and Muller-Hill, 1990; Rohan de Silva et al., 1997), while the main isoforms produced in the periphery are APP770 and APP751. The levels of beta-amyloid are much higher in the brain than in the periphery. Measurements of amyloid-beta in the cerebrospinal fluid (CSF) compared with the plasma indicate that they are 5-15 times higher in the former (Mehta et al., 2001). This could easily be explained due to the high volume of the cardiovascular system, which would dilute peripheral Aβ concentrations. But it could also mean that Aβ is processed more often in the non-

amyloidogenic pathway and therefore cleaved by α-secretase or cleared by specific peripheral pathways (Delvaux et al., 2013).

Aβ can be cleared from the brain using many different pathways: via proteolytic degradation by enzymes like neprilysin or insulin-degrading enzyme; via endocytosis, phagocytosis or micropinocytosis by neurons, astrocytes, microglia, oligodendrocytes and perivascular macrophages. Additionally, Aß can be cleared via efflux into the peripheral pool through the blood-brain-barrier (BBB) using transporter like LDL-related protein 1 (LRP1) (Mackic et al., 1998), through the blood-CFS barrier (BCB) mediated by arachnoid villi which absorb the Aβ before releasing it into the blood circulation, or the glymphatic-lymphatic pathway. It has been shown that 40-60% of the Aβ produced in the brain is cleared via transport into the periphery (Xiang et al., 2015), which highlights the importance that peripheral tissues and organs have in Aβ clearance, how important the interaction between brain Aβ pool and peripheral pool might be, but also how important their flawless functioning for AD pathogenesis might be. How Aβ is cleared in the periphery remains poorly understood so far. Several pathways have been associated with peripheral clearance: via Aβ-binding lipoproteins like apolipoprotein E (ApoE) and apolipoprotein J (ApoJ) including uptake and phago- or endocytosis by macrophages, monocytes, hepatocytes or lymphocytes (Bradshaw et al., 2013; Kanekiyo and Bu, 2014); proteolytic degradation by Aβ-degrading enzymes (Liu et al., 2012); excretion via urine (Ghiso et al., 1997).

It is not totally clear if or how peripheral produced Aβ can enter the brain, but recent studies in humans and mice provide strong evidence that peripheral AB can cross the BBB (Jaunmuktane et al., 2015; Ritchie et al., 2017). The receptor for advanced glycation end products (RAGE) has been suggested to be the potential mediator for transporting Aβ from the periphery into the brain via the BBB (Deane et al., 2003) meaning that the BBB would act bidirectional regarding Aβ transport (whereas the glymphatic-lymphatic and the arachnoid villi mediated pathways are unidirectional). Moreover, there is evidence that peripheral derived Aβ worsens AD pathology once in the brain, but also that the rate in which peripheral Aβ is cleared influences the amount of brain derived Aβ that can enter the peripheral pool via BBB (Eisele et al., 2014; Eisele et al., 2010). These new insights highlight how both pools of Aβ are affecting each other, although more work is needed to fully understand the mechanism underlying each.

1.1.7 Microtubule associated protein tau

Even if the amyloid-beta hypothesis suggests that Aβ is the initial cause of AD, the amount of insoluble senile plaques in patients affected by the disease does not correlate with severity of cognitive decline and dementia, whereas tau pathology, in the form of neurofibrillary tangles, clearly does (De Strooper and Karran, 2016; Hardy and Selkoe, 2002; Spires-Jones and Hyman, 2014). These tangles are composed of insoluble microtubule-associated protein tau (MAPT or tau) fibrils which highlights the gene's importance in AD pathology. MAPT is a natively unfolded protein, which is highly concentrated in the axonal part of neurons. It is associated with the assembly and stabilization of microtubules and therefore thought to support cell differentiation, polarization, and other processes involving the cytoskeleton. Recent work also suggests an additional role for tau in other neuronal compartments like dendrites (Ittner et al., 2010). In the human brain, six different isoforms of MAPT can be found, which are produced by alternative splicing of the mRNA of the MAPT gene located on chromosome 17q21.31 (Andreadis et al., 1992; Goedert et al., 1989). These splicing isoforms differ from each other by the absence or presence of a 29- (N1) or 58-amino acid (N2) long insert, encoded by exons 2 and 3 respectively, in the N-terminal acidic region of the protein resulting therefore in the three isoforms 0N-, 1N0- and 2N-TAU respectively. Depending on the inclusion or exclusion of a 31-aminoacid repeat region in the microtubule binding domain in the carboxy-terminal half of the protein encoded by exon 10, these three isoforms can have a total of 3 repeats (3R) or 4 repeats (4R) resulting in 0N3R, 1N3R, 2N3R or 0N4R, 1N4R and 2N4R-TAU, respectively (Goedert and Jakes, 1990). Figure 10 shows a schematic overview of the longest TAU isoform 4R2N and lists the other potential isoforms as well.

In the human cerebral cortex of healthy adults, an equimolar ratio of these 3R and 4R tau isoforms exists (Goedert and Jakes, 1990), and it has been shown that shifting the ratio in either direction results in impaired cellular functions (like axonal transport) and leads to clinical manifestations of tauopathies. For example, shifting the ratio towards 3R tau results in Pick's disease, whereas a shift

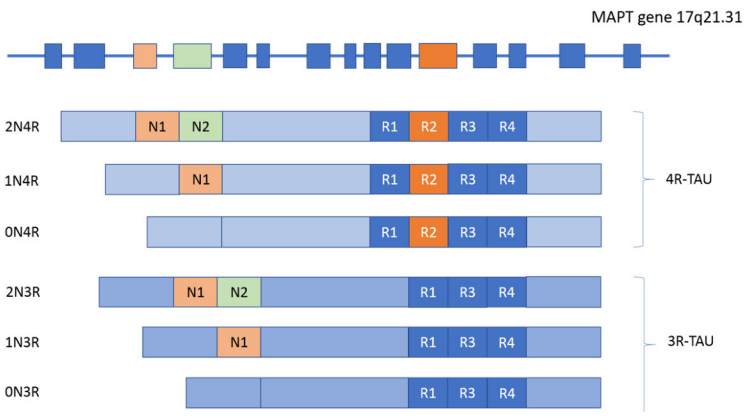

Figure 10. Scheme of different isoforms of TAU. The six isoforms differ by the number of microtubule binding domains in the C-terminal part and by the presence or absence of one or two 29 amino-acids-long inserts in the N-terminal part.

towards 4R is highly associated with corticobasal degeneration (Ksiezak-Reding et al., 1994). Tau undergoes several post-translational modifications, of which acetylation and phosphorylation at its serine, threonine and tyrosine residues are the most common.

In AD, tau toxicity is mainly caused by pathological forms of tau, which aggregate in neuronal compartments with normally low concentrations of tau like the soma or dendritic spines. It is hypothesized that post-translational modifications, particularly phosphorylation (called hyper-phosphorylation), as well as acetylation lead to or intensify tau aggregation. While it is still being elucidated how axonal MAPT is able to accumulate in the somato-dendritic compartment, it is hypothesized that MAPT, once hyper-phosphorylated, is able to detach from microtubules and, as its cytoplasmatic levels increase, pass retrograde through the axon initial segment, which provides a diffusion barrier for normal phosphorylated MAPT. Hyperphosphorylated MAPT can then accumulate and aggregate in the soma and dendrites (Li and Gotz, 2017), forming insoluble fibrils and neurofibrillary tangles that can fill almost the entire soma.

Being natively unfolded, tau assembles into insoluble filaments after transitioning from a random-coil structure to a cross-β structure characteristic of all amyloid filaments and finally into neurofibrillary tangles, which are highly associated with progressive loss of dendritic spines and dendritic atrophy. Fibril assembly itself occurs through its tandem repeats, with the carboxy-terminus and the amino-terminus forming the so called “fuzzy coat” of the filament (Goedert et al., 1988; von Bergen et al., 2005; Wegmann et al., 2013; Wischik et al., 1988). Importantly, preceding fibril formation, tau first forms oligomers which by themselves have been associated with severe synaptic dysfunction and memory loss (Lasagna-Reeves et al., 2011; Usenovic et al., 2015). It is still debated if the intraneuronal neurofibrillary tangles cause toxicity by active cascades post formation, or if instead, they are inert neuronal threats that merely disrupt and impair physiological functions inside the neuron due simply to their size (Merino-Serrais et al., 2013; Santacruz et al., 2005).

In a healthy brain one mole of tau protein has an average of 1.9 moles of phosphate, whereas tau found in the abnormal filaments of AD patients has an average of 6-8 moles of phosphate (Kayed et al., 2007). Some sites are more phosphorylated in the diseased brain, other are *de novo* and solely phosphorylated. Tau hyperphosphorylation by virtue of increased activity of kinases and also decreased activity by phosphatases, is assumed to be required for accumulation of fibrillar tau in the somatodendritic compartment (Hoover et al., 2010; Xia et al., 2015). Over the past years many potential phosphorylation sites (Ser202, Thr205, Ser396, Ser404 e.g.) and the

potential appropriate kinases associated with tau-phosphorylation have been investigated. Prolin-directed kinases like glycogen synthase 3 (GSK3), cyclin-dependent kinase 5 (CDK5) and mitogen-activated protein (MAP) kinases have been implicated in the hyperphosphorylation of tau as well as several SRC kinases, especially the tyrosine-protein kinase FYN (Goedert and Spillantini, 2006; Hanger et al., 2009; Lee et al., 1998; Pelech, 1995). One of the most prominent phosphatases involved in de-phosphorylation is protein phosphatase 2 (PP2A), which has been reported to be less expressed and active in the brain of patients suffering from AD (Gong et al., 1993; Vogelsberg-Ragaglia et al., 2001). How easily tau becomes phosphorylated or de-phosphorylated strongly depends on its conformation, with the *cis*-conformation being a pathogenic driver in AD (cis-confirmation is more resistant to PP2A dependent de-phosphorylation and degradation). If tau becomes hyperphosphorylated, it becomes unable to interact with microtubule, disrupting existing microtubule networks, sequestering normal unphosphorylated tau and other proteins like microtubule associated protein 2 (MAP2) and ultimately impairing neuronal function leading to axonal degeneration. Mediated by microtubule-dependent kinesin motor proteins, hyperphosphorylated tau also impairs the anterograde axonal transport of cargos, like mitochondria or even APP (which will be further discussed in the section Crosstalk Aβ and TAU). Hyperphosphorylated TAU has additionally been shown to reduce hippocampal excitability by relocating the axon initial segment further down the axon, resulted in reduced excitability and decreased action potential firing (Hatch et al., 2017). Tau can also undergo acetylation, which predominately occurs post phosphorylation and both impairs tau's ability to bind to microtubule and increases its tendency to assembly into filaments (Cohen et al., 2011; Irwin et al., 2012; Min et al., 2010).

1.1.8 Crosstalk between Aβ and tau

According to the amyloid-beta hypothesis, an imbalance of production and clearance of Aβ42 and its related peptides starts a cascade that leads to downstream hyperphosphorylation of tau and neurofibrillary tangles (Selkoe and Hardy, 2016). Recent studies have additionally painted a more complex picture about how Aβ and tau can influence and interact with each other directly) to mediate toxicity in neurons. Aβ and tau can interact synergistically in many different neuronal compartments and pathways. In dendrites and spines, tau can mediate Aβ toxicity by initiating the localization of the tyrosine kinase FYN into this compartment. Tyrosine Kinase FYN can then phosphorylate the NR2B subunit of NMDA receptors, recruiting post synaptic density protein 95 (PSD95) and forming a NMDA receptor-PSD95-complex. Aβ can then mediate excitotoxicity

through this complex. The kinase FYN seems to be an important mediator between Aβ and tau in AD pathology because it has also been shown that Aβ oligomers are able to start tau *de novo* synthesis in the somato-dendritic compartment, a process mediated by FYN, ribosomal protein S6, MAPK1 and MAPK3 kinases (Li and Gotz, 2017). Another pathway involved is the calcium/calmodulkin-dependent protein kinase 2 (CAMKK2)-AMP kinase pathway, which involves Aβ*56 oligomers. These type I oligomers are able to form a complex with NMDA receptors, leading to aberrant increases in intracellular calcium levels while also activating calcium/calmodulin-dependent protein kinase type II subunit-α (CaMKIIα) to phosphorylate tau and facilitate the assembly of the postsynaptic excitotoxic signaling complex. Last but not least, Aβ oligomers can utilize microtubules broken down by tau as well as the proteins tubulin tubulin-tyrosine ligase-like protein 6 and spastin to cause synaptic damage (Zempel et al., 2013).

Aβ and tau can additionally interact synergistically to lower mitochondrial membrane potential and synthesis of ATP and respiration, thereby lowering energy production while simultaneously increasing the amount of damaging reactive oxygen species (ROS). AB and tau also further impair mitochondrial functions such as transport, fission and fusion, as well as impair mitophagy (Amadoro et al., 2014; Manczak and Reddy, 2012; Perez et al., 2018; Rhein et al., 2009; Vossel et al., 2015). Overall, tau is not only a mediator but also an essential factor driving Aβ‘s toxicity, and their cumulative interactions result in impaired and interrupted neuronal energy homeostasis, excitotoxicity, synaptic damage and neuronal degeneration. It will therefore be important to continue analyzing the synergistic pathological effects Aβ and tau have.

1.1.9 Familial Alzheimer’s disease and its relevance

Most AD cases are sporadic, with an age of onset 65 years and older. However, 1-5% of cases are familial, with an early age of onset (therefore called early-onset or familial AD (eoAD or fAD, respectively)). Familial AD is caused by mutations in the genes amyloid precursor protein (APP), Presenlin 1 (PS1) or Presenilin 2 (PS2), and so far 32 APP, 179 PS1 and 14 PS2 gene mutations have been discovered (Tanzi, 2012). Most of these mutations are clustered close to the proteolytic cleavage sites of β- and γ-secretase that are responsible for generation of beta-amyloid. Most pathogenic missense mutations in the genes PS1 and PS2, coding for the catalytic sub-units of γ-secretase, shift the γ-secretase cleavage site towards longer, more aggregation prone Aβ peptides. As this current work will investigate mutations solely in the gene APP, we will set the focus on these.

All known AD causing mutations in the gene APP are dominantly inherited except for an A673V (AV; "Italian mutation") mutation at amino acid position 673 in Exon 16, which was reported first in an Italian family (Di Fede et al., 2009) and is inherited recessively. The 32 discovered mutations are point mutations on 17 different residues, most of them in close proximity to secretase cleavage sites (Zhang et al., 2017). Many of them have been studied and have been shown to cause fAD by either inhibiting the non-amyloidogenic α-cleavage of APP (E693G, "Arctic mutation") (Nilsberth et al., 2001; Sahlin et al., 2007), by accelerating Aβ40 fibril formation (D694N; "Iowa mutation; E693Q, Dutch mutation;) (Van Nostrand et al., 2001; Wisniewski et al., 1991), by increasing the Aβ42 levels or the ratio of Aβ42/40 (I716V Florida mutation; V717I, London mutation) (Eckman et al., 1997; Goate et al., 1991), by increasing total levels of Aβ42 and Aβ40 and C99 production (KM670/671NL, Swedish mutation) (Deng et al., 2013; Mullan et al., 1992; Perez et al., 1996) or by altering the Aβ's oligomerization and aggregation properties (A673V, Italian mutation) (Di Fede et al., 2009; Maloney et al., 2014).

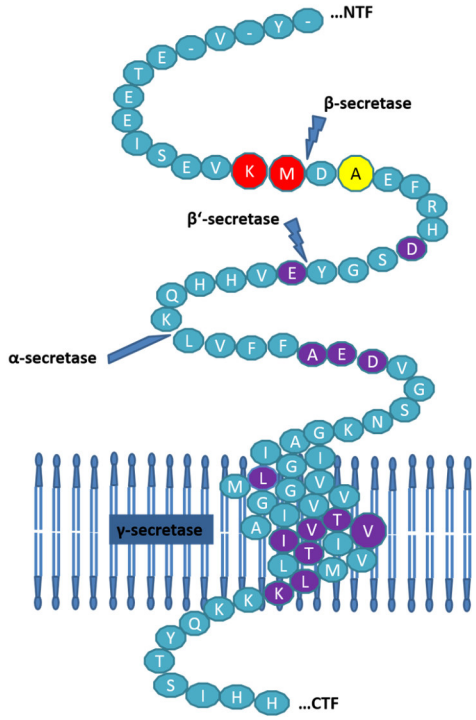

Figure 11. Scheme of fAD associated mutations in APP. Pathogenic mutations are highlighted in purple. Swedish mutation is highlighted in red, protective AT and pathogenic AV mutation are highlighted in yellow at position 673 highlighted in yellow.

However, a protective mutation in APP, also at amino acid 673, A673T (AT, "Icelandic mutation"), protective not only against AD development but also cognitive decline in the elderly in general, has recently been reported (Jonsson et al., 2012), resulting in decreased cleavage by β-secretase and increased cleavage by α-secretase. The finding suggests that amino acid position 673 of APP might be very crucial and eventually critical for BACE1 cleavage site selection during APP processing (Figure 11).

It is important to highlight that most of the fAD mutations in APP not only increase the amount of total Aβ, its Aβ42/Aβ40 or its metabolites like C99, but they also modify aggregation kinetics of Aβ and therefore its toxicity as well as APP's

turnover rate for cleavage by BACE1, making it a more or less favorable substrate for the secretase.

1.2 Derivation of human induced pluripotent stem cells

In 2006, Takahashi and Yamanaka published groundbreaking data on the generation of pluripotent stem cells from mouse embryonic fibroblasts (MEFs). They stated that by ectopic expression of four transcription factors, Oct4, Sox2, c-Myc, and Klf-4 (Takahashi and Yamanaka, 2006), delivered by viral transduction, they could reprogram somatic cells and turn them into a pluripotent state. They called these cells induced pluripotent stem cells (iPSCs)(Takahashi and Yamanaka, 2006). Soon after this amazing discovery, other groups recapitulated and confirmed their factor based reprogramming method in murine cells (Maherali et al., 2007; Wernig et al., 2007) and shortly after it was reported that iPSCs could be generated from human somatic cells as well, maintaining a normal complement of chromosomes and behaving like ESCs derived from human embryos (Park et al., 2008; Takahashi et al., 2007; Yu et al., 2007).

Looking back, the invention and production of iPSCs built upon a combination of numerous important findings from the past, mainly influenced by three different scientific areas. First, experiments by Gurdon, et al, demonstrated that a nucleus taken from a differentiated frog cell could, when injected into unfertilized eggs, give rise to tadpoles and fully developed frogs (Gurdon, 1962). Prior to this time, it was thought that an irreversible change occurred in cells as they became more specialized. Indeed, there is currently no evidence in biology of development moving backwards, or of cells acquiring the potential to become other cell types under natural conditions. Gurdons experiments thus demonstrated a paradigm shift indicating that the differentiated state of a cell is plastic and reprogrammable. These experiments were complemented more than three decades later by Wilmut and colleagues, who reported the successful cloning of the sheep “Dolly” by somatic nuclear transfer (SCNT) (Wilmut et al., 1997), expanding Gurdon’s experiment to mammals. These experiments not only proved that oocytes contain all the necessary material/transcription factors to reprogram nuclei from somatic cells, but that even differentiated, somatic cells contain all the necessary information required for the development of whole new organisms. These experiments clearly raised the possibility that any differentiated cell could be restored to a pluripotent state which, in turn, could re-differentiate into any cell type.

These scientific breakthroughs were additionally accompanied by advances in the field of transcriptional networks. In 1987, Schneuwly and colleagues reported the discovery of a transcription factor in Drosophila, which when ectopically expressed lead to the formation of legs instead of antennae (Schneuwly et al., 1987). This was then followed by the discovery of the mammalian transcription factor MyoD, which is sufficient to convert fibroblasts into myocytes (Davis et al., 1987). These data suggested that a core transcriptional network existed and that special transcription factors, “master regulators”, are able to induce and determine a cells fate towards a special lineage. Perturbing these master transcription factors might then be sufficient to reprogram already differentiated cell back to a pluripotent state.

Lastly, the field of embryonic stem cells further complemented the above experiments and set the stage of the development of iPSCs. Mouse embryonic stem cells (mESC) were first derived from the inner cell mass (ICM) of the preimplantation mouse blastocyst in 1981 (Evans and Kaufman, 1981) followed by the derivation of human embryonic stem cells (hESC) by Thomson et al in 1998 (Thomson et al., 1998). Several other groups followed these studies (Akutsu et al., 2006; Cowan et al., 2004) and optimal culture conditions were established (Smith et al., 1988; Thomson et al., 1998). One of the defining characteristics of an ESC line is the ability to differentiate into any cell type of the three germ layers- endoderm, mesoderm, and ecotoderm. In practice, this is typically shown by the *in vitro* differentiation of the tested line into many different cell types. *In vivo,* this is shown by injecting the cells under the kidney capsule of immunocompromised mice, observing the formation of a teratoma, and histologically analyzing the teratoma for tissues from all three germ layers. The development of ESCs as well as the concomitant advances in transcription factors as master regulators (see above) then resulted in the identification of the core network of transcription factors (TFs) that maintain ESC pluripotency. Three transcription factors, Oct3/4, Sox2, and Nanog, form this network. These factors do not exist in concert in any differentiated cell type, and serve as defining markers of pluripotent cells (Figure 12) (Babaie et al., 2007; Mitsui et al., 2003; Nichols et al., 1998).

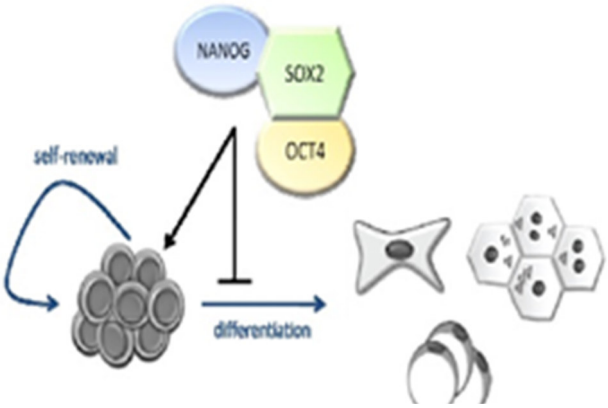

Figure 12. Scheme of the embryonic stem cell switch. The three transcriptions factors Nanog, Sox2, and Oct4 act as a switch between pluripotent and differentiated states by maintaining self-renewal and inhibiting differentiation. OCT4, SOX2, and NANOG have a unique expression pattern in ES cells and they play essential roles as master regulators of transcriptional control during early embryonic development (Avilion et al., 2003; Chambers et al., 2003; Mitsui et al., 2003).

All of these scientific advances combined to lead to the groundbreaking series of experiments of Takahashi and Yamanaka in 2006. In these experiments, they chose 24 genes, highly expressed in pluripotent cells, and expressed different combinations of each in mouse fibroblasts via integrating retroviruses. They then screened the mouse fibroblasts for both morphology and growth properties that are characteristic of ES cells as well as their expression of ES cell marker genes. They then showed that subcutaneous transplantation into nude mice results in tumors containing all 3 germ layers and that injection into blastocysts can drive mouse embryonic development (Takahashi and Yamanaka, 2006). Following shortly after and using a similar approach, successful transformation of human fibroblasts into hiPSCs was reported by two different groups through the retroviral expression of the same four crucial genes Oct4, Sox2, Klf4, and c-Myc (Takahashi et al., 2007) or by Oct4, Sox2, Nanog, and Lin28, using a lentiviral system (Yu et al., 2007). These experiments were performed at a time when the potential of hESCs had already been recognized and first proof of principle experiments had already highlighted their potential- not only as a source for cell-replacement therapies but also as a new *in vitro* tool to model and gain insight on human development and differentiation. Several burdens however, existed.

Ethical issues are a main concern that prohibited fast development of hESC research, since derivation of hESCs inevitably requires the destruction of human embryos (de Wert and Mummery, 2003; McLaren, 2001; Roche and Grodin, 2000). Besides that, the number of embryos for science is a limiting factor. Additionally, hESCs used in cell-replacement therapies can cause severe complications due to immune rejections. In contrast, hiPSCs cells are derived from available cell populations such as fibroblasts and keratinocytes, with the harm therefore limited to those

associated with skin-punch biopsies and hair pulls. Since there are also no destruction of human embryo's, the ethical debate largely subsided for induced iPSCS compared to hESCs. Furthermore, hiPSCs could theoretically provide an unlimited number of cells, and risks of immune rejection in cell-replacement therapies are minimized due to patient specific derivation. While there has been debate about the extent of similarity between hiPSCs and human embryonic stem cells (Deng et al., 2009; Guenther et al., 2010; Kim et al., 2011; Newman and Cooper, 2010), hiPSCs nevertheless offer a huge potential for use in regenerative medicine and clinical applications and provide a compelling alternative from hESCs for scientific research.

1.2.1 iPS cells and the promise of regenerative medicine

An important first proof-of-principle experiment performed by Rudolph Jaenisch's lab demonstrated the possibility of gene therapy followed by cell replacement therapy using iPSCs in a humanized knock-in mouse model of sickle cell anemia (Hanna et al., 2007). In this model, the mouse α- and β-globin were replaced with human α-globin and human Aγ and β^S (sickle) mutant globin genes. While the mice were viable for up to 18 months, homozygous β^S mice showed severe symptoms of anemia due to erythrocyte sickling (Hanna et al., 2007). iPSCs were derived from mutant mouse somatic fibroblasts and the disease-causing mutation was then repaired through via homologous recombination *in vitro*. Once the disease mutation was repaired, the "corrected" mouse iPSCs were then differentiated into hematopoietic precursor cells (HPs) *in vitro*. When transplanted into irradiated mice, these hematopoietic precursor cells repopulated the blood system and effectively abolished the sickle cell disease phenotype, suggesting the utility of iSPCs, gene therapy and cell replacement for new and effective therapeutics.

However, despite the promise of iPSCs and cell therapies, there remain some problems and challenges. C-Myc is an oncogene and increased expression has been associated with lethal teratoma formation in mice. However, the same study also showed that although the oncogene c-Myc increases the efficiency of iPSC induction, it is not necessary for nuclear reprogramming (Nakagawa et al., 2008). Other studies have linked the introduction of Oct-4 (Hochedlinger et al., 2005), Lin28 and Klf4 (Daley and Scadden, 2008) with oncogenesis when expressed in somatic cells. Additionally, hiPSCs were initially were reprogrammed via retro- or lentiviral transduction, therefore carrying high risk of viral contamination and adverse genome mutations caused by the stable integration of the transcription factor cDNA into the genome, a problem reported in earlier

trials in gene therapy (Hacein-Bey-Abina et al., 2003; Stein et al., 2010). Since then efforts to generate integration-free hiPSCs have resulted in the development and generation of iPSCs using several other methods including synthesized RNAs (Warren et al., 2010), non-integrating virus like Sendai virus (Fusaki et al., 2009) or Adeno virus (Stadtfeld et al., 2008), plasmids (Okita et al., 2011), proteins (Kim et al., 2009) or small molecules (Ichida et al., 2009).

Significant progress has been made in the past two decades towards a molecular understanding of many human diseases. With the advent of genome wide association studies many genes and their variants contributing to diseases can be identified (Genomes Project et al., 2015). Based on their genetic components, diseases can be broadly grouped into either monogenic and polygenic diseases. Monogenic diseases are caused by a single defective inherited gene (single-gene Mendelian). They account for 95% of the disease genes identified to date (Botstein and Risch, 2003; Glazier et al., 2002) Glazier et al., 2002) and since we can predict how certain mutations will affect a protein's function, there is a high degree of correlation between mutation and phenotype seen *in vivo*. Polygenetic diseases, on the other hand, are influenced by several genetic and environmental factors. Since hiPSCs are cable of differentiating into any cell type (Figure 13) they not only hold great promise for potential cell replacement therapies, but also for modeling diseases *in vitro* – "modeling or curing human diseases in a dish". Until recently, studying the pathology of disease, particularly neurodegenerative diseases, relied on animal models or post-mortem tissue. While both have improved our knowledge, each has certain limitations and drawbacks. Tissues, taken via biopsy, are inherently very limited and difficult to obtain, and often the cell type of interest that is affected in disease is already lost by the time of biopsy. Most important, these samples only reflect one timepoint in pathology. Early stages and potential triggering processes of the disease are extremely important in neurodegenerative disorders like AD or Parkinson disease (PD), where disease pathology starts 10-15 years before onset of symptoms. Additionally, murine model systems are different than humans and while useful, do not fully recapitulate pathology seen in humans.

Importantly, hiPSCs can be derived from patients with genetic disorders and then can be differentiated into the cell type most affected by the disease. Often, a disease-associated genotype will not manifest as a disease phenotype in pluripotent cells, but rather in differentiated and specialized cells, where the disease gene is more active depending on the given transcriptional and proteomic context of that specialized cell type. hiPSCs therefore enable researchers to

characterize phenotypes along the differentiation pathway, while also allowing functional analyses and drug screenings in the terminal differentiated and most affected cell types.

hiPSCs can faithfully recapitulate *in vivo* development *in vitro* using specialized media and small molecules. The type and composition of the media, supplemented at different timepoints, for certain amounts of time, with various small molecules, increases patterning of hiPSCs to a certain lineage. In fact, many important cell types have been successfully generated from hiPSCs using defined protocols, including cardiomyocytes (Burridge et al., 2014), dopaminergic neurons (Ma et al., 2011), hepatocytes (Si-Tayeb et al., 2010), motor neurons (Karumbayaram et al., 2009), pancreatic β-cells (Zhang et al., 2009), skeletal myogenic cells (Maffioletti et al., 2015), neural stem cells (Chambers et al., 2009) and endothelia cells (Patsch et al., 2015).

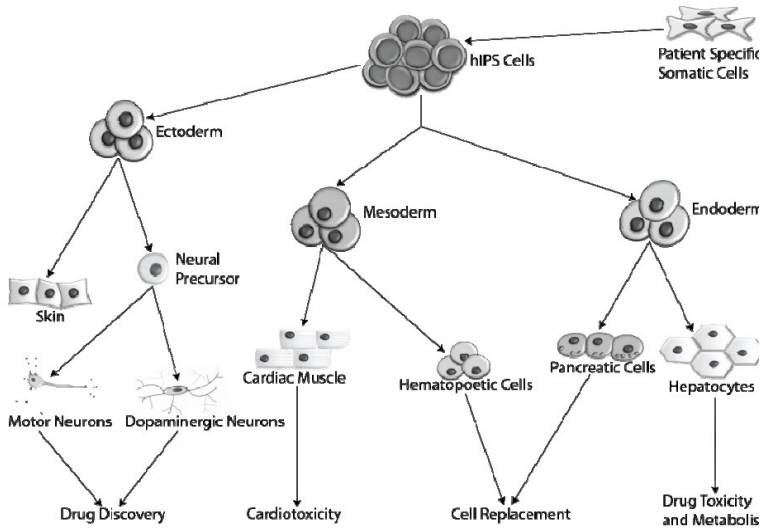

Figure 13. Scheme of hiPSC differentiation *in vitro*. Patient derived fibroblasts are reprogrammed into hiPSC and can be differentiated into cell of all three germ layers, giving rise to motor neurons, pancreatic β-cells, cardiac muscle and others.

Using patient-derived hiPSCs, many groups have used differentiation protocols to model monogenic and even complex diseases (Dimos et al., 2008; Park et al., 2008). These include cells derived from patients suffering from Gaucher disease (GD) type III, Duchenne (DMD) Becker muscular dystrophy (BMD), Parkinson disease (PD) (Kriks et al., 2011), Huntington disease (HD), Shwachman-Bodian-Diamond syndrome (SBDS), juvenile onset, type 1 diabetes mellitus (JDM), Down syndrome (DS)/trisomy 21, platelet deficiency (Takayama et al., 2010) and the carrier state of Lesch-Nyhan syndrome and Alzheimer's disease. Furthermore, these patient-specific hiPSC derived lines recapitulated aspects of disease phenotypes of both monogenic and polygenic diseases such as Parkinson's disease (Devine et al., 2011), late onset Alzheimer's disease (Israel et al., 2012) and schizophrenia (Brennand and Gage, 2011). Indeed, the number of hiPSCs used in different model of human disease confirm this fast, and constantly growing trend.

hiPSCs thus have the potential to complement previous experimental systems for modeling human disease *in vitro*. However, the differentiation of hiPSCs is still an emerging area, and despite many published protocols to differentiate hiPSCs into motor neurons or cortical neurons, it remains a challenging process.

One obstacle that needs to be overcome is the maturity of cells produced from iPSCs. This is especially a problem with disease models focused on neurodegenerative diseases or pathologies highly correlated with human aging. Recent improvements to address this issue include the replacement of the dominating 2-D culture systems with more sophisticated three-dimensional (3D) culture systems, allowing the differentiation of hiPSCs into organoids – small functional units consisting of different cells types, which can be kept in culture for longer periods of time and which seem to recapitulate features closer to tissues instead of just single cell types (Lancaster et al., 2013). Additionally, exposing cells to stressors, which are highly associated with ageing has been one solution (Studer et al., 2015), followed by co-culture with cells found to accompany them *in vivo,* can improve the maturation process and increase the speed of assays. Overall, using hiPSCs as a tool represents a major step forward in disease modeling, with the potential to facilitate both our understanding of the cellular and molecular basis of disease as well as improve the drug discovery process.

1.3 Genome editing

The human genome contains approximately 3 billion base pairs. The ability to change or to delete certain base pairs at precise locations holds great promise, not only for basic research but for therapeutic applications. Therefore, developing the necessary biological tools to introduce changes in the genome has been a long-awaited goal in molecular biology and recent groundbreaking discoveries have been made this goal a close reality.

Genome editing in human and mammalian cells has historically been challenging. It was the work of Capecchi and Smithies in the 1980's that proved that mammalian cells are capable of integrating an exogenous template of DNA into their genome by a process called homologous recombination (HR) (Capecchi, 1989; Smithies et al., 1985). However, the occurrence of successful HR was very inefficient (only 1 out of 10^3 – 10^9 cells) and also accompanied by the risk of random integration of the template into other genomic loci. Breakthrough studies in yeast (Rudin et al., 1989) and in mice (Rouet et al., 1994) revealed that a double-strand-break (DSB) introduced by an expressed endonuclease enzyme increased the likelihood of HR manifold. These studies are the

foundation for the ongoing genome engineering strategies using programmable nucleases in mammalian cells. Over the years, several of these nucleases have been invented, including zinc finger nucleases (ZFNs) (Porteus and Carroll, 2005; Urnov et al., 2005), transcription activator-like-effector nucleases (TALENs) (Boch et al., 2009; Hockemeyer et al., 2011; Miller et al., 2011) and very recently the clustered regularly interspaced short palindromic repeat (CRISPR)-associated protein 9 (Cas9) (Doudna and Charpentier, 2014). All of these nucleases can be engineered so that they target a specific site in the genome, cause a DSB and activate the cell's endogenous machinery to repair the DSB. Two primary ways of DNA repair pathways exist: non-homologous-end-joing (NHEJ) and homologous-directed repair (HDR) (Kanaar et al., 1998). NHEJ is the major repair-pathway in the cell. It is highly error-prone and often results in insertions or deletions (InDels) of base pairs. These InDels can lead to frameshifts and therefore often knock-outs (KOs) of the targeted genes (Porteus, 2016). Homologous-directed repair instead relies on recombination and uses a donor template to synthesize new DNA, allowing precise and controlled genomic edits (Kanaar et al., 1998).

The first designed programmable endonucleases were ZFNs, followed by TALENs. Both are artificial fusion proteins that consist of a DNA binding domain (DBD) fused to the nuclease domain of a *FOK*I restriction endonuclease, which becomes catalytically active upon *in situ* dimerization. However, the DBDs of ZFN and TALENs differ from each other. ZFNs usually contain as DBD with 3-6 common Zinc finger motifs, wherein each motif (Cys_2-His_2) is zinc ion regulated and able to recognize a 3-base pair sequence, resulting in a 9-36 base pair sequence that can be targeted (Klug and Rhodes, 1987). TALENs on the other hand usually have DBDs consisting of 35 residues in lengths (Boch et al., 2009). ZFNs and TALENs both successfully increased genome targeting events, however, broader use of these tools was limited by the fact that each target site required the design and synthesis of a new protein, which is technically challenging, costly, and not guaranteed effective (Porteus and Baltimore, 2003).

1.3.1 Genome editing using CRISPR-Cas9

CRISPR has become a crucial tool in biological research within only a few years after its discovery. By revolutionizing the accuracy, speed, and cost of genome editing, CRISPR and CRISPR-based technologies and applications are single handedly transforming clinical and biological research.

Prior to its discovery as a genome editing tool, however, CRISPR was known as a prokaryote DNA repeat element (Ishino et al., 1987). It was later discovered that this repeat DNA element, as well as the associated proteins, were involved in an adaptive immune system found in prokaryotes, including bacteria (40%) and most archaea (90%)(Mojica et al., 2000). In this system, invading viral DNA is cleaved by the host's endonuclease Cas and the resulting cleaved DNA fragments are then incorporated and stored within the CRISPR locus. These spacers, the incorporated viral DNA fragments, are separated by DNA repeat sequences (CRISPR repeats) and together, these spacers and repeats (called the CRISPR array) reside adjacent to CRISPR-associated (CAS) genes, encoding the Cas endonuclease (Jansen et al., 2002). If a host gets infected again by phages or viruses, these spacers are transcribed resulting in the production of crRNA, which guide the Cas endonuclease to the invading DNA. If the crRNA is able to bind to the foreign DNA through complementary base-pairing, the Cas endonuclease cleaves the DNA (Barrangou et al., 2007), subsequently provides protection against exogenous DNA via a specific and precise targeting mechanism.

Evolution and the constant struggle of bacteria to survive invasion of foreign, mobile elements, has yielded a variety of CRISPR systems, most of them distinguishable by the Cas genes located next to the CRISPR array (Makarova et al., 2011). Two different classes have been described so far, each of them containing various types of CRIPSR systems involving different endonucleases, CRISPR arrays, and targeting mechanisms. Class 1 CRISPR systems consist of both type I and type III CRISPR systems, and are largely found in Archaea, whereas the class 2 CRISPR system contains type II, IV and VI CRISPR systems (Koonin et al., 2017).

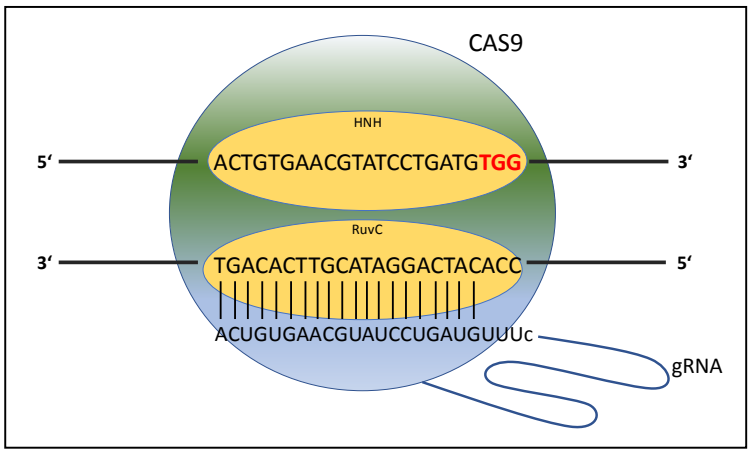

Figure 14. 20 nucleotides long protospacer of the sgRNA binds via Watson-crick base-pairing and leads CAS9 to the target-site. HNH and RuvC domains will cleave the strands if protospacer is followed by PAM sequence.

While a few of these CRISPR-systems have been utilized for genome targeting, the type II CRISPR system, called CRISPR/CAS9 (Cong et al., 2013), derived from *Streptococcus pyogenes*, is the predominant system used for genomic editing. The

type II system is composed of the endonuclease Cas9, which has two catalytically active domains (RuvC and HNH) and two different RNAs, a trans-activating crRNA (tracrRNA) and a sequence specific CRISRP RNA (crRNA), the former connecting crRNA and Cas9 and stabilizing the complex and the latter guiding the Cas9 to the target site. In practice, the tracrRNA and crRNA have been fused as a chimeric tracrRNA:crRNA RNA called single-guide RNA (sgRNA)(Zhang et al., 2014). Distinct from the protein-guided DNA cleavage of ZFNs and TALENs, CRISPR-Cas9 depends solely on RNA-DNA interaction prior to causing the DSB. The endonuclease Cas9 is then directed to the target site by the crRNA (or sgRNA, in case of the chimeric RNA) via a 20-base pair long sequence, called the "protospacer", which binds via Watson-Crick base pairing (Figure 14) (Mojica et al., 2009). However, Cas9 will only bind to the target site and creates DSBs, if the site contains a protospacer adjacent motif (PAM). The PAM is unique and depends on the organism it is derived from. For example, the PAM for Cas9, derived from *Streptococcus pyogenes* (spCas9), consists of the sequence "NGG", which occurs frequently in the genome, allowing many potential target sites. Alternatively, the PAM sequence for Cas9 derived from other bacteria are more complex like those of *Staphylococcus aureus* (SaCas9) *"*NNGRRT" or *Streptococcus thermophilus'* (St1Cas9) "NNAGA AW" offering a more limited targeting scope. In the case of spCas9, successful detection of the PAM after homology binding by the sgRNA leads to DSBs 3 bp 5'upstream of the PAM. The DSB can then either be repaired via NHEJ with a high probability of creating InDels or via HR in the event that a DNA sequence is provided for use as a template. Performing CRISPR mediated genome editing therefore requires transfection of different plasmids, depending on the experimental setup. In the case for knock-out mutagenesis, 1 plasmid expressing both CAS9 (or any of the other CRISPR associated endonucleases) and sgRNA needs to be transfected. For knock-in mutagenesis, transfection of the Cas9 and sgRNA (designed to target a specific locus) expressing plasmid must be accompanied by a targeting vector or at least single-stranded-oligos, which can then serve as templates during the homologous recombination.

By providing the ability to precisely modify the genome, at low cost and low technical difficulty (compared to the protein engineering of ZFNs and TALENs), the CRISPR system has become incredibly popular. However, despite this popularity, a critical concern inherent to the system is the potential for off-target effects (Hsu et al., 2013) (Cho et al., 2014). The protospacers or gRNAs, designed to bind to a 20 nt long target sequence in the genome can tolerate up to 7 mismatches. That means that other sites, similar in sequence to the main target site, but not identical, can be recognized by the gRNAs as well and cleaved by Cas9. This tolerance for

promiscuous cutting is due in large part to the origin of the CRISPR system as a bacterial defense mechanism, and therefore tolerating a few mismatches is an important for successful defense against ever-evolving viruses. However, unfortunately, this limits the use of CRISPR and its human applications *in vivo- requiring* cation for safety, extensive *in vitro* karyotypically analysis, as well as off-target analysis via deep sequencing and confirmation of targeted genes via WB of knock-in *in vitro* models. Advances to reduce these off-target effect have been made, for example with the development of the nickase Cas9 (nCas9)(Ran et al., 2013). nCas9 only has one functional cleaving domain resulting in only one single DNA strand break. For successful targeting and creation of DSBs, two Cas9 and two different gRNAs (one targeting the upper, one targeting the lower strand) are required, minimizing the risk of off-target effect due to the unlikely probability of both gRNAs binding at the same off-target side. Besides reducing the risk for off-target effects, other modifications based on the original CRISPR system have been made, allowing regulation and control of gene expression. The deactivated Cas9 or dead Cas9 (dCas9) (Qi et al., 2013) has been generated that is nuclease deficient. However, since it still possesses its binding ability, dCas9 can be guided to a target site via sgRNA and it can interfere with other DNA binding proteins like RNA Polymerase II, decreasing transcription and causes a knock-down via steric interference (referred to as crispr interference (CRISPRi)). This effect can be strengthened by fusing strong repressors like Kruppel associated box (KRAB) directly to dCas9 or by recruiting them via sgRNA scaffold, resulting in strong repression of a promotor and gene expression after binding to the target site (Gilbert et al., 2013). Alternatively, strong transcriptional activators like VP64, P65 or heat shock transcription activator (HSF1) can also be fused to the dCas9 and targeting of regions like promotor or other up-regulatory elements can lead to increased expression. Other functions like epigenetic modulation (Xiong et al., 2017)(Liu et al., 2016) or chromatin manipulation (Morgan et

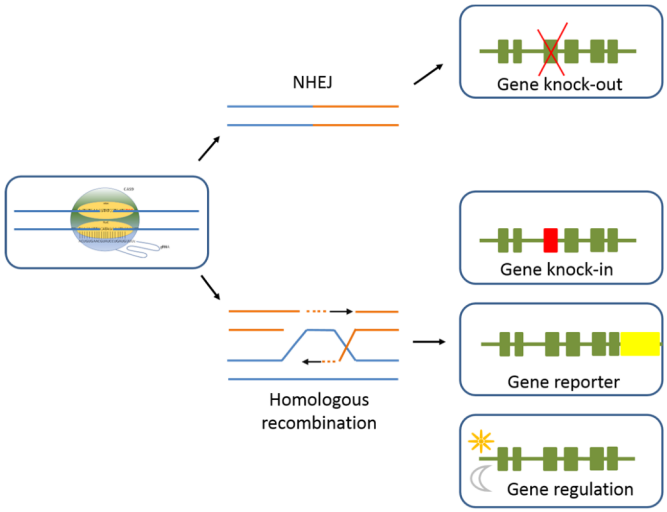

Figure 15. Genetic modifications via CRISPR/CAS9 system include knock-outs, knock-ins, transcriptional regulation as well as reporter gene insertion.

al., 2017) and even live cell fluorescent imaging have become new and advanced applications for the Crispr systems.

With all of these applications (Figure 15), CRISPR is set to have a huge potential impact on disease-related research. The advent of hiPSCs and therefore the option to generate patient specific human cell lines or random control lines, enhanced by the advances in DNA genome sequencing can make CRISPR an extremely valuable tool. One avenue is through personalized medicine with therapeutic transplants coming from cells derived by patient iPSCs and therefore excluding any risk of immune response. Another avenue is through specific disease modeling, where patient derived hiPSCs can be modified via CRISPR-Cas9 to either carry or lack a disease associated single nucleotide polymorphisms. These engineered lines, when differentiated into the cell type of interest then provide an excellent platform to study human disease in a dish, as well as screen for compounds that reverse or suppress a disease related phenotype.

1.3.2 Crosstalk: Disease modeling using hiPSCs and the CRISPR/Cas9 system

There are different avenues to model a disease *in vitro* using hiPSCs- the classic approach and the isogenic approach. The former approach is based on the derivation of hiPSC lines from different patients (patient disease lines) who are suffering from the disease of interest. Fibroblasts are taken from the patients and the cells are reprogramed to a pluripotent state. To choose proper controls for the experiments random lines are chosen from age matched, healthy control donors and derived by reprogramming as well. While this is by far the most convenient approach and it has the advantage that no genome-editing is required, it comes with 2 main drawbacks. The first drawback is line-to-line genetic variabilities, wherein any number of unknown background mutation in each line can cause phenotypic differences and noise. The second drawback is the well-known line to line variation of lines often used as control in these experiments. Even if we neglect the potential background mutation in each line used in this experimental setup, it is known that each separate line has different properties. Each line has a unique potential to differentiate into a special cell type, each line is more or less sensitive for being kept in culture and each line reacts different to genome editing approaches, to transductions, to stressors or treatments. Therefore, this approach is imprecise, and results derived from this setup can be confounded and inappropriately based on/influenced by the existing variations between randomly chosen hiPSC lines.

In contrast, the isogenic approach instead requires genome editing, but allows more direct comparison of disease alleles. There are two options with the isogenic approach- the first is to start with a patient disease line and to correct the disease-causing mutation, the second to start with a control line and to introduce the mutations of interests via genome editing. In both strategies, each single line generated is identically to the parent line except the mutation of interest and therefore only confounding background mutations and line variability are minimized (Figure 16).

While both of the above-mentioned isogenic options are adequate to model diseases caused by only one mutation, in diseases where several mutations are known to cause a disease phenotype, the first isogenic option would not be efficient. For example, for every single patient disease line carrying one of the known disease-causing mutations, an isogenic control line would have to be created for that line. Besides ending up with many lines, it would additionally prevent comparing the different lines with each other, as the issue of unknown background mutations and line to line variation described earlier, would apply to this scenario as well. Starting with one parent line and using genome editing techniques to introduce the mutations of interest eliminates these disadvantages.

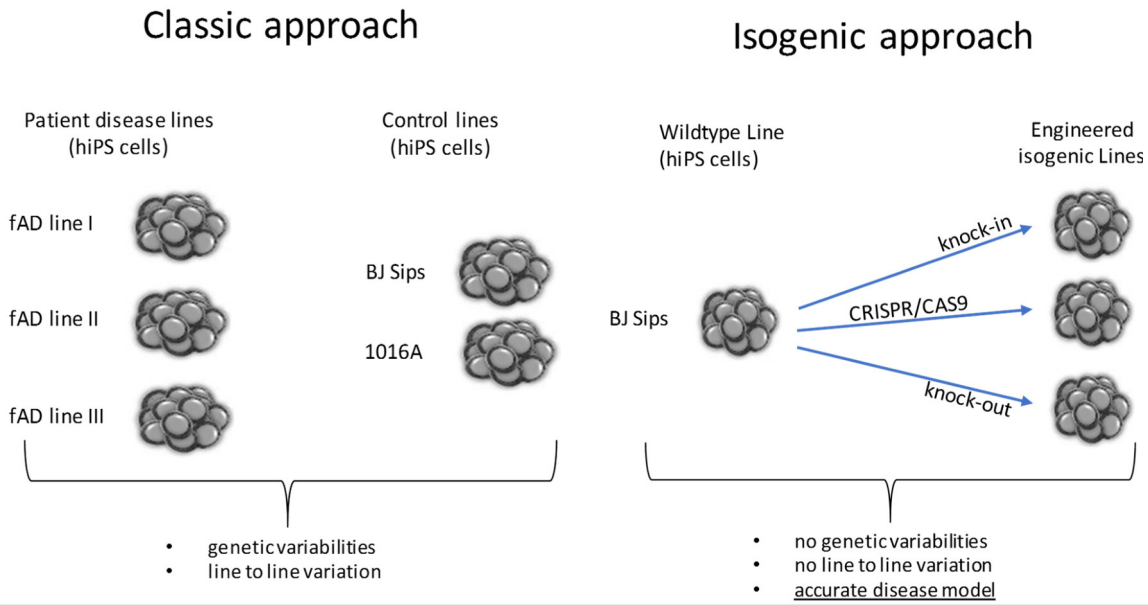

Figure 16. Different approaches for disease modeling using hiPSCs. Use of (left) patient derived lines and random control lines (right) wildtype line as control line and isogenic, engineered lines are created via knock-in or knock-out mutagenesis using the CRISPR/CAS9 system.

Aims

The main objective of this thesis is to create a robust and highly functional isogenic model of familial Alzheimer's disease. This model system will enable precise studies of fAD *in vitro*, revealing new insights, pathways and targets that are relevant to the mechanisms underlying early-onset AD. It is the ultimate goal to complement this isogenic system with maturation *in vitro*, not only increasing the capability of recapitulating AD pathology seen *in vivo*, but also enabling a temporal understanding of the pathologic changes that occur between disease onset and end-stage of disease.

Aim 1: Generate isogenic fAD disease lines using human induced pluripotent stem cells

State-of-the-art genome editing techniques will be used to engineer the genome of control human induced pluripotent stem cells, such that they have introduced mutations in the gene amyloid precursor protein. These mutations include: APP KM670/671NL, APP A673V, and APP V717I , which are causative of fAD; a mutation APP A673T recently associated with protection against Alzheimer's disease and cognitive decline; and a total APP knockout. These generated isogenic hiPSC lines will then be differentiated in 3-D culture into cortical neurons- one of the cell types most affected by familial Alzheimer's disease. State of the art genome editing tools will again be utilized to create fAD isogenic cortical reporter lines, expressing a fluorophore under the control of a cortical gene promotor. These will enable the purification of and direct comparison of the fAD isogenic lines in cortical neuron populations.

Aim 2: Characterization of isogenic familial AD lines – hunt for a phenotype *in vitro*

The isogenic fAD lines will be characterized throughout all stages of differentiation- starting first with characterization in the pluripotent state through differentiation into mature cortical neurons. We will investigate whether our *in vitro* model is able to recapitulate aspects of AD pathology seen *in vivo* and whether our system has the potential to model a neurodegenerative disease like fAD "in a dish". Specifically, the mutant lines will be evaluated for differences in hallmark AD pathologies– Aβ and phosphorylated TAU. Additionally, the proliferation rates of each line, as well as their morphology and their potential to differentiate into cortical neurons will be analyzed. Lastly, the potential of the isogenic lines to mature *in vitro* with prolonged culture and their ability to generate cerebral organoids will be evaluated and characterized further for late-stage AD pathologies.

Aim 3: In-depth analysis of isogenic lines

The isogenic fAD lines will be treated with cellular stressors and analyzed using live-cell imaging to uncover if the diseased lines are more vulnerable to stressors compared to controls. Lastly, to unravel what pathways are involved in fAD and which genes are dysregulated in mutant diseased lines compared to control and protective lines, the isogenic lines will be analyzed using global proteomics and single cell transcriptomics and I will present the current status of these important large-scale-projects.

Materials and Methods

Propagation and maintenance of hiPSCs

Human iPSCs (BJsipsD), were derived from fibroblast of a healthy male donor and reprogramed by the Harvard iPS Core. hiPSCSs were cultured on matrigel-coated plates (ESC qualified, BD Biosciences) using either hESC mTeSR-1 (StemCell Technologies,) or STEMFLEX cell culture medium (Life Technologies, Thermo Fisher Scientific), containing 1% Pen Strep (Life Technologies) (vol/vol), under conditions of 37°C, 95% air, and 5% CO2 in a humidified incubator, as previously described (Schinzel et al., 2011).

When reaching 40% confluency media was aspirated and cells were washed with D-PBS (Wako) without calcium and magnesium once. 2.25 ml or 4 ml of Accutase (StemCell Technologies) were added to each 10 cm or 15 cm plate respectively and plates were incubated at 37°C for 3 to 5 min. Plates were checked under the microscope every other minute. When visually confirmed that colonies started to detach from the plate, cells were washed off and collected in 15 or 50 ml falcon tubes. Cells were spun down at 800 rpm for 5 min, resuspended in pre-warmed media and 1/12 of the resuspension was added to each of the freshly coated plates containing pre-warmed media.

hiPSC adaption and maintenance in Spinner Flasks for cortical differentiation

Prior to adaption to spinner-flask culture, hiPSCs were expanded in 15-cm dishes (Corning) until they reached 90% confluence. Cells were dissociated using Accutase (StemCell Technologies) for approximately 5 min incubation at 37°C or until colonies detached from the plate. Cells were washed off using PBS (Wako), collected in 15 ml falcon tubes (Corning) and spun down at 800 rpm for 5 min. Cells were resuspended in pre-warmed media and cells were counted using the Biorad automated cell counter. 80 million individual pluripotent stem cells were seeded into a 125-ml disposable spinner flask (Corning, VWR) on a nine-position stir plate (Dura-Mag) in 120 ml of mTeSR medium (StemCell Technologies) supplemented with 10 µM RHOK inhibitor Y-27632 (StemCell Technologies) to increase cell viability. The stir plate was kept at a speed of 55 rpm, in a 37°C incubator with 5% CO_2 as previously reported (Rigamonti et al., 2016). Spheres formed spontaneously, and after 24 h, spinner flasks were taken out of the incubator and cells/ spheres were allowed to settle for 20 min before half of the culture medium was replaced with prewarmed

mTesR-1. The cells were maintained as undifferentiated pluripotent spheres in spin culture, with medium changes every day until the spheres were approximately 50–100 µm in diameter in size.

Differentiation of pluripotent spheres into cortical neurons in spin-culture

Differentiation was initiated through a 75% medium switch using differentiation medium d0. Subsequently medium was changed every other day by removing approximately 80 % of the medium after spheres were allowed to settle by gravity for about 20min. Differentiation medium has a changing composition over time. The basic medium contained 50% Advanced Dulbecco's Modified Eagle Medium (Advanced DMEM) (Thermo Fisher Scientific), 50% Neurobasal (Thermo Fisher Scientific), supplemented with 1% (vol/vol) N2 (Life Technologies), 2% (vol/vol) B27-vitA (without Vitamin A; Invitrogen), 0.1mM 2-mercaptoethanol (0.1 mM) (Life Technologies), 1% (vol/vol) Glutamax (Thermo Fisher Scientific) and Ascorbic Acid (200uM) (Sigma Aldrich). To induce forebrain fate the basic differentiation medium was supplemented from day 0 – 12 with the WNT inhibitor XAV939 (Stemgent) (2 µM) along with the TGF-ß/activin inhibitor SB431542 (10 µM) (Stemgent) and the BMP inhibitor LDN193189 (Stemgent) (1 µM) resulting in dual-SMAD inhibition. Terminal differentiation medium from day 20 - 45 contained basic differentiation medium supplemented with 20 ng/ML BDNF (R&D Systems) and was changed every other day.

Dissociation of differentiated spheres

Spheres were collected from spinner flasks and were transferred into a falcon tube and settled by gravity. After washing with PBS, cells were incubated on a shaker (which model) for ~4 minutes in 2 ml Trypsin 0.25% supplemented with DNAse (50 µg/ml of Trypsin) (Worthington Biochemical) at 37°C. The enzymatic digest was stopped by adding 1:1 Fetal Bovine Horse Serum (FBS, Sigma Aldrich) supplemented with Ovomucoid (1:5) and 0.50 mg/ml DNAse (Worthington Biochemical)] and spheres were gently triturated 5 times using a 5-ml serological pipette. Spheres were spun at 800 RPM for 5 min and resuspended in 5 ml of freshly prepared dissociation buffer. Dissociation buffer contained 91,2% PBS, 5% FBS, 25 mM Glucose, 5 mM Glutamax and 5ug/ml of Papain (Worthington) and 14ug/ml DNAse. Spheres were pipetted up and down using a P1000 pipette 20 times followed by 2 min to let them settle again and supernatant was carefully transferred into new falcon tube containing prewarmed terminal differentiation medium supplemented with 20 ng/ml BDNF, 20 ng/ml GDNF (R&D Systems) and 20 ng/ml CNTF (R&D

Systems). Process was repeated until most spheres were broken up. Dissociated spheres/neurons were spun down for 5 min at 800 rpm, resuspended and filtered through a 40-micron mesh (VWR). Process was repeated, and cells were counted using an automated cell counter (Biorad – need exact model) and live cell dye Trypan blue (Life Technologies).

For long term culture of dissociated spheres, cells were plated on dishes coated with PBS (WAKO) supplemented with borate buffer (20x) (Life Technologies) and 50 ug/ml poly-d-lysine (Sigma Aldrich) overnight, followed by three washes and by 3 h incubation time with PBS supplemented with 50 µg/ml fibronectin (Sigma-Aldrich) and4 µg/ml laminin (BD Biosciences) at a 37°C incubator with 5% CO_2. Cells were seeded at appropriate densities using terminal differentiation medium supplemented with 20 ng/ml BDNF, 20 ng/ml GDNF and 20 ng/ml CNTF in either 96 well plates (Greiner) or 24 well plates (Corning) at densities of $8x10^4$ or $1x10^6$, respecitvely). In case of the presence of too many glial cells post dissociation ARA-C (1µM) was added.

Generation of cerebral organoids

Prior to adaption to spinner-flask culture, hiPSCs were expanded in 10-cm dishes (Corning) until they reached 50% confluence. Cells were dissociated using Accutase (StemCell Technologies) for approximately 5 min incubation at 37°C or until colonies detached from the plate, collected, spun down at 800 rpm for 5 min and then resuspended. Cells were counted using Biorad automated cell counter and 9000 cells were seeded per well of an ultra-low attachment multiwell 96 well plates (Corning) containing a final volume of 200 µl of mTeSR medium (StemCell Technologies) supplemented with 50 µM RHOK inhibitor Y-27632 (STEMCELL) to increase cell viability. 96 well plates were incubated at 37°C with 5% CO_2 for 24 h and observed under the microscope. If small embryoid bodies (EBs) had formed plates were further incubated like described. EBs were fed every day by aspirating half of the volume and adding fresh mTeSR supplemented with 50 µM RHOK inhibitor and FGF (10 ng/ml) (Life Technologies) until EBs reached a size of 400 µm. Media was switched to mTeSR without supplements until EBs reached 600-650 µm in size. 200 µl pipette tips were cut using sterile razor blades to generate an opening of 2 mm to make sure the EBs could be carefully sucked in and transferred without being disrupted. Each EBs was then transferred into one well of an ultra-low attachment 24-well plates containing 1 ml of pre-warmed neural induction media (NIM). NIM media contained Advanced DMEM, supplemented with 1% Glutamax (vol/vol), 1% N2 supplement (vol/vol), 1% MEM-NEAA (vol/vol)

and a final concentration of Heparin of 1 µg/ml. EBs were observed under the microscope daily and media was changed every day by removing half of the volume and adding the same amount of fresh media until EBs showed smooth edges and translucent surface that was brighter on the outside, indicating neuroectodermal differentiation. When these regions started to show mostly radially organized pseudostratified epithelium, EBs were ready for embedding process.

Parafilm was prepared by spanning it over an empty tip tray for size 1000 µl tips and grids with 8x8 dimples were created by using a 1000 µl filter tip and pressing the parafilm on top gently into the holes below. Frozen Matrigel aliquots were put on ice to thaw very slowly. Each EBs/neuroephitelia tissue was transferred into one dimple using cut 200 µl tips like described above and remaining media was carefully removed. Immediately 50 µl was added into each dimple to prevent the tissues from drying out and the tissues were carefully moved to the center of the Matrigel drops. Each grid was placed into a 10 cm tissue culture dish and incubated at 37°C for 1-1.5 h until the Matrigel polymerized. 10 ml of pre-warmed organoid differentiation media containing 50% Neurobasal, 50% advanced DMEM, 1% Glutamax (vol/vol), 0.5% N2 supplement (vol/vol), 0.5% MEM-NEAA (vol/vol), 1% PenStrep (vol/vol), 1% B27-vitA supplement (vol/vol), 0.18% 2-Mercaptoethanol, was added to each dish and the polymerized matrigel drops enclosing the tissues were gently removed from the parafilm and were released into the media by turning the parafilm gently over and by moving and stretching it gently. The embedded organoids were kept in static culture for 4 to 6 days and half of the media was changed every other day until more expanded neuroepithelium was visible. Up to 24 embedded organoids were then transferred into one 125 ml spinner flasks and kept on magnetic stir plates under conditions described before. Media was changed every 2 days for the first 20 days after being transferred into the spinners and then every 4 days. Due to the increasing size of the organoids over time, we reduced the speed of the stir plate to 47 rpm starting day 45. Organoids were kept in culture for at least 180 days.

Preparation for cryosectioning

Using a wide cut open 1 ml filter tip each organoid and some organoid media were transferred at different timepoints from the spinner into 1.5 ml Eppendorf tubes and immediately an equal volume of D-PBS supplemented with 8% PFA was added. Cerebral organoids were fixed overnight in an orbital shaker at 4°C. Cerebral organoids were washed twice with D-PBS, 15% sucrose (Sigma-Aldrich) solution was added and organoids were again put in an orbital shaker at 4°C for 48 hours allowing organoids to sink into the solution. Organoids were removed from Eppendorf tubes

using wide cut-open 1 ml filter tip and 1 - 4 organoids were transferred into one medium size Tissue-Tek Cryomold (Thermo Fisher Scientific) boxes filled with OCT solution, positioned close to each other and snap-frozen by immediately putting the Cryomold boxes on dry-ice.

Generation of isogenic lines

Original plasmid expressing Cas9 and -after insertion- specific gRNA was obtained from addgene: pX330-U6-Chimeric_BB-CBh-hSpCas9 (Addgene plasmid # 42230 https://www.addgene.org/42230/). Plasmid was digested with BAMHI and a gBlock, containing P2A-enhanced GFP sequence (IDT) and two 5 prime and 3 prime 35 bp overhangs homolog to the plasmid sequence 5 prime and 3 prime to the restriction site, was introduced via Gibson cloning post the bGHpA (ployA tail) site using gibson assembly mastermix (NEB) according to the manufacturer's instructions. Successful cloning was confirmed via sequencing (Macrogen) using forward primer (TCTCAGCTGGGAGGCGACAA) and reverse primer (CTCCTTACGCATCTGTGCGGTATT) flanking the newly introduced P2A-GFP region.

Sequence of gBlock to generate px330-nGFP:

CCACGAAAAAGGCCGGCCAGGCAAAAAAGAAAAAGGAGGGCAGAGGAAGTCTGCTAACATGCGGTGACG
TCGAGGAGAATCCTGGCCCAATGGGTTGCTGTTTCTCCAAGACCGCAGCGAAGGGAGAAGCCGCCGCGGA
GAGGCCTGGGGAGGCGGCTGTGGCCTCGTCGCCTTCCAAAGCGAACGGACAGGAGAATGGCCACGTGAA
GGTAGGATCCGTGAGCAAGGGCGAGGAGCTGTTCACCGGGGTGGTGCCCATCCTGGTCGAGCTGGACGG
CGACGTAAACGGCCACAAGTTCAGCGTGTCCGGCGAGGGCGAGGGCGATGCCACCTACGGCAAGCTGACC
CTGAAGTTCATCTGCACCACCGGCAAGCTGCCCGTGCCCTGGCCCACCCTCGTGACCACCCTGACCTACGGC
GTGCAGTGCTTCAGCCGCTACCCCGACCACATGAAGCAGCACGACTTCTTCAAGTCCGCCATGCCCGAAGG
CTACGTCCAGGAGCGCACCATCTTCTTCAAGGACGACGGCAACTACAAGACCCGCGCCGAGGTGAAGTTCG
AGGGCGACACCCTGGTGAACCGCATCGAGCTGAAGGGCATCGACTTCAAGGAGGACGGCAACATCCTGGG
GCACAAGCTGGAGTACAACTACAACAGCCACAACGTCTATATCATGGCCGACAAGCAGAAGAACGGCATCA
AGGTGAACTTCAAGATCCGCCACAACATCGAGGACGGCAGCGTGCAGCTCGCCGACCACTACCAGCAGAA
CACCCCCATCGGCGACGGCCCCGTGCTGCTGCCCGACAACCACTACCTGAGCACCCAGTCCGCCCTGAGCA
AAGACCCCAACGAGAAGCGCGATCACATGGTCCTGCTGGAGTTCGTGACCGCCGCCGGGATCACTCTCGGC
ATGGACGAGCTGTACAAGTAAGAATTCCTAGAGCTCGCTGATCAGCCTCGACT

Generation of isogenic knock-out lines

Two 20 bp long gRNAs were manually chosen while analyzing sequence of APP Exon 2 for adequate PAM sequences ('NGG') *in silico* using Geneious software program (Biomatters). Overhangs for ligation into Bbsl restriction site of px330-nGFP were added to the gRNAs according

to scheme X and gRNAs (CRISPR) were ordered as single-stranded oligos (ssOligos) for upper (CRISPR FOR) and lower strand (CRISPR REV) (life technologies).

Schematic view of 20 bp long gRNAs incl. overhangs for ligation into px300-nGFP vector digested with Bbsl; ssOligos ordered to generate CRISPR targeting Exon 2:

5' – CACCGNNNNNNNNNNNNNNNNNN – 3'

3' – CNNNNNNNNNNNNNNNNNNCAAA – 5'

Name	Type	Sequence	Size
Crispr5	FOR	CACCCCCAGATTGCCATGTTCTG	20 bp
	REV	AAACCAGAACATGGCAATCTGGG	
Crispr4	FOR	CACCTGCACATGAATGTCCAGAA	20 bp
	REV	AAACTTCTGGACATTCATGTGCA	

Table 1: ssOligos ordered to generate CRISPR targeting Exon 2 of APP.

Ssoligos were annealed using 10 ul reactions, consisting of 1 ul CRISPR FOR and 1 uL CRISPR REV (of 100 uM stock), 1 ul ligation buffer T4 (NEB) 10x, 0.5 ul T4 PNK (NEB) and 6.5 ul H_2O and incubated for 30 min at 37°C, followed by 5 min at 95°C before ramping down to 25°C at a speed of 5°C/min. Annealed oligos were diluted 1:250 in H_2O. Oligos were cloned into px330-nGFP in a single digestion/ligation reaction. Reactions were prepared according to the following scheme:

- 100 ng of px330-nGFP vector: x ul
- phosphorylated and ligated oligo duplex from 1:250 dilution: 2uL
- 10X Tango buffer (or Fast digestion buffer): 2 uL
- DTT (100 mM, final 1 mM): 0.1 uL
- ATP (25 mM, final 1 mM): 0.4 uL
- FastDigest Bbsl (Thermo Scientific), or Bpil: 1 uL
- T7 DNA ligase: 0.5 uL
- H_2O: volume remaining up to 10 ul

Reaction were incubated in PCR thermos-cycler using the following program:

1) 5 min at 37°C

2) 5 min at 23°C

3) go to 1) 6 times (total run 1h)

4) store at 4°C

2 ul of each reaction was used for transformation of Stble3 bacteria. Transformation as well as isolation of the new plasmids were performed like described in the material and methods part "transformations". Samples were sent out for sequencing at a concentration of 80-120 ug/ul to confirm the successful ligation of the double stranded annealed gRNA oligo using the Primer U6: ACTATCATATGCTTACCGTAAC.

Nucleofection was performed using the 4-D nucleofector system (AMAXA) and the P3 Primary Cell 4D-Nucleofector Kit (Lonza). $1*10^{\wedge 6}$ cells were dissociated using Accutase (StemCell Technologies) like described before, washed off with D-PBS and collected in 15 ml falcon tubes. Cells were spun down at 800 rpm for 5 min and resuspended in 100 µl P3 nucleofection solution supplemented 2.5 ug each of two different px330 CRISPR-CAS-nGFP plasmids, both of them expressing the Cas9 endonuclease and one unique gRNA targeting exon 2 of APP: gRNA CRISPR5 Exon 2: GCCCAGATTGCCATGTTCTG, gRNA CRISPR4 Exon 2: TGCACATGAATGTCCAGAA. Solution was transferred into nucleofections cuvettes and put on ice for 5 min before proceeding. The standard program CB-150 was used for all nucleofections. Immediately post nucleofection 500 µl of pre-warmed media was added to each cuvette and cells were transferred to Matrigel coated dishes containing mTeSR media with 4 µM RHOK inhibitor to improve survival. RHOK inhibitor was removed 24 h post nucleofection. To enrich for cells that had received the px330 CRISPR-CA-nGFP plasmids we enriched for GFP+ cells using fluorescence activated cell *sorting* 24-48 h post nucleofection. We collected 100.000 cells and plated them at clonal densities on freshly coated 10 cm plates. Individual colonies were picked and expanded. Cells of each picked clone were transferred into 96 deep well plates (Thermo Scientific) and gDNA was extracted by adding 100 ul of DirectPCR lysis reagent (CELL)(Viagen) and Proteinase K (Viagen) mix in ratio 1:20. Plates were sealed with sticky lids and placed on a rocking plate in PCR machine at 55^{o}C for 6h followed by incubation at 85^{o}C for 45 min and then cooled down to 4^{o}C. gDNA was stored at -20^{o}C until further usage. The following 3 primer sets flanking the exon 2 were designed *in silico* using Geneious software:

Table 2: Primer ordered to analyze Exon 2 of APP

No.	Type	Sequence	Size
Primer 1	FOR	CCTCTGCCTTGGAGCTATGG	249 bp
	REV	CCACCGGACAGGACTTACTT	
Primer 2	FOR	CCCTGTTCTTCCTCCAAGCC	261 bp
	REV	GAATTGCTAGCCACCGGACA	
Primer 3	FOR	CCTCTGCCTTGGAGCTATGG	259 bp
	REV	TAGCCACCGGACAGGACTTA	

20 ul reactions PCR reactions were prepared consisting of 8 uL H_20 + 1uL each primer 10uM + 1 uL DNA+ 10 ul Phusion High-Fidelity PCR Master Mix with HF Buffer (NEB) and PCR program TD64 was run.

Table 3: PCR program TD64

Step	°C	Time (s)	Step	
1	98	30	Initial denaturing step	
2	98	5	denature	Step 2-4: repeat 35 cycles
3	variable	15	anneal	
4	72	30	elongate	
5	72	300	final elongation	

10 ul of each reaction were sent out for sequencing, which was performed using 5 nM forward sequencing primer. Clones positive for homozygous deletions in exon 2 were expanded and knock-out of APP protein was confirmed via western blot using commercially available AB recognizing full length APP (abcam 32136).

Generation of isogenic AD knock-in lines

For generation of isogenic fAD knock-in lines specific gRNAs targeting Exon 16 of APP for generation of isogenic fAD knock-in lines were designed and one 20 bp long gRNAs in closest proximity to the targeting site were manually chosen while analyzing sequence of APP Exon 2 for adequate PAM sequences ('NGG') *in silico* using Geneious software program

Guide RNAS were cloned into the px330-nGPF plasmid like described in the material and methods part “Generation of isogenic knock-out line”.

Table 4: ssOligos ordered to generate CRISPR targeting Exon 16 of APP

No.	Type	Sequence	Size
Crispr 1	FOR	CACCGCAGAATTCCGACATGACTC	20 bp
	REV	AAACGAGTCATGTCGGAATTCTGC	20 bp
Crispr 2	FOR	CACCGGAGATCTCTGAAGTGAAGA	20 bp
	REV	AAACTCTTCACTTCAGAGATCTCC	20 bp

Table 5: ssOligos ordered to generate CRISPR targeting Exon 17 of APP

No.	Type	Sequence	Size
Crispr 1	FOR	CACCGACAGTGATCGTCATCACCT	20 bp
	REV	AAACAGGTGATGACGATCACTGTC	20 bp

We ordered the commercially available vector HR120-PA1, which was used as backbone (https://www.systembio.com/products/CRISPR-Cas9-Systems/HR-Targeting-Vectors/GFP-pA-LoxP-EF1-alpha-RFP-T2A-Puro-pA-LoxP-MCS/). Backbone was digested with restrictions enzymes EcoR1 and NRU1 to exclude copGFP, WPRE and SV40 promotor region to decrease vector size -resulting in HR120-PA- but also to avoid GFP signal expressed by targeting vector. For each knock-in line, 2 unique gBlocks were ordered (IDT).

The 5 prime gBlock consisted of 440 bp homolog to the 5 prime region of the specific locus we were targeting and also included the SNP itself, which we wanted to introduce. The 3 prime gBlock consisted 440 bp homolog to the 3 prime region of Exon 16, with its sequence starting in the intron next to our targeting site of interest. Each gBlock had 35 bp of overhangs on each side. These overhangs or homology arms are overlap sequences between the vector and insert, which allows cloning and assembly of insert and vector via Gibson assembly (NEB).

Table 6: Overhangs required to clone 5 prime and 3 prime homology arms into the HR120-PA vector.

HR120-p2A:	NheI and BamHI
TCCACCGCGGTGGCGGCCGCTCTAGA	5 Prime 1st overhang (NheI digest)
TCTAGAACTAGTGGATCCCCCGGGCT	5 Prime 2nd overhang (NheI digest)

CACGTAAGTAGAACATGAAATAACCTAGATCGGATC	3 Prime 1st overhang (BamHI digest)
GATCCCCGTCGACTGCATGCAAGCTTGGCGTAATC	3 Prime 2nd overhang (BamHI digest)

Besides that, each gBlock contained silent mutations introduced to avoid binding of the gRNAs and therefore cutting by the Cas9 endonuclease after being successful used for homologous recombination. The following gBlocks were ordered:

To generate HR-120-PA-AT:
TCCACCGCGGTGGCGGCCGCTCTAGAAATTGAAGTTTTAAATATAGGGTATCATTTTTCTTTAAGAGTCATTT
ATCAATTTTCTTCTAACTTCAGGCCTAGAAAGAAGTTTTGGGTAGGCTTTGTCTTACAGTGTTATTATTTATG
AGTAAAACTAATTGGTTGTCCTGCATACTTTAATTATGATGTAATACAGGTTCTGGGTTAACGAACATAAAA
ACCGAGGAGATCTCTGAAGTGAAGATGGATACAGAGTTTCGCCACGATTCCGGATATGAAGTTCATCATCA
AAAATTGGTACGTAAAATAATTTACCTCTTTCCACTACTGTTTGTCTTGCCAAATGACCTATTAACTCTGGTTC
ATCCTGTGCTAGAAATCAAATTAAGGAAAAGATAAAAATACAATGCTTGCCTATAGGATTACCATGAAAAC
ATGAAGAAAATAAATAGGCTAGGCTGAGCGCAGTGGCTCTCTAGAACTAGTGGATCCCCCGGGCT

To generate HR-120-PA-AV:

TCCACCGCGGTGGCGGCCGCTCTAGAAATTGAAGTTTTAAATATAGGGTATCATTTTTCTTTAAGAGTCATTT
ATCAATTTTCTTCTAACTTCAGGCCTAGAAAGAAGTTTTGGGTAGGCTTTGTCTTACAGTGTTATTATTTATG
AGTAAAACTAATTGGTTGTCCTGCATACTTTAATTATGATGTAATACAGGTTCTGGGTTAACGAACATAAAA
ACCGAGGAGATCTCTGAAGTGAAGATGGATGTAGAGTTTCGCCACGATTCCGGATATGAAGTTCATCATCA
AAAATTGGTACGTAAAATAATTTACCTCTTTCCACTACTGTTTGTCTTGCCAAATGACCTATTAACTCTGGTTC
ATCCTGTGCTAGAAATCAAATTAAGGAAAAGATAAAAATACAATGCTTGCCTATAGGATTACCATGAAAAC
ATGAAGAAAATAAATAGGCTAGGCTGAGCGCAGTGGCTCTCTAGAACTAGTGGATCCCCCGGGCT

To generate HR-120-PA-SWE:

TCCACCGCGGTGGCGGCCGCTCTAGAAATTGAAGTTTTAAATATAGGGTATCATTTTTCTTTAAGAGTCATTT
ATCAATTTTCTTCTAACTTCAGGCCTAGAAAGAAGTTTTGGGTAGGCTTTGTCTTACAGTGTTATTATTTATG
AGTAAAACTAATTGGTTGTCCTGCATACTTTAATTATGATGTAATACAGGTTCTGGGTTAACGAACATAAAA
ACCGAGGAGATCTCTGAAGTGAATCTAGATGCAGAGTTTCGCCACGATTCCGGATATGAAGTTCATCATCA
AAAATTGGTACGTAAAATAATTTACCTCTTTCCACTACTGTTTGTCTTGCCAAATGACCTATTAACTCTGGTTC
ATCCTGTGCTAGAAATCAAATTAAGGAAAAGATAAAAATACAATGCTTGCCTATAGGATTACCATGAAAAC
ATGAAGAAAATAAATAGGCTAGGCTGAGCGCAGTGGCTCTCTAGAACTAGTGGATCCCCCGGGCT

Insertion of 5 prime and 3 prime gBlocks is achieved in through several cloning steps. To introduce the 5 prime homology arm, HR120-PA is digested first with the restriction enzyme NHEI, followed by Gibson assembly using the digested vector and the 5 prime gBlock. In a subsequent step, the vector has to be cut with the restriction enzyme BAMHI, followed by Gibson assembly with the 3 prime homology arm. The gBlocks were resuspended with TBE to a final concentration

of 10 ng/ul and Gibson reaction was performed according to he manufacture (NEB) after making calculations in silico using a ligation calculator (http://www.insilico.uni-duesseldorf.de/Lig_Input.html). 2 ul of each Gibson reaction was transformed into Stble3 bactria and grown overnight on agar plates containing ampicillin. Grown colonies were selected and expanded in LB media. Plasmids were isolated using QIAPrep Spin Miniprep Kit (Qiagen) and send out for sequencing (Macrogen) at a final concentration of 80-120 ng/ul. Correct integration of the gBlock was confirmed using the universal primer M13F: GTAAAACGACGGCCAGT. Successful clones were expanded using the Plasmid Maxi Kit (Qiagen) and plasmids were stored at -20 until usage.

Nucleofection was performed using the 4-D nucleofector system (AMAXA) and the P3 nucleofection kit 1*10^6 cells were dissociated using Accutase (StemCell Technologies) washed off with PBS and collected in 15 ml falcon tubes. Cells were spun down at 800 rpm for 5 min and resuspended in 100 µl nucleofection solution supplemented with two different plasmids: 5 µg px330-nGFP and 20 µg of each targeting vector were transferred into the nucleofection cuvette and stored on ice for 5 min before proceeding. The standard program CB-150 was used for all nucleofections. Immediately post nucleofection 500 µl of pre-warmed media was added to each cuvette and cells were transferred to Matrigel coated dishes containing mTeSR media with 4 µM RHOK inhibitor to improve survival. RHOK inhibitor was removed 24 h post nucleofection. Media was changed to mTeSR supplemented with puromycin (2 µM) 48 h post nucleofection to start selection for successfully targeted clones for 7 days to exclude false positive clones due to episomal activity of the targeting vector. We then observed the emergence of Puromycin-resistant clones that maintained hiPSC-like morphology. Cells were allowed to grow to confluence. To excise the selection cassette we nucleofected mixed clones containing at least 100 colonies with pCAG-Cre:GFP (Matsuda and Cepko, 2007). To enrich for cells that received the CRE plasmid we enriched for GFP containing cells using fluorescence-activated cell sorting. To exclude cells, that received the CRE plasmid, but which were still expressing the dsRED, which is flanked by loxP-sites, we sorted for GFP+/dsRED- cells. Post Cre excision we screened for homologous recombination and corrected insertions using primers flanking the exon of interest, run PCRs and send the results out for sequencing (Macrogen) like described before. Confirmed positive clones were expanded and used for experiments. Primer flanking Exon 16 and 17 were ordered (lifetechnologies) according to table 7 and 8.

Table 7: 3 primer sets flanking the exon 16 were, designed *in silico* using Geneious software

No.	Type	Sequence	Size

Primer 1	FOR	GCAGCAGAAGCCTTACTTTGA	539 bp
	REV	CTCCCAAAGTGCTGGGATTA	
Primer 2	FOR	CAGGTTTCCCTTACCCTTTCA	485 bp
	REV	GCGCTCAGCCTAGCCTATTT	
Primer 3	FOR	ACAGGTTCTGGGTTGACAAA	186 bp
	REV	TTCTAGCACAGGATGAACCAGA	

Table 8: 3 primer sets flanking the exon 17 were, designed *in silico* using Geneious software

No.	Type	Sequence	Size
Primer 1	FOR	TGTGGGTTCAAACAAAGGTGC	208 bp
	REV	AGTTCTTAGCAAAAAGCTAAGCC	
Primer 2	FOR	GTGGGTTCAAACAAAGGTGC	200 bp
	REV	AGCAAAAAGCTAAGCCTAATTCTCT	
Primer 3	FOR	TCATTGGACTCATGGTGGGC	235 bp
	REV	CAAGCATCATGGAAGCACAC	

Generation of CTIP2 reporter lines: mNeonGreen targeting vector

The final vectors were derived through modifications of the our standard available HR120-PA-1 vector (https://www.systembio.com/genome-engineering-precisionx-HR-vectors/gene-tagging). To create a new multicistronic vector the copGFP-polyA cassette was removed using EcoRI and NruI and the vector sequence was restored via gBlock cloning which introduced a P2A cassette. In subsequent steps the XhoI site and Gibson assembly was used to introduce the gBlock with mNeonGreen CDS followed by a WPRE element. The following gBlock was ordered to generate HR120-PA-mNeonGreen:

ACGTTGTAAAACGACGGCCAGTGAATTCAGCTAGCGGAAGCGGAGCTACTAACTTCAGCCTGTTGAAACAA
GCAGGGGATGTCGAAGAGAATCCCGGGCCATTGAAGACAAAATCAACCTCTGGATTACAAAATTTGTGAAA
GATTGACTGGTATTCTTAACTATGTTGCTCCTTTTACGCTATGTGGATACGCTGCTTTAATGCCTTTGTATCAT
GCTATTGCTTCCCGTATGGCTTTCATTTTCTCCTCCTTGTATAAATCCTGGTTGCTGTCTCTTTATGAGGAGTT
GTGGCCCGTTGTCAGGCAACGTGGCGTGGTGTGCACTGTGTTTGCTGACGCAACCCCCACTGGTTGGGGCA
TTGCCACCACCTGTCAGCTCCTTTCCGGGACTTTCGCTTTCCCCCTCCCTATTGCCACGGCGGAACTCATCGC
CGCCTGCCTTGCCCGCTGCTGGACAGGGGCTCGGCTGTTGGGCACTGACAATTCCGTGGTGTTGTCGGGGA
AATCATCGTCCTTTCCTTGGCTGCTCGCCTGTGTTGCCACCTGGATTCTGCGCGGGACGTCCTTCTGCTACGT
CCCTTCGGCCCTCAATCCAGCGGACCTTCCTTCCCGCGGCCTGCTGCCGGCTCTGCGGCCTCTTCCGCGTCTT
CGCCTTCGCCCTCAGACGAGTCGGATCTCCCTTTGGGCCGCCTCCCCGGAGAAAAGGGGGGAC

For introduction of our 5-prime homology arm the plasmid had to be digested with NHEI first, followed by BAMHI in a second cloning round to insert the 3-prime arm like reported before. The 5-prime homology arm ends before the stop codon of the gene of interest to allow for a fusion protein or multicistronic expression. The necessary overhangs are shown in detail in Table 9. In the case of the CTIP2 targeting vector (HR120-mNeonGreen-CTIP2), we used ~420-bp sequences with homology to the targeted CTIP2 locus, that can act as homology arms and the last exon of the CTIP2 gene after removal of the stop codon is fused to an in frame p2A-mNeonGreen sequence followed by the WPRE site and a loxP-flanked drug-resistance cassette.

Table 9: Nucleotide sequence that can be used to create overlapping sequences for Gibson assembly of vector and 5 prime / 3 prime gBlocks**.**

HR120-p2A-mNeonGreen:	NheI and BamHI
GACGTTGTAAAACGACGGCCAGTGAATTCAGCTAG	5 Prime 1st overhang (NheI digest)
GCTAGCGGAAGCGGAGCTACTAACTTCAGCCTGTTGA	5 Prime 2nd overhang (NheI digest)
CACGTAAGTAGAACATGAAATAACCTAGATCGGATC	3 Prime 1st overhang (BamHI digest)
GATCCCCGTCGACTGCATGCAAGCTTGGCGTAATC	3 Prime 2nd overhang (BamHI digest)

Sequence of 5 prime gBlock to generate HR120-PA-mNeonGreen:

GACGTTGTAAAACGACGGCCAGTGAATTCAGCTAGCCGCAGCGACACGTGCGAGTACTGCGGCAAGGTGT
TCAAGAACTGCAGCAACTTGACGGTGCACCGGCGGAGCCACACCGGCGAGCGGCCTTACAAGTGCGAGCT
GTGCAACTACGCGTGCGCGCAGAGCAGCAAGCTCACGCGCCACATGAAGACGCACGGGCAGATCGGCAAG
GAGGTGTACCGCTGCGACATCTGCCAGATGCCCTTCAGCGTCTACAGCACCCTGGAGAAACACATGAAAAA
GTGGCACGGCGAGCACTTGCTGACTAACGACGTCAAAATCGAGCAGGCCGAGAGGAGCAGCGGAAGCGG
AGCTACTAACTTCAGCCTGTTGA

Sequence of 3 prime gBlock to generate HR120-PA-mNeonGreen:

CACGTAAGTAGAACATGAAATAACCTAGATCGGCGCGCGGGCCCCGGCGCCCCGCACCTGTACAGTGGAA
CCGTTGCCAACCGAGAGAATGCTGACCTGACTTGCCTCCGTGTCACCGCCACCCCGCACCCCGCGTGTCCCC
GGGGCCCAGGGGAGGCGGCACTCCAACCTAACCTGTGTCTGCGAAGTCCTATGGAAACCCGAGGGTTGAT
TAAGGCAGTACAAATTGTGGAGCCTTTTAACTGTGCAATAATTTCTGTATTTATTGGGTTTTGTAATTTTTTTG
GCATGTGCAGGTACTTTTTATTATTATTTTTTCTGTTTGAATTCCTTTAAGAGATTTTGTTGGGTATCCATCCC
TTCTTTGTTTTTTTTTTAACCCGGTAGTAGCCTGAGCAATGACTCGCAAGCAATGTTAGAGGGGAAGCATAT
CTTTTAAATTATAATTTGGGCCCGTCGACTGCATGCAAGCTTGGCGTAATC

Table 10: CRISPR used to target CTIP2 in close proximity to the last exon

No.	Type	Sequence	Size
Crispr 1	FOR	CACCCGAGAGGAGCTAAGCGCGC	20 bp

	REV	AAACGCGCGCTTAGCTCCTCTCGG	20 bp

Table 11: CRISPR used to target CTIP2 in close proximity to the last exon

No.	Type	Sequence	Size
Primer 1	FOR	TGGTATCCGGAGCCATCTACCATGGC	858 bp
	REV	CATCCTGCAATGCGCAGGACAGC	
Primer 2	FOR	TCATCACAGGACCGTCAGCAGG	912 bp
	REV	CATCCTGCAATGCGCAGGACAGC	

Generation of CTIP2-reporter knock-in lines

Nucleofection was performed like described under the material and methods part "Generation of isogenic AD knock-in lines" using 2 different plasmids: 5 µg px330-GFP-CTIP2 DNA and 20 µg of Hr120-mNeonGreen-CTIP2 targeting vector were transferred into the nucleofection cuvette and stored on ice for 5 min before proceeding. The standard program CB-150 was used for all nucleofections. Immediately post nucleofection 500 µl of pre-warmed media was added to each cuvette and cells were transferred to Matrigel coated dishes containing mTeSR media with 4 µM RHOK inhibitor to improve survival.

To improve the odds of successful targeting we created CRISPR/CAS9 constructs by cloning CRISPR guide sequences into the pX330 Cas9 plasmid (Cong et al., 2013). We selected CRISPR guide sequences that were located on opposite strands overlapping with the stop codon of the CTIP2 gene. Guides were designed to exhibit overlapping sequences in both homology arms to prevent binding of the CRISPR to the targeting vector (Figure 43B) After nucleofection of hiPSCs with both CTIP2-CRISPR-Cas9 expression vectors as well as the pHR120-CTIP2:mNeonGreen-WPRE plasmid, cells were recovered in mTESR supplemented with 4 µM RHOK inhibitor Y-27632 (StemCell Technologies) to increase viability for 24h on plates pre-coated with BD Matrigel and then switched back to normal mTESR. Henceforth they were cultured in the presence of Puromycin for 7 days to exclude potential resistance resulting from episomal activity of the targeting vector. We then observed the emergence of Puromycin-resistant clones that maintained hiPSC-like morphology. Cells were allowed to grow to confluence. To excise the selection cassette we nucleofected mixed clones containing 100 to 200 selected colonies with pCAG-Cre:GFP

(Matsuda and Cepko, 2007). To enrich for cells that received the CRE plasmid we enriched for GFP containing cells using flow sorting Post Cre excision we screened for homologous recombination and correct gene insertion using primers outside the targeting arm and inside the targeting vector. Primer inside the targeting vector were only able to bind and the PCR was successful, if mNeonGreen had been introduced into the targeted locus via homologous recombination. PCR products were sent out for sequencing and positive clones were expanded and differentiated into cortical neurons using the differentiation protocol. Clones were checked for mNeonGreen expression every 3 to 4 days and positive clones were dissociated at d45 and immunofluorescence-staining (IF) with commercially available CTIP2 antibody was performed to check colocalization of endogenous and IF signal.

Immunocytochemistry and Image Analysis

Cells (**iPSCs, cortical cultures or organoids**) were fixed in 4% paraformaldehyde (PFA) at room temperature for 20 minutes, washed 3 times in phosphate buffered saline (PBS), and blocked for 1 hour in 10% goat or horse serum/PBS with 0.1% triton. Cells were incubated in primary antibody overnight in blocking solution. After primary antibody incubation, cells were washed 3 times in PBS for ten minutes each and then incubated in secondary antibody in blocking solution for 1 hour. Secondary antibodies were conjugated to Alexa 488, 568, or 647 (Life Technologies, 1:500). Hoechst 33342 (Life Technologies) was used for nuclear staining. Images of cortical neurons were captured using an automated Operetta wide field live-imaging microscope (PerkinElmer) at 20X magnification. Subsequent image quantification was performed using the associated Columbus Image Data Storage and Analysis System software (PerkinElmer).

A size and morphology threshold based on Hoechst was used to eliminate apoptotic nuclei from quantification. Neurons were identified by MAP2 fluorescence in the cytoplasm and once the boundaries of the cells and their nuclei were defined, the fluorescence intensities of the indicated antibody-labeled proteins were added up giving the “total intensity” in arbitrary units. That number was then divided by the number of pixels in that region, resulting in the “mean intensity” (of a pixel in the cell), in a way that is independent of the cell size. The average intensity of a given protein per cell was averaged across at least 25 random fields per well and 3-5 wells per condition, containing, in total hundreds to thousands of neurons. For each experiment, five wells with no primary antibody were used to determine background fluorescence intensity.

In the case of **brain organoids**, these were transferred from the spinner flask into a 1.5 ml eppendorf tube containing 4% PFA and were kept rotating at 4ºC over night. Next, they were washed with PBS 3 times every ten minutes and transferred to 15% sucrose, rotating at 4ºC over night for cryoprotection. They were then transferred to 30% sucrose in similar conditions and finally embedded in OCT and slowly froze in pure ethanol with dry ice. The embedded brain organoids were sectioned at 12 µm thickness using a cryostat (Leica CM 1950) and collected on slides. Samples were rinsed in PBS, permeabilized and blocked in 10% normal goat serum (NGS), 0.25% Triton-X100 under constant shaking for 30 min in PBS for 30 min. Samples were incubated with primary antibodies and secondary antibodies as described above and mounted with Vectashield with DAPI (Vectorlabs). Images were captured with LSM 700 Inverted Confocal (Leica) and Axio Scan Z1 (Zeiss).

ATP Quantification

ATPliteTM is an Adenosine TriPhosphate (ATP) monitoring system based on firefly luciferase (Photinus pyralis). This luminescence assay is used to evaluate proliferation and cytotoxicity. ATP is a marker for cell viability because it is present in all metabolically active cells and the concentration declines very rapidly when the cells undergo necrosis or apoptosis. The ATPlite assay is based on the production of light caused by the reaction of ATP with added luciferase and its substrate d-luceferin. This is illustrated in the following reaction scheme:

$$\text{ATP} + \text{D-Luciferin} + O_2 \xrightarrow[Mg^{2+}]{\text{LUCIFERASE}} \text{Oxyluciferin} + \text{AMP} + PP_i + CO_2 + \text{Light}$$

The emitted light is proportional to the ATP concentration. The lysis buffer raises the pH of the cell culture medium, which inactivates the endogenous ATPases. The subsequent addition of the substrate solution (Luciferase/Luciferin) lowers the pH to a suitable level so that the reaction can occur.

The ATP measurements were performed following manufacturer instructions. Briefly, white 96-microplates (PerkinElmer) were coating with matrigel for 1 hour at room temperature and then 4.000 iPSCs plated per well in presence of RHOK Inhibitor over night to prevent cell death and promote the adhesion of the cells to the wells. Between 5-10 well per line per plate and 3 plates -1

for each time-point- were prepared per experiment. Media was changed the next day and ATP measurement performed 2, 4 and 6 days later.

Right before starting the procedure media was changed again to ensure that each well contained exactly 100 µl of media. 50 µl of cell lysis solution were then added per well and the plate shook for five minutes. Each plate additionally contained, besides the iPSCs experimental samples,10 extra wells where an ATP standard curve was prepared. 100 µL of complete culture medium without cells were pipetted into these designed wells. The first point of the ATP standard was 10 µM and from it 8 1:5 serial dilutions with distilled water down to blank were made in independent tubes. 10 µL of the ATP dilution series were pipetted into the "ATP standard wells" and the plate shook for five minutes. 50 µl of substrate solution were added to all wells and the plate incubated again for five minutes shaking. The plates were then protected from light for ten more minutes and luminescence then measured by using an EnVisionTM device.

Enzyme Linked Immunosorbent Assay (ELISA)

Aβ42 and Aβ40 levels were determined by ELISA (Life technologies). To determine Aβ42 and Aβ40 levels from iPSCs, cells were seeded, neurons were seeded in 24 well plates and spheres were cultured in ultra-low attachment six-well plates. Fresh media was added, and 1 ml of media was collected after 72 h of culturing. The assay was performed following the manufacturer´s protocol.

To determine protein concentration, hiPSCs / neurons / spheres were collected and lysed in RIPA Lysis buffer (Sigma Aldrich) supplemented with 2% SDS (VWR) and 100x Phosphatase inhibitor (Thermo Fisher Scientific) and Protease inhibitor (Santa Cruz Biotechnology), homogenized and boiled at 95C for 10 min and stored at -20C until further use. Protein concentration was quantified using BCA assay kit (Pierce) and absorbance was measured at 548nm.

Flow analysis and FACS of CTIP2+ CXNs

To assess the percentage and create pure cultures of CTIP2+ cells, spheres were analyzed and sorted using a BD FACSAria II+ flow sorter. Cells were dissociated and counted and medium adjusted to contain no more than 2 million cells per ml and transferred into Falcon® 5mL round-bottom Polystyrene test tubes, with cell strainer snap caps and run on the 15-parameter BD

FACSAria II+, customized for small particle to average cell (<0.1 microns) sorting using a low-pressure nozzle and custom settings. Forward scatter (FSC) and side scatter (SSC) was used to eliminate debris in conjunction with (FSW) and (SSC) to focus on single cells. mNeonGreen fluorescence versus GFP fluorescence was used to select CTIP2 positive cells and remove dead cells (auto-fluorescence in the red channel). Data was analyzed using FlowJo software. Dissociation of tight neurospheres is a critical step as the process will inevitably lead to cell death and debris. Debris and dead cells typically have a lower level of forward and side scatter (FSC-A/SSC-A) and are found in the lower left part of the scatter plot (Top row). We gated to exclude most dead cells and debris. We used a pulse geometry gate FSC-W & SSC-H to gate out doublets (middle row). We quantified CTIP2 expression on a GFP-A PE-GFP green-A gate against a negative pluripotent control. Usually we performed experiments in triplicates. Some experiments were quantified using more differentiation replicates.

Western Blots

Cells were lysed in RIPA Lysis buffer (Sigma Aldrich) supplemented with 2% SDS (VWR) and 100x Phosphatase inhibitor (Thermo Fisher Scientific) and Protease inhibitor (Santa Cruz Biotechnology), homogenized and boiled at 95C for 10 min and stored at -20C until further use. Protein concentration was quantified using BCA assay kit (Pierce) and absorbance was measured at 548nm. For Western blot analysis 20-40 µg total protein supplemented with 4x Laemmli Sample Buffer (Bio-Rad) and denatured under reducing conditions for 10min at 95□C. Samples were loaded onto a x% Bis-Tris (Bio Rad) gel, and run at X,Y,Z, and then transferred to PVDF membrane (0.22 µm; Millipore) using the Criterion Blotter system (Bio Rad).

Membranes were blocked for 1hr at room temperature in 5% w/v non-fat milk (Santa Cruz) in TBS containing 0.1% v/v Tween-20 (Fisher Scientific; TBS-T). Membranes were then incubated in the indicated primary antibody (in 5% milk/TBS-T) overnight at 4□C, washed 4x in TBS-T for 30min - 1h, incubated in species-specific HRP-conjugated secondary antibody (in 5% milk/TBS-T) for 1hr at room temperature, and then washed 4x in TBS-T. Membranes were subsequently developed with ECL western blotting substrate (Pierce) using the XXX developer. Membranes were then washed 1x in TBS-T and stripped in stripping buffer [look up which one we are using 25mM Glycine HCl, pH 2.0 and 1% w/v SDS] with vigorous shaking to remove primary and secondary antibody, washed 3x in TBS-T, and blocked for 1hr (in 5% milk/TBS-T) at room

temperature before probing with the next primary antibody overnight at 4°C. Signal intensity of bands was measured with Bio-Rad image software and quantified with Microsoft Excel.

Transformations

Transformations were performed using One Shot™ Stbl3™ Chemically Competent E. coli bacteria. Stbl3 were thawed on ice and 0.2 to 1 µL of the Plasmid (50 pg to 500 ng) into a vial of One Shot™ cells and gently mixed. Vial(s) were incubated for 20 min on ice and then heat-shocked at 42°C for 40 seconds. Vial(s) were put back on ice for 2 min and 250 µL of pre-warmed S.O.C. Medium (Invitrogen) to each vial was added to each. Vial(s) were put into a shaker and shook at 225 rpm in a shaking incubator at 37°C for 1 hour. Vial(s) were spun down at 2500 rpm for 4 min and 250 µL were taken out. Bacterial pellet was gently resuspended by shaking and tipping the vial(s). 10-20 µL from each transformation was put on a pre-warmed ampicillin selective plates. Plates were inverted and incubated overnight at 37°C. Colonies were picked next day and each colony was transferred into falcon tubes containing 6 ml of pre-warmed LB media supplemented with ampicillin (1 mg/ml) and incubated overnight at 37°C at 225 rpm in a shaking incubator. 5 ml were taken out and Plasmid(s) were isolated using the QIAprep Spin Miniprep Kit (250) (Qiagen), purity/quantity was measured via Nanodrop and analyzed via PCR followed by sequencing (Macrogen). The remaining ml was stored at 4°C until validation of plasmid via sequencing. To obtain a high yield of plasmid, 1ml was added to a glass bottle containing 250 ml of LB media supplemented with ampicillin and incubated at 37°C at 225 rpm in a shaking incubator overnight. Plasmid(s) were isolated using the QIAprep Spin Maxi Kit (25) (Qiagen) purity/quantity was measured via Nanodrop and plasmids were stored at -20°C until use.

Antibodies and chemicals

The following antibodies were used for cell experiments for WB and IF:
mouse β-actin (Cell Signaling Technology, 3700S); rabbit β-tubulin (Abcam, ab6046); rabbit amyloid precursor protein (Abcam, ab32136), mouse β-amyloid (Biolegend, SIG-39220, 4G8), mouse β-amyloid (Biolegend, SIG-39320, 6E10), mouse phospho-tau (Thermo Fisher Scientific, MN1020, AT8), mouse TAU (Abcam, ab80579, TAU-5), rat CTIP2 (Abcam ab18465, 25B6), chicken MAP2 (Lifespan Biosciences LS-C61805).

The following chemicals were used for cell experiments for WB and IF and live-cell imaging: Thapsigargin (Life technologies, T7458), Tunicamycin (Sigma Aldrich T7765), MG132 (Thermo Fisher Scientific, NC9326288), BACE-1 β-secretase inhibitor IV xnM (EMD Millipore), Compound E (Enzo life sciences), DAPT xnM (Sigma Aldrich), DMSO (Thermo Fisher Scientific), DAPI (Life technologies, P-36931), Vectashield (Vector Laboratories H-1200).

Automated time-lapse live-imaging and survival assays

Cell tracking and image analysis

Image analysis was performed using CL-Quant software (Nikon Corporation), and Nikon specialized viewer software to easily review the analysis results from these data sets was designed by Nikon. To detect the morphologic properties of the cells in the culture, morphologic filters (or masks) were designed to identify and quantify the different features of the neurons, including cell body number, neurite length, cell body size, compactness, and intensity, in the raw image. This filter combination was then used to identify cells and neurites in the raw images. After the filters for detection of each cell were optimized, the tracking was performed using the filter for cell body. The setting parameters used in CL-Quant for this tracking are as follows: minimum object size: 50, maximum object size: 999999, maximum search range: 200, split threshold: 0.90, merge threshold: 0.70, minimum trajectory length: 5, object split: ignore split, object merge: merge with partition, enable lineage: off, enable robust measurement: off, object-to-object overlap: off, remove short track when merging: off.

Survival assay

Spheres of all isogenic lines were dissociated like described before and 2 x10^6 cells of each line were seeded into 1 well of a 24 well plate containing FluoroBrite DMEM (Thermo Fisher Scientific) media supplemented with 1%/vol N2 supplement and 5%/vol B27-vitA supplement + 10ng/ml BDNF, CNTF and GDNF. 24 well plates were pre-coated with Laminin/Fibronectin before plating the cells like described before. Cells were kept in incubator overnight and next day medium was aspirated gently, and cells were incubated with calcein-red (10nM) solution for 30 min of incubation time at 37C and then washed several times. Pre-warmed FluoroBrite media containing DMSO (10nM), MG132 (10nM), Tunicamycin (10nM) or Thapsagargin (10nM) was added and plates were transferred into Biostation live-cell imager (Nikon). Four technical replicate wells per

conditions per line per experiment were imaged. A 10× objective was used to acquire phase and fluorescent images at each time point. For each well, a 12 × 12 stitched tiling captured an area of 3.2 × 3.2 mm. Images were automatically captured every 6 hours for a total of 138h.

Statistical Analysis

Statistical significance was determined by analysis of one-way-variance (ANOVA) for groups of 3 or more in experiments were there was only one variable, followed by a Dunnett's Multiple Comparison post-test. Two-way ANOVA analysis was performed for experiments with 3 or more groups and more than one variable followed by a Bonferroni Multiple Comparison post-test. A confidence interval of 95% was used for all comparisons. All experiments represent the result of at least 3 biological replicates.

Proteomics, Cell lysis and protein digestion

Cells were lysed in 8M urea, 50 mM EPPS (pH 8.0), 150 mM NaCl, 0.5% NP-40 and sonicated. The homogenate was sedimented by centrifugation at 21,000 x g for 5 min. Proteins were subjected to disulfide bond reduction with 5 mM tris (2-carboxyethyl)phosphine (room temperature, 30 min) and alkylation with 10 mM chloroacetamide (room temperature, 30 min in the dark). Methanol-chloroform precipitation was performed prior to protease digestion. Samples were resuspended in 100ul of 100 mM EPPS, pH 8.5 buffer and digested at 37°C for 2 h with LysC protease at a 200:1 protein-to-protease ratio. Trypsin was then added at a 100:1 protein-to-protease ratio and the reaction was incubated for a further 6 h at 37°C.

Proteomics, Tandem mass tag labeling

Tandem mass tag (TMT) 10-plex labeling was based on previously published protocols (Paulo and Gygi, 2015; Paulo et al., 2015). In brief, 100 µg of peptides from each sample were labeled with TMT reagent. A total of 10 µL of the 20 ng/µL stock of TMT reagent was added to the peptides along with anhydrous acetonitrile to achieve a final acetonitrile concentration of approximately 30% (v/v). Following incubation at room temperature for 1 h, the reaction was quenched with hydroxylamine to a final concentration of 0.5% (v/v) for 15 min. The TMT-labeled samples were pooled at a 1:1:1:1:1:1:1:1:1:1 ratio. The sample was vacuum centrifuged to near dryness and subjected to C18 solid-phase extraction (SPE) (Sep-Pak, Waters).

Proteomics, Off-line basic pH reversed-phase (BPRP) fractionation

We fractionated the pooled TMT-labeled peptide sample using BPRP HPLC (Wang et al., 2011). Samples were then offline fractionated over a 90 min run, into 96 fractions by high pH reverse-phase HPLC (Agilent LC1260) through an aeris peptide xb-c18 column (phenomenex; 250mmx3.6mm) with mobile phase A containing 5% acetonitrile and 10 mM NH4HCO3 in LC-MS grade H2O, and mobile phase B containing 90% acetonitrile and 10 mM NH4HCO3 in LC-MS grade H2O (both pH 8.0). The 96 resulting fractions were then pooled in a non-continuous manner into 24 fractions (as outlined in Supplemental Figure 5 of (Paulo et al., 2016a)) and 12 fractions (even numbers) were used for subsequent mass spectrometry analysis. Fractions were vacuum centrifuged to near dryness. Each consolidated fraction was desalted via StageTip, dried again via vacuum centrifugation, and reconstituted in 5% acetonitrile, 1% formic acid for LC-MS/MS processing.

Proteomics, Liquid chromatography and tandem mass spectrometry

Our mass spectrometry data were collected using an Orbitrap Fusion Lumos mass spectrometer (Thermo Fisher Scientific, San Jose, CA) coupled to a Proxeon EASY-nLC 1000 liquid chromatography (LC) pump (Thermo Fisher Scientific). The capillary column was a 100 µm inner diameter microcapillary column packed with ~35 cm of Accucore resin (2.6 µm, 150 Å, Sepax, Newark, DE). For each analysis, we loaded ~2 µg onto the column.

Each peptide fraction was separated using a 2.5 h gradient of 6 to 26% acetonitrile in 0.125% formic acid at a flow rate of ~450 nL/min. Each analysis used the Multi-Notch MS3-based TMT method (McAlister et al., 2014) which has been shown to reduce ion interference compared to MS2 quantification (Paulo et al., 2016b). The scan sequence began with an MS1 spectrum (Orbitrap analysis; resolution 120,000; mass range 400−1400 m/z; automatic gain control (AGC) target 2 × 105; maximum injection time 100 ms). Precursors for MS2/MS3 analysis were selected using a TopSpeed of 2 sec. MS2 analysis consisted of collision-induced dissociation (quadrupole ion trap analysis; AGC 4 × 103; normalized collision energy (NCE) 35; maximum injection time 150 ms). Following acquisition of each MS2 spectrum, we collected an MS3 spectrum using SPS (10) method (McAlister et al., 2014). MS3 precursors were fragmented by high energy collision-induced dissociation (HCD) and analyzed using the Orbitrap (NCE 65; AGC 5 × 104; maximum injection time 150 ms, resolution was 60,000 at 200 Th).

Proteomics, Data analysis

Mass spectra were processed using a Sequest-based in-house software pipeline (Huttlin et al., 2010). Spectra were converted to mzXML using a modified version of ReAdW.exe. Database searching included all entries from the human UniProt database. This database was concatenated with one composed of all protein sequences in the reversed order. Searches were performed using a 20 ppm precursor ion tolerance for total protein level analysis. The product ion tolerance was set to 0.9 Da. These wide mass tolerance windows were chosen to maximize sensitivity in conjunction with Sequest searches and linear discriminant analysis (Beausoleil et al., 2006; Huttlin et al., 2010). TMT tags on lysine residues and peptide N termini (+229.163 Da) and carbamidomethylation of cysteine residues (+57.021 Da) were set as static modifications, while oxidation of methionine residues (+15.995 Da) was set as a variable modification.

Peptide-spectrum matches (PSMs) were adjusted to a 1% false discovery rate (FDR) (Elias and Gygi, 2007; Elias and Gygi, 2010). PSM filtering was performed using a linear discriminant analysis, as described previously (Huttlin et al., 2010), while considering the following parameters: XCorr, ΔCn, missed cleavages, peptide length, charge state, and precursor mass accuracy. For TMT-based reporter ion quantitation, we extracted the summed signal-to-noise (S:N) ratio for each TMT channel and found the closest matching centroid to the expected mass of the TMT reporter ion. For protein-level comparisons, PSMs were identified, quantified, and collapsed to a 1% peptide false discovery rate (FDR) and then collapsed further to a final protein-level FDR of 1%. Moreover, protein assembly was guided by principles of parsimony to produce the smallest set of proteins necessary to account for all observed peptides. Proteins were quantified by summing reporter ion counts across all matching PSMs using in-house software, as described previously (Huttlin et al., 2010). PSMs with poor quality, MS3 spectra with more than 9 TMT reporter ion channels missing, MS3 spectra with TMT reporter summed signal-to-noise ratio that were less than 150, or had no MS3 spectra were excluded from quantification (McAlister et al., 2012). Protein quantification values were exported for further analysis in Microsoft Excel and Perseus (Tyanova, S., Temu, T., Sinitcyn, P., Carlson, A., Hein, M. Y., Geiger, T., et al. . Nature Methods, 13, 731 EP –. http://doi.org/10.1038/nmeth.3901). Each reporter ion channel was summed across all quantified proteins and normalized assuming equal protein loading of all 10 samples. Data access. RAW files will be made available upon request. Supplemental data Table 2 list all quantified proteins as well as associated TMT reporter ion intensities used for quantitative analysis.

Proteomics, Statistical analysis

If not otherwise stated experiments, were carried out in clonal isogenic cell lines in at least 3 differentiation experiments that were separated by time in culture. The experiments were not randomized. The investigators were not blinded during experiments and outcome assessment. Proteomics data was acquired with technical replicates from two differentiation experiments. Immunofluorescence experiments were repeated independently 2 times and at least 20 cells were analyzed from a single experiment. Error bars are mostly presented as the means ± standard deviation (s.d.) unless otherwise specified. Statistical comparisons between pairs were made using Student's t-test. Statistical analysis for gene expression analysis is denoted in the supplementary file that allows replication of the data analysis.

scRNAseq / InDrop

For inDrops-seq the cells were encapsulated in droplets and the libraries were made following the steps: 1) encapsulation, 2) cleavage of photocleavable linkers, 3) reverse transcription, 4) second strand synthesis, 5) IVT, 6) fragmentation, 7) reverse transcription, 8) PCR, 9) QC like previously described protocol (Klein et al., 2015; Zilionis et al., 2017), with the following modifications in the primer sequences.

RT primers on hydrogel beads-

5'CGATTGATCAACGTAATACGACTCACTATAGGGTGTCGGGTGCAG[bc1,8nt]GTCTCGTGGGCTCGGAGATGTGTATAAGAGACAG[bc2,8nt]NNNNNNTTTTTTTTTTTTTTTTTTV- 3'

R1-N6 primer sequence (step 151 in the library prep protocol in [2])-

5'TCGTCGGCAGCGTCAGATGTGTATAAGAGACAGNNNNNN-3'

PCR primer sequences (steps 157 and 160 in the library prep protocol in [2])-

5'-AATGATACGGCGACCACCGAGATCTACACXXXXXXXXTCGTCGGCAGCGTC-3', where XXXXXX is an index sequence for multiplexing libraries.

5'-CAAGCAGAAGACGGCATACGAGATGGGTGTCGGGTGCAG-3'

With these modifications in the primer sequences, custom sequencing primers are no longer required.

Single-cell RNA-sequencing

For the scRNA-seq experiments libraries of each isogenic cell line were analyzed. 2x 3 libraries were pooled based on their molar concentrations. Pooled libraries were then loaded at 2.07 pM and sequenced on a NextSeq 500 instrument (Illumina) with 26 bases for read1, 57 bases for read2 and 8 bases for Index1. Cell Ranger (version 1.2) (10X Genomics) was used to perform sample de multiplexing, barcode processing and single cell gene unique molecular identifier (UMI) counting,

while a digital expression matrix was obtained for each experiment with default parameters (Zheng et al., 2017), mapped to the 10x reference for mm10, version 1.2.0.

ssRNA raw data processing:

Basic processing and visualization of the scRNA-seq data were performed using the Seurat package (version 2.3) in R (version 3.3.4) (Butler et al., 2018; Macosko et al., 2015; Satija et al., 2015).

Results

4.1 Generation of isogenic familial Alzheimer's disease lines

Mutations in just three genes – APP, Presenilin 1, and Presenilin 2 – have been linked to familiar Alzheimer's disease, with most of the research in the AD field focusing on the latter two. To explore the role of the third gene in fAD, I decided to establish a fAD model focused on APP. Due to the advantages of the system described earlier, I decided to take an isogenic approach. Therefore, I chose to start the experiments with a pluripotent human stem cell control line, BJsipsD, derived from fibroblast of a healthy donor and reprogramed to pluripotency, and introduced mutations highly associated with fAD via genome engineering using the CRISPR/Cas9 system solely or in combination with very efficient targeting vectors. To successfully edit the hiPSCs, my targeting approach required the generation of different targeting vectors to be able to perform knock-out and knock-in mutagenesis workflows (Figure 17).

Knock-out mutagenesis

For APP knock-out mutagenesis we successfully modified the commercially available pX330-U6-Chimeric_BB-CBh-hSpCas9 plasmid for our purposes and added a P2A-nGFP, resulting in pX330-U6-Chimeric_BB-CBh-hSpCas9-P2A-nGFP (px330-GFP). The correct sequence of the plasmid was confirmed using Macrogen. Using the px330-GFP plasmid, we successfully nucleofected the BJsipsD hiPSCs and targeted Exon 2 of the APP gene using two different gRNAs resulting in derivation of several mutant clones (Figure 18E), many of them carrying InDels in Exon 2. The 32bp deletions resulted in a frame-shift leading to loss-of function of the APP locus and therefore protein depletion, which was further proven when cells from APP KO clones were subjected to western blots (Figure 19). Two APP-KO clones were expanded and used for further experiments.

Cell Line	Genome engineering	Codon Change	Type
BJsips Ct	-	-	Control
BJsips "A673T"	Knock-in	Exon 16: GCA -> ACA	protective
BJsips "A673V"	Knock-in	Exon 16: GCA -> GTA	pathogenic
BJsips "Swedish"	Knock-in	Exon 16: AAG/ATG -> AAT/CTG	pathogenic
BJsips "London"	Knock-in	Exon 17: GTC -> ATC	pathogenic
BJsips AD "KO"	Knock-out	14 bp	loss of function

Figure 17. Via CRISPR/CAS9, generated isogenic lines introducing SNPs (first 4 rows) or deletion (last row) in the gene amyloid precursor protein.

Knock-in mutagenesis

We successfully generated one targeting-vector used as a template during homologous recombination for each knock-in approach. The targeting vector was modified as described in the material and methods part. Further, each cloned targeting vector HR120-PA-fAD consisted of two 500 bp homology arms (HA) upstream (5 prime) and downstream (3 prime) of the targeting sites to increase the rate of homologue recombination, whereas each mutation of interest was included in our 5 prime HA. To prevent cleavage by CAS9 of the introduced HA carrying the mutation in case of successful homolog recombination events, silent mutations were introduced that prevented binding of the protospacer due to the number of mismatches.

BJsipsDs were subjected to nucleofection with targeting vector and px330-GFP vector, and following our knock-in mutagenesis workflow (Figure 17D) the following lines were derived, each of them homozygous for the mutation of interest: BJsipsD-Icelandic (AT), BJ BJsipsD-Italian (AV), BJsipsD-Swedish (SWE), BJsipsD-London (LON), carrying mutations in Exon 16 or 17, which have been reported to cause familial Alzheimer's disease (AV, SWE, LON) (Di Fede et al., 2009; Goate et al., 1991; Mullan et al., 1992) or decrease (AT) (Jonsson et al., 2012) the risk of developing familial AD and dementia in general. Successful targeted clones were confirmed via sequencing (Macrogen) (Figure 18) and at least 2 clones per line were derived and expanded for further experiments.

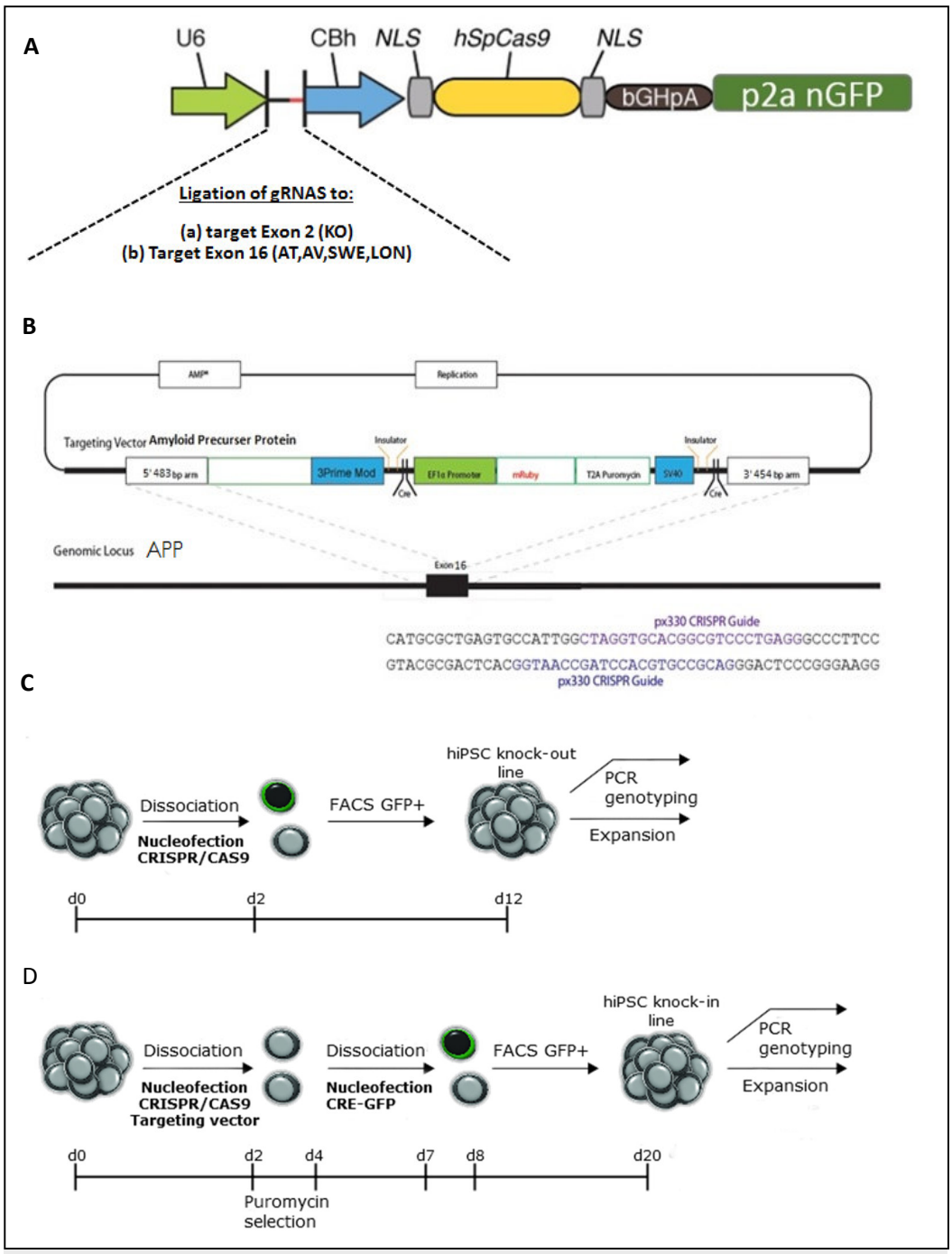

Figure 18. generated constructs required for genome engineering of hiPSCs: (**A**) modified px330-nGFP vector, expressing gRNAs to target Exon 2 or Exon 16 of APP resulting in DSBs via expressed Cas9 endonuclease followed by InDel generation or homologous recombination; (**B**) Scheme of knock-in HR120-PA-fAD targeting vector used for knock-in mutagenesis to generate HR120-PA-SWE, HR120-PA-AT and HR120-PA-AV. Vector expresses 2 unique homology arms, which include the SNP, followed flanking the targeting exon and carrying the mutation of interest loxP-flanked mRuby and drug-resistance cassette; (**C**) highly efficient knock-out workflow used to generate APP-KO line; (**D**) highly efficient knock-in mutagenesis workflow to generate lines carrying fAD mutations.

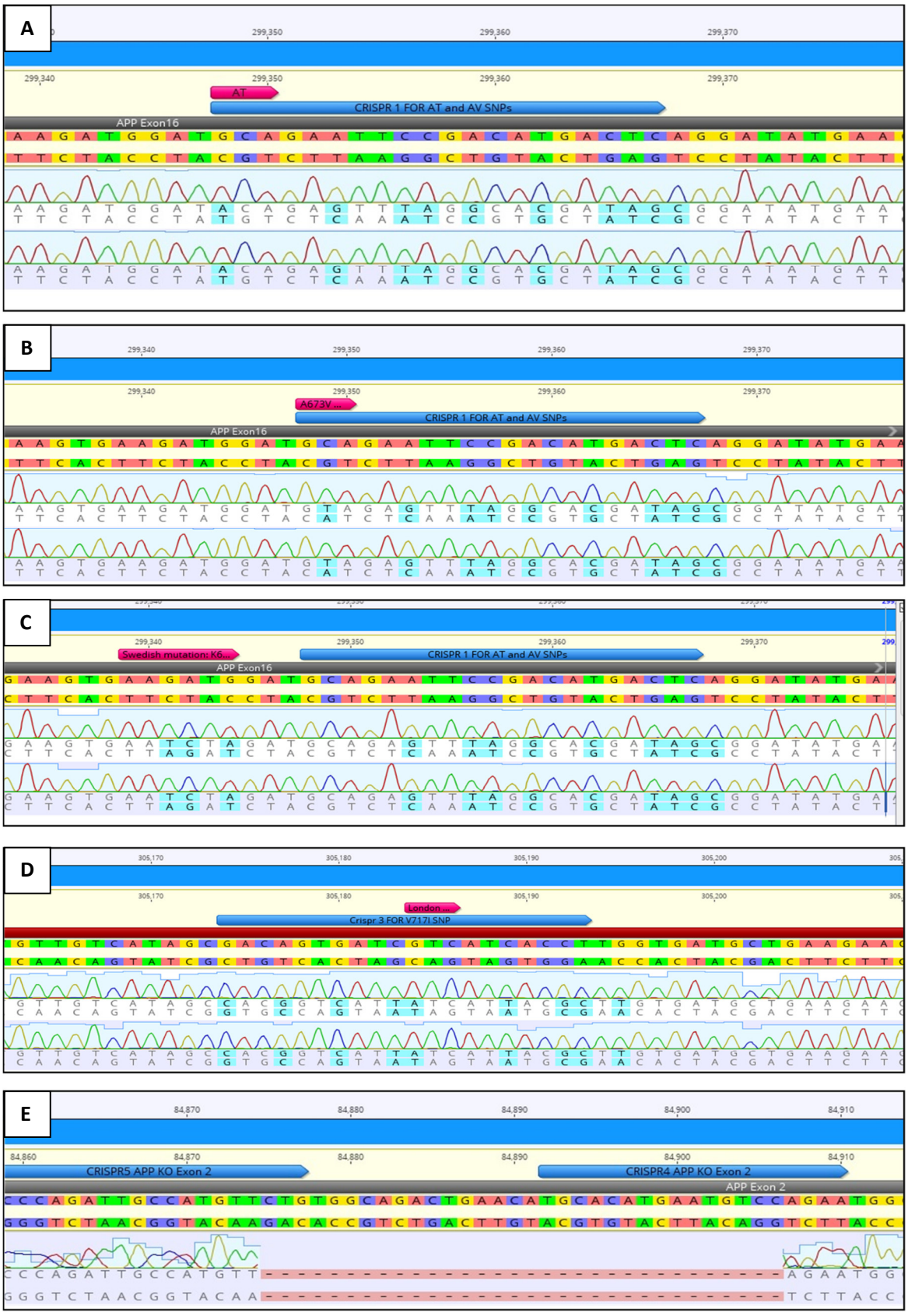
A
299,350
299,360
299,370
299,340
AT
CRISPR 1 FOR AT and AV SNPs
APP Exon16
B
299,340
299,350
299,360
299,370
A673V....
CRISPR 1 FOR AT and AV SNPs
APP Exon16
C
299,340
299,350
299,360
299,370
Swedish mutation: K6...
CRISPR 1 FOR AT and AV SNPs
APP Exon16
D
305,170
305,180
305,190
305,200
London....
Crispr 3 FOR V717I SNP
E
84,860
84,870
84,880
84,890
84,900
84,910
CRISPR5 APP KO Exon 2
CRISPR4 APP KO Exon 2
APP Exon 2

Figure 19. Sequenced gDNA of successful targeted clones aligned to APP wildtype (Wt) sequence showing 2 confirmed clones for (**A**) AT-line (GCA->ACA) , (**B**) AV-line (GCA->GTA), (**C**) SWE-line (AAG,ATG->AAT,CTA), (**D**) LON-line (GTC->ATC) and 1 confirmed clone for (**E**) KO line: 32 bp deletion; introduced silent mutation are in light blue, sgRNA for px330-GFP in dark blue; WT = wildtype, # = # of successful targeted clone.

Excluding potential off-target effects

Genome editing in combination with the use of hiPSCs allows modeling of neurodegenerative diseases on a whole new level, but unfortunately even the latest discovered programmable endonuclease Cas9 and the CRISPR/Cas9 system we used in our targeting approach can lead to unwanted off-target effects. These effects and DNA DSBs up- or downstream of the targeting site causing InDels, which lead to loss-off-function mutations. Besides sequencing the targeted exon, it is crucial to check that the protein of interest itself is translated and detectable.

To exclude any potential off target effect caused by the CRISPR/Cas9 approach in the gene APP, we extracted lysates from three different passages of all isogenic lines (except KO n=2), extracted protein and performed Western Blots using APP and Actin AB. All lines displayed APP protein as expected showing that the genome had been successfully edited and SNPs introduced without affecting the protein's function. The two bands refer to APP 770/751 and APP695, which has a lower molecular weight, because it is lacking the KPI domain. Untargeted cells (WT) showed more APP compared with isogenic mutant lines, which could be explained with increased activity and therefore cleavage of APP by α-secretase (AT) or β-secretase (AV, SWE, LON), which is then shortly processed afterwards by γ-secretase and therefore non-detectable by the AB (Figure 20).

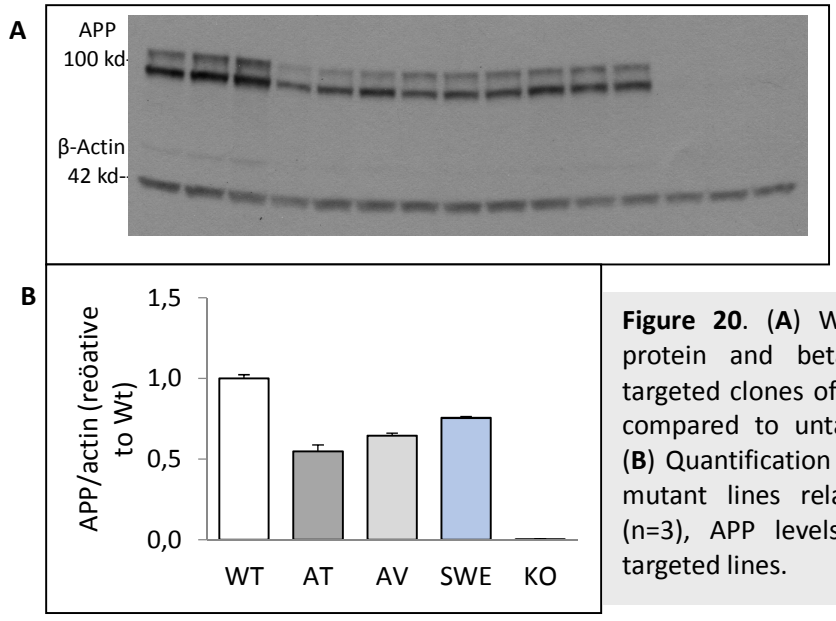

Figure 20. (**A**) Western Blot shows APP protein and beta-Actin for 3 different targeted clones of all isogenic mutant lines compared to untargeted wildtype clones, (**B**) Quantification of APP levels of isogenic mutant lines related to untargeted WT (n=3), APP levels are decreased in the targeted lines.

Another explanation could be that full mature APP protein is transported more frequently to and degraded by the lysosome more often in lines carrying mutations within the Aβ-peptide sequence or in close proximity to it (Zhang et al., 2017), which matches with our results. We have successfully created several isogenic familial AD lines, three of them carrying SNPs known to cause familial Alzheimer's disease and a rare one known to be protective. As all of them are isogenic, therefore genetically identical to the untargeted wildtype line except for the mutation of interest, we are able to overcome genetic variability and line-to-line variations that do exist in non-isogenic models. Therefore, being isogenic is the main advantage of this model compared with traditional iPSC models. Any change detected between mutant and control line is solely caused by the mutation of interest and potential downstream targets. The engineered AT-line will serve as an additional control in all further experiments, as it has been reported to be protective against Alzheimer's disease and cognitive decline as well, because it reduces Aβ production throughout life (Jonsson et al., 2012). We assume that especially aggregation-prone Aβ42 (but also Aβ40) initiates AD pathology (Selkoe and Hardy, 2016) and that either mutations or an imbalanced clearance mechanism is responsible for the increases seen in AD. Therefore, generating a line that will produce and accumulate less amounts of Aβ over time might be an even better control than the original untargeted wildtype line, even if we do mature our cells *in vitro* for a long time. The APP KO line will serve as an additional control as well, to investigate if any seen phenotype is solely due to Aβ production and therefore cannot be seen in the KO line and therefore also serve as a confirmation of the amyloid-beta hypothesis. Two clones of each isogenic line were subjected to karyotypic analysis (WiCell) (Figure 21).

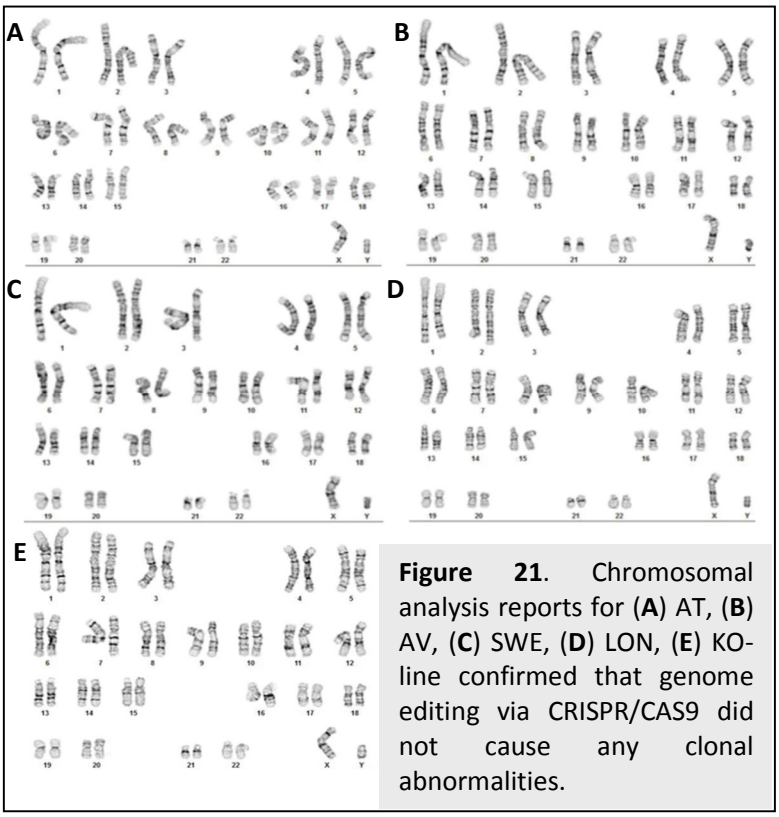

Figure 21. Chromosomal analysis reports for (**A**) AT, (**B**) AV, (**C**) SWE, (**D**) LON, (**E**) KO-line confirmed that genome editing via CRISPR/CAS9 did not cause any clonal abnormalities.

Genetically engineered hiPSCs lines carry the risk of unwanted off-target effects (often resulting in loss-of-function mutations) within the targeted gene due to the characteristic of the gRNA to tolerate up to 7 mismatches in the targeted DNA sequence, but they might also lead to chromosomal abnormalities, but causing two DSBs far away from each other and outside the target sequence that could indeed lead to chromosomal abnormalities. Analyzing the chromosomes is therefore of high importance. All clones displayed normal karyotype and no clonal abnormalities were detected at the stated band solution. The results clearly demonstrate that our targeting approach did not cause any detectable off-target effects resulting in clonal abnormalities, which allowed us to proceed with further experiments using the analyzed clones. As the fAD model is isogenic, potential differences between lines are therefore based on the mutation of interest and off-target effect can be excluded as a potential cause.

4.2 Characterization of the isogenic AD iPSC lines

All lines were subjected to immunocytochemistry (ICC) for the pluripotency markers Oct4 and Sox2. We also proved that all lines had the potential to differentiate into the 3 embryonic lineages, endoderm, ectoderm, and mesoderm types of cells, as expected for fully reprogrammed iPS lines (Takahashi et al., 2007). Between 90 to 95% of all cells were Oct4+ and Sox2+ (Figure 22B, C). These results validate that all lines were undifferentiated and completely reprogrammed human pluripotent stem cells. Additionally, we stained the iPSC colonies against p-Histone3 (p-H3) antibody to determine the percentage of cells undergoing mitosis at a given time point during the culture. Approximately 4% of all iPSCs from the AV and SWE lines were p-H3+, similar to the value obtained for the BJ control. We found a small although significant difference for the APP KO line, where only ~3% of the iPSCs were p-H3+ (Figure 23), and a downward trend in the AT line. Similar results were obtained with by performing immunostaining against Ki67, a protein required to maintain chromosomal organization during mitosis (Figure 23). These data may indicate that APP KO iPSCs, and to a lesser extend AT, could present an alteration in their proliferation rate.

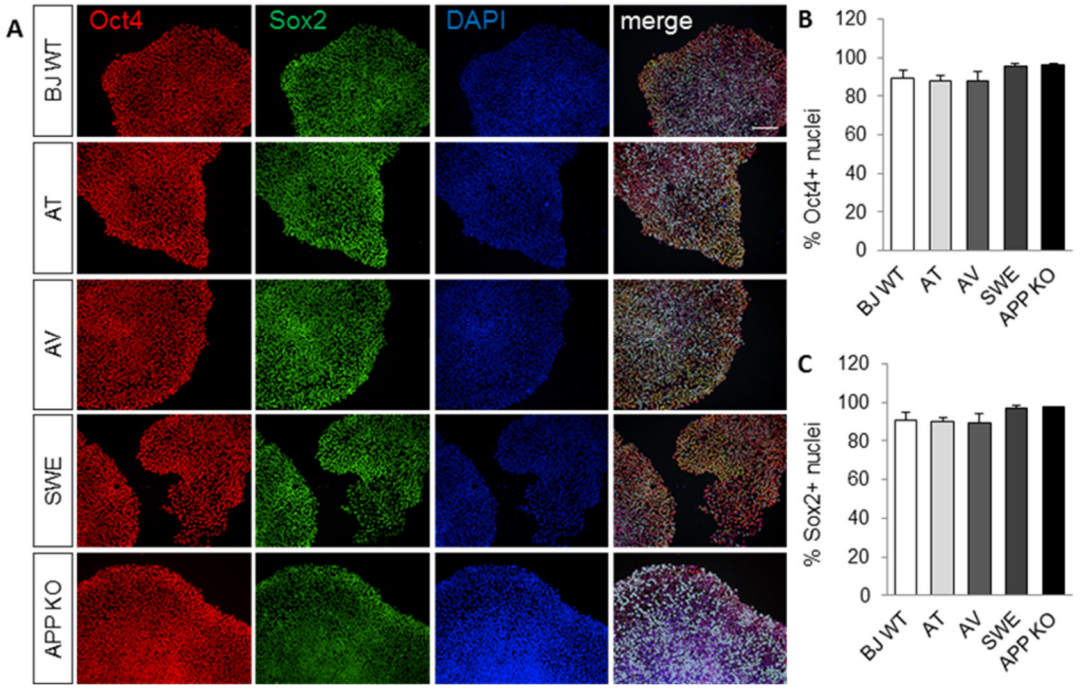

Figure 22. (**A**) Control (Wt), AT (positive mutation), AV and SWE (negative mutations) and APP KO iPSCs were plated in matrigel-coated 96-well plates, fixed and immunostained against the pluripotency markers Oct4 (red) and Sox2 (green). Nuclei are stained with DAPI (blue) and the percentage of Oct4 and Sox2 positive nuclei is calculated in (**B**) and (**C**). Scale bar, 10 µm.

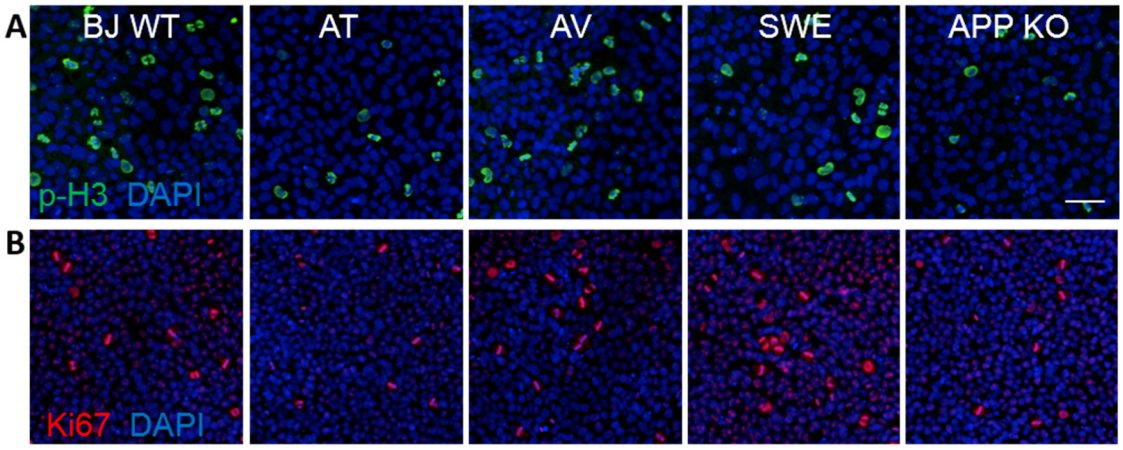

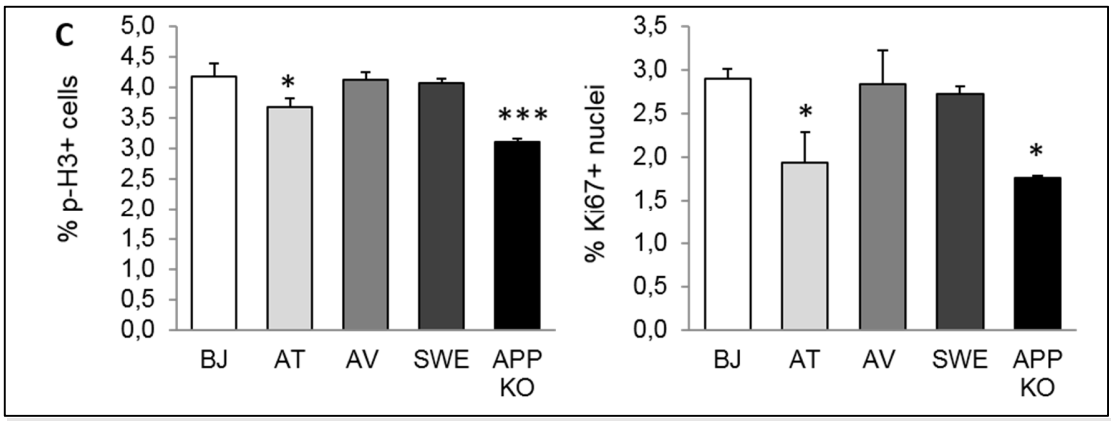

Figure 23. Wt, AT, AV, SWE and KO line were immunostained against the mitotic marker (**A**) p-H3 (green) (**B**) Ki67 (red). Nuclei stained with DAPI (blue) and the percentage of p-H3+ cells and Ki67+ nuclei is quantified in (**C**) One-way ANNOVA, Dunnett's Multiple Comparison Test.* p-value<0.05; *** p-value<0.001 was performed for calculation of p-H3+ cells, One-way ANNOVA, Dunnett's Multiple Comparison Test for Ki67+ nuclei. Scale bar = 10 µm.

To explore further this possibility, we performed a proliferation assay based on the Click-iT-Edu technology. Edu is a fluorescent labeled, modified thymidine that is efficiently incorporated into newly synthesized DNA that enables to detect proliferating cells. We added Edu to the cultured iPSCs, and two hours later, we fixed and developed the Edu signal. Whereas we did not detect any significant difference between the BJ control line and the AT, AV and SWE lines (all presenting ~60% Edu+ cells), we did observe a significant increase in the percentage of Edu+ cells in the APP KO line (Figure 24).

These data, together with our above described results on p-H3 and Ki67 could be explained by two different scenarios: a) APP null iPSCs –and to some extent the AT line– have a longer S-phase, which results in more cells stained with Edu and less cells undergoing mitosis (decreased cells labeled with mitotic markers); this scenario would suggest a proliferation defect in the APP KO and AT lines, or b) increased proliferation rate, which would correlate with an enhanced number of cells in S-phase and a decreased amount of mitotic cells at any given time point, which on the contrary would be indicative of a higher proliferation rate than the normal levels.

In order to discriminate between these two possibilities, we performed longitudinal assays by quantifying the number of iPSC nuclei stained in DAPI from two days after plating and until seven days in culture. We plated the same number of cells per line, fixed each plate at those time-points and imaged, and quantified the total nuclei number by relating the number of nuclei at each day by the number of nuclei at the first time-point (day 2) per line.

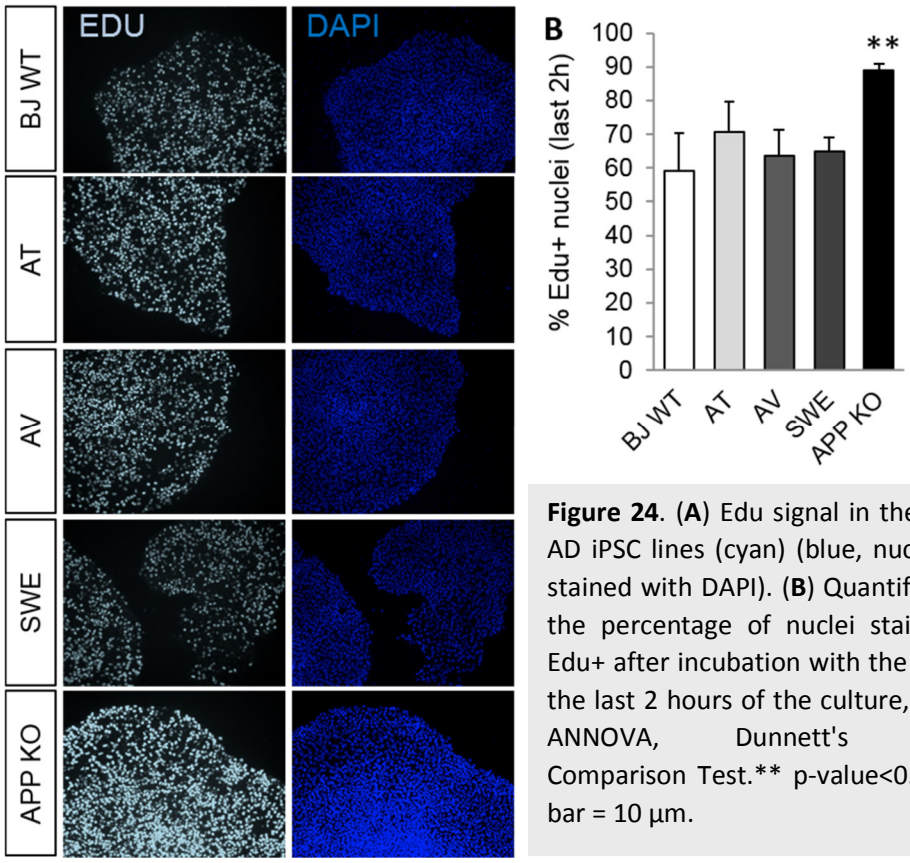

Figure 24. (**A**) Edu signal in the isogenic AD iPSC lines (cyan) (blue, nuclear DNA stained with DAPI). (**B**) Quantification of the percentage of nuclei stained with Edu+ after incubation with the molecule the last 2 hours of the culture, One-way ANNOVA, Dunnett's Multiple Comparison Test.** p-value<0.01. Scale bar = 10 µm.

As shown in Figure 25, the number of nuclei per line increases over time and is notably faster in the APP KO and AT lines compared to the BJ, AV, and SWE lines. These data suggest that the above-mentioned option “b” would be the right one and that the lack of APP could increase the proliferation rate of iPSCs. It is also possible that there is an increased efficiency of α-secretase in cleaving APP protein over β-secretase (which increases the amount of sAPPα) could explain this increased proliferation rate. Indeed this theory, a higher proliferation rate for the AT, would be supported by findings of Ohsawa et al. who reported increased proliferation rates induced by sAPPα in rat neural stem cells (Ohsawa et al., 1999), murine neural progenitors (Caille et al., 2004) and human decidua parietalis placenta stem cells (Demars et al., 2011). As the AT line is more frequently cleaved by α-secretase compared with all the other lines, sAPPα levels are higher,

which in return might lead to increased proliferation rates not only as in neural stem cells as reported, but as well in an iPS state. On the other hand, increased proliferation in the KO line could be explained with the absence of sAPPβ, which contrary to sAPPα, can have toxic effects by binding to death receptor 6 and inducing apoptosis. That could imply proliferation rates are increased for the KO because of depleted effects caused by sAPPβ.

Finally, to validate these results, we performed an ATP-monitoring luminescence assay to quantitatively evaluate the proliferation rate of these iPSCs. Given that ATP is present in all metabolically active cells, we used the ATPlite luminescence assay (Perkin Elmer) to measure cell proliferation based on the production of light caused by the reaction of intracellular ATP with added luciferase and its substrate D-luciferin. We performed ATP measurements at different time-points after plating and observed that APP KO iPSCs showed the highest levels, followed by the AT line, and displaying AV and SWE much lower levels and similar to the BJ control line (Figure 25). Altogether, these results indicate that indeed the APP KO and AT lines show a higher proliferation rate than the BJ control and the lines carrying the negative mutations (AV and SWE).

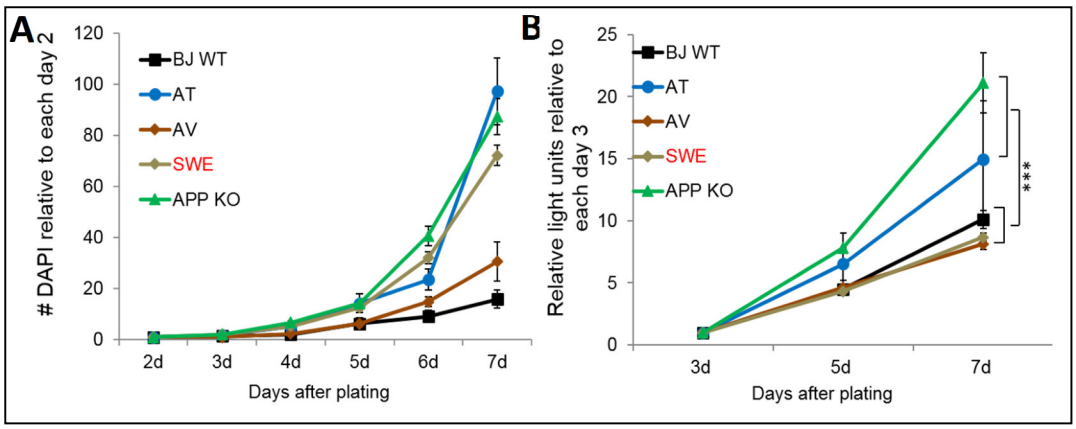

Figure 25. (**A**) Quantification of the number of nuclei, stained with DAPI, of isogenic AD iPSCs over time. iPSC colonies were dissociated, counted and the same number of cells per well per line was plate in multiple 96-well plates. Each plate was fixed at a different time-point and the wells imaged using the automatic Operetta microscope. (**B**) Quantification of the luminescence (RLU, Relative Light Units), equivalent of ATP production, as a measurement of cell proliferation. iPSCs were treated as in (A) and ATP measurement determined 3, 5 and 7 days after plating. Two-way ANOVA, Bonferroni post-tests.

4.3 Characterization of the isogenic AD iPSC-derived cortical neurons

Once I analyzed the pluripotency properties and the proliferation rates of the AD iPSC lines, I next explored their potential to differentiate into cortico-neural cultures. Often, a disease-associated genotype will not manifest as a disease phenotype in pluripotent cells, but rather in differentiated and specialized cells, in which the disease gene is more active depending on a given the transcriptional and proteomic context in that special type of cell. Therefore, it is of high importance to prove that I am able to differentiate them into cortical neurons. To do so, following the differentiation protocol described in the corresponding Methods section, I dissociated the 3D spheres 45-50 days after initiating the spinner culture, and plated the resulting neurons in coated 96-well plates to analyze their phenotye by utilizing and performing high-content imaging. Untargeted (Wt) and the different AD cortical neurons were plated in the same plate and fixed at different time-points for their study (3, 6, 9 and 12 days after plating).

Interestingly, I first observed that the number of cells in the cortical cultures carrying the negative mutations AV and SWE increased over time, compared to the Wt and AT or APP KO cortical neurons, which number remained fairly constant (Figure 26). This feature is robust and not clone-dependent since I have observed the same results from different clones and between multiple differentiations/experiments. Interestingly, it seems to be due to a higher propensity of the AV and SWE iPSCs to produce glial, since treatment with the proliferation inhibitor Ara-C from plating notably abolished this effect (data not shown).

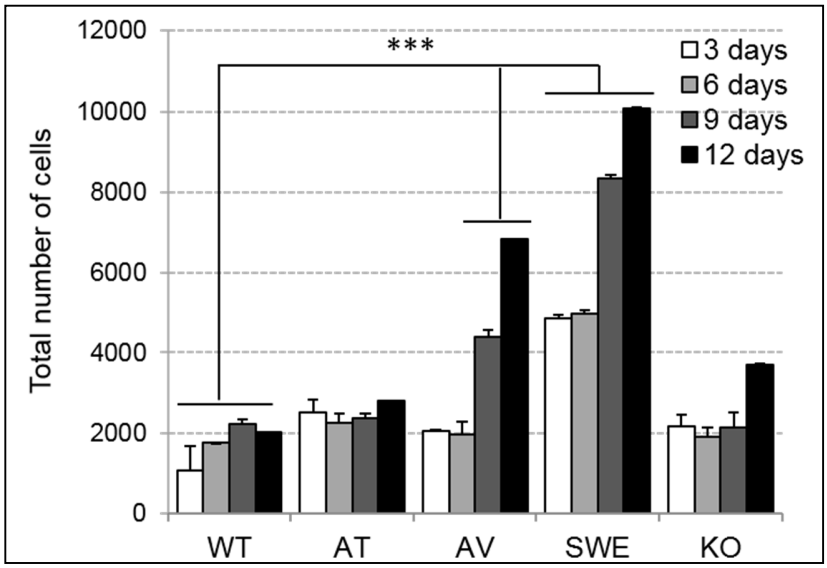

Figure 26. Quantification of proliferation rates of cortical neurons obtained from all isogenic lines in culture over 12 days post dissociation at day45. Two-way ANOVA, Bonferroni post tests.*** p-value<0.001.

Next, I studied the percentage of neurons in these cultures, stained for MAP2, as well as the percentage of CTIP2+ cortical neurons. The results showed that the percentage of MAP2+ neurons was around 90% for the WT and AT lines, remaining constant throughout the culture, slightly lower for the APP KO line –where I also observed a small decrease over time– , and notably lower and declining over time for the negative AV and SWE lines (Figure 27). Two important conclusions arise from these results. First, we confirmed the efficiency of our cortico-neuronal differention protocol and the capabilty of the isogenic AD lines to generate neurons, and specifically, cortical neurons. Second, we identified important differences between Wt/AT and the negatively mutated AV/SWE cortical neurons. These data, together with the results shown above on the increase in the total number of cells over time for these two lines, could simply indicate that from day 9 onwards there are more cells that are non-neurons for these two lines, and not that MAP2+ neurons degenerate and die in the AD lines carrying the negative mutations. However, since a decrease in the %MAP2 in AV and SWE can be detected already at the first time –after 3 days in culture– when the total number of cells is identical for Wt, AT and AV lines, these results would rather indicate that the later is also true and neurons are more prone to dying when the negative mutations are present.

Similar results for CTIP2+ neurons were found. The percentage of CTIP2+ neurons was around 50% for Wt and AT after 6 days in culture, and much lower for AV and SWE. Intermediate values were found for the APP KO cultures. Except for the AV line, in all cases there was a tendency of the percentage of CTIP2+ cells to increase over time, which could indicate that the more mature the neurons get, the more CTIP2 levels they express.

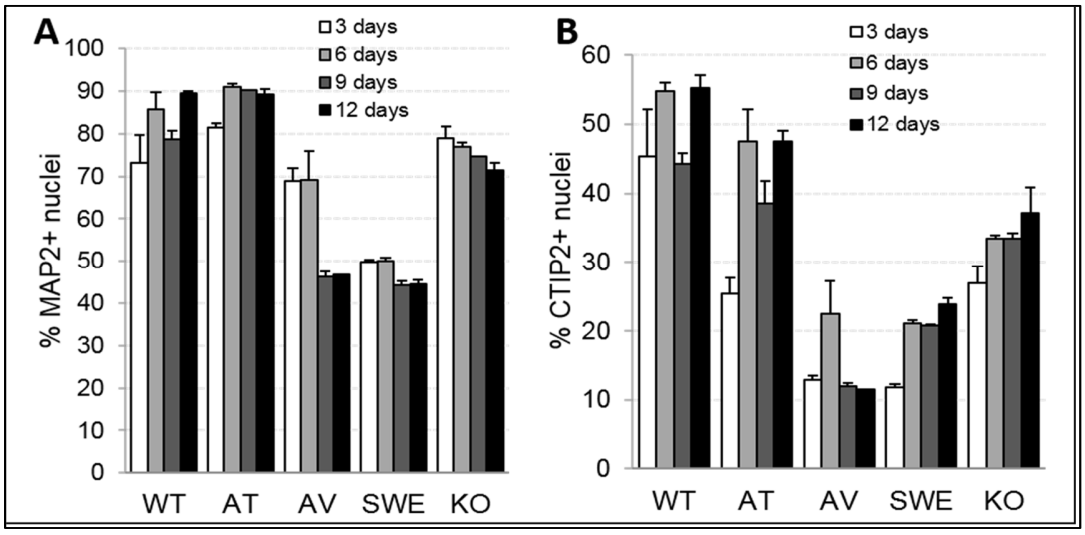

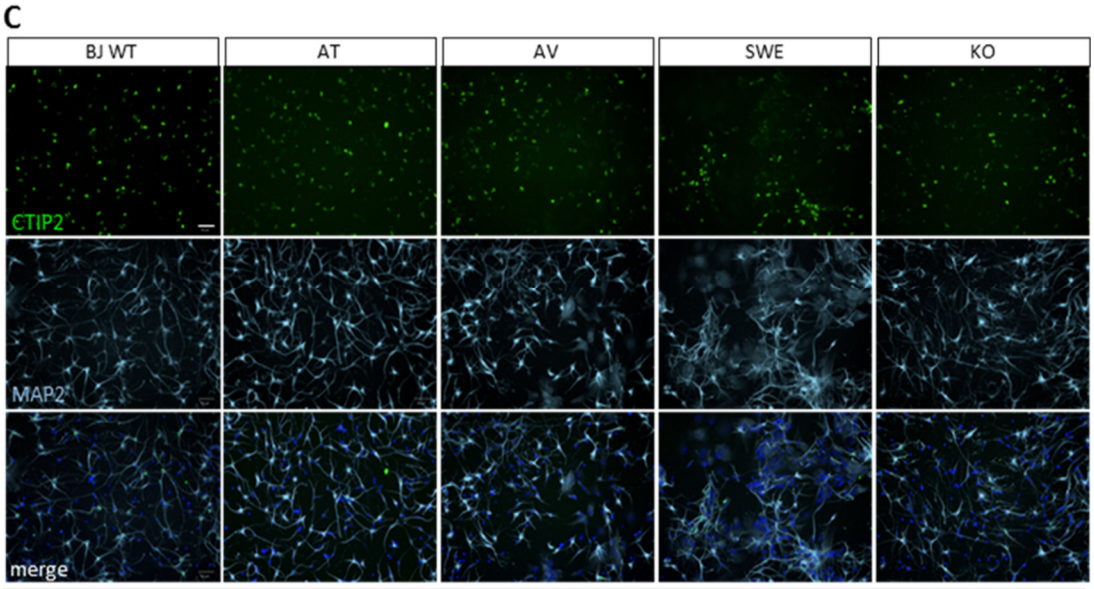

Figure 27. Quantification of immunostained cortico-neural cultures for (**A**) cortical marker CTIP2 (**B**) neural marker MAP2. (**C**) Representative images showing cortical neurons 6 days after plating. Scale bar = 10 µm.

I next determined the levels of APP protein that these neuronal cultures expressed in comparison to the Wt control and over time in culture. First, I observed that the levels of APP detected in the cytoplasm of cortical neurons seem to increase over time in culture, regardless of the genotype (Figure 28). Second, notably, APP levels are higher in Wt than in the other three AD lines, which suggests that since APP is cleaved more efficiently in the fAD mutant lines and the AT line. In the AT line, the turnover rate or catalytic cleavage (*Vmax*) of APP by α-secretase ADAM10 is increased. On the other hand in the SWE and AV line *Vmax* is increased for the β-secretase BACE-1 (Maloney et al., 2014). Increases of *Vmax* in these mutant lines, and therefore faster proteolytic processing of APP into its different metabolites, explain why there is less APP present in the plasmamembrane where it gets processed quickly by α-secretase, as well as in the cytoplasms, where it usually get processed by β-secretase.

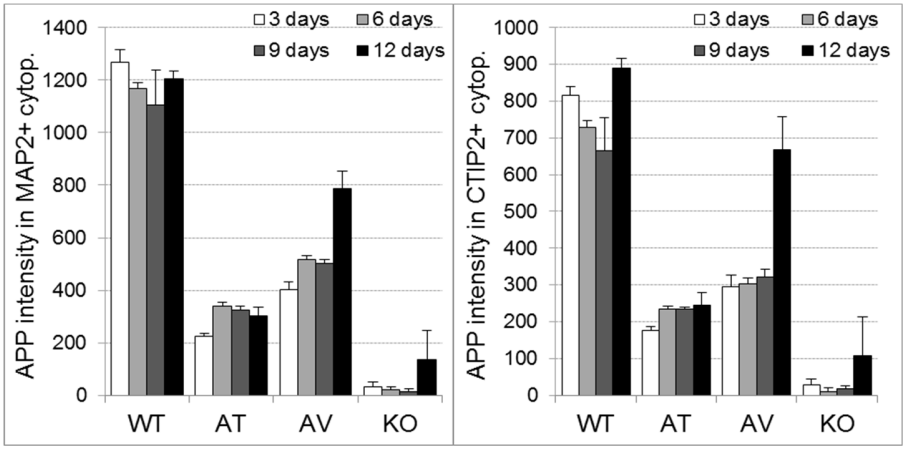

Figure 28. Quantification of immunostaining for APP in cytoplasm over time course of 12 days in (**A**) MAP2+ neurons (**B**) CTIP2+ neurons.

In order to confirm that APP levels measured by intensity of fluoresence in the cytoplasm of cortical neurons are indeed higher in Wt than in the other AD lines, I performed immunostaining on cortical neurons plated in glass coverslips and analyzed them by confocal microscopy. As the images below show, indeed BJ Wt MAP2 positive neurons showed the highest APP levels compared to the other lines. APP KO cortical neurons were also immunostained as negative control and the fluoresence signal detected is considered background from the secondary antibody (Figure 29).

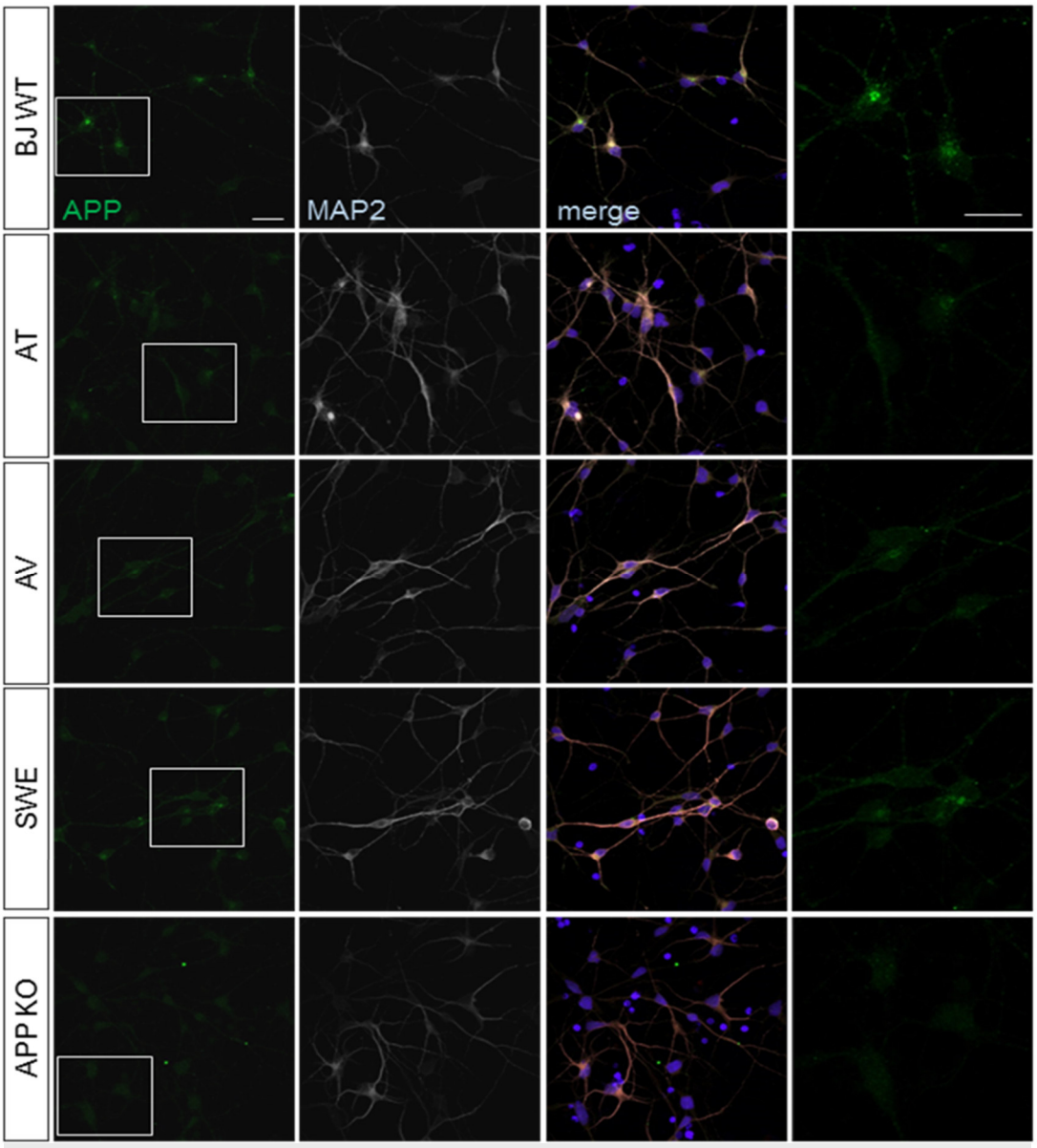

Figure 29. Confocal images of cortical neurons day 55 of all isogenic lines, immunostained for APP (green) and MAP2 (white). Column on the far right shows magnification of box marked in column on the far left. Scale bar = 20 µm.

Next, I studied the levels of phosphor-Tau in CTIP2+ neurons and MAP2+ neurons in general across the different AD lines. I observed that pTAU levels were higher in AV and SWE than in BJ and AT at early time-point. However, whereas pTAU levels increase over time in BJ and AT, they remain more constant in the neurons carrying the negative mutations. Phosphorylation of Tau in different residues has been shown to have different connotations, being the hyperphosphorylation a pro-degeneration feature or a sign of cytoprotection, depending on the amino acid affected by the postranslational modification. These results therefore could indicate that WT neurons, and to a higher degree AT, phosphorylate Tau as a protective response, allowing them to survive better in culture; whereas AV, SWE and KO CTIP2+ neurons, not displaying that pattern, could be more susceptible to death.

Another potentially interesting result is that the levels of pTAU in CTIP2+ neurons seem to be slightly, but consistenly, lower than in general population of MAP2+ neurons (Figure 30), and the APP KO neurons display the lowest Tau phosphorylation at the residues studied, which could suggest that Tau phosphorylation is downstream of APP.

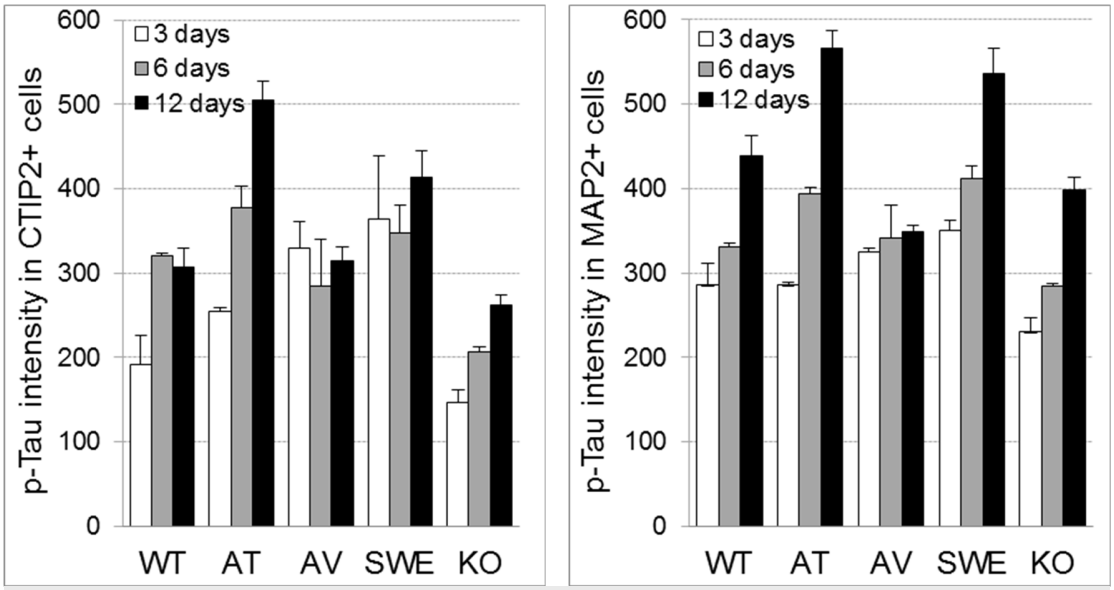

Figure 30. Quantification of immunostaining for pTAU in cortical cultures of all isogenic lines 3,6, and 12 days post dissociation for (**A**) CTIP2+ cells (**B**) MAP2+ cells.

4.4 ELISA to detect Aβ40 and Aβ 42 from iPSC lines, EBs and differentiated cortical neurons

One of the most important assays I needed to perform in order to confirm that the isogenic AD iPSC lines that I had generated constituted indeed a human model to study AD *in vitro*, was the measurement of the Aβ40 and Aβ42 peptides produced after the cleavage of APP protein.

As described in page 14 of the introduction, I was expecting to see a decrease in the production of both species in the AD line carrying the positive AT mutation, given that presence of the A to T substitution close to the Aβ producing β-secretase cleavage site Asp^1 decreases the catabolic turn-over rate of APP by Bace-1 and also increases cleavage by α-secretase.

In contrast, I expected to detect a notable increase in the production of both peptides in the line carrying the negative SWE mutation since it increases the efficiency of APP β-secretase cleavage by β-secretase. Regarding the lines carrying the negative AV mutation, I expected similar results to the ones for the SWE lines. As the A to V substitution shifts β-secretase's preferential cleavage site from the Glu11 to the Asp1 site, resulting in less truncated but more functional Aβ, I expected to detect increased production of both peptides as well. Besides enhanced Bace-1 activity in both negative mutation lines, I still expected lower increases in the total amounts of Aβ peptides in the AV lines, as it has been reported that SWE and AV produce similar amounts of CTFs C99 and are therefore both similarly often processed by β-secretase, the CTFs carrying the AV mutation are more often degraded by the proteasome, explaining the discrepancy between produced C99 and Aβ production (Zhang et al., 2017). Specially, I did not expect to see an increase in the ratio of Aβ42:Aβ40 towards the more aggregation prone Aβ 42 in the AV and SWE lines. The mutations in both lines should not affect cleavage of the CTFs by γ-secretase, which is the rate limiting step in determining the ratio of Aβ42:Aβ40 and which is influenced by mutations in APP closer to the transmembrane domain or by presenilin 1, respectively (Muratore et al., 2014).

However, it is reported in the literature that the detection of the Aβ42 peptide constitutes a challenge if neurons are plated at densities usually used for neuronal *in vitro* experiments (Israel et al., 2012) as the values are often close or below the cut off for the detection range of most commercially available ELISA Aβ42 kits. For this reason, and assuming that the levels of Aβ42 released in the culture media of differentiated cortical neurons could be below the sensibility limits of the ELISA, I decided to start measuring these two peptides in iPSCs, which can be kept in the dish at a much higher density, increasing therefore our chances of detecting Aβ42. As Figure 31 shows, the Aβ40 levels detected in the media from the AT iPSCs was much lower than for the control Wt line and the amounts detected for the SWE line was more than 2.5 fold higher compared to the Wt cells. I did not observe significant changes for the AV line. The APP KO line was used as a negative control for all the experiments since no Aβ40 or 42 was expected, the results confirmed that prediction. Importantly, I was able to detect the less abundant Aβ42 fragments in iPSCs. This time the levels in the positive line, AT, were similar to the control line but

a 2-2.5 fold increase was observed for the AV and SWE lines, respectively (Figure 31). These very promising data were a clear indication that the introduction of the chosen mutations into the lines had been successful, resulting in the expected and desired phenotype, a main AD hallmark.

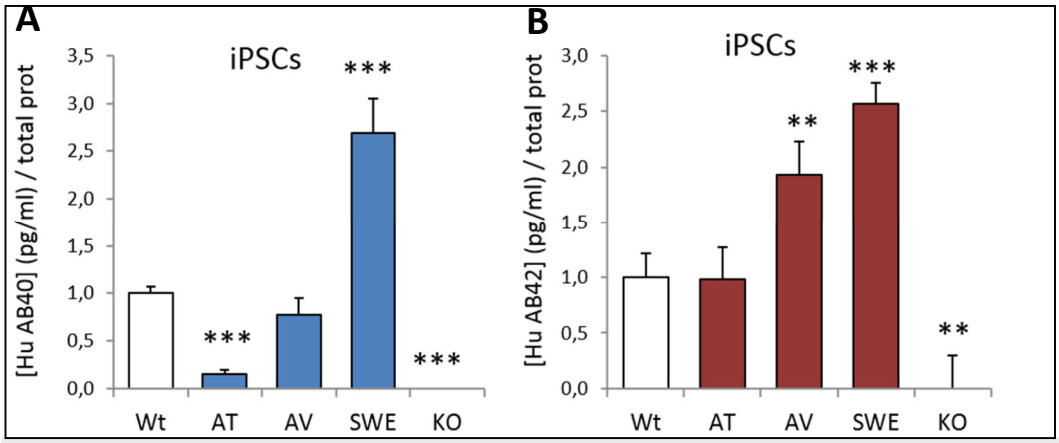

Figure 31. Quantification of Aβ40 (**A**) and Aβ42 (**B**) APP-derived peptides in the culture media from isogenic AD iPSC lines. iPSCs were plated in 6-well plates and when they reached approximately 80% confluence media, in contact with them for at least 24 hours, was collected and used for ELISA quantification. One-way analysis of variance; Bonferroni's Multiple Comparison Test.

These results also encouraged me to test whether a similar diseased phenotype could be detected in cortical neurons derived from the iPSC lines following our differentiation protocol. First, for a similar reason that justified performing the ELISA assay in iPSCs, I explored whether the detection of both peptides was possible in whole 3D spheres, 50 days into the differentiation protocol. Importantly, as shown in Figure 32, and similarly to what I observed for the iPSC lines, I could detect both peptides -although the absolute values were always several magnitudes higher for Aβ40 than for Aβ42-. Interestingly, the results are very similar to the ones observed for the iPSCs. AT showed about 50% less of both fragments compared to the Wt 3D cortical spheres, and media from the AV and SWE spheres presented notably higher levels of both fragments than the Wt ones. Surprisingly, SWE cortical spheres reached a 15-fold increase for Aβ42 compared to Wt, much higher than for the Aβ40 peptide. While it has been reported that the SWE mutation produces the highest amounts of Aβ42 and Aβ40 , an increase in the ratio of Aβ42:Aβ40 has not been associated with that mutation yet. However, published data is currently lacking results generated from spheres carrying that mutation and our results indicate that the ratio indeed does change, when the cells are differentiated in vitro in 3D culture.

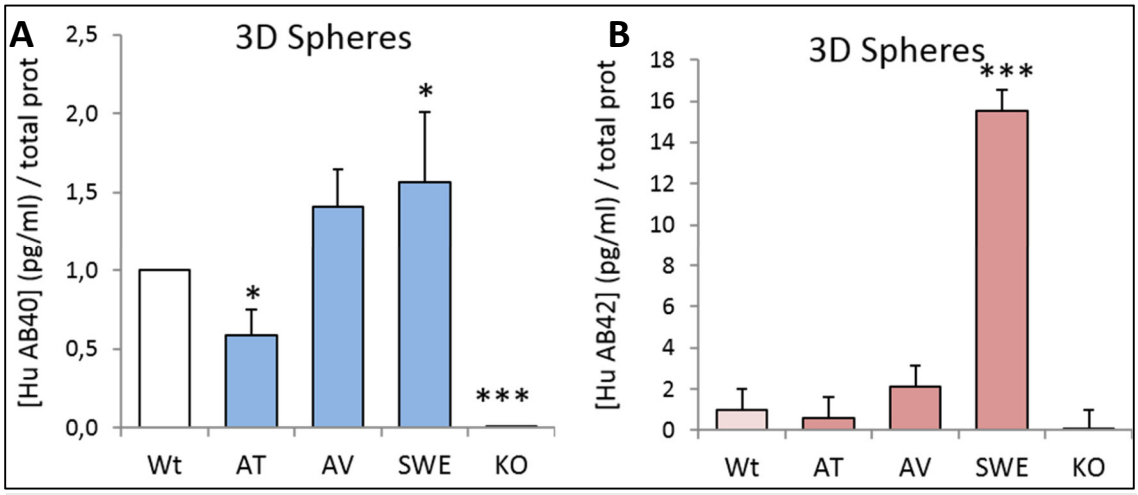

Figure 32. Quantification Aβ 40 (**A**) and Abeta42 (**B**) peptides in the culture media from isogenic 3D spheres 50 days into the differentiation protocol. After 30 days in spinning culture, a similar number of spheres per line was transferred to ultra-low attachment plates and for an additional 20 days, during which media was changed every 3 days. At day 50 media was collected and processed for ELISA measurement of the APP fragments. One-way analysis of variance; Bonferroni's Multiple Comparison Test.

Finally, I explored Aβ40 and Aβ42 levels in the media of cultured cortical neurons. To my surprise, I could detect both fragments and the results were in the same line as the data obtained for the iPSC lines and the cortical spheres. However, it is important to note that the levels of Aβ40 are also in this case much higher than for Aβ42.

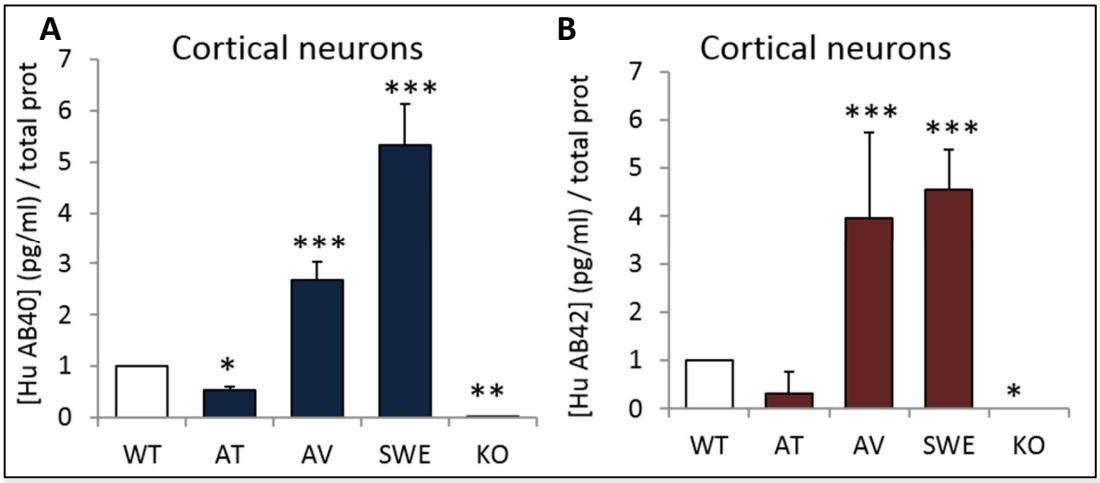

Figure 33. ELISA quantification of Aβ 40 (**A**) and Aβ42 (**B**) peptides in the culture media from AD differentiated neurons 12 days after the 3D spheres were dissociated and plated. Bonferroni's Multiple Comparison Test.

The medium in contact with AT cortical neurons presented lower amounts of Aβ40 and 42 compared to the Wt neurons, and media from AV and SWE neurons showed a marked increase in both peptides compared to Wt, being the highest levels again the SWE ones. As expected, APP KO cortical neurons show undetectable levels of both peptides (Figure 33).

With these positive results I ought to investigate whether the production of these APP fragments and their subsequent release into the medium remain constant over time, or whether their levels increase or decrease as the cortical neurons get more mature in culture. To answer this question, I analyzed their amount in cortical neurons 6, 9 and 12 days after dissociation. Since the samples for each time-point were processed in different ELISA sets, I related the values for each time-point to the levels obtained for each Wt control (being therefore Wt values for the three time-points "1", Figure 34). The results indicated that, whereas the levels of Aβ40 do not change over time for the AT cortical neurons, they do increase for the AV and SWE neurons. Unfortunately, no reliable data could be obtained for Aβ42 given the variability of the results due to the low values detected and the insufficient number of samples available.

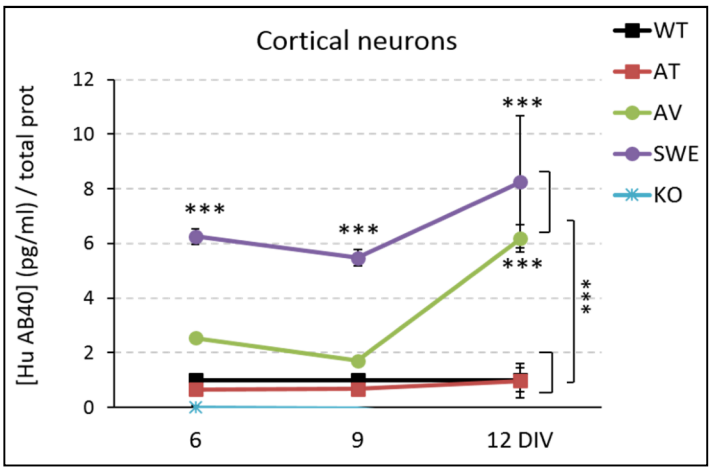

Figure 34. ELISA quantification of the levels of Aβ40 peptide in the culture media from AD differentiated neurons 6, 9 and 12 days after plating. One-way analysis of variance; Bonferroni's Multiple Comparison Test.

Finally, I decided to explore the efficiency of β-secretase and γ-secretase inhibitors at reducing the production of these two APP fragments to determine the responsiveness of these isogenic cells and therefore to validate their potential as an accurate AD *in vitro* model system. After 50 days in culture, spheres were dissociated, and cortical neurons cultured in 24-well plates. 3 days later Bace-1 (β-secretase inhibitor), DAPT or Compound E (both γ-secretase inhibitors) were added at the indicated concentrations for 6, 9 or 12 additional days. I observed that all inhibitors drastically reduced the levels of both fragments in all lines (Figure 35). , DAPT and Compound E treatment in the AV and SWE cortical neurons led to Aβ40 levels comparable to the ones observed for the Wt and AT cells, and, since the basal DMSO-control Aβ40 levels for the neurons carrying

the negative mutations are much higher than for the Wt and AT, we could affirm that the efficiency of both types of inhibitors is even higher for these diseased cells. These results were expected since in AV and SWE neurons, the efficiency of the β- and γ-secretases is enhanced compared to the Wt or AT cells. Given that the effect of the inhibitors was so dramatic already after 6 days of treatment, the long time-points did not provide significant difference, only a further decrease in the peptide levels reaching undetectable values in most cases (Figures 35). A comparable reduction of Aβ42 for all neuronal types at the 3 time-points was observed (data not shown).

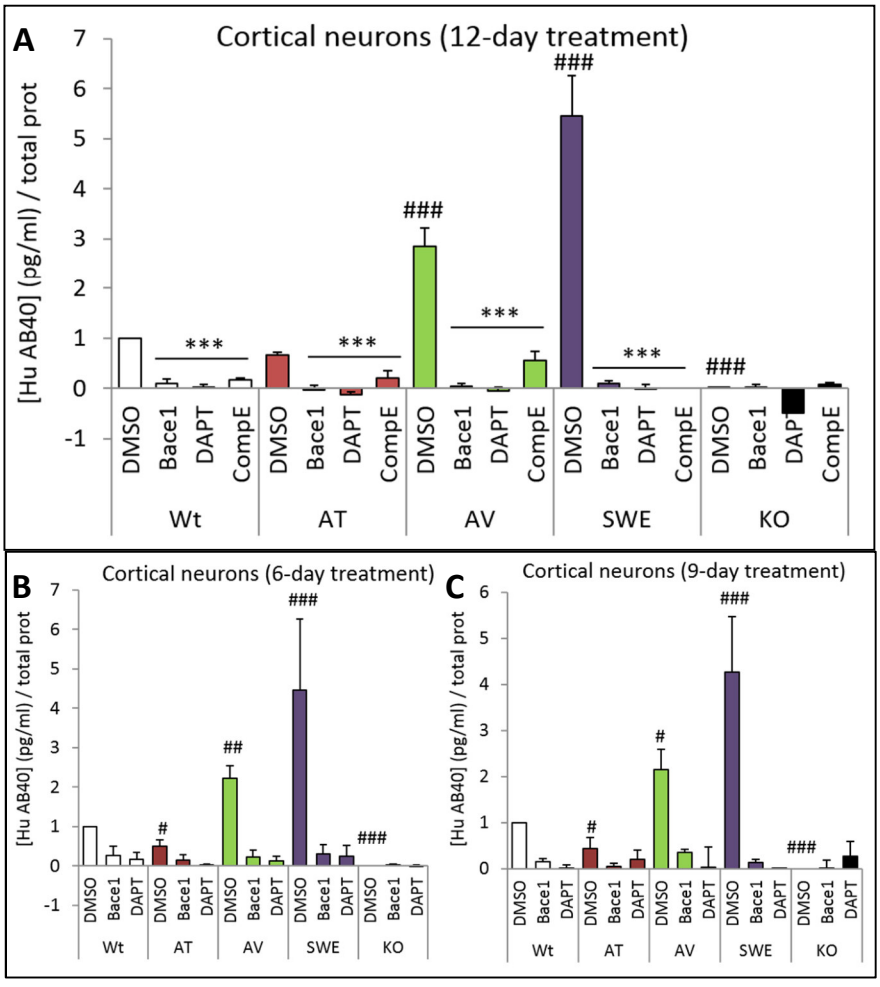

Figure 35. ELISA quantification of Aβ40 levels in the culture media from AD differentiated neurons (**A**) 12 days (**B**) 6 days, (**C**) 9 days after plating in the presence or absence of the β-secretase inhibitor, Bace-1 (5µm), or γ-secretase inhibitors, DAPT and Compound E (5nm). Two-way ANOVA, Bonferroni post tests.***p-value<0.001 (comparing inhibitors to DMSO within the same line; ### p-value<0.001 (comparing each line to Wt).

Lastly, I wanted to investigate whether the decrease in the levels of Aβ40 and Aβ 42 detected by ELISA upon the exposure of the cortical neurons to the beta and gamma-secretase inhibitors would correlate with an increase in the amount of total APP in the cells measured by immunostaining. Similarly, to the experiments detailed above, plated cortical neurons were treated with Base-1, Compound E, the combination of both inhibitors or DAPT for 3, 6, 9 and 12

days, refreshing the addition of the compounds every media change (3 days). As shown in Figure 36, all inhibitors increased the amount of cellular APP in all cell lines and at all time-points studied. At the shortest time-point, 3 days of treatment, I observed that γ-secretase inhibitors CompE and DAPT had a higher effect than the treatment with β-secretase , which could explain that the combination treatment does not result in higher APP levels than Bace-1 or CompE independently. However, at later time-points (9 and 12 days) Bace-1 seemed to have a more potent effect on APP levels than the γ-secretase inhibitors.

Regarding how the treatments affected the levels of pTAU, I observed that none of the inhibitors had a significant effect in any of the neuronal types after 3 days of treatment (Figure 37), however, a consistent effect appeared at later time-points. Whereas in Wt and AT Bace-1 alone did not affect pTAU, its combination with the γ-secretase inhibitor CompE and DAPT notably reduced its levels. Interestingly, this effect was very different to the one observed for the neurons carrying the negative mutations AV and SWE, where none of the treatments have an effect except for DAPT, which significantly increased pTAU. These results indicate that, in the Wt neurons and the ones carrying the positive AT mutations, β- and γ-secretase inhibitors by decreasing the production of Aβ peptides and increasing therefore the levels of APP in the neurons, result in a decrease in the phosphorylation levels of Tau, at least at the residue studied, suggesting that APP is upstream of Tau phosphorylation in these neurons.

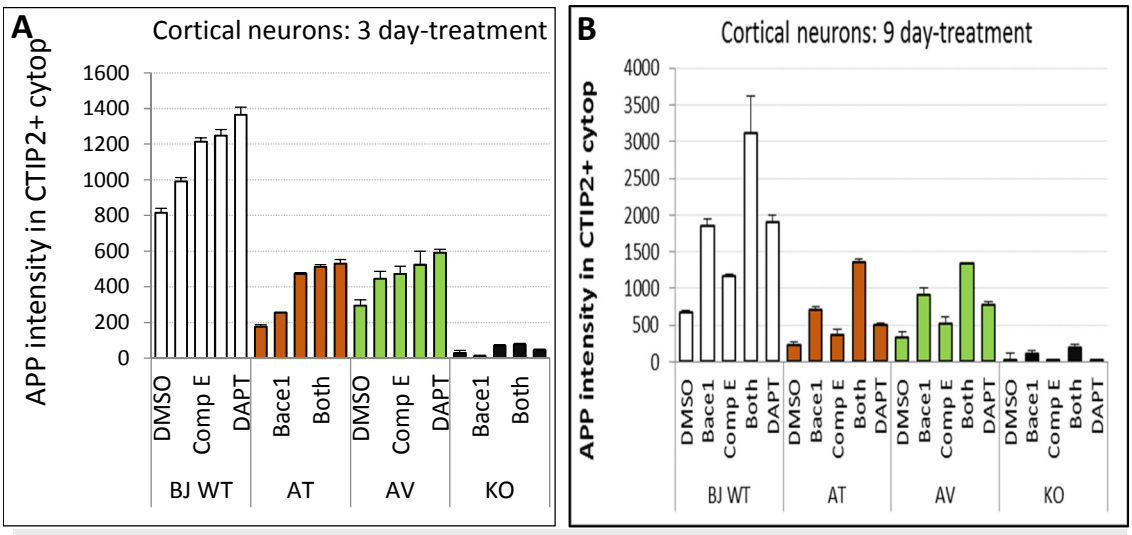

Figure 36. Quantification of APP in CTIP2+ cortical neurons at day 3 (**A**) day 9 (**B**) after plating in the presence or absence of the β-secretase inhibitor, Bace-1 (5µm), or γ-secretase inhibitors, DAPT and Compound E (5nm).

On the contrary, in the neurons carrying the AD-linked mutations, where the inhibitors have the same effect on APP total levels and the blockage of its cleavage (see ELISA data Figure 35) as in the Wt and AT neurons, the lack of effect in pTAU to 2 of the 3 inhibitors could be the result of two different phenomena: first, it could indicate that the phosphorylation of Tau is not downstream of APP levels and that DAPT-mediated pTAU increase after a prolong treatment may be a secondary phenomenon unrelated to APP. Secondly, pTAU could increase as a direct or indirect consequence of accumulating CTFs, as treatment with DAPT inhibits γ-secretase and results in accumulation of CTFs C83 post α-secretase cleavage and C99 post β-secretase proteolytic processing. Especially the C99 fragments have gained more attention in recent years, because they have been associated with mitochondrial dysfunction, endo-lysosomal and autophagic anomalies (Lauritzen et al., 2016; Nixon, 2007; Zhang et al., 2017).

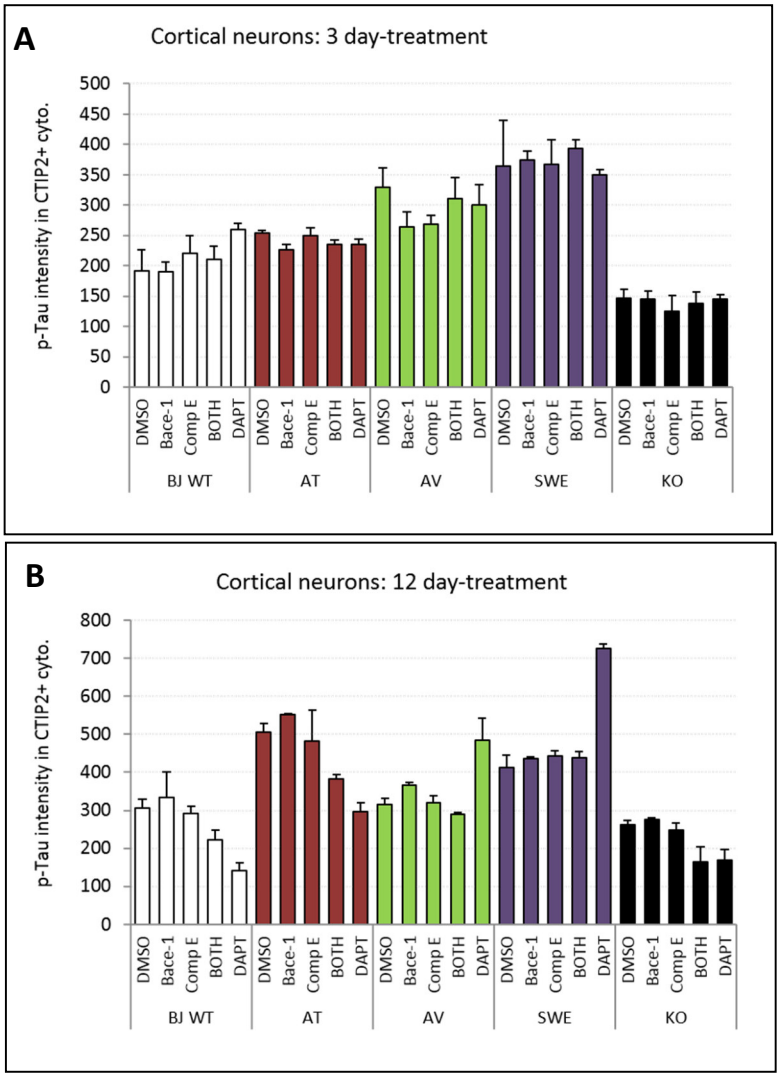

Figure 37. Quantification of pTAU intensity in CTIP2+ neurons treated with DMSO (5µm), Bace-1 (5µm), Compound E (5nm), Bace-1 + Compound E (5µm), DAPT (5n) at day (**A**) 3 and (**B**) 12.

Indeed, that specific effect of DAPT could be due to an increase in neuronal survival, number or length of neurites, since I detected a small but consistent increase total number of neurons MAP2+ upon DAPT treatment, specifically in the AV and SWE lines, and more marked after 12 days of treatment than after only 3 (Figure 38).

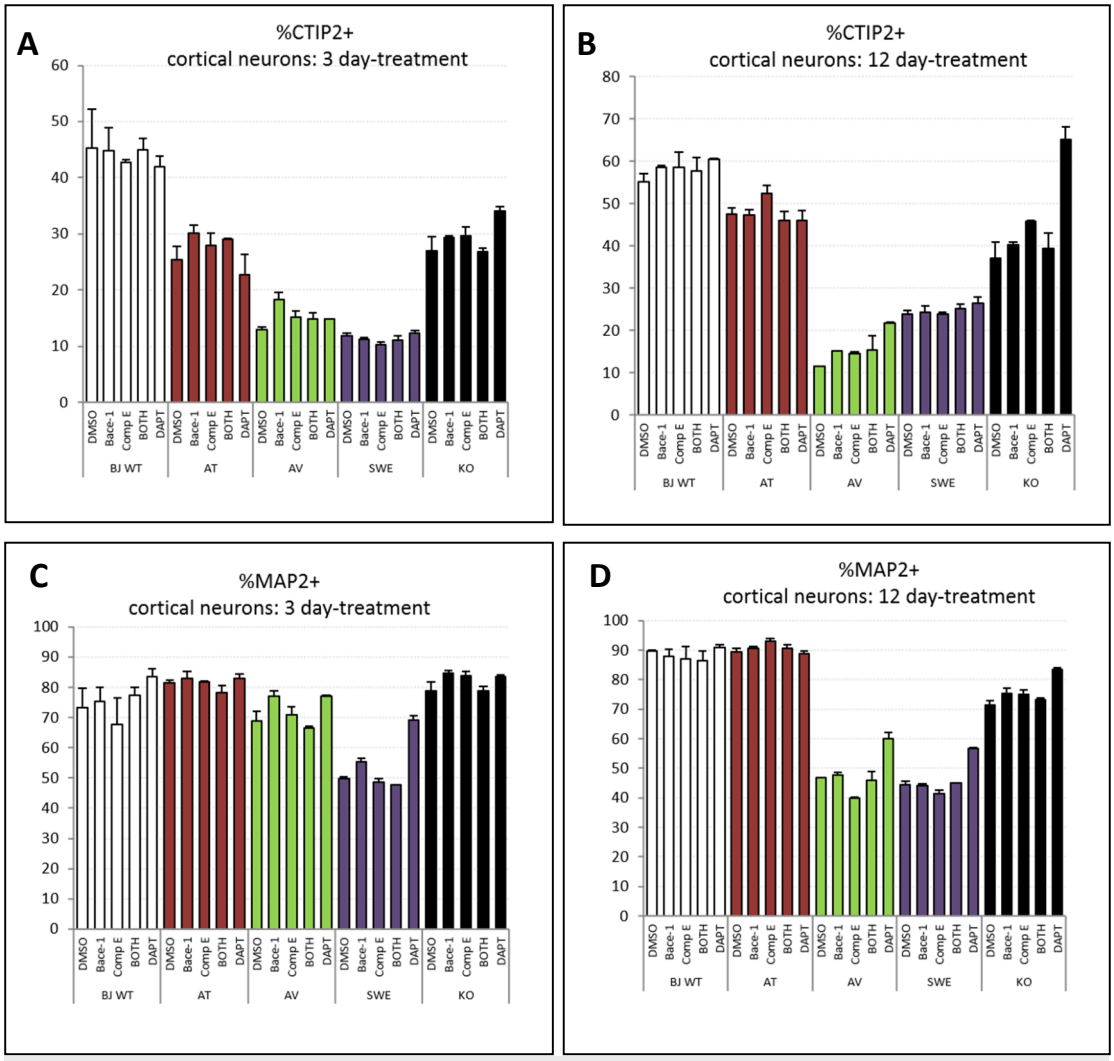

Figure 38. Quantification of CTIP2+ neurons at (**A**) day 3 and (**B**) day 12, MAP2+ neurons (**C**) day 3 and (**D**) day 12, treated with DMSO (5µm), Bace-1 (5µm), Compound E (5nm), Bace-1 + Compound E (5µm), DAPT (5n).

4.5 WB Analysis

To complete the characterization and analysis of our neuronal cultures, I decided to extract lysates of all cortical culture post dissociation to analyze protein levels at different time-points. To make sure that the conditions before extraction were the same, neurons were counted

and seeded at same densities in 24 well plates. I set the focus on APP, pTAU as well as normal TAU. Based on the results from the IF high throughput imaging analysis I was expecting to see some differences in protein levels between lines.

At first, I extracted lysates of untreated cells at three different time-points after plating them at day 45 and I analyzed protein levels for APP, pTAU, TAU and TUJ1 (Figure 39A). The results show a constant increase of APP across all lines, which confirms the results we have seen in the IF (Figure 28). APP levels are highest in Wt, followed by AT. In both fAD lines APP levels are significantly lower and I postulate it is because of increase proteolytic processing by β-secretase (Figure 39B).

Next, I checked protein levels for pTAU. It also increases over time with lowest levels at day 3 and highest levels at day 12 in all lines (Figure 39C). Interestingly, pTAU basal levels were lowest in the Wt, but highest in the KO line, and the strongest increase over time was found in the SWE. Another observation is that pTAU levels in AT and KO seem to be on a plateau and they only show an increase from day 6 to day 12. While the high levels of pTAU in the KO line had not been observed before, the high levels and strong increase of pTAU in SWE confirmed the results seen via IF. I again conclude that pTAU is increased in the SWE as a direct consequence of its elevated Aβ production, in agreement to the amyloid-beta-hypothesis. Increased levels of pTAU over time are also observed in the second fAD line, AV, but not as high as in the SWE line. Given the fact that the AV produces much less Aβ40 and Aβ42 compared with SWE we would expect pTAU to be lower. Again, I postulate that pTAU, phosphorylated Ser^{202}, Thr^{205} is protective in the AT and KO line, as it protects against Aβ mediated hyperexcitoxicity, whereas pTAU increase in the fAD is just an indicator for TAU being phosphorylated at many different residues, being Ser^{202} and Thr^{205} simply among them.

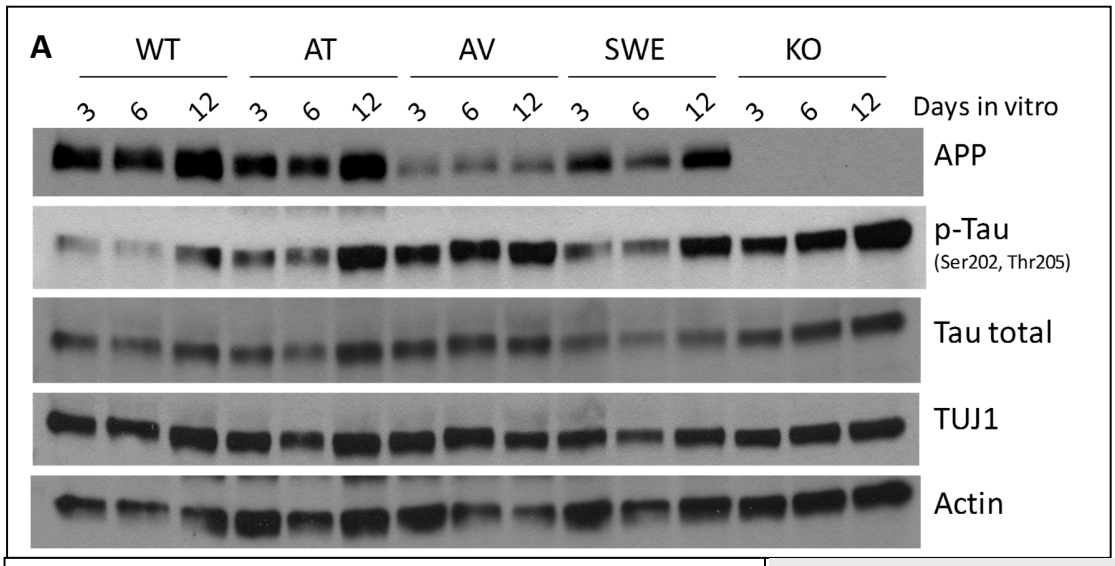

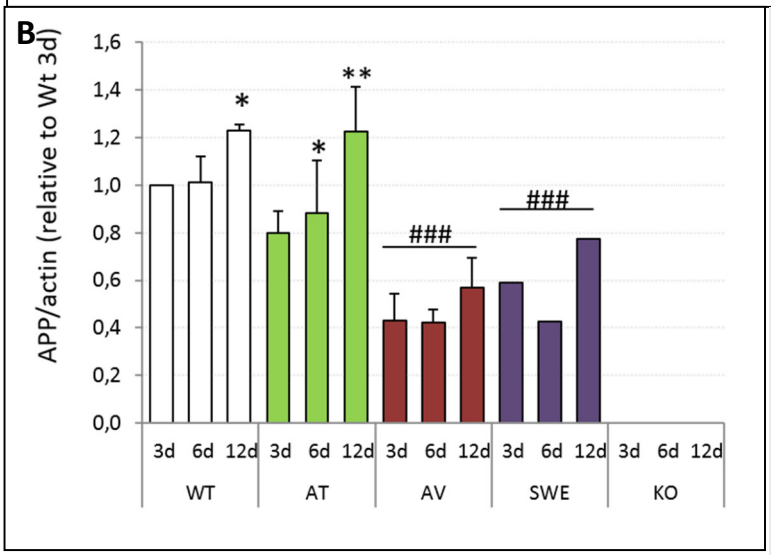

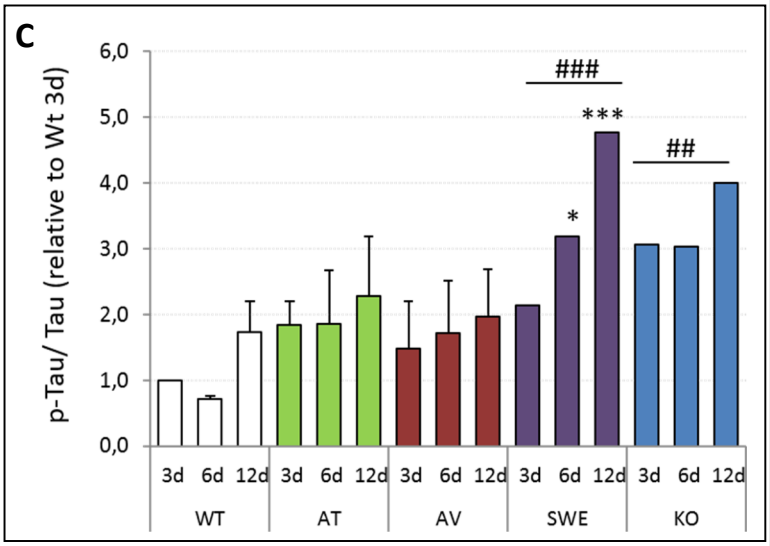

Figure 39. (**A**) representative Western Blot Gel for lysates taken from untreated neuronal cultures of all isogenic lines, extracted at day 3, 6, and 12; Two-way ANOVA, Bonferroni post tests.*p-value<0.05; **p-value<0.01 (comparing 6 and 12 days to 3 days within the same line; ### p-value<0.001 (comparing Wt to AV and SWE) (**B**) APP levels of all lines show time-dependent increase in all lines except KO; APP levels are highest in Wt and decreased in fAD lines; (**C**) pTAU increases over time in all lines with highest levels in SWE and KO line. Two-way ANOVA, Bonferroni post-tests. *p-value<0.05; ***p-value<0.001 (comparing 6 and 12 days to 3 days within the same line; ## p-value<0.01; ### p-value<0.001 (comparing Wt to AV and SWE).

Next, I wanted to investigate if we could detect changes in APP or pTAU protein levels after treatment with β- and γ-secretase inhibitors (Figure 40). I plated cells like described before, but this time added fresh media containing β- and γ-secretase inhibitors every three days.

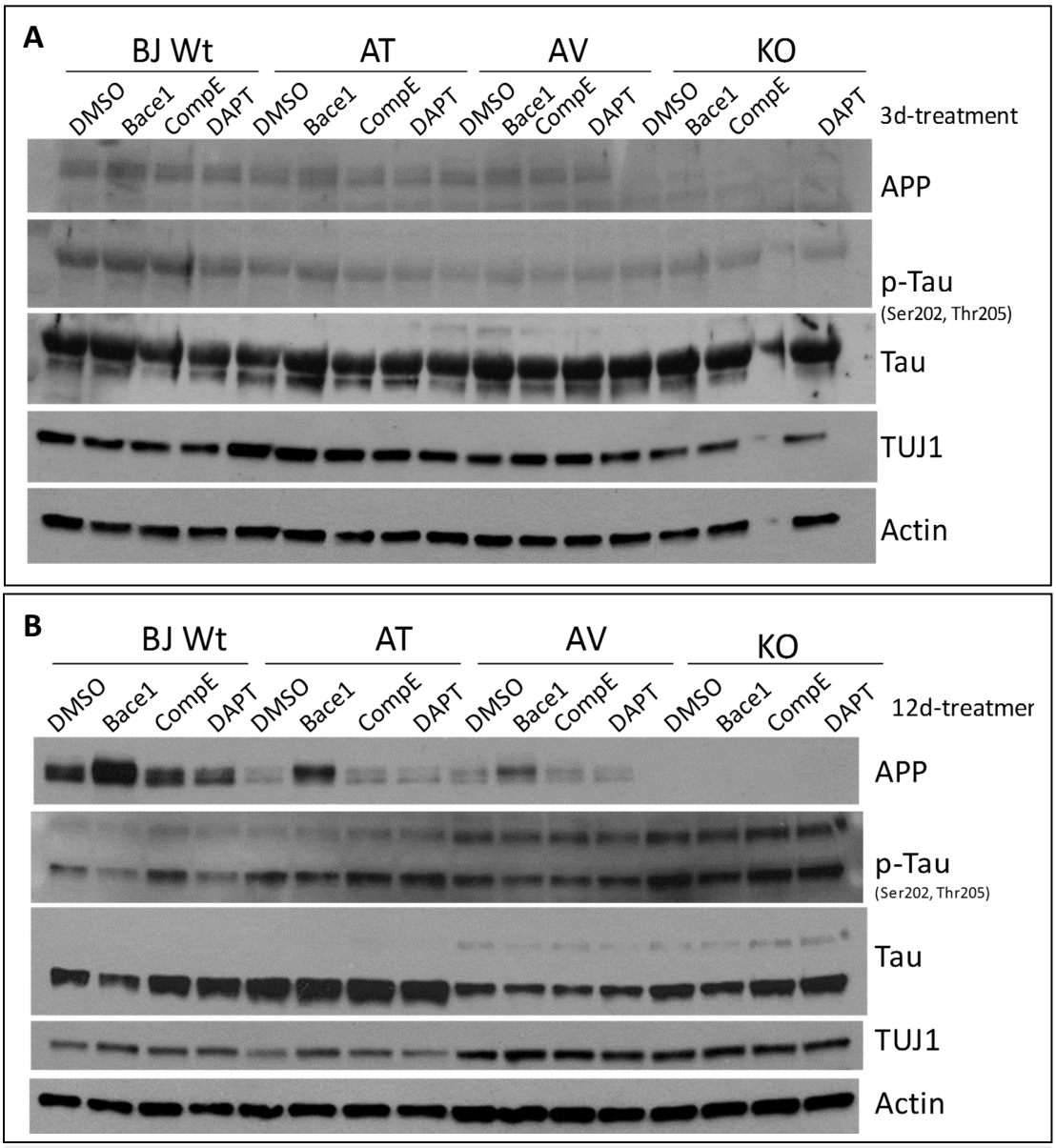

Figure 40. Representative WBs showing APP, pTAU, Tau and TUJ1 protein levels of dissociated cortical neurons at day 48 of the differentiation protocol and treated for 3 (**A**) or 12 (**B**) days with the beta or gamma-secretase inhibitors.

Treatment with β-secretase inhibitor Bace-1 seemed to have a potent effect as increases of APP levels in all lines -related to their own DMSO control- were detected already 3 days post first treatment. AV showed the highest increase at day 3, which is reasonable as I expect that AV is cleaved more often by β-secretase than Wt and AT, therefore blocking of β-secretase should result in a robust increase. AT showed an increase of APP upon Bace-1 treatment at day 3, which was lower than the one observed in Wt (Figure 41A). As I assume that APP carrying the AT mutation is predominantly but not exclusively cleaved by α-secretase, an increase lower than the one measured for Wt was expected. However, none of the γ-secretase inhibitors, Compound E and DAPT, showed a potent effect across lines, except DAPT in Wt at day 3, when it increased APP levels. APP increase after Bace-1 treatment at day 12 for the AV and Wt seemed to be on the same level as they were on day 3 (Figure 41B). This suggests that Bace-1 is so potent that a one-time dosage is enough to reach the maximum effect on APP cleavage blockage. This could indicate that the increase of APP is not limited by concentration and frequency of dosages of Bace-1, but by the amount of APP within each cell. Unexpectedly, I noticed a strong increase in APP levels in the AT line at day 12, which was much higher than at day 3. Further studies are required in order to confirm these results and find an explanation.

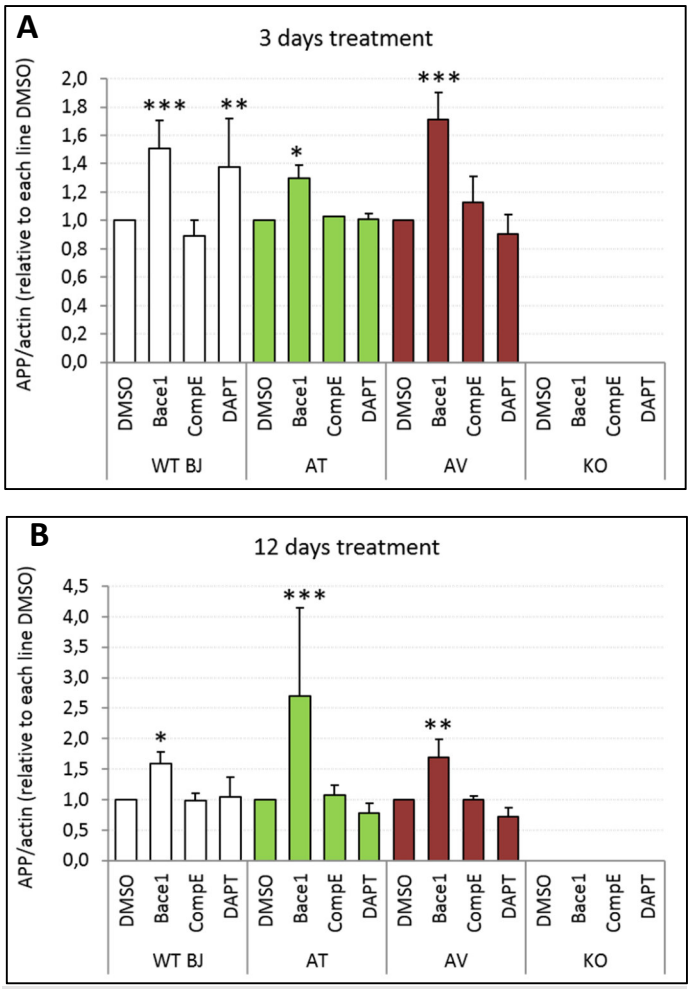

Figure 41. R Western blot quantification showing APP protein levels (relative to the loading control Actin) 3 days (**A**) and 12 days (**B**) post treatment with β- and γ-secretase inhibitors. Numbers are shown relative to the DMSO-treated APP levels for each of the AD lines.

Regarding pTau levels upon treatment with the inhibitors, no major change was observed after 3 days except for an increase in Wt upon DAPT exposure. However, after 12 days significant decreases in pTau upon Bace-1 treatment were detected for all lines. These results might indicate that pTau is downstream of APP or Aβ production. The apparent controversy between these results and the ones obtained by immunofluorescence could be explained by the fact that these data were obtained by quantifying pTau only in the neuronal bodies, whereas by WB we detect pTau in total lysates, including neuronal projections, where this protein is reported to be mainly located.

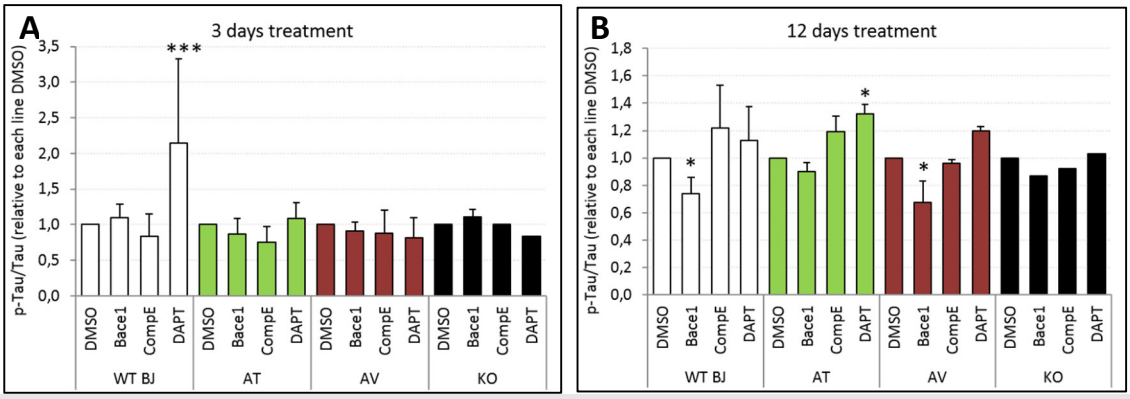

Figure 42. Western blot quantification showing pTAU protein levels (relative to the loading control Actin) 3 days (**A**) and 12 days (**B)** post treatment with β- and γ-secretase inhibitors. Numbers are shown relative to the DMSO-treated APP levels for each of the AD lines.

4.6 Generation of isogenic reporter lines

Despite our 3D-spinner cortical neuron differentiation protocol is highly efficient, producing more than 90% neurons (MAP2 and TUJ1 positive) and a high percentage of cells expressing cortical markers, such as CTIP2, these cultures contain different types of neurons, and in some cases (as described before) glial cells. Therefore, given that these cultures are not pure and that we cannot control the possible differential neuronal heterogeneity between AD lines, which can affect the experimental outcome to an unknown extend, we decided to generate reporter lines for specific cortical neuron types. I decided to target the gene CTIP2, a gene highly expressed in the deep cortical layers V and VI and therefore an excellent marker to ensure cortical identity of our cultures. Hence, I generated a targeting vector expressing the novel, monomeric yellow-green fluorophore mNeonGreen (Shaner et al., 2013) and targeted all isogenic lines using the knock-in approach described earlier (Figures 43 and 44 below). Targeting using CRISPR/Cas9 in concert with HR120-CTIP2-mNeonGreen resulted in mNeonGreen fluorescence under the

expression of the CTIP2 promotor via P2A and successful targeted clones were confirmed as described in the material and methods section. I then differentiated the chosen clones of each line and mNeonGreen signal was observed in cortical spheres during the differentiation as well in dissociated neurons (Figures 43 and 44).

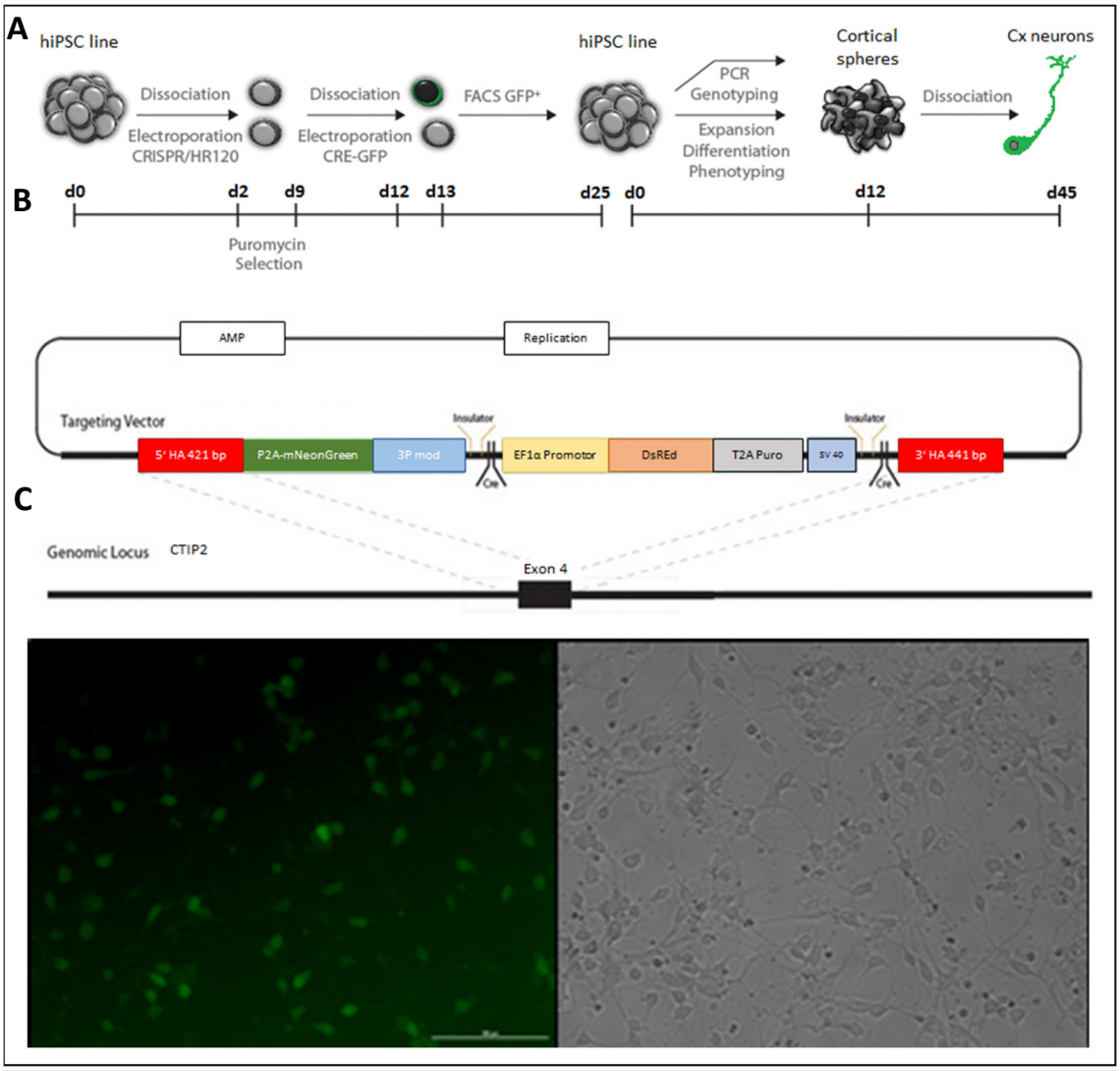

Figure 43. (**A**) Targeting scheme invented to create reporter line. (**B**) Schematic view of novel and via genome editing generated targeting vector HR120-PA-CTIP2-P2A-mNeoNGreen used to generate the CTIP2 reporter lines. (**C**) mNeonGreen expression in CTIP2+ neurons from dissociated neurons AT line d45.

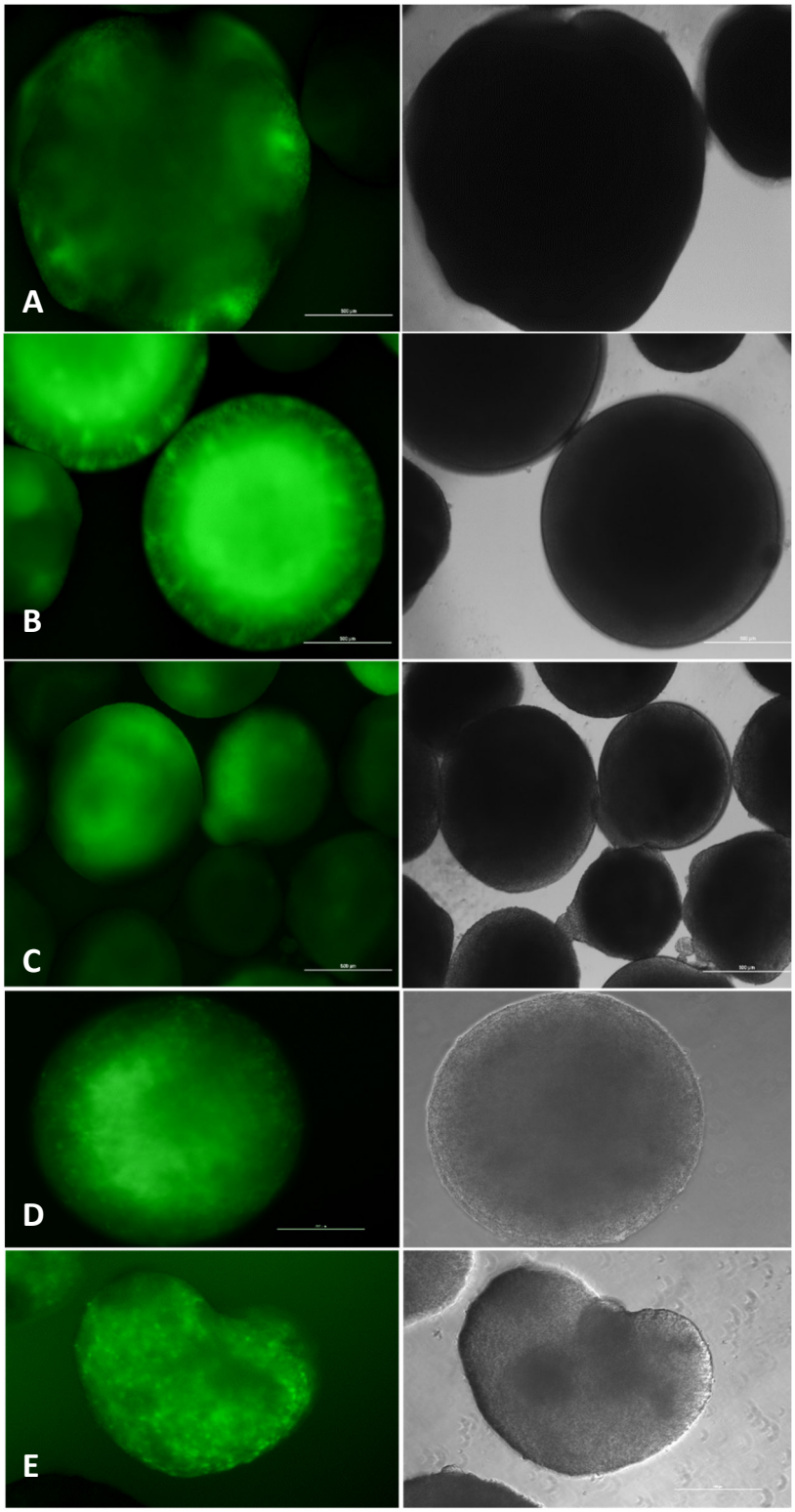

Figure 44. CTIP2 expression in cortical spheres at d35 in (**A**) WT, (**B**) AT, (**C**) AV, (**D**) AV, (**E**) KO line (left column 1 s exposure time, 10x bright field; right column 100 ms exposure time, 10x bright field). mNeonGreen expression was first detected around d18-d20 during the differentiation into cortical spheres in 3-D spin culture.

I next ought to confirm the specificity of the generated reporter lines to prove that mNeonGreen expression is actually driven by CTIP2 expression. As it can be observed in Figure 45, the colocalization between the antibody-labeled neurons (red) and the ones expressing the endogenous signal (green) reaches 85-95% for most of the clones selected, being only lower for the APP KO clones (~65%). We could observe that when the overlapping between CTIP2+ cells by immunostaining and CTIP2+ reporter cells is not 100% is always due to a higher number of reporter than antibody-labeled cells. The most plausible explanation for this is that the reporter is more sensitive and therefore as soon as a cell expresses some CTIP2, the signal is detectable due to the reporter but still not strong enough to be picked by the antibody. This explanation also supports the data shown on the characterization of the cortical cultures, that showed a small increase over time in the percentage of immunostained CTIP2+ cells despite the number of nuclei remained the same (Figure 27). These data validated, not only the efficiency of our protocol to differentiate iPSCs into cortical neurons, but also the specificity of the CTIP2 reporter. Therefore, the lines will provide me with the option to perform further experiments with purified neuronal populations across all isogenic lines.

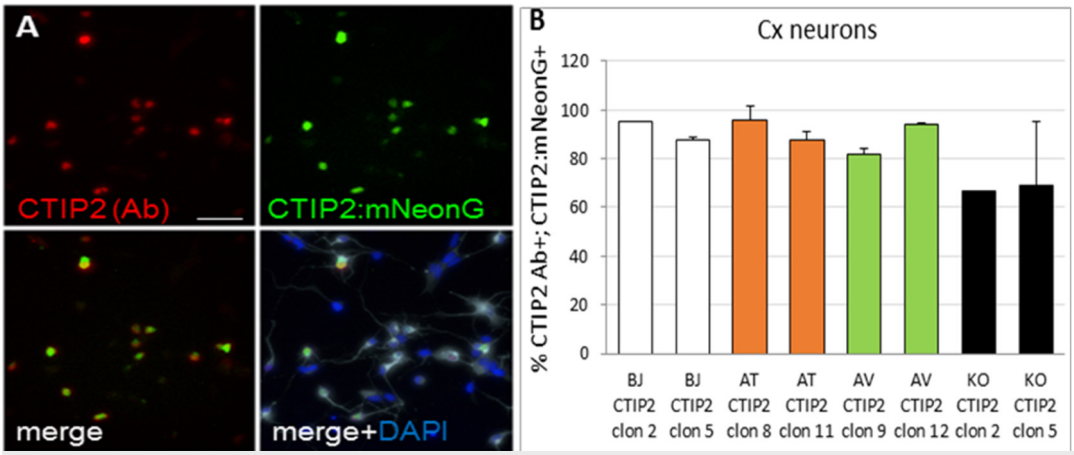

Figure 45. (**A**) Representative image from a CTIP2:mNeonGreen targeted iPSC clone showing antibody immunostaining against CTIP2 (red) and green signal from the CTIP2 genetically modified locus. Nuclei are stained with DAPI (blue). Scale bar = 20 µm. (**B**) Quantification of the percentage of nuclei that are positive for the immunostaining and also express green reporter signal. Two targeted iPSC clones per line are shown.

I then wanted to measure the differentiation efficiency of all isogenic lines into cortical neurons using the CTIP2 reporter lines. We differentiated the isogenic lines for 45 days and purified CTIP2+ populations via fluorescence activated cell sorting (FACS) right post dissociation. The quantification shows that 62 – 80 % of our differentiated cells are CTIP2+ (Figure 46).

Interestingly, the line showing the lowest amount of CTIP2+ neurons is the AT line, whereas both negative lines AV and SWE show ~10% higher values compared to AT. That result pointed us into an interesting direction. Using IF based high content imaging I showed earlier that WT and AT do have higher percentage of CTIP2+ neurons at all time-points studied after the cortical cultures are plated. From those results we considered the possibility that AV and SWE lines maybe display an impaired differentiation into cortical neurons; however, this new result shows that the pathogenic mutations do not affect the potential of iPSCs to differentiate into CTIP2+ cortical neurons. Together, these data suggest that upon the presence of the negative AD mutations, CTIP2+ neurons are more vulnerable and therefore even at the first measurement of the high content imaging three days after plating many of them already died.

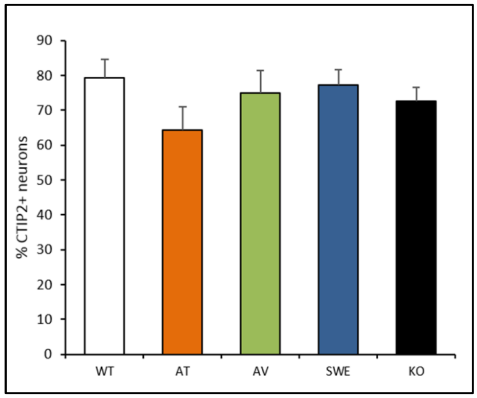

Figure 46. Percentage of CTIP2+ neurons of dissociated cortical spheres at d45 shows variability across and within each line (n=3).

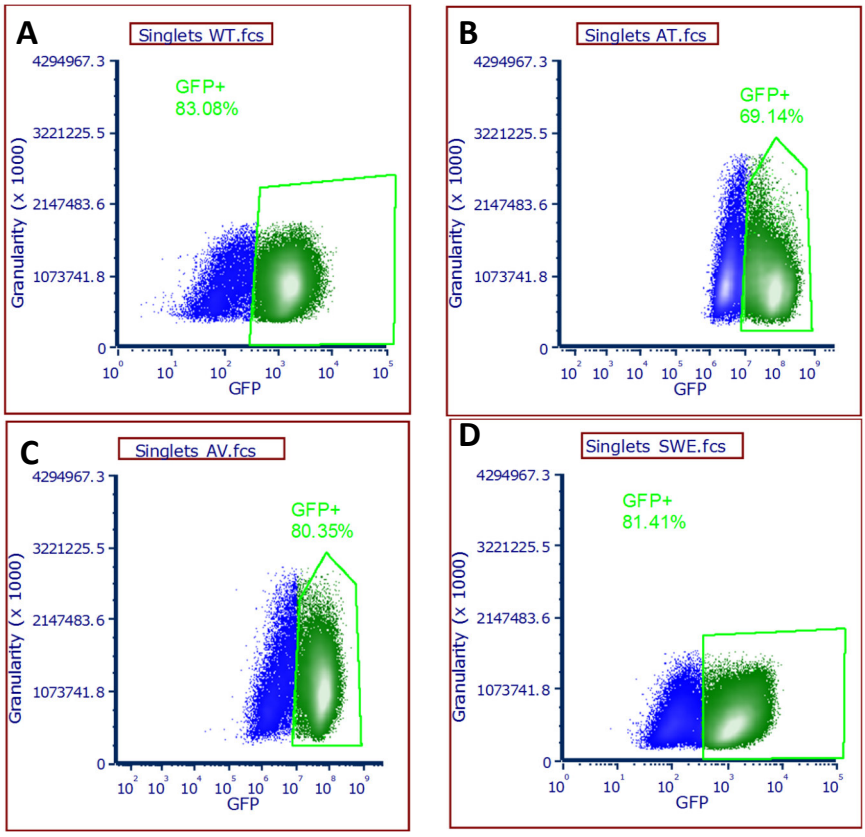

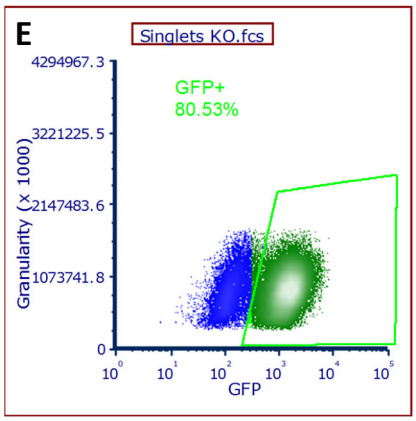

Figure 47. Fluorescence-activated cell sorting shows high percentage of freshly dissociated CTIP2+ cells at d45 following the cortical differentiation protocol for (**A**) WT, (**B**) AT, (**C**) AV, (**D**) SWE, (**E**) LON and (**F**) KO-line; CTIP2+ cells in green, CTIP2- in blue.

4.7 Survival assay via live-cell imaging

Given that the ELISA assays have shown that the lines carrying fAD mutation produce higher amounts of Aβ42 and Aβ40 (Figures 31-34) and given that Aβ and its multifarious toxicity is supposed to be a main driver of neurodegeneration in AD (Figure 9), I next wanted to investigate if these higher levels in the fAD lines would inversely correlate with cell survival *in vitro* compared to the WT, AT and KO lines. Recent studies from our lab have shown that derived neurons from iPSCs carrying a given disease phenotype can be employed to perform survival assays *in vitro (Rodriguez-Muela et al., 2017).* Following a similar idea, I used a new technique of time-lapse automated live cell imaging to test the survival of all isogenic cortical neurons.

As cortical neurons are one of the cell types most severely effected in fAD and sAD and therefore more prone to die compared to other neuronal types, and since I was able to show, that the cx neurons dissociated at day 45 of the differentiation express the cortical marker CTIP2 at a high percentage (Figures 27 and 46), I decided to measure their survival when exposed to stressors or control conditions. I decided to add stressors for two reasons: first, to make potential differences in survival that might be significant but hard to detect more obvious, and second, the added stressors could expose neurons to an environment that resembles more closely the one that fAD neurons may face *in vivo* when homeostasis is impaired. With each treatment we added the fluorescent viability dye calcein red-orange (Invitrogen) to allow detection and automatic quantification of survival, as only viable cells would take up the dye (Figure 48).

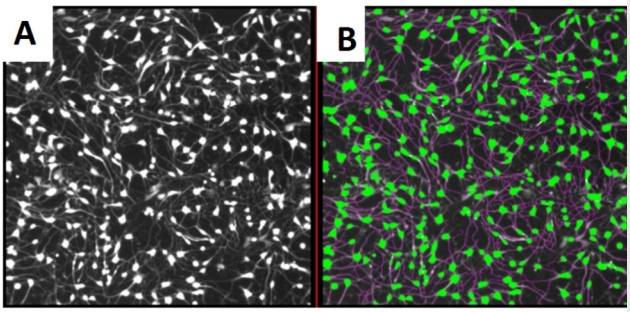

Figure 48. Representative picture of automated live cell imaging analysis: cortical AT neurons d45 after treatment with DMSO and the calcein-red viability dye. (**A**) Signal detected by the Biostation live-imaging system (**B**) Detection by the Nikon software to track cells and neurites and to allow single-cell labeling.

At first, I measured survival of cortical neurons from isogenic lines 45 days after differentiation in two different conditions. In the first condition neurons were untreated (DMSO control) and in the second condition neurons were treated with Thapsigargin (TG) (Figure 49). TG is an inhibitor of the arco/endoplasmatic reticulum Ca^{2+}-ATPase (SERCA), and its inhibition not only abnormally raises intracellular calcium levels leading to ER stress, but it also induces an autophagy failure by inhibiting the fusion of lysosomes and autophagosomes, the final step of autophagy, finally leading to apoptosis after some hours of exposure to the neurons.

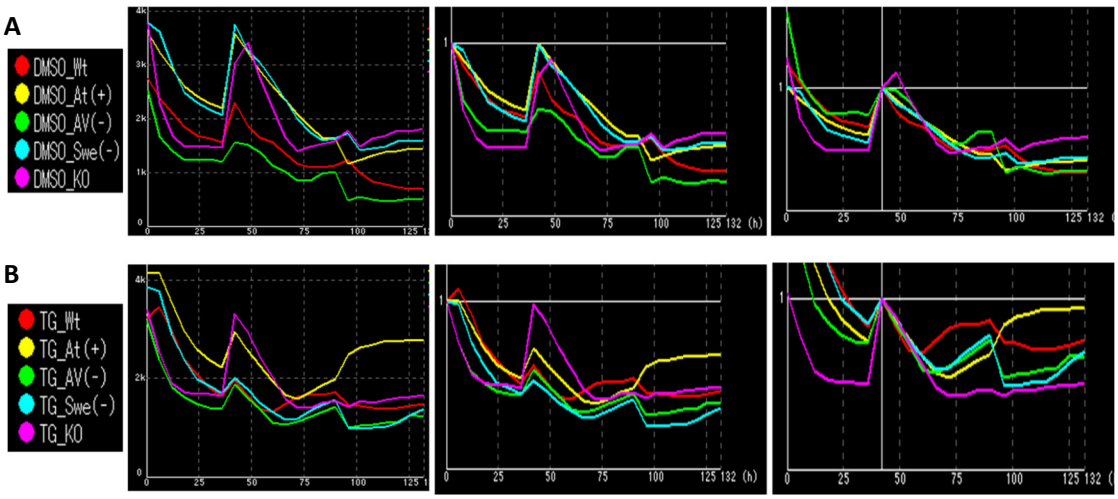

Figure 49. Quantification of the survival of CTIP2+ cortical neurons by using automated live cell imaging analysis. Cortical neurons from all isogenic lines were treated every 48h with (**A**) DMSO or (**B**) Thapsigargin for 138h, and cell numbers counted every 6 hours. AT line shows no difference in survival compared to AV and SWE in control condition, but increase in survival becomes more obvious in stressor conditions around 85h after first treatment (b,c) as AT seems to be less vulnerable; row (1) total cell count, (2) normalized to 1st and (3) to 2nd treatment; all treatments 10 nM, n=4.

No difference in survival between AT line compared with AV and SWE lines was detected when the neurons were treated with DMSO only over the time-course of the experiment.

Noticeable difference in survival was detected when cells were treated with the stressor TG, in this scenario AT showed much higher survival than all other lines starting at 90h and continuing until the end of the time-lapse experiment.

I then subjected dissociated cortical neurons from all lines to treatment of MG132 (MG), a peptide aldehyde (carbobenzoxy-Leu-Leu-leucinal) potent proteasomal inhibitor by blocking proteolytic activity of the 26S complex (Han et al., 2009). Additionally, I decided to subject cells to treatment with Tunicamycin (Tun), which is another ER stressor. Tun inhibits the GlcNAc phosphotransferase (GPT), an enzyme that catalyzes the first step of glycoprotein synthesis by transferring N-acetylglutosamine-1-phosphate from UDP-N-acteylsamine to dolichol phosphate. As glycosylation is necessary for the solubility, the stability and the folding properties of proteins as well treatment with Tun leads to accumulation of misfolded proteins in the ER, which induces ER stress, activate the control system of the ER and if prolonged apoptosis signaling is activated (Banerjee et al., 2011).

No significant difference in cell survival between lines was detected over the observed period of 138 hours in the control condition (DMSO treated), even though survival in AT, WT and KO was slightly better than in SWE and AV related to the second treatment of calcein-red and total number was highest in the AT line throughout the whole time-course of the experiment.

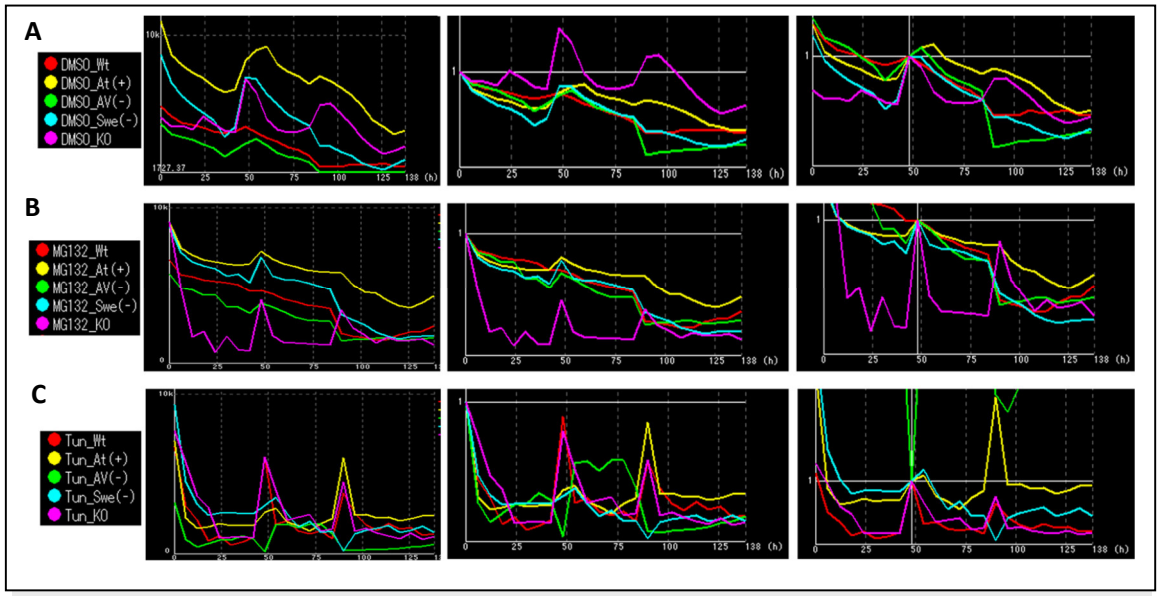

Figure 50. Live cell imaging analysis results: cortical neurons of all isogenic lines treated every 48h with (**A**) DMSO, (**B**) MG132 or (**C**) Tunicamycin for 138h, cell number counted every 6 hours. Row (1) total cell count, (2) normalized to 1st and (3) to 2nd treatment; all treatments 10 nM, n=4.

However, in both stressor conditions, MG- and Tun-treated, AT neurons showed much better survival compared to SWE and AV (Figure 50). The difference in survival seems to get more obvious at around 85 to 90 hours into the experiment.

As conclusion, in the two major experiments run, and after the analysis of many thousands of cortical neurons in an unbiased, automatic way, AT neurons show a slight increase in survival compared to the negative mutation lines in the control condition. In both experiments the increase in survival becomes more obvious in the stressor conditions, especially at around 80 to 85 hours after start of the experiments. As the survival of the AT line is even better than WT, the data suggests that the positive mutations may offer a protective effect. The obvious AT protective effect detected at around 80 or 85 hours could be explained by the third stressor treatment, which magnifies the differences between the fAD lines. As both, WT and AT cortical neurons show higher survival rates compared to AV and SWE, it indicates that our differentiated cortical neurons are already mature enough to have the potential to show fAD-linked pathological phenotypes which would explain their higher vulnerability to ER- and autophagy-related stressors and decreased general survival potential, made me wonder whether the most important AD hallmark, the accumulation of Aβ extracellular deposits, could be detected in more complex tridimentional structures that can be also maintained in culture for longer, such as brain organoids.

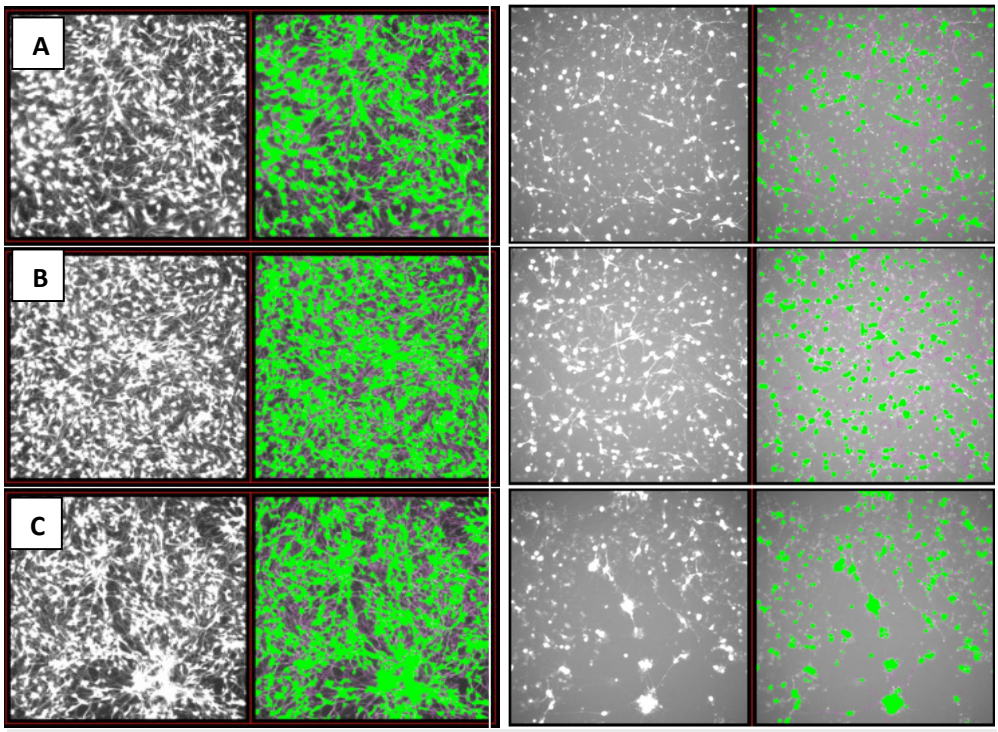

Figure 51. Representatives images showing WT (**A**), AT (**B**) and SWE (**C**) CTIP2 positive neurons 12h after first treatment with TG (10nM) (images in column 1 and 2) and after 84h (12h post third treatment) (images in 3 and 4).

This high-through-put live imaging approach has been a useful tool to further characterize the phenotype of cortical AD neurons and future applications will be explained in the discussion section as this system constitutes an ideal platform for performing survival assays, which represents an important part of isogenic disease modeling.

4.8 Generation of cerebral organoids

In recent years, the field of cerebral organoids has gained more and more attention and, despite it is still in its infancy, it seems to hold great potential to model human disease *in vitro*. Cerebral organoids are highly complex and, importantly, self-organizing structures, which can be kept in culture for long periods of time and which complexity mimics the interstitial compartment found in the human brain (Camp et al., 2015; Lancaster et al., 2013), a feature that might be crucial to model a neurodegenerative disease like AD *in vitro*. As I have already proven that the isogenic AD lines differentiate well into cortical neurons after 45 days in 3D culture, expressing not only high levels of the neuronal marker MAP2 but also CTIP2 (Figure 27), and are therefore highly amenable to be differentiated into this neuronal lineage affected in the disease, I next thought to test their potential to generate cerebral organoids.

As I have also shown that the fAD lines AV and SWE produce more Aβ42 and Aβ40 -detected by ELISA- in an iPS state as well as when differentiated into cortical neurons. I was hoping that by keeping them in culture for many months and therefore extending the period of time for maturation manifold compared to the cortical spheroids, fAD related phenotypes would become more obvious. To do so, I developed a protocol to differentiate all isogenic lines in 3D into cerebral organoids, based on modifications of a method previously published (Lancaster et al., 2013) and I have kept them in culture for more than 180 days.

In a first step, I developed a method to grow them in ultra-low-attachment 96 well plates until cells of all lines showed homogenous generation of well-rounded EBs, which I have observed constitutes a crucial for the successful generation of the organoids.

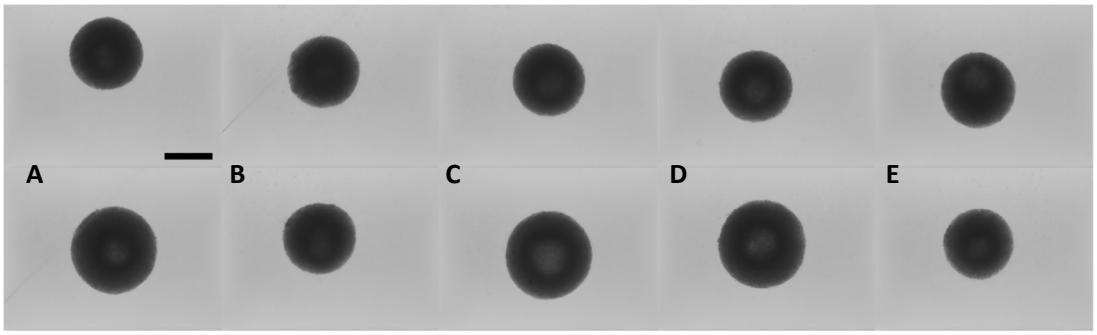

Figure 52. Cells of all isogenic lines formed very homogenous EBs within 2 days after transferring them into 96 well ultra-low attachment plates. Shown are two EBs of Wt (**A**), AT (**B**), AV (**C**), SWE (**D**), KO (**E**), bar = 500 µm.

Next, I was able to incapsulate the EBs into Matrigel drops and adapt them to 3D spinning culture following the modified cerebral organoid protocol (described in material and methods). During different time-points starting at day 120, single organoids of all lines were collected, fixed and sectioned for later immunohistochemistry (IHC) analysis.

One set of organoids, fixed at day 134, was analyzed to show some preliminary data for this work. As Figure 53 shows, sectioning of the organoids was successful, and organoids of all isogenic lines show high percentage of MAP2 positive neurons (data not shown) distributed throughout the entire structure. The organoids show dense three-dimensional neuronal network formation and surprisingly they also show fluid-filled cavities, resembling the lateral ventricle in the developing brain *in vivo* (Figure 53, (A), (C), (D)), a striking event that was spontaneously discovered by (Camp et al., 2015) Treutlein's group.

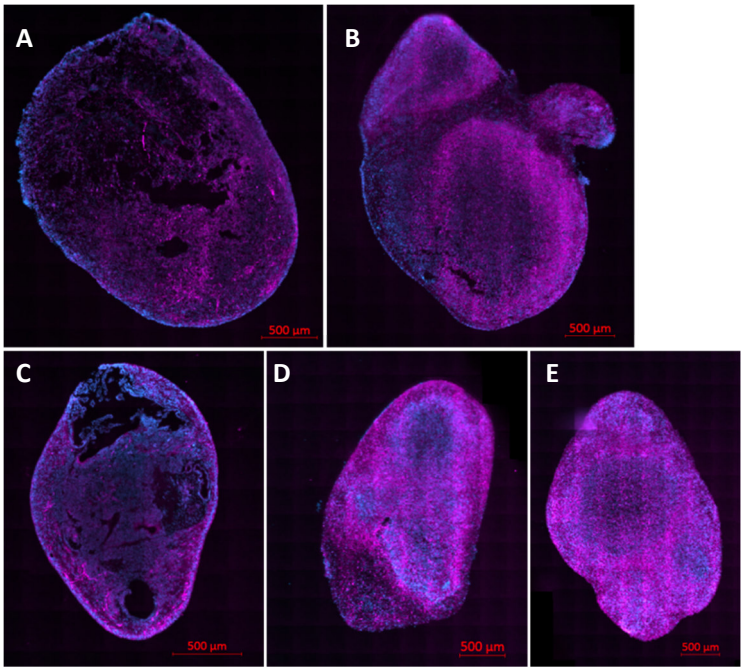

Figure 53. Representative images from cerebral organoids fixed, cryopreserved and sectioned after 134 days in culture. (**A**) WT, (**B**) AT, (**C**) AV, (**D**) SWE, (**E**) APP KO. Neurons are stained with MAP2 antibody (red) and nuclei are labelled with DAPI (blue). Sections are 5 µm. The entire section of each organoid was imaged and self-assembled with AxioScan Z1 microscope.

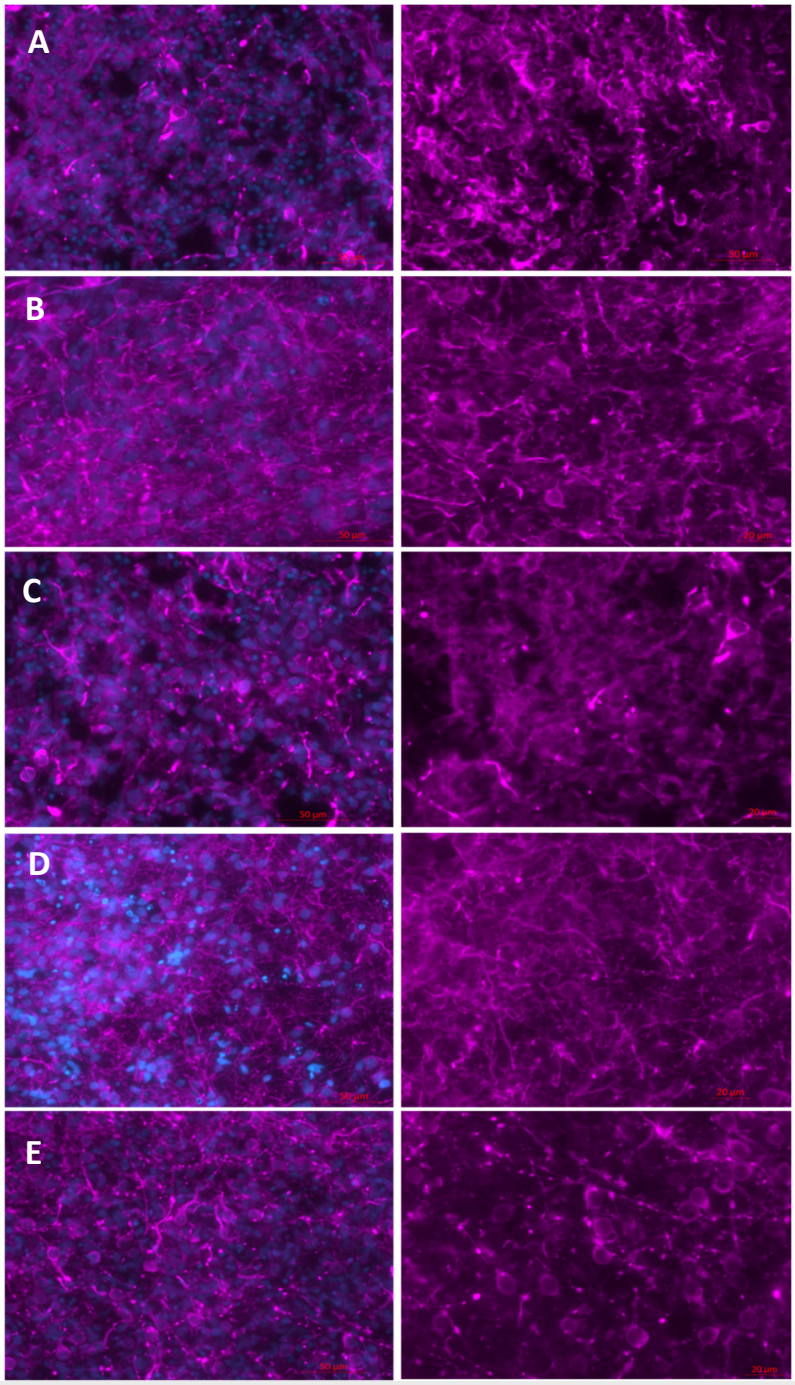

Figure 54. Organoids of (**A**) Wt, (**B**) AT, (**C**) AV, (**D**) SWE, (**E**) KO line, immunostained for DAPI/MAP2 (left column) or MAP2 (right column), showed high percentage of neuronal marker MAP2 at d134 even in the center of the cerebral organoids.

As the organoids were much bigger in size and diameter compared with the cortical spheres I had generated before, I decided to explore whether MAP2 positive neurons could be found also in the center of all organoids, which would confirm that neuronal patterning and

therefore neuronal network formation of neurons is also possible further away from the surface and would rule out the possibility of necrosis is that region of the organoid not so exposed to nutrients. Confocal pictures of all organoids taken at randomly chosen locations in the core showed a dense tridimensional and MAP2+ neurons network formation (Figure 54), which was surprising and encouraging, given that the organoids reach up to 2 mm in diameter (see pictures in supplements).

Next, I decided to stain the organoid sections for the most important pathological markers in fAD, Aβ and pTAU. At first, I expected to see lower levels of Aβ in the AT organoids and increased levels in the SWE and AV ones based on the ELISA results. However, it was questionable how much Aβ we would be able to detect, where (intracellular versus extracellular), in which form (as small or big deposits), and if any at all. The fact that Aβ, quickly after being generated in multi vesicular bodies, mitochondria associated membranes of the ER and lysosomes, is transported into the lumen and diffuses into the media, could decrease the chances to detect intracellular and soluble Aβ via IHC. That is the challenge that traditional 2D and even most advanced 3D culture systems have faced to date. However, I hypothesized that the complex structure of the organoids themselves might increase the intracellular Aβ levels by acting as a natural diffusion barrier and therefore enabling me to detect it. Regarding pTAU, I expected to see comparable levels in Wt, AT, AV and SWE based on the IF results on dissociated cortical neurons and decreased levels in the KO.

I was not able to detect pTAU in a reliable manner, as the signal was too weak in all samples studied probably due to a poor sensitivity of the primary antibody. Due to the size of the organoids, to the fact that I needed to image their whole surface and scan many different sections from 5 different lines in an unbiased way, I decided to use an automated, high-throughput microscope with a 40X magnification. This extremely useful microscope is however not confocal and therefore the quality of the images, when the signal is already weak, did not allow me to detect a trustworthy and reliable signal for this AD pathological marker. Regarding Aβ analysis, as expected, no Aβ was detected in the KO line (Figure 55), which confirmed specificity of the 4G8 antibody used. Aβ was detected in Wt and also in AT organoids (Figures 56 and 57), although notably less in AT than in Wt, therefore validating our ELISA results and the hypothesis that less Aβ42 and Aβ40 are produced in that protective line. However, I did detect a drastic increase in Aβ in either the AV or the SWE organoids compared to the Wt (Figures 58 and 59). Strong signal was detected in the soma, but also in dendrites of neurons. To my surprise, I also detected strong, diffuse extracellular signal surrounding the MAP2 positive neurons in both lines (Figures 60-61).

The extracellular signal was not detected in Wt or AT organoids. As it has been reported that the 4G8 antibody is not only able to detect soluble intracellular Aβ but extracellular, senile plagues as well, these preliminary results are extremely exciting and promising, as they may indicate that our isogenic AD *in vitro* model might be able to recapitulate the most important hallmark of fAD, aspect that had not been achieved to date using hiPSCs or any other cellular model without overexpressing several different mutations affecting APP and presenilins at the same time. However, these preliminary data need to be confirmed and more thoroughly investigated, more samples need to be processed and different staining methods need to be applied to unravel the entity of these diffuse extracellular Aβ accumulations. Furthermore, the staining with pTAU needs to be repeated as well using different antibodies and confocal microscopy at a higher magnification.

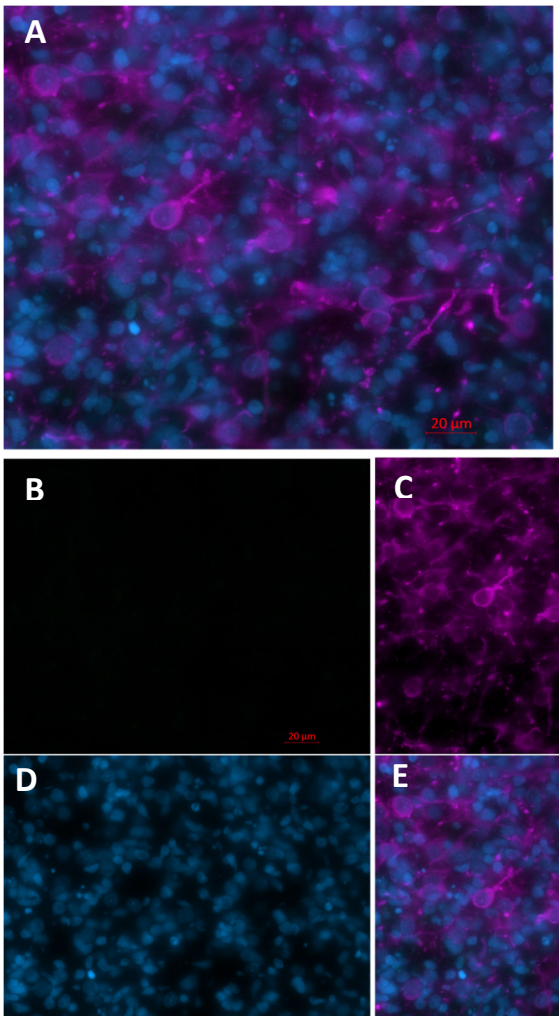

Figure 55. APP KO organoid at d134 immunostained for Aβ (**B**), MAP2 (**C**), DAPI (**D**), merged (**A, E**), no Aβ was detected in the dense MAP2+ neuronal network.

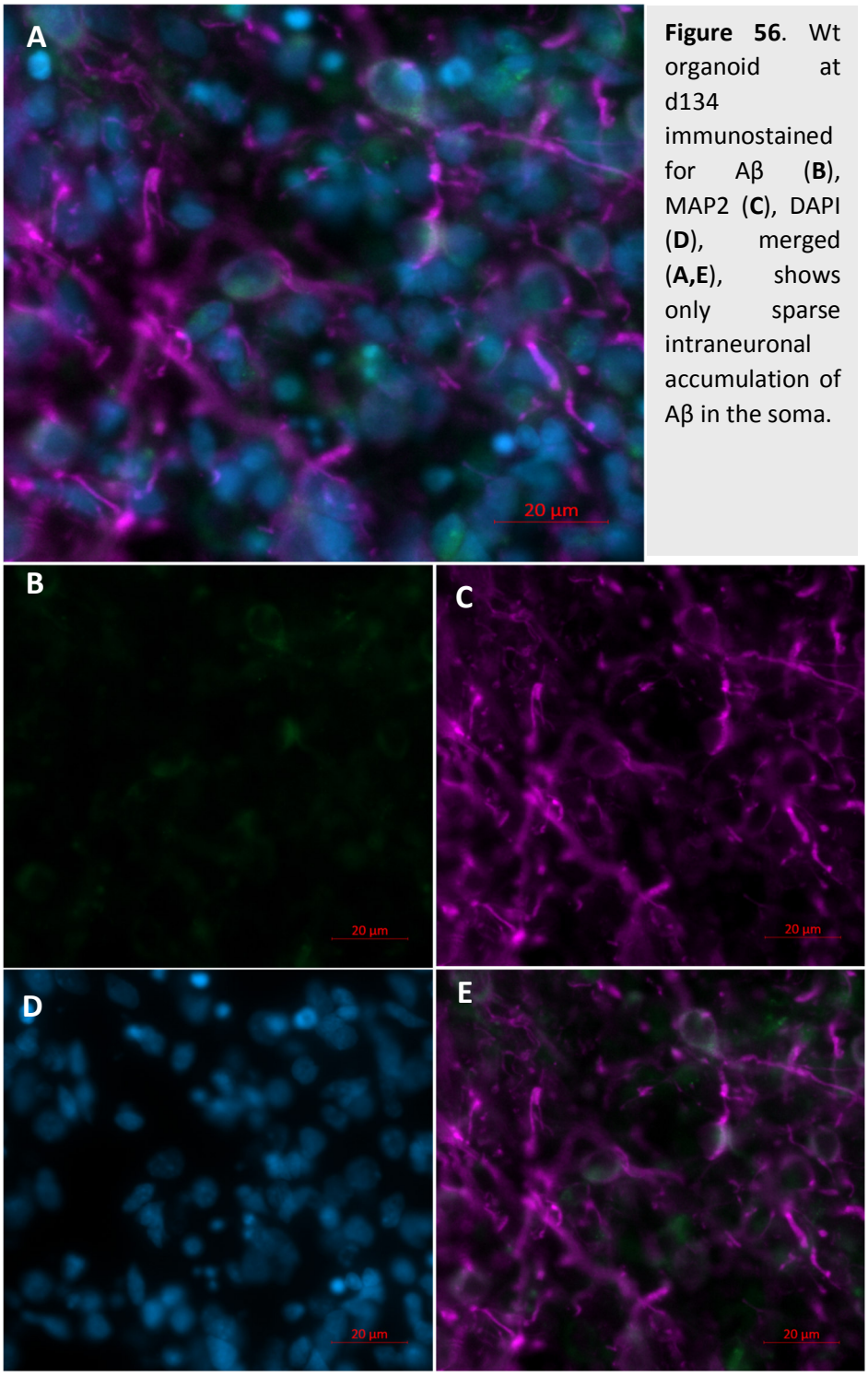

Figure 56. Wt organoid at d134 immunostained for Aβ (**B**), MAP2 (**C**), DAPI (**D**), merged (**A,E**), shows only sparse intraneuronal accumulation of Aβ in the soma.

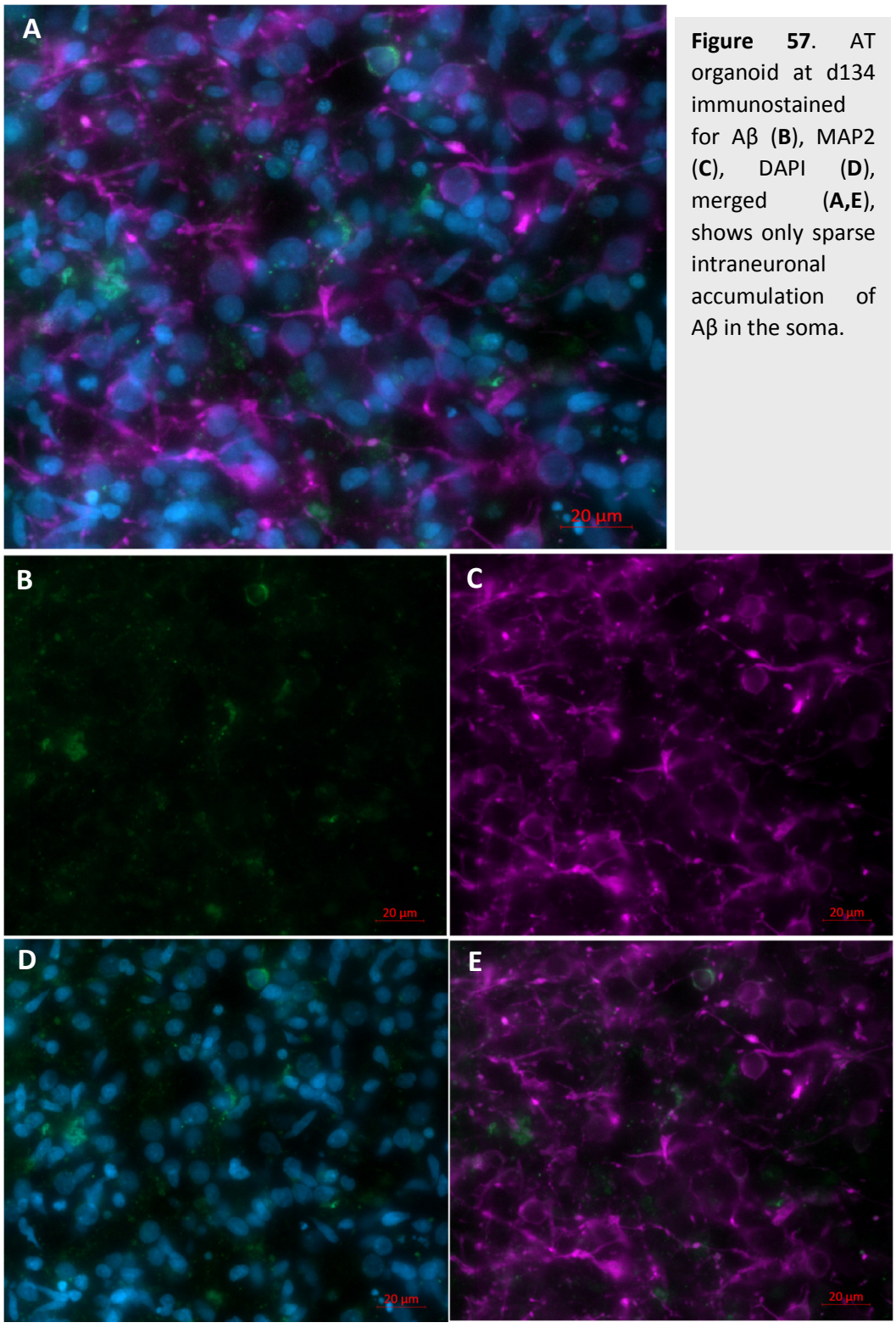

Figure 57. AT organoid at d134 immunostained for Aβ (**B**), MAP2 (**C**), DAPI (**D**), merged (**A,E**), shows only sparse intraneuronal accumulation of Aβ in the soma.

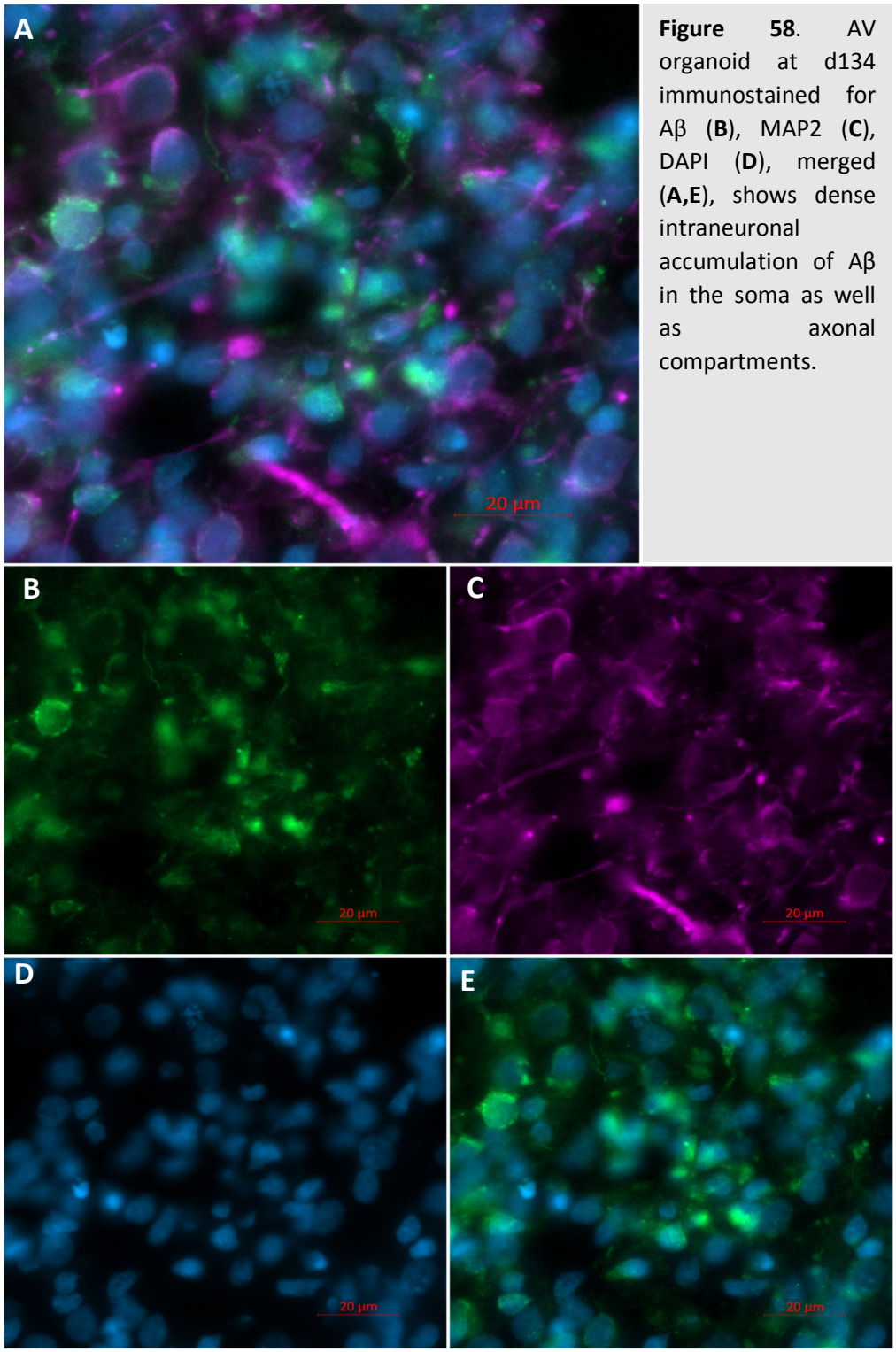

Figure 58. AV organoid at d134 immunostained for Aβ (**B**), MAP2 (**C**), DAPI (**D**), merged (**A,E**), shows dense intraneuronal accumulation of Aβ in the soma as well as axonal compartments.

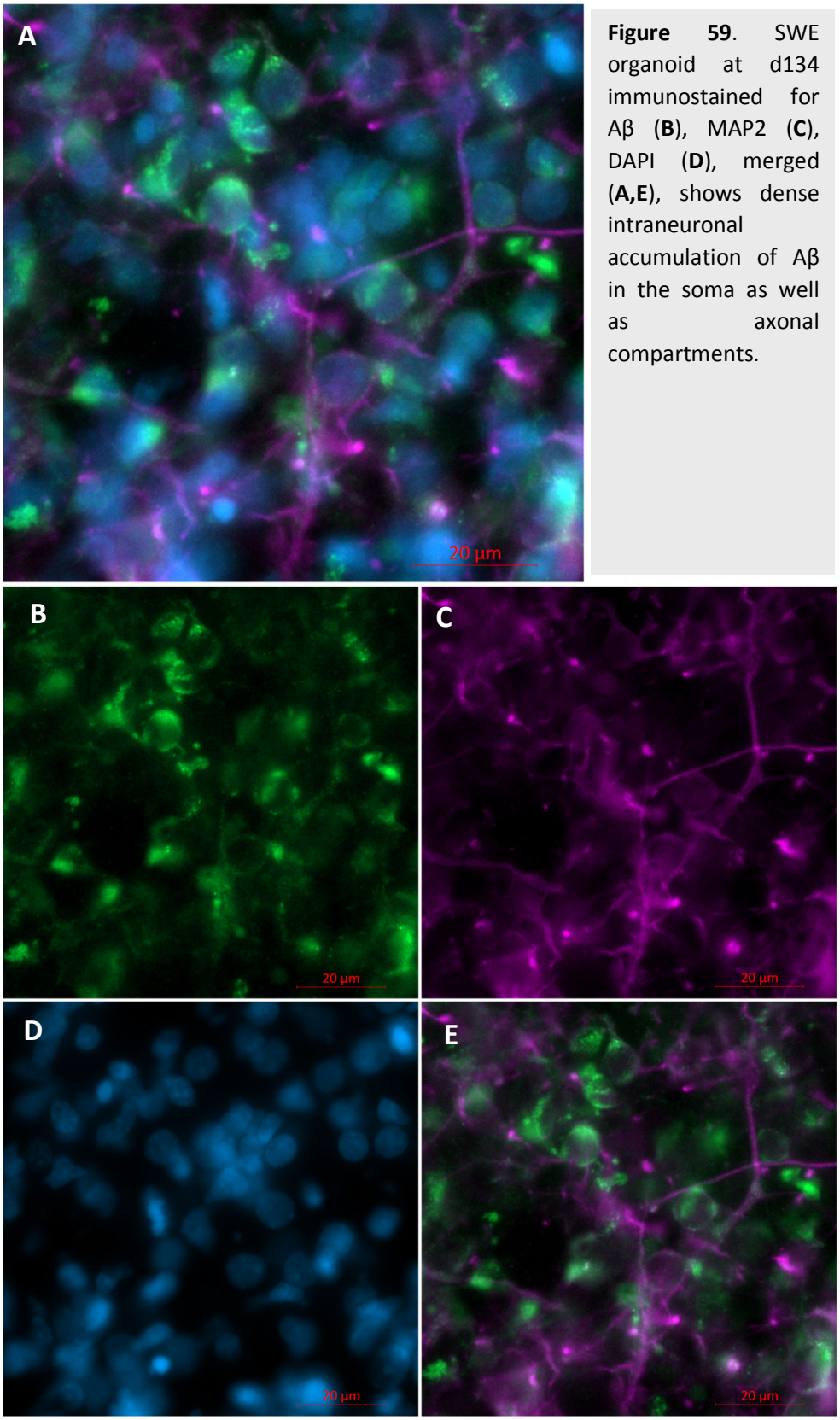

Figure 59. SWE organoid at d134 immunostained for Aβ (**B**), MAP2 (**C**), DAPI (**D**), merged (**A,E**), shows dense intraneuronal accumulation of Aβ in the soma as well as axonal compartments.

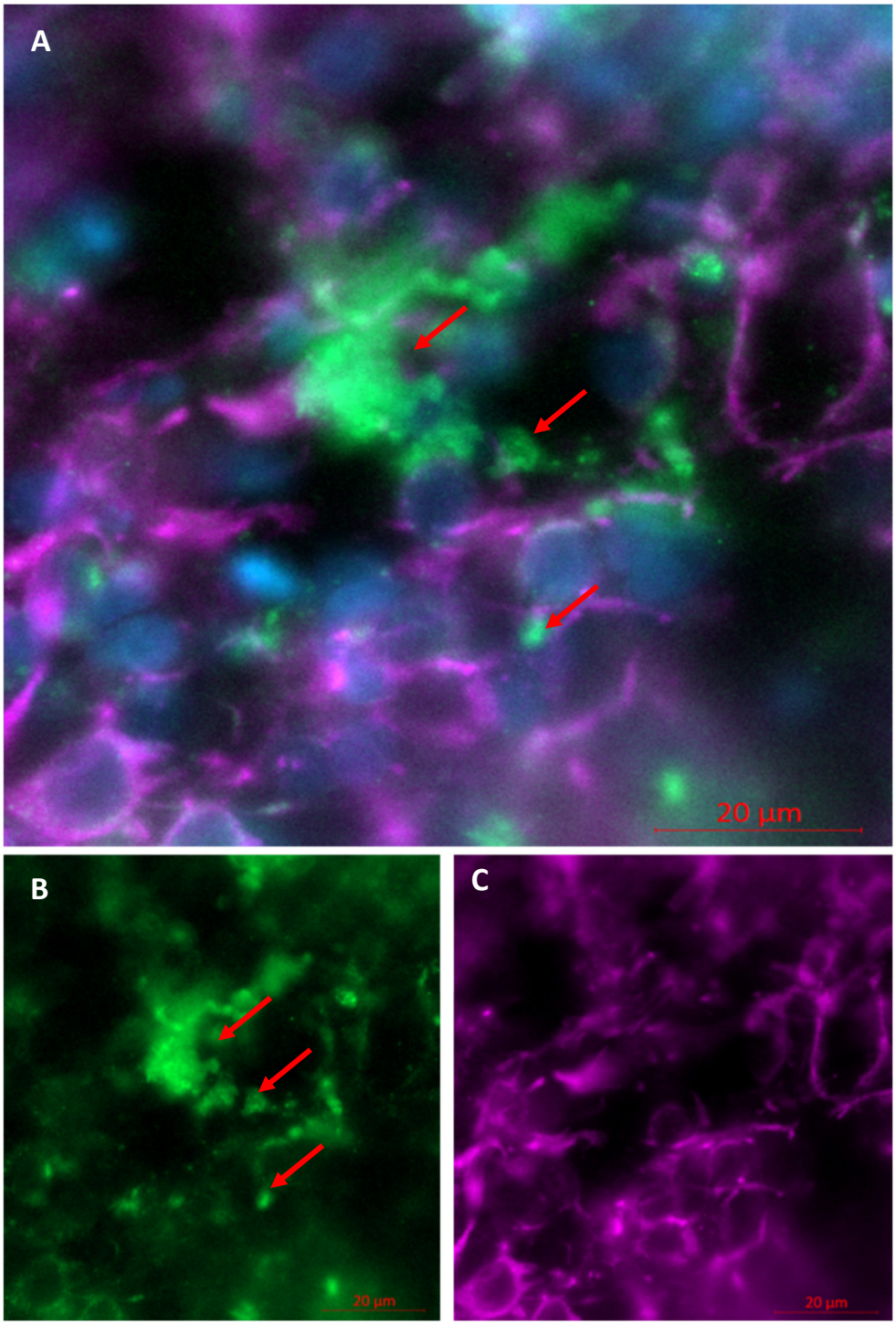

Figure 60. AV organoid sectioned at d134 and immunostained for Aβ (**B**), MAP2 (**C**), merged with DAPI (**A**) shows extracellular aggregates composed of Aβ which looks like neuritic plagues, red arrows mark Aβ extracellular aggregates.

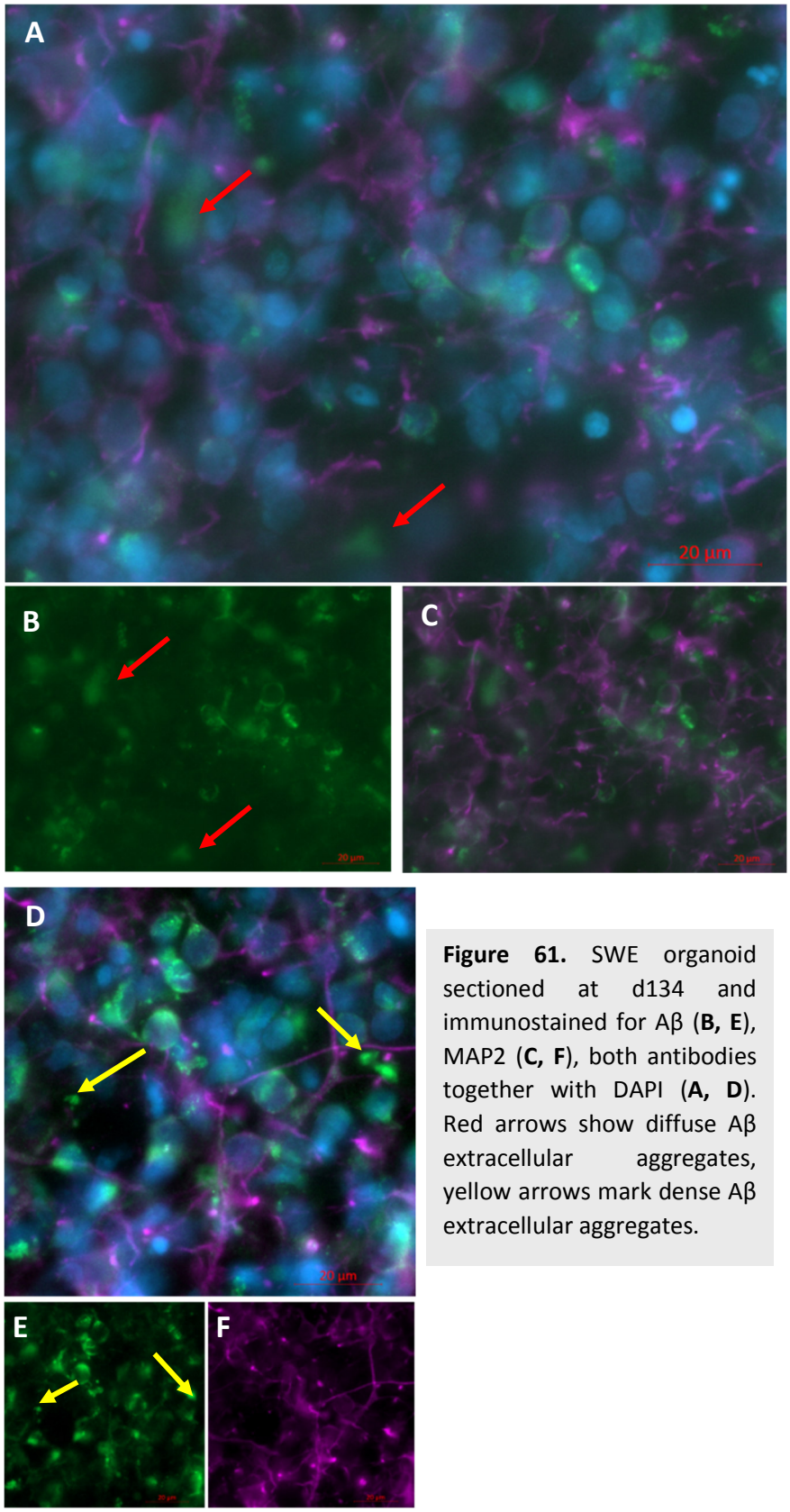

Figure 61. SWE organoid sectioned at d134 and immunostained for Aβ (**B, E**), MAP2 (**C, F**), both antibodies together with DAPI (**A, D**). Red arrows show diffuse Aβ extracellular aggregates, yellow arrows mark dense Aβ extracellular aggregates.

4.9 Proteomic analysis of isogenic AD lines

As I have shown that the introduced mutations in APP result in different levels of APP and its metabolites across the isogenic lines (Figures 27, 30-33, 39), I wanted to investigate if changes were also detectable on a protein level. Therefore, I decided to do proteomic analysis. I have demonstrated that the isogenic lines differentiate into cortical neurons in a similar manner (Figure 46) and usually 65 to x 80% of cells are positive for the cortical layer 5 marker CTIP2 after 45 days of differentiation in 3D culture. So even though the lines seem to differentiate into the terminal cell type quite even, I still wanted to minimize the risk of finding different expression patterns between lines, that are caused by different compositions of cell populations in each line, but not by the mutation of interest. That is why I decided to use the cortical reporter lines for this experiment as they allow me to purify cortical neurons based on CTIP2-mNeonGreen expression. Cortical spheres from Wt, AT, AV and KO line were dissociated at day 45 and CTIP2+ neurons were selected via fluorescence activated cell sorting and proteomic analysis was performed like described in the materials and methods section.

More than 8200 proteins were quantified, and I did detect statistically significant differences in protein expression between the lines (Figures 62B, 63), but surprisingly the overall number of genes showing high fold changes compared to Wt was not as elevated as expected prior to the experiment, at least for this specific time-Point after 45 days of differentiation (Figures 62B, 63). I detected a high fold change and a significant lack of APP in the KO line, compared to all other lines, but besides that, the expression pattern looked very homogenous like displayed in Figure 62. Even though these results seemed to confirm the technical success of creating an isogenic model, which by itself could explain the homogenous proteome between lines, I would have expected more significant differences in protein expression levels as a direct consequence of the mutated APP variants and the increased Aβ40 and Aβ42 in the negative lines. However, several explanations are possible: first, maybe the timepoint I chose for the experiment was too early during the differentiation and maybe by just maturing them longer in culture changes in protein expression levels would have become more obvious. Another option could be that mutations in APP simply do not have a strong impact on the proteome of these CTIP2+ neurons and maybe differences would have been more obvious, if we had decided to sort for a different terminal differentiated cell type, maybe even from a different layer of the cortex. Lastly, maybe the cortical neurons were stressed out by the FAC sorting to such an intent,

that the stress responses of all cell lines masked potential differences in protein expression levels making it hard to see differences between lines.

A

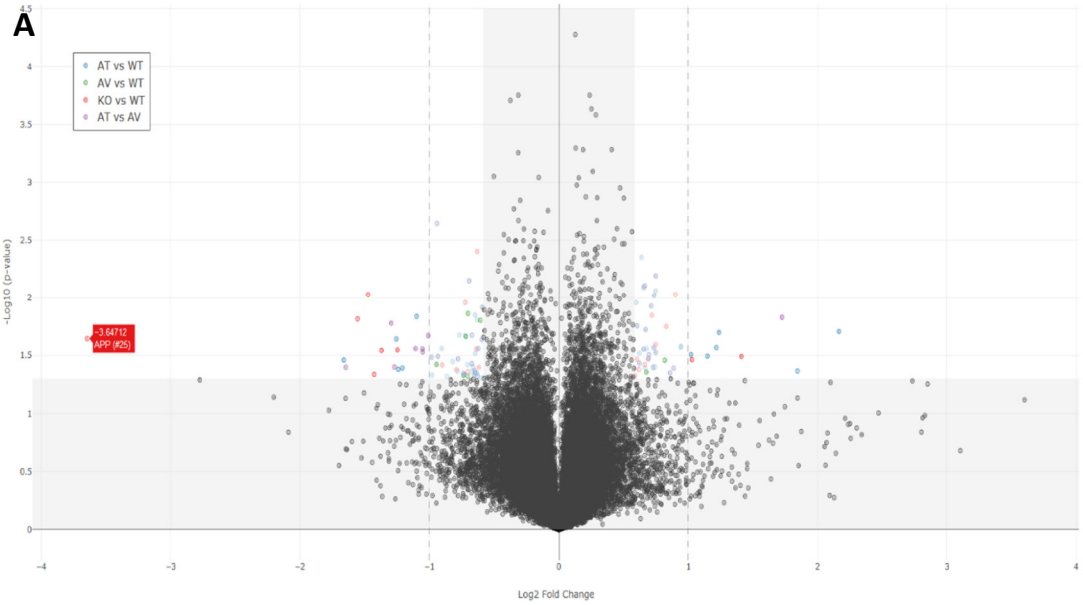

B

Gene	relative to Wt	Description
EBF2	12,13	Transcription factor COE2
EOMES	8,60	Eomesodermin homolog
KLHL14	7,21	Kelch-like protein 14
TBR1	7,11	T-box brain protein 1
EMX1	6,98	Homeobox protein EMX1
EBF3	6,65	Transcription factor COE3 O
EBF1	5,55	Transcription factor COE1
MAB21L1	5,07	Putative nucleotidyltransferase MAB21L1
NPTX1	4,72	Neuronal pentraxin-1
ZNF423	4,49	Zinc finger protein 423
NEUROD2	4,22	Neurogenic differentiation factor 2
NFIA	3,67	Nuclear factor 1
FEZF1	3,62	Fez family zinc finger protein 1
TPBG	3,59	Trophoblast glycoprotein
ALDH1A1	3,59	Retinal dehydrogenase 1
LHX2	3,36	LIM/homeobox protein Lhx2
CACNA2D1	3,17	Voltage-dependent calcium channel subunit alpha-2/delta-1
PRKCQ	3,08	Protein kinase C theta type
NFIB	2,75	Nuclear factor 1 B-type
CPNE6	2,74	Copine-6
CHCHD2	2,71	Coiled-coil-helix-coiled-coil-helix domain-containing protein 2
ZNF536	2,71	Zinc finger protein 536 (Fragment)
SOX5	2,53	Transcription factor SOX-5
TPX2	2,53	Targeting protein for Xklp2
PDE1A	2,46	Calcium/calmodulin-dependent 3',5' -cyclic nucleotide phosphodiesterase 1A

Gene	relative to Wt	Description
SIX3	0,15	Homeobox protein SIX3
SP9	0,32	Transcription factor Sp9
NTS	0,32	Neurotensin/neuromedin N
VPS37B	0,35	Vacuolar protein sorting-associated protein 37B
PRICKLE2	0,35	Prickle-like protein 2
ZFHX4	0,38	Zinc finger homeobox protein 4
GPD1	0,38	Glycerol-3-phosphate dehydrogenase [NAD(+)], cytoplasmic
MT3	0,40	Metallothionein-3
NT5DC3	0,40	5'-nucleotidase domain-containing protein 3
GRIK3	0,41	Glutamate receptor ionotropic, kainate 3
CAT	0,42	Catalase
SLC32A1	0,42	Vesicular inhibitory amino acid transporter
NGEF	0,42	Ephexin-1
NRGN	0,43	Neurogranin
GAD2	0,43	Glutamate decarboxylase 2
ATRNL1	0,43	Attractin-like protein 1
VGF	0,44	Neurosecretory protein VGF
PCP4L1	0,44	Purkinje cell protein 4-like protein 1
VSNL1	0,45	Visinin-like protein 1
DLX6	0,45	Homeobox protein DLX-6
PLCXD3	0,46	PI-PLC X domain-containing protein 3
TOMM7	0,46	Mitochondrial import receptor subunit TOM7 homolog
LDB2	0,46	LIM domain-binding protein 2
ALK	0,46	ALK tyrosine kinase receptor
SLC8A1	0,46	Sodium/calcium exchanger 1

Figure 62. Volcano plot of whole cell proteome of CTIP2+ neurons day 45 purified via fluorescence activated cell sorting, fold change compared to Wt; genes highlighted in color are significant as fold change over 0.585 (1.5 fold) with p-value < 0.05. Red square marks APP (**A**), Proteomic analysis of CTIP2+ neurons of AT line revealed up- (left) and downregulated (right) genes relatively to Wt (**B**).

A

Gene	relative to Wt	Description
EOMES	2,76	Eomesodermin homolog
MAB21L1	2,64	Putative nucleotidyltransferase MAB21L1
CKB	2,58	Creatine kinase B-type (Fragment)
PRKCQ	2,25	Protein kinase C theta type
HNRNPD	2,25	Heterogeneous nuclear ribonucleoprotein D0 (Fragment)
NEUROD2	2,08	Neurogenic differentiation factor 2
RELN	1,94	Reelin
PCP4	1,89	Purkinje cell protein 4
UQCRB	1,87	Cytochrome b-c1 complex subunit 7
RIT2	1,86	GTP-binding protein Rit2
CALB1	1,77	Calbindin
TPBG	1,76	Trophoblast glycoprotein
ALDH1A1	1,76	Retinal dehydrogenase 1
KLHL14	1,73	Kelch-like protein 14
EBF2	1,73	Transcription factor COE2
TBR1	1,69	T-box brain protein 1
FEZF1	1,67	Fez family zinc finger protein 1
ALCAM	1,62	CD166 antigen
PGAM2	1,60	Phosphoglycerate mutase 2
KHDRBS2	1,60	KH domain-containing, RNA-binding, signal transduction-associated protein 2
EMX1	1,58	Homeobox protein EMX1
SLC25A36	1,55	Solute carrier family 25 member 36
NFIA	1,54	Nuclear factor 1
CACNA2D1	1,54	Voltage-dependent calcium channel subunit alpha-2/delta-1
LHX2	1,51	LIM/homeobox protein Lhx2

Gene	relative to Wt	Description
NT5C	0,39	5'(3')-deoxyribonucleotidase, cytosolic type
MRPL17	0,40	39S ribosomal protein L17, mitochondrial
MRPL41	0,40	39S ribosomal protein L41, mitochondrial
RBFOX2	0,41	RNA binding protein fox-1 homolog 2
TTC9C	0,42	Tetratricopeptide repeat protein 9C
COX6A1	0,44	Cytochrome c oxidase subunit 6A1, mitochondrial
MLLT11	0,50	Protein AF1q
SF3B5	0,50	Splicing factor 3B subunit 5
MIF	0,50	Macrophage migration inhibitory factor
GLIPR2	0,51	Golgi-associated plant pathogenesis-related protein 1
PLIN2	0,52	Perilipin-2
PNPO	0,52	Pyridoxine-5'-phosphate oxidase
GEMIN7	0,53	Gem-associated protein 7
SLIRP	0,54	SRA stem-loop-interacting RNA-binding protein, mitochondrial
MRPS7	0,54	28S ribosomal protein S7, mitochondrial
HSPB1	0,54	Heat shock protein beta-1
P4HA1	0,54	Prolyl 4-hydroxylase subunit alpha-1
FAM103A1	0,56	RNMT-activating mini protein
GAMT	0,57	Guanidinoacetate N-methyltransferase
DDT	0,58	D-dopachrome decarboxylase
RPA3	0,59	Replication protein A 14 kDa subunit
UBE2I	0,59	SUMO-conjugating enzyme UBC9
MRPS14	0,59	28S ribosomal protein S14, mitochondrial
LGALS1	0,59	Galectin-1
INO80C	0,59	INO80 complex subunit C

B

Gene	relative to Wt	Description
ZNF503	4,94	Zinc finger protein 503
NEFL	4,78	Neurofilament light polypeptide
TMSB4X	4,37	Thymosin beta-4
CPNE6	4,29	Copine-6
TMSB10	4,27	Thymosin beta-10
FOSL2	3,21	Fos-related antigen 2
EBF1	3,15	Transcription factor COE1
TPD52L1	2,93	Tumor protein D53
SAMSN1	2,92	SAM domain-containing protein SAMSN-1
FAT3	2,66	Protocadherin Fat 3
DUSP4	2,63	Dual specificity protein phosphatase 4
NRGN	2,62	Neurogranin
DBI	2,58	Acyl-CoA-binding protein
LDOC1	2,57	Protein LDOC1
BCL11A	2,49	B-cell lymphoma/leukemia 11A
ATP5J	2,42	ATP synthase-coupling factor 6, mitochondrial
TES	2,39	Testin
PCP4	2,33	Purkinje cell protein 4
STAMBPL1	2,33	AMSH-like protease
PEG10	2,28	HCG1642748, isoform CRA_b
RELN	2,27	Reelin
NEFM	2,26	Neurofilament medium polypeptide
DLG2	2,26	Disks large homolog 2
FOXP1	2,24	Forkhead box protein P1
RBP1	2,22	Retinol-binding protein 1

Gene	relative to Wt	Description
APP	0,08	Amyloid beta A4 protein
TXNRD2	0,23	Thioredoxin reductase 2, mitochondrial
MPPED1	0,34	Metallophosphoesterase domain-containing protein 1
RCN3	0,35	Reticulocalbin-3
NR2F2	0,36	COUP transcription factor 2
SNCB	0,37	Beta-synuclein
FEZF1	0,38	Fez family zinc finger protein 1
TKTL1	0,38	Transketolase-like protein 1
EOMES	0,38	Eomesodermin homolog
SYNPR	0,38	Synaptoporin
NR2F1	0,39	COUP transcription factor 1
IGSF8	0,40	Immunoglobulin superfamily member 8
HK2	0,40	Hexokinase-2
ALDH1L2	0,42	Mitochondrial 10-formyltetrahydrofolate dehydrogenase
SLC16A3	0,42	Monocarboxylate transporter 4
MAB21L1	0,43	Putative nucleotidyltransferase MAB21L1
TSPAN6	0,44	Tetraspanin-6
SLC38A10	0,44	Putative sodium-coupled neutral amino acid transporter 10
EMX1	0,45	Homeobox protein EMX1
FABP3	0,45	Fatty acid-binding protein, heart
PDXDC1	0,46	Pyridoxal-dependent decarboxylase domain-containing protein 1
P4HA1	0,46	Prolyl 4-hydroxylase subunit alpha-1
COMT	0,46	Catechol O-methyltransferase
SOX6	0,46	Transcription factor SOX-6
SYT13	0,47	Synaptotagmin-13

Figure 63. Proteomic analysis of purified CTIP2+ neurons revealed up- (left) and downregulated (right) genes for AV (**A**) and KO line (**B**) relative to Wt.

In order to unravel which of the given scenarios might be true, I next decided to do the proteomic analysis from non-purified populations. Again, hiPSCs were differentiated for 45 days, this time including the SWE and LON line and proteomic analysis was performed right post dissociation. More than 8700 different proteins were quantified (Figure 64). The results show that protein expression between the lines is more heterogenous when compared with the results obtained from the purified CTIP2+ population, but overall still very even.

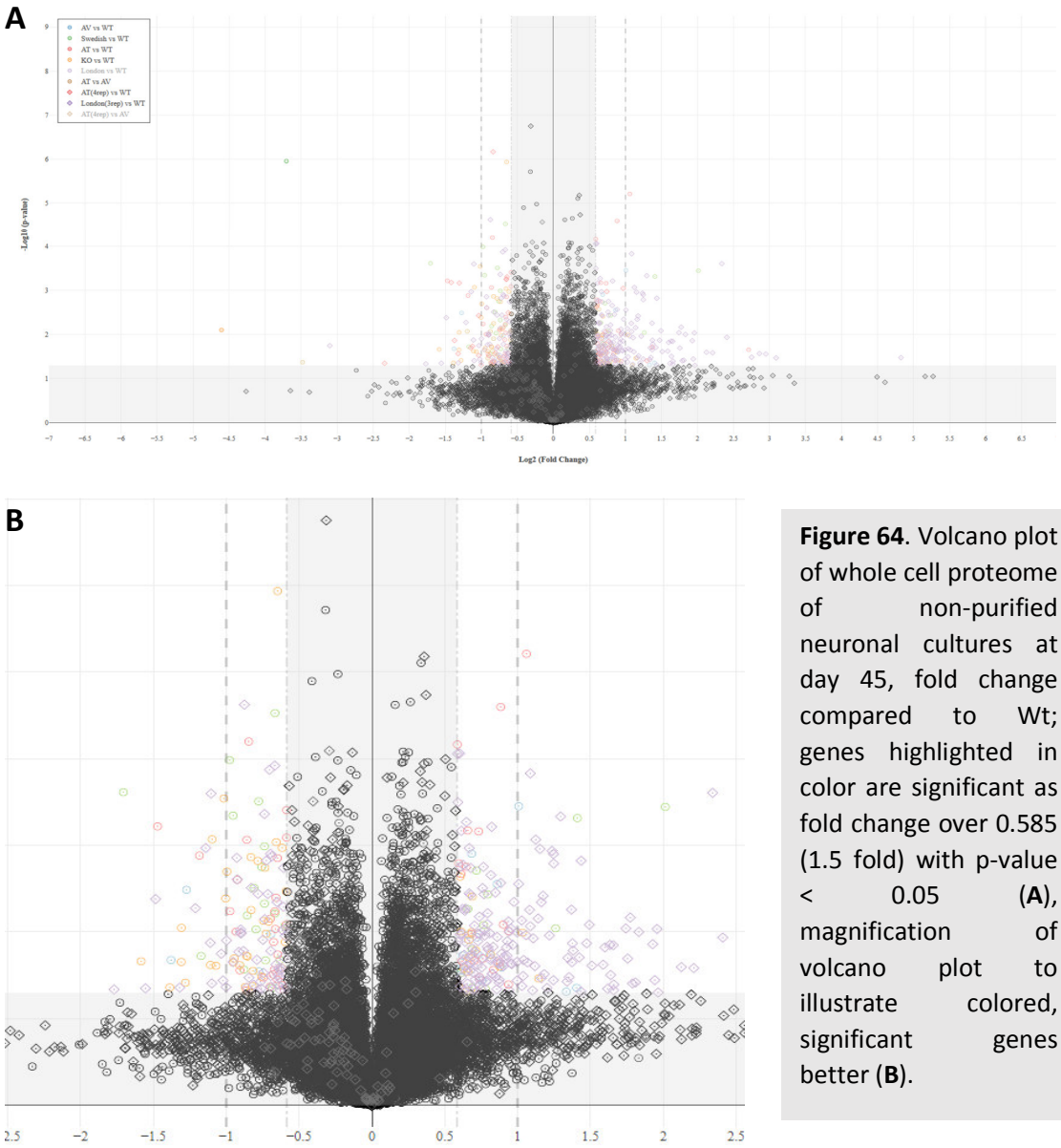

Figure 64. Volcano plot of whole cell proteome of non-purified neuronal cultures at day 45, fold change compared to Wt; genes highlighted in color are significant as fold change over 0.585 (1.5 fold) with p-value < 0.05 (**A**), magnification of volcano plot to illustrate colored, significant genes better (**B**).

First analysis of the raw data led to several genes statistically up- or downregulated in mutant lines compared to Wt (Figures 65 and 66).

A

Gene	relative to Wt	Description
BDNF	6,55	Brain-derived neurotrophic factor
CPNE6	2,09	Copine-6
PNPO	1,92	Pyridoxine-5'-phosphate oxidase
SPATA18	1,92	Mitochondria-eating protein
GNG8	1,87	Guanine nucleotide-binding protein G(I)/G(S)/G(O) subunit gamma-8
NQO1	1,85	NAD(P)H dehydrogenase [quinone] 1
CDK18	1,84	Cyclin-dependent kinase 18
CYP27A1	1,78	Sterol 26-hydroxylase, mitochondrial
HEBP1	1,70	Heme-binding protein 1
AK4; LOC100507855	1,67	Adenylate kinase 4, mitochondrial
CNTNAP3B	1,66	Contactin-associated protein-like 3B
MRPS14	1,63	28S ribosomal protein S14, mitochondrial
MRPL43	1,61	39S ribosomal protein L43, mitochondrial
CYB561	1,58	Cytochrome b561
SEC14L2	1,57	SEC14-like protein 2
GPRC5C	1,54	G-protein coupled receptor family C group 5 membe C
CALB1	1,53	Calbindin
AUH	1,51	Methylglutaconyl-CoA hydratase, mitochondrial
C3orf58	1,50	Deleted in autism protein 1

Gene	relative to Wt	Description
GPR98; ADGRV1	0,36	G-protein coupled receptor 98
EPHA3	0,44	Ephrin type-A receptor 3
SH3RF3	0,51	SH3 domain-containing RING finger protein 3
TYMS	0,52	Thymidylate synthase
DPP4	0,53	Dipeptidyl peptidase 4
SLC4A4	0,53	Electrogenic sodium bicarbonate cotransporter 1
GAS2L3	0,55	GAS2-like protein 3
SOX6	0,55	Transcription factor SOX-6
APP	0,56	Amyloid-beta A4 protein
AKAP5	0,60	A-kinase anchor protein 5
PDE1B	0,62	Calcium/calmodulin-dependent 3',5'-cyclic nucleotide phosphodiesterase 1B
STK39	0,62	STE20/SPS1-related proline-alanine-rich protein kinase
KIAA1211	0,62	Uncharacterized protein KIAA1211
ARX	0,63	Homeobox protein ARX
ELMO1	0,63	Engulfment and cell motility protein 1
CLVS2	0,63	Clavesin-2
ARHGEF26	0,63	Rho guanine nucleotide exchange factor 26
ZNF704	0,63	Zinc finger protein 704 =1
C1orf122	0,64	Uncharacterized protein C1orf122
PLEKHG3	0,64	Pleckstrin homology domain-containing family G member 3
JAM3	0,64	Junctional adhesion molecule C
CCDC88A	0,65	Girdin
GRM5	0,66	Metabotropic glutamate receptor 5
FAM125A; MVB12A	0,66	Multivesicular body subunit 12A
CPLX2	0,67	Complexin-2
ENOX1	0,67	Ecto-NOX disulfide-thiol exchanger 1

B

Gene	relative to Wt	Description
SPHKAP	2,65	A-kinase anchor protein SPHKAP
PCP4	2,52	Calmodulin regulator protein PCP4
PNPO	2,01	Pyridoxine-5'-phosphate oxidase
SF3B5	1,85	Splicing factor 3B subunit 5
TRMT112	1,82	Multifunctional methyltransferase subunit TRM112-like protein
CHRDL1	1,76	Chordin-like protein 1
CLU	1,69	Clusterin
ADCY2	1,66	Adenylate cyclase type 2
POMP	1,65	Proteasome maturation protein
RPA3	1,61	Replication protein A 14 kDa subunit
CDK2	1,59	Cyclin-dependent kinase 2
BMP7	1,54	Bone morphogenetic protein 7
FAM125A; MVB12A	1,52	Multivesicular body subunit 12A
IL1RAPL1	1,50	Interleukin-1 receptor accessory protein-like 1

Gene	relative to Wt	Description
EIF1	0,38	Eukaryotic translation initiation factor 1
SRP19	0,41	Signal recognition particle 19 kDa protein
RAP1GAP2	0,58	Rap1 GTPase-activating protein 2
GRIK3	0,62	Glutamate receptor ionotropic, kainate 3
SCAND1	0,64	SCAN domain-containing protein 1

C

Gene	relative to Wt	Description
THEM6	4,04	Thioesterase Superfamily Member 6
TTR	2,66	Transthyretin
WNT8B	2,40	Protein Wnt-8b
RPS26; RPS26P25; LOC101929876	1,74	40S ribosomal protein S26
PCP4	1,72	Calmodulin regulator protein PCP4
TXN2	1,70	Thioredoxin, mitochondrial
ALG8	1,64	Probable dolichyl pyrophosphate Glc1Man9GlcNAc2 alpha-1,3-glucosyltransferase
C12orf29	1,61	Uncharacterized protein C12orf29
DHFR; DHFRP1	1,61	Dihydrofolate reductase
NELL2	1,58	Protein kinase C-binding protein NELL2
FBLIM1	1,53	Filamin-binding LIM protein 1

Gene	relative to Wt	Description
TXNRD2	0,08	Thioredoxin reductase 2, mitochondrial
COMT	0,31	Catechol O-methyltransferase
EIF1	0,44	Eukaryotic translation initiation factor 1
CBR1; SETD4	0,51	Carbonyl reductase [NADPH] 1
S100A6	0,52	Protein S100-A6
SDHB	0,54	Succinate dehydrogenase [ubiquinone] iron-sulfur subunit, mitochondrial
ALG3	0,55	Dol-P-Man:Man(5)GlcNAc(2)-PP-Dol alpha-1,3-mannosyltransferase
SDHD	0,57	Succinate dehydrogenase [ubiquinone] cytochrome b small subunit, mitochondrial
C14orf159; DGLUCY	0,58	D-glutamate cyclase, mitochondrial
TARS2	0,58	Threonine--tRNA ligase, mitochondrial
LDHD	0,59	Probable D-lactate dehydrogenase, mitochondrial
ACSF2	0,60	Acyl-CoA synthetase family member 2, mitochondrial
SDHC	0,60	Succinate dehydrogenase cytochrome b560 subunit, mitochondrial
SRP19	0,60	Signal recognition particle 19 kDa protein
SPTY2D1	0,62	Protein SPT2 homolog
NLRP2	0,63	NACHT, LRR and PYD domains-containing protein 2
HIST1H1B	0,63	Histone H1.5
PSAP	0,65	Prosaposin
PLP1	0,66	Myelin proteolipid protein

Figure 65. Proteomic analysis of unsorted cortical neurons d45 revealed statistically significant up- (row 1) and downregulated (row 2) genes for AT (**A**), AV (**B**) and SWE line (**C**) relatively to Wt.

A

Gene	relative to Wt	Description
AQP1	28,33	Aquaporin-1
OCLN	8,52	Occludin
PPL	7,73	Periplakin
MYOF	7,26	Myoferlin
ANXA4	6,74	Annexin A4
ALDH1A1	5,31	Retinal dehydrogenase 1
APOE	5,06	Apolipoprotein E
LEPREL2; P3H3	4,63	Prolyl 3-hydroxylase 3
ANXA6	4,36	Annexin
PDLIM7	3,90	PDZ and LIM domain protein 7
TPD52L1	3,89	Tumor protein D53
AHNAK	3,84	Neuroblast differentiation-associated protein AHNAK
DSG2	3,81	Desmoglein-2
ANXA3	3,56	Annexin A3
SERINC5	3,51	Serine incorporator 5
WNT8B	3,46	Protein Wnt-8b
SNAP23	3,42	Synaptosomal-associated protein 23
P4HA2	3,38	Prolyl 4-hydroxylase subunit alpha-2
PODXL	3,35	Podocalyxin
MAN2A1	3,16	Alpha-mannosidase 2
ASS1	3,16	Argininosuccinate synthase
ARHGEF16	3,15	Rho guanine nucleotide exchange factor 16
GPX8	3,12	Probable glutathione peroxidase 8
METTL7A	3,11	Methyltransferase-like protein 7A
RTKN	3,07	Rhotekin
LGMN	3,03	Legumain
AK4; LOC100507855	3,01	Adenylate kinase 4, mitochondrial
UACA	2,85	Uveal autoantigen with coiled-coil domains and ankyrin repeats
PARP14	2,81	Poly [ADP-ribose] polymerase 14
ANXA11	2,78	Annexin A11

Gene	relative to Wt	Description
TAF9B	0,12	Transcription initiation factor TFIID subunit 9B
PLAT	0,29	Tissue-type plasminogen activator
ISLR2	0,34	Immunoglobulin superfamily containing leucine-rich repeat protein 2
EPHA3	0,36	Ephrin type-A receptor 3
ROBO1	0,40	Roundabout homolog 1
LIMCH1	0,43	LIM and calponin homology domains-containing protein 1
HIST1H1B	0,45	Histone H1.5
GPC2	0,46	Glypican-2
BANF1	0,47	Barrier-to-autointegration factor
FABP3	0,47	Fatty acid-binding protein, heart
HMGCS1	0,49	Hydroxymethylglutaryl-CoA synthase, cytoplasmic
MAOA	0,49	Amine oxidase [flavin-containing] A
GPR56; ADGRG1	0,50	Adhesion G-protein coupled receptor G1
OSTC	0,50	Oligosaccharyltransferase complex subunit OSTC
ARL2BP	0,52	ADP-ribosylation factor-like protein 2-binding protein
SYBU	0,53	Syntabulin
MAGED4; MAGED4B	0,53	Melanoma-associated antigen D4
ACTR3B	0,53	Actin-related protein 3B
HIST1H4A; HIST1H4F; HIST1H4D; HIST1H4J; HIST1H4H; HIST1H4C; HIST4H4; HIST2H4B; HIST1H4E; HIST1H4I; HIST1H4B; HIST2H4A; HIST1H4K; HIST1H4L	0,54	Histone H4
H3F3A; H3F3AP4; H3F3B	0,54	Histone H3.3
CNTFR	0,54	Ciliary neurotrophic factor receptor subunit alpha
RAB8B	0,54	Ras-related protein Rab-8B
GLTPD1; CPTP	0,55	Ceramide-1-phosphate transfer protein
ARL4D	0,55	ADP-ribosylation factor-like protein 4D
SUV420H2; KMT5C	0,56	Histone-lysine N-methyltransferase KMT5C
HINT1	0,56	Histidine triad nucleotide-binding protein 1
DFNA5; GSDME	0,57	Gasdermin-E
TSPYL1	0,58	Testis-specific Y-encoded-like protein 1
KLC1	0,58	Kinesin light chain 1
ITGA2	0,58	Integrin alpha-2

B

Gene	relative to Wt	Description
EPB41L3	2,21	Band 4.1-like protein 3
EPHA5	2,05	Ephrin type-A receptor 5
EPB41L3	1,84	Band 4.1-like protein 3
IL1RAPL1	1,76	Interleukin-1 receptor accessory protein-like 1
OTX1	1,66	Homeobox protein OTX1
C12orf29	1,64	Uncharacterized protein C12orf29
NR2F2	1,61	COUP transcription factor 2
NR2F1	1,61	COUP transcription factor 1
POMP	1,59	Proteasome maturation protein
GARNL3	1,59	GTPase-activating Rap/Ran-GAP domain-like protein 3
GRM5	1,58	Metabotropic glutamate receptor 5
GRIA3	1,57	Glutamate receptor 3
AKAP5	1,55	A-kinase anchor protein 5
HECW1	1,53	E3 ubiquitin-protein ligase HECW1
PID1	1,52	PTB-containing, cubilin and LRP1-interacting protein
HDAC9	1,51	Histone deacetylase 9

Gene	relative to Wt	Description
APP	0,04	Amyloid-beta A4 protein
SIX3	0,33	Homeobox protein SIX3
TH	0,38	Tyrosine 3-monooxygenase
PDE5A	0,40	cGMP-specific 3',5'-cyclic phosphodiesterase
DPPA4	0,40	Developmental pluripotency-associated protein 4
TXNRD2	0,41	Thioredoxin reductase 2, mitochondrial
CRYM	0,46	Ketimine reductase mu-crystallin
ZFHX3	0,47	Zinc finger homeobox protein 3
TRIM71	0,48	E3 ubiquitin-protein ligase TRIM71
MPPED2	0,49	Metallophosphoesterase MPPED2
RAB11FIP1	0,50	Rab11 family-interacting protein 1
GRIK3	0,50	Glutamate receptor ionotropic, kainate 3
DPYD	0,52	Dihydropyrimidine dehydrogenase [NADP(+)]
MXRA7	0,52	Matrix-remodeling-associated protein 7
SYNM	0,53	Synemin
CXXC4	0,55	CXXC-type zinc finger protein 4
GPRC5C	0,55	G-protein coupled receptor family C group 5 member
RCN3	0,55	Reticulocalbin-3
CYP2S1	0,56	Cytochrome P450 2S1
RAB11FIP2	0,56	VPS10 domain-containing receptor SorCS1
GRIK4	0,56	E3 ubiquitin-protein ligase TRIM22
DPYD	0,57	Forkhead box protein P2
MXRA8	0,57	NADH-cytochrome b5 reductase 2
SYNM	0,58	Barrier-to-autointegration factor
CXXC5	0,59	Low-density lipoprotein receptor-related protein 2
GPRC5C	0,60	Catechol O-methyltransferase
RCN4	0,60	Copine-6
CYP2S2	0,60	Tropomyosin alpha-1 chain
RAB11FIP3	0,61	Zinc finger homeobox protein 4
GRIK5	0,63	L-lactate dehydrogenase A chain
DPYD	0,64	Transcription factor BTF3
MXRA9	0,65	Teashirt homolog 1
SYNM	0,65	Glutaminase kidney isoform, mitochondrial
CXXC6	0,66	Actin-related protein 2/3 complex subunit 1B
GPRC5C	0,66	BAG family molecular chaperone regulator 3

Figure 66. Proteomic analysis of unsorted cortical neurons d45 revealed statistically significant up- (row 1) and downregulated (row 2) genes for LON (**A**) and KO line (**B**) relatively to Wt.

The listed up- or down regulated genes represent just preliminary data and even though it is very tempting to go through the data and look for patterns and potential candidates involved in fAD pathology, generating the list of significant up- or downregulated genes has just been the first step in analyzing the immense data sets. Nonetheless, certain things seem to be obvious even by just touching the surface of the data.

One gene consistently downregulated in purified and unpurified cells of the fAD lines and the KO line, but upregulated in the protective AT line is Thioredoxin reductase 2 (TXNRD2) (Figure 67). TXNRD2 is a mitochondrial protein necessary for reducing reactive oxygen species generated by oxidative phosphorylation and other mitochondrial functions. Oxidative stress has been linked to neuronal cell death and certain neurodegenerative diseases like PD or AD before (Andersen, 2004; Huang et al., 2016; Sultana and Butterfield, 2010), which is caused by an imbalance of oxidants and antioxidants in favor of the former, termed reactive oxygen species (ROS). However, TRNXD2, binds substrates via its active selenocysteine and reduces thioredoxins as well as other substrates, therefore playing a key role in redox homeostasis. Upregulation of TXNDR2 might be directly correlated with increased scavenging of ROS in mitochondria, decreased oxidative stress levels and increased neuronal survival. protection of mitochondria and oxidative stress.

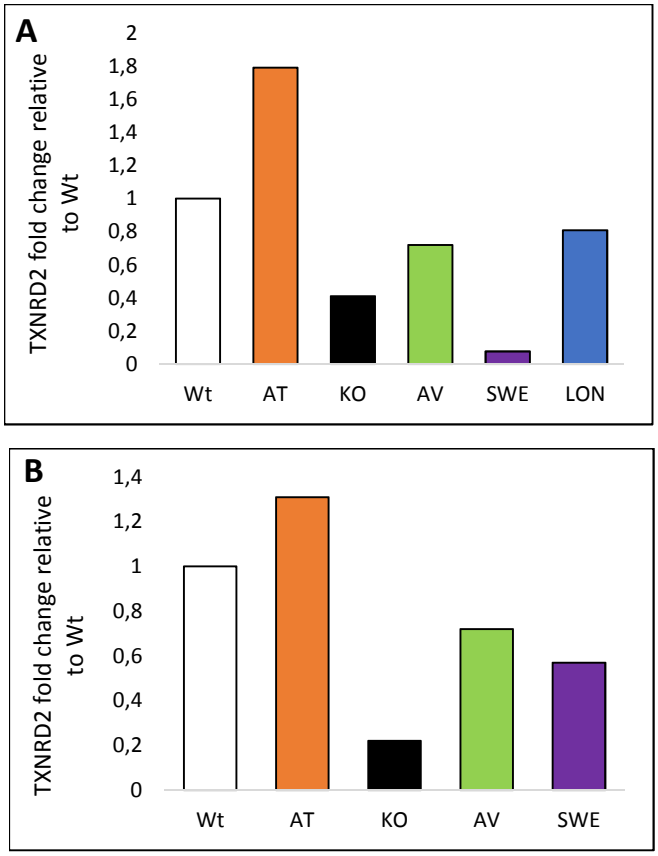

Figure 67. Proteomic analysis of unsorted (**A**) and sorted cortical neurons (**B**) revealed that TXNRD2 is upregulated in the protective AT line, but down-regulated in the fAD and the KO line as well.

The theory of potentially increased oxidative stress and decreased mitochondrial function in the negative fAD lines and a protective effect caused by the AT mutation is indeed supported by the data presented in Figures 65 and 66. Several mitochondria related genes are downregulated in the negative mutation lines like Succinate Dehydrogenase Complex Subunit C (SDHC), one of the key enzymes of the mitochondrial complex II, which is crucial complex of the tricarboxylic acid cycle and respiratory chains of mitochondria, whereas Spermatogenesis Associated 18 (SPATA18), a gene known as “Mitochondria-eating protein”, which is a key regulator in mitochondria quality control by repairing or degrading unhealthy mitochondria, is 2-fold upregulated in the AT.

However, while the influence of oxidative stress and mitochondria damage in fAD seems to be an interesting avenue to continue, deeper investigation is needed including pathway analysis for all the discovered up- and downregulated proteins to fully interpret the data and to be able to make final conclusions. Additionally, I will also analyze protein expression levels of genes already associated with fAD pathology, as well as other proteins that are upregulated, but which are not shown in the Figures yet, because in the first preliminary analysis I focused on proteins with a fold change higher than 1.5. Solid data analysis will hopefully reveal involved pathways in fAD and most importantly more candidate genes that might be potential drug targets.

4.10 InDrop and scRNAseq

The results of the proteomic analysis revealed some interesting candidate genes that I will investigate further to unravel their potential involvement in fAD pathology. They also let me postulate that the generated fAD model is truly isogenic, which is why the expression of genes across all lines is even more homogenous than I expected. I wanted to perform the proteomic analysis with populations of the isogenic lines, which are most affected by the disease, because I postulated that their increased vulnerability would result in very distinct proteomic profiles, but also because it would be the most appropriate cell type to be used for drug screenings. Until the last proteomic experiment is completed and the data is completely analyzed, I will not be able to make further conclusions about potential masking effects caused by the Fac sorting, so in the meantime I wanted to expand the search for the population of cells that is most affected by the fAD mutations.

One way of doing this could have been to target all isogenic lines with different reporters, each of them very specific for a neuronal cell-type, fac-sort them to purify them and repeat the proteomics until I see significant differences in protein expression between the lines. Implementing this approach would have required an almost unlimited amount of time. I decided to take advantage of another option, which is still time-consuming, but more realistic for this purpose. I employed single-cell technology (SCT) to profile the transcriptome of single cells of every cell line of this isogenic model. SCT has the advantage that it can unmasked molecular changes and transcriptomic effects in very specific cell types, that otherwise could not be seen by using proteomics even with CTIP2+ FAC-sorted neurons or normal bulk sequencing techniques. Still it takes a long time to plan, carry out and then analyze the huge raw data set appropriately, which can take easily months by itself. Even if the experiment is still ongoing, I would like to present recent progress that has been made so far. I differentiated all isogenic lines into cortical neurons and freshly dissociated neurons at day 45 were barcoded on a single-cell level using droplet microfluids. The libraries were created as previously described (Zilionis et al., 2017) for each line and a total of 3000 single cells were employed to unbiased high-throughput single-cell RNA sequencing (scRNA-seq). First, quality control of all samples was performed to assure that the generated data via sequencing is of high quality. In a second step the number of genes detected per cell was calculated and despite the SWE samples showed less detected genes per cell compared with the other lines, all of them passed the cut-off of 500 genes per cell and could be included in further analysis (Figure 68).

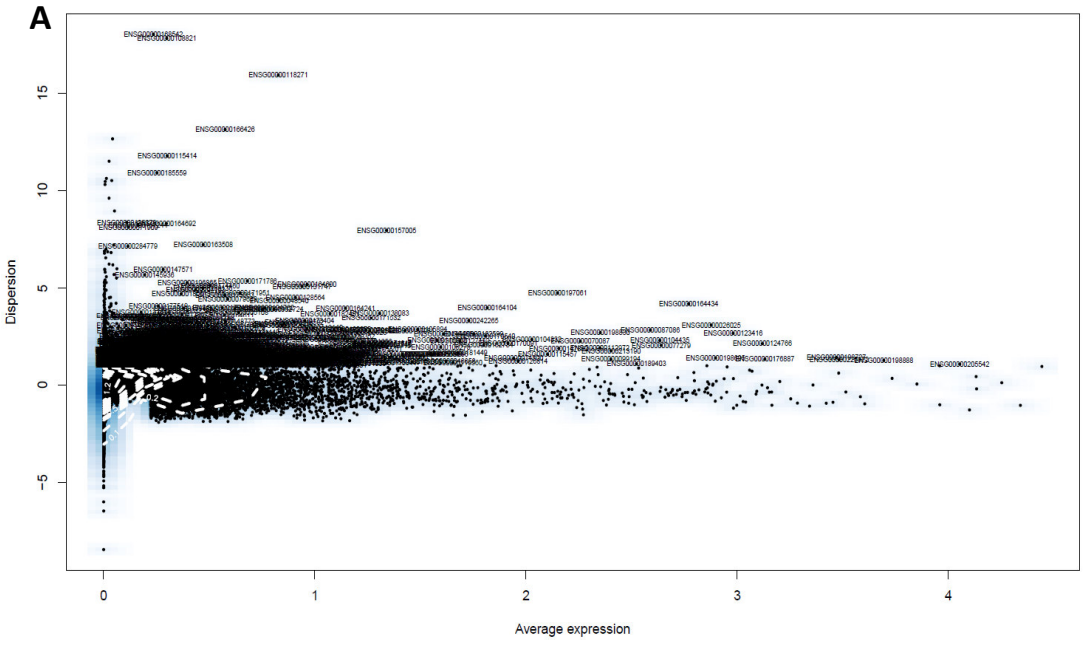

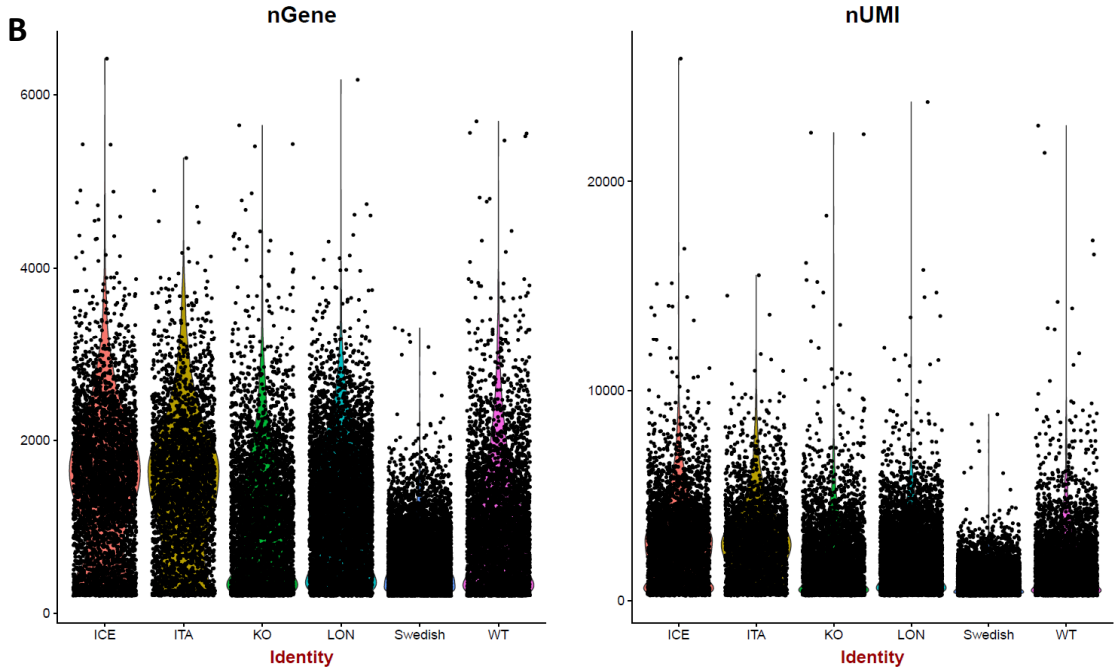

Figure 68. Detection of variable genes across single cells in the form of a dispersion plot (**A**), Violin with Scatter Plot overlay depicting the number of genes detected per cell in a given sample. SWE line shows lower number of genes per cell compared to other lines, but still enough to pass the quality cut-off (**B**).

For the last step of the quality control and also for the beginning of the analysis I used a graph-based clustering approach, in which cells with similar transcription profiles aggregate. I excluded clusters that seem to be of dead cells, low quality or debris. I finally ended up with 15,427 cells, post quality control and the clustering approach showed 5 different cell populations, each of them identified by the expression of well-known marker genes for the specific cell-types, which is visualized via t-distributed stochastic neighbor embedding (tSNE) projection. Interestingly, besides four big clusters a small, very stringent cluster (Figure 69) could be detected as well.

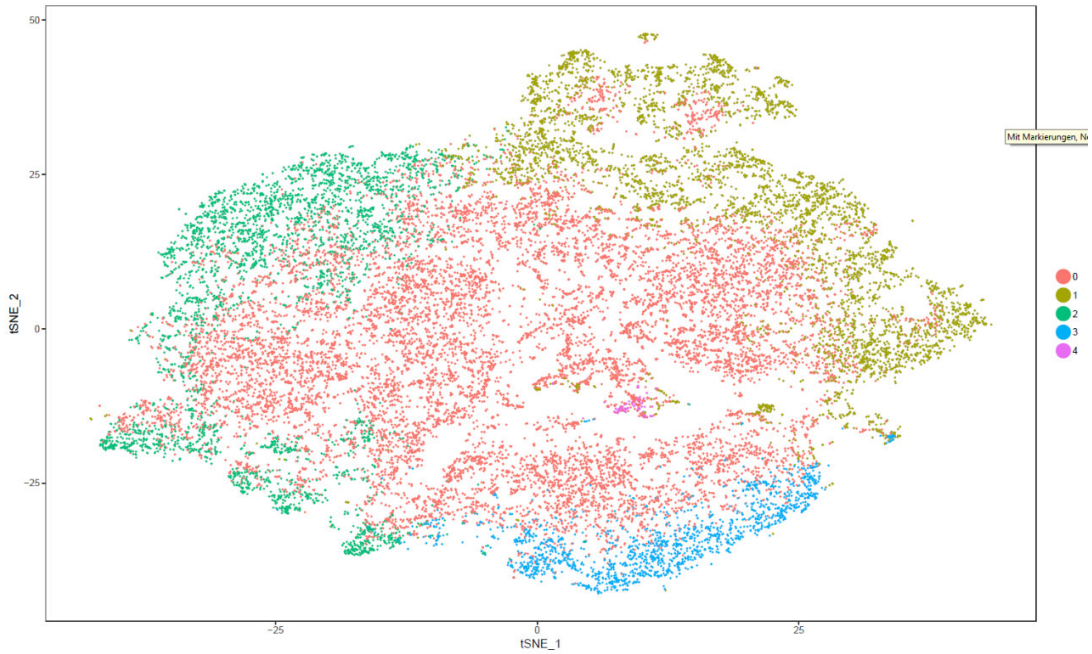

Figure 69. tSNE plot of single cells assigned to candidate clusters using PCA dimensional reduction incorporating the first 15 principal components with a perplexity of 30, resulting in 4 big clusters, and 1 very small cluster marked by yellow arrow.

So, in a first step, I was able to point out that I do have different population of cells within the differentiated cortical lines, in a second step I applied the same principal component analysis (PCA) again, but this time I used a tSNE plot clustered as described for Figure 69 and color coded based on sample. The result is very interesting. As visualized in Figure 70, a few cells of each line can be found in each of the clusters, however, each line seems to have the majority of their cells in only 1 or maybe 2 out of the five clusters. The cells of the AT are mostly present in cluster number 3 and also account almost solely for cluster number 4, which could be very exciting. The Wt is most present in cluster number 2 and cluster 0. The negative mutations also distribute differently. Whereas the SWE line is most present in cluster 0 and 1, the LON line is in cluster 2 and the AV is present in cluster 0, 1 and 2. The sequencing data gives us different options now. First, we can figure out, what the transcriptomic profile is of the cells belonging to one cluster. By looking for expression of cell type specific marker genes, I will be able to define the 5 different populations or sub-populations in more detail (Figure 70). Determining the distinct populations enables us to quantify the percentage of cell of all lines that are present, less present or not present at all in each population of cells. If the Wt, AT and maybe even the KO appear in cluster number 2, but AV, SWE and LON do not, it would be very likely that I found the special sub-population of cells, where

cells carrying fAD mutations are most vulnerable, probably because it is the subset of cells most affected by fAD pathology.

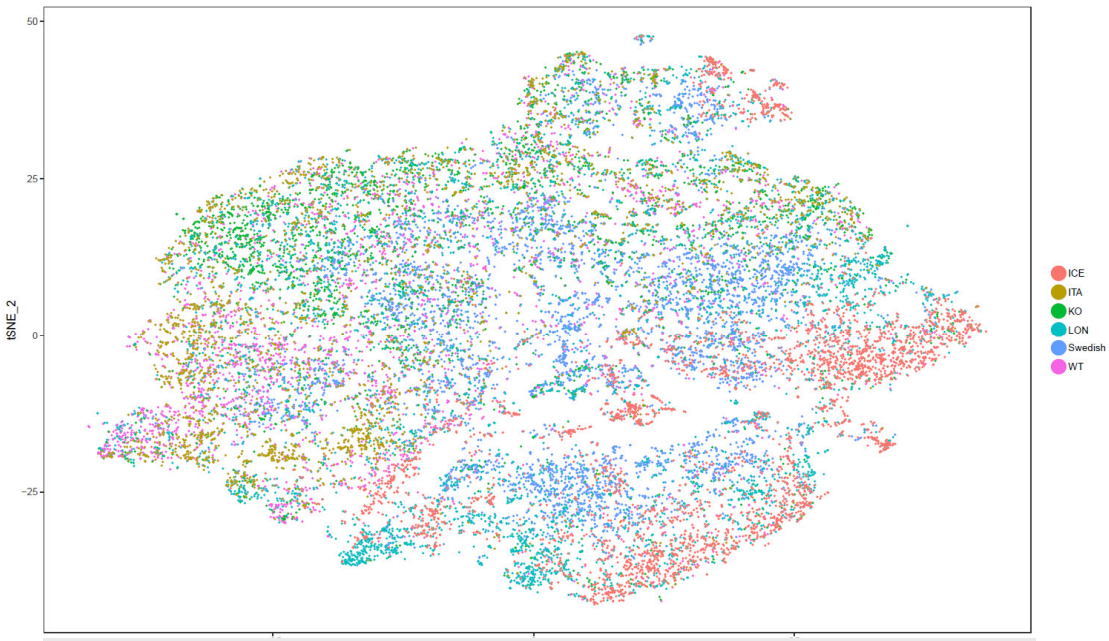

Figure 70. tSNE plot color coded based on sample.

Besides analyzing the single clusters, I also do have the option now to choose from identified genes in the whole population and overlay them on the created cluster plot. Figure 72 shows APP expression in all analyzed samples, ranging from very strong expressed (red) to very poorly expressed (light yellow). As we can see APP is randomly highly expressed, but most abundant in an area where cluster 2 and cluster 0 overlap. Figure 71 shows, that it is the Wt line which accounts for the majority of cell clustered in that region of the tSNE plot. That data confirms the results obtained from WBs and IF which showed that Wt cells express higher levels of APP compared with any other line and is a perfect proof of principle for the scRNA seq experiment. I will have to analyze the data further to make more conclusions from here on though.

The generated scRNAseq data provides great value and will enable me to investigate not only single gene expression across the whole population, but also among specific clusters (Figure 72) or most importantly to run a comparative analysis to identify transcripts highly upregulate or downregulated between fAD lines and Wt, AT and KO lines the isogenic lines, like visualized in Figures 73 and 74, that display expression levels of six randomly chosen genes in the isogenic lines.

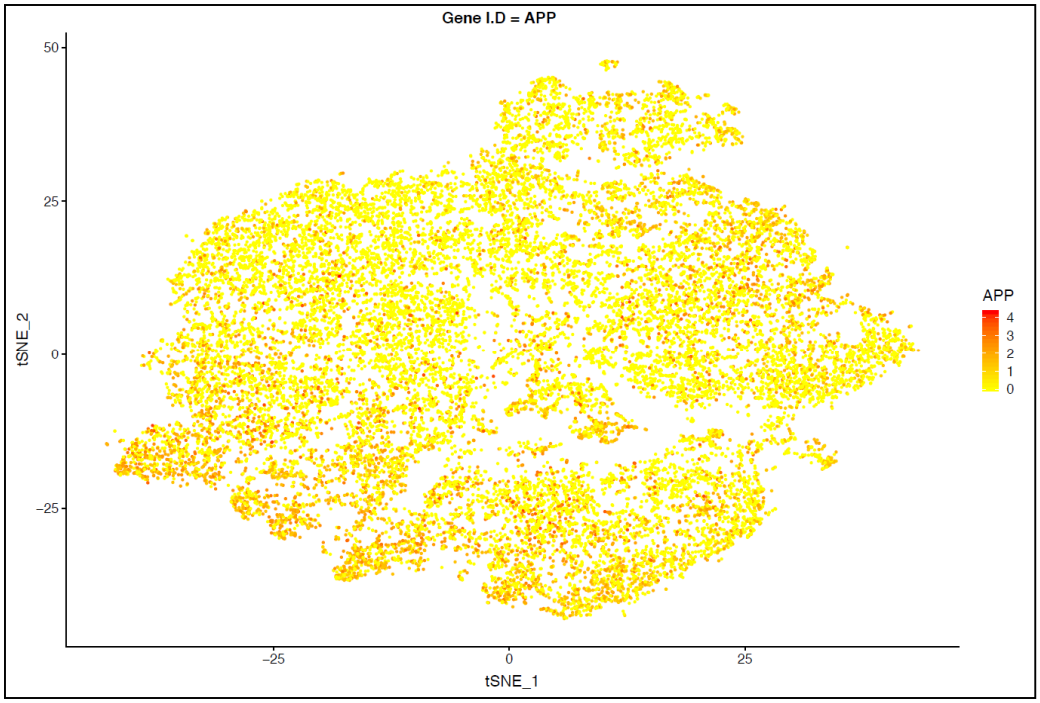

Figure 71. APP expression for a given cell overlaid on tSNE plot clusters. Expression gradient range depicts high expression in Red and low expression in Yellow.

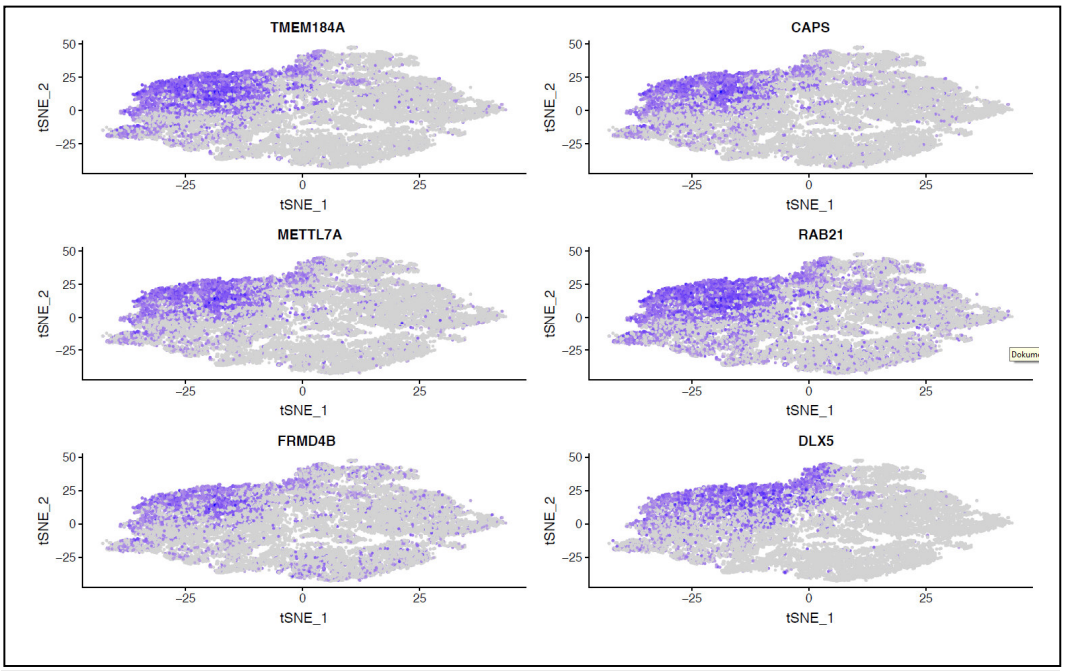

Figure 72. Ridge Plots depicting single cell expression distributions across each sample for genes that specific Cluster 2 and are upregulated > 2 fold.

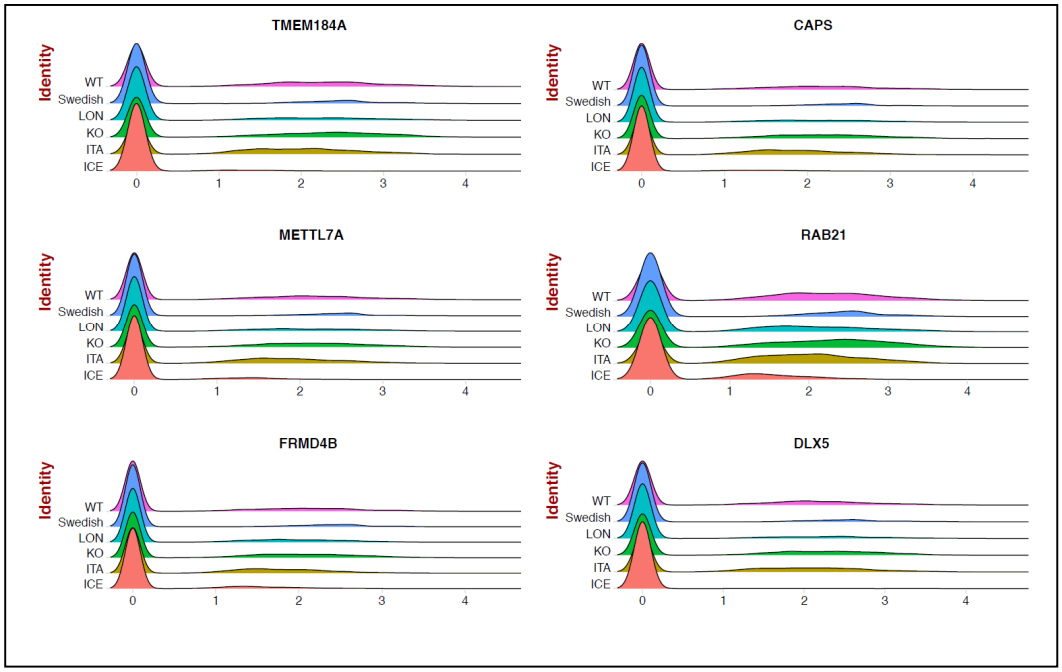

Figure 73. Expression at the single cell level of Cluster 2 markers overlaid on a tSNE plot, 6 genes randomly chosen.

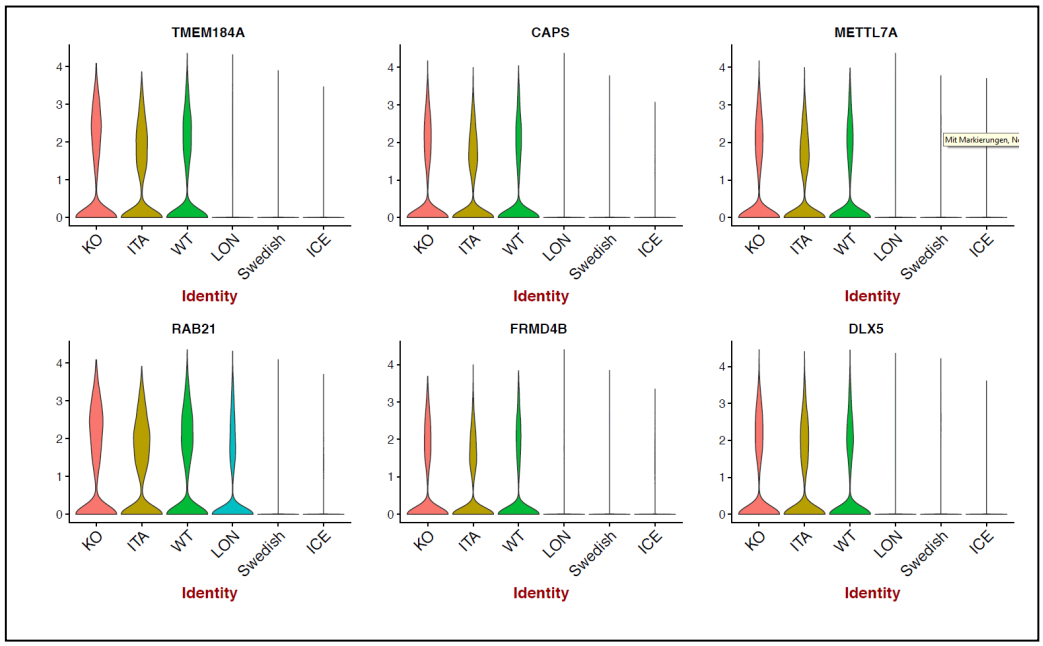

Figure 74. Violin Plots depicting single cell expression distributions across each sample for genes specific for Cluster 2 and are upregulated > 2 fold. Shape of Violin plot is scaled proportional to the number of cells within a given sample.

Discussion

Generation of isogenic lines

I was able to generate an **isogenic hiPSC model for familial Alzheimer's disease** and it is the first time that a model consisting of this combination and scope of these lines has been reported so far, regardless of whether in an isogenic or a non-isogenic context. While a few models for AD using iPSCs have been created by other groups, most of them used patient derived hiPSC lines from familial or sporadic patients (Israel et al., 2012; Kondo et al., 2013; Moore et al., 2015; Muratore et al., 2014) and only one group reported the use of fAD neurons in an isogenic context, however the group used commercially available pre-made neurons (Cellular Dynamics International Inc) (Maloney et al., 2014).

Besides two lines carrying mutations that are fully penetrant and that are highly associated with the early onset form of the disease (AV, SWE respectively), I further generated a line carrying a mutation that was first found in the Icelandic population and that is supposed to be protective against the disease (AT). As these three mutations do all appear in the gene *APP* I expanded the model by creating an APP knock-out line (KO) to be able to investigate the phenotype in a hiPSC line lacking that crucial protein compared with the mutant lines and the wildtype line. The crucial feature of this model is being isogenic, because line-to-line variations and genetic variabilities always existing in disease models based on hiPSC lines derived from patients don't exist and can be excluded. Therefore, this model allows me to study the impact and the consequences of the chosen negative and protective mutations in APP in a very precise way. Whatever changes between lines are observed during any of the conducted experiments, they can clearly and solely be attributed to the introduced mutations the lines differ from each other.
Importantly, I was able to show that no chromosomal abnormalities resulted from the genome editing procedures in all isogenic lines (Figure 21).

The generation of the isogenic knock-in lines, which provide undoubtedly the backbone of this thesis, was only possible after making certain changes in the targeting strategies and the involved CRISPR-CAS9 system. When I started this work several groups reported efficient genome editing in murine cells, zebrafish and other organisms, using the novel CRISPR-CAS9 system in combination with single-stranded-oligos (ssOligos), which will be used as a template during homologous recombination (HR) to introduce mutations of interest (Schwank et al., 2013; Zhao et

al., 2014). Despite immense effort I had to realize that after several rounds of targeting attempt, the frequency of successful homozygous targeted clones was below 0.1 % as only 2 clones out of 2.300 colonies were carrying the new mutation. The huge disadvantage of this targeting strategy was that by the time the gRNA and CAS9 from the px330-nGFP were expressed, the ssOligos added during the nucleofection, were already degraded and therefore no template available to stimulate HR. The new approach, using a two-vector system to generate the knock-in lines overcomes the issue as gRNA, CAS9 and HR-template are now expressed simultaneously and by the time the DSB is created the template is still expressed. Another important improvement in targeting-efficiency was to do antibiotic selection for at least 7 days. The plasmid expressing the template for HR consists of an antibiotic resistance cassette. Unfortunately, short periods of antibiotic selection for up to 48h can result in false-positive clones, because cells might survive not because the vector integrated into their genome, but due to episomal activity of it. After implementing these changes, the targeting efficiency for knock-in's increased to 4-11% of all clones picked post antibiotic selection (data not shown), whereas targeting efficiency to generate the knock-out was higher from the beginning (8-15%), as solely two px33-nGFP plasmids expressing CAS9 and two different gRNAs were used.

The CRISPR-CAS9 has been shown to be an effective tool to edit the genome of hiPSCs and the programmable nuclease CAS9 can be directed to the targeting site *in vitro* and it cuts in general very precisely and like predicted 3 to 4 nucleotides upstream of the PAM sequences. However, certain risks remain and therefore researchers have to cautious. In some cases I noticed that additional DSBs were created further upstream or downstream of the targeting site resulting in unwanted frameshifts in one or both alleles during knock-in mutagenesis (data not shown). Therefore, analyzing the exons and introns close to the original targeting site is highly recommended. Furthermore, it is highly recommended to choose gRNAs that don't have many off-target binding-sites, to reduce the risks of crating mutations far up- or downstream the originally target-site. Nowadays, off-target effects can be calculate and predicted based on the gRNA sequence chosen and tools to do so are available online (http://crispr.mit.edu/; https://crispr.ml/). Lastly, it is recommended to karyotype the generated cell lines to make sure, that no chromosomal abnormalities resulted from the genome editing.

Characterization of isogenic AD iPSC lines

The characterization of the isogenic lines is a crucial part of this work and represents the first time that (isogenic) hiPSC lines carrying fAD mutations as well as protective and knock-out line have been described and analyzed in a pluripotent state. Most studies focused on characterization of already terminally differentiated cells generated from patient derived lines or while being differentiated (find sources). Starting in an iPS state might be very important in a regenerative disease like AD, because we know that the disease pathology in humans starts 10 to 20 years before onset of symptoms and clinical trials have suggested that post-symptomatic treatment might be ineffective (source and example). Early characterization even in undifferentiated cells therefore might help us in contributing to the big question: Is it possible to find early sign of disease onset?

IHC for pluripotency markers revealed that all isogenic lines remained their potential to be pluripotent as measured values for OCT4 and Sox2 were comparable high across lines. This indicates that neither the introduced mutations or APP knock-out impact the lines' capability to be pluripotent directly or indirectly, especially I was able to show that even in a pluripotent state AV and SWE already produce much more Aβ, compared to Wt and AT (Figure 31). Further it shows that the complex genome editing I applied to all of the lines except Wt, did not lead to unwanted off-target effects in genes required to remain pluripotency.

An interesting avenue has opened up based on the results of the performed proliferation assay of all lines. The results clearly show that KO and protective AT line proliferate faster than Wt and especially than both lines carrying the fAD mutations (Figure 25 B). The convincing results generated via ATP-monitoring luminescence assay and confirmed via regular EDU staining clearly show that more cells are in S-Phase, whereas the IF assay for mitotic marker pH3 and Ki67 let us conclude, that AT and KO do have a shorter mitotic phase. These results are very interesting to follow up. So far it has been reported that sAPPα is able to stimulate proliferation in human neural precursor cells and that it acts in an epidermal growth factor (EGF)- and basic fibroblast growth factor (bFGF) independent way (Demars et al., 2011). However, it has not been linked with increased proliferation rates in an iPS state so far. Further, based on the results I postulate that we are dealing with two different phenomena here. While sAPPα is definitely increased in the AT line due to preferred proteolytic cleavage of α-secretase and seems to stimulate proliferation, I postulate that Aβ, or one the peptides generated after cleavage of β-secretase, sAPPβ or CTF-99 respectively, may also be considered to impair the proliferation rate in contrasting way. Little is known about how these peptides might influence proliferation and published reports have mostly

been using murine neural precursor cells and results have been inconsistent (Donovan et al., 2006; Haughey et al., 2002; Jin et al., 2004).

As the proliferation is increased in the KO line, it points into the direction that absence of APP and therefore sAPPα, sAPPβ, CTF-99 and Aβ itself leads to an increase in proliferation, an increase higher than the one caused by elevated sAPPα levels in the AT line. Hence, I hypothesize that the influence of one of the peptides generated by β-secretase mediated cleavage is stronger than the one caused by sAPPα. That would explain why the proliferation of AT is still lower than the one seen in the KO line, because sAPPα is at least partially able to compensate for the decrease in proliferation although not fully. This pathway seems to be very interesting for us to investigate more deeply, and especially as we can see the difference in proliferation even in a pluripotent state, it allows us to proceed fast with further experiments.

Characterization of the isogenic AD iPSC-derived cortical neurons

The characterization of the cortical neurons, analyzed via high-throughput imaging, revealed interesting findings about the lines and also the differentiated neurons. First, all lines differentiated successful into cortical neurons, which is a crucial step in disease modeling using hiPSCs. If the cells are unable to differentiate into the cell type most affected by the disease one is trying to build a model for, the experiment will not be able to generate any reliable data at all. By confirming the neuronal identity of our cells via MAP2+ IF and the cortical identity via CTIP2+ IF, it was made sure that this important step in hiPSC disease modeling was passed. Interestingly a huge difference in the percentage of MAP2+ cells between Wt, AT, KO and fAD lines was detected which remained over the analyzed period of 12 days. Whereas the percentages for the first two remained constant and only slightly decreased for the KO line over the time-course, the number of MAP2+ cells for both fAD lines was already much lower at day 3 and decreased again by day 9. This phenomenon points out that neurons of both lines, AV and SWE are more prone to die, because they seem to be more vulnerable, a hypothesis that is strongly supported by the data generated from the live-imaging experiment (Figures 49 and 50) as well. In the live-imaging experiment a difference in survival between fAD lines and especially the AT line became more obvious after 75 to 85 hours in the control condition, and even more evident in the conditions that included stressors. The live-imaging data therefore aligns very well with the data shown in Figure 27B, because selective vulnerability for neurons of the fAD lines might explain the decrease in MAP2+ cells after 3 days already compared to Wt and AT. Unfortunately, the second decrease at day 9 was not observed by the live-imaging experiment, because it was stopped after 6 days (138 hours).

There many reasons why the fAD lines could be more vulnerable, given the toxic effects increased levels of Aβ itself have, but also the ones it initiates downstream. Analyzing the selective vulnerability for MAP2+ and CTIP2+ neurons carrying the familial AD mutations will be conducted in the future and hopefully the results from the experiments introduced in aim 3 will provide some hints, which pathways and which genes are involved in mediating this vulnerability. Using this data as input would allow us to screen for small molecules that bring back the survival rates to levels similar to Wt and AT.

Interesting results could also be obtained regarding APP and pTAU levels in our differentiated and dissociated cultures. There is clearly a constant increase in APP over time, detected via high-throughput imaging. Increases of APP in a time-dependent manner have been reported by other groups (Muratore et al., 2014). Additionally, there is clearly more APP in the Wt line compared with others at all time-points measured, which was measured via high-throughput imaging as well as confocal microscopy (Figure 28). Two different scenarios are possible: One option could be that APP is decreased in the mutated lines, because APP is cleaved more often by APP cleaving secretases, AT preferentially by α-secretase, AV mostly by β-secretase, which is what I expect to happen. The other option could be that the mature full lengths APP undergoes lysosomal-dependent degradation more rapidly in the mutated lines mediated by the SNPs. One group using patient derived iPSCs has observed the same phenomenon and they hypothesized that fAD mutations in APP could result in a direct transport of a significant portion of the protein to the lysosome for degradation instead of being transported to the cell-surface (Zhang et al., 2017). However, based on the results in section x of this work, I would postulate that the decrease in the mutated lines is at least partially due to increased secretase activity, as treatment with β-inhibitors resulted in increased APP levels in the AV line, shown via IF, and results obtained from WBs showed that the levels even exceeded the amount of APP observed in the Wt. Further experiments are needed to make more solid conclusions of these results and to determine the impact of the lysosomal-degradation pathway as well as the activity of the secretases. Treatment of cultures with lysosomal inhibitors like CHL and proteasomal inhibitors like MG132 could reveal the impact of the lysosomal-degradation pathway. On the other hand, biochemical studies could be used to investigate the affinity of the secretases using mutated APP as a substrate, but also define the catalytic turnover rates (*Vmax*) to shed light on the question, if reduction in APP levels are the consequence of increased enzymatic activity or increased lysosomal degradation.

Increases in APP levels over time were accompanied by increases in pTAU in our differentiated lines as well. Even thoug the AV and SWE lines showed high levels of pTAU at early timepoints compared to Wt, AT and KO, interestingly the increases of pTAU measured in all lines at later timepoints were stronger in the Wt and especially in the AT. Usually pTAU is associated with a toxic phenotype, as NFTs consisting of pTAU are one of the hallmarks that can be found in the human brain tissue of diseased people post mortem (Gomez-Isla et al., 1997). However, the results here indicate that phosphorylation of TAU can also have a cyto-protective function. The antibody I used for this experiment recognizes phosphorylation of TAU at two different residues, Serine^{202} (S202) and Threonine^{205} (T205). Like described earlier in the chapters 4.3 and 4.5, one recent report has shown that phosphorylation excatly at these residues can be neuroprotective by decreasing Aβ induced excitotoxicity and spine loss (Ittner et al., 2016). Aβ induced excitotoxicity can be mediated in different ways, one of them is via PSD95-fynKinase-TAU-NMDA receptor interaction, and TAU usually directly interacts with fyn. If TAU gets phosphorylated at T205 by mitogen activated kinase p38γ fyn dissociates from TAU resulting in dissociation of the whole excitotoxic complex. Increased phosphorylation at T205 would explain the high levels in the protective and the Wt line. Further IF using ABs targeting different phosphorylated residues on TAU like PHF1, directed against Serine^{396} and Serine^{404} will be used to test this hypothesis. If elevated pTAU levels in AT and Wt are mostly due to protective phosphorylation of T205, lower intensity for ABs like PHF1 should be observed.

However, as pTAU levels increase over time as well as levels of APP, a direct link between these two key proteins in AD, reported by several groups (Kristofikova et al., 2014; Nisbet et al., 2015; Zheng et al., 2002), is also indicated in our *in vitro* model, which points out again, that it is fully capable to recapitulate important mechanims of AD pathology. Importantly, as the KO lines displays the lowest Tau phosphorylation at the residues studied, it not only shows that TAU gets phosphorylated at specific residues even in the absense of APP, but it seems to indicate that in the presense of APP, Tau phosphorylation happens downstream of APP and its metabolites, which confirms the amyloid-beta-hypothesis (Hardy and Allsop, 1991).

Western Blots results

Analysis of the lysates extracted at different time-points after dissociation of the cortical neurons confirmed some of the results I was able to detect via IF before, but also revealed some

new insights. The results showed a constant increase of APP over time in all isogenic lines (except KO) as well constant increases of pTAU in both lines carrying mutations associated with familial AD (AV, SWE, respectively).

The most important finding coming out of these experiments is that I was able to directly link Aβ production to pTAU levels in our neuronal cultures. Treatment with the β-secretase inhibitor Bace-1 resulted in decreased pTAU levels after only 12 days in culture, which were strongest in AV and Wt (Figure 42). Therefore the results prove the amyloid-beta-hypothesis as they confirm that pTAU is acting downstream of Aβ (Selkoe and Hardy, 2016). They also demonstrate that the isogenic AD system is highly amenable to treatments, which highlights its importance for its use in the bear future as a potential screening platform to look for small molecules that might be able to modify AD pathology.

Further, the results support the hypothesis that phosphorylation of pTAU at Ser^{202}, Thr^{205} can be protective by preventing hyper-excitotoxicity (Ittner et al., 2016). I postulate that phosphorylation of TAU at these residues does happen in an Aβ independent mechanism, which is supported by the findings of the AT line, which shows higher levels of pTAU compared to Wt, but only subtle decrease of pTAU after treatment with Bace-1, therefore indicating that a big part of the high basal levels are not the cause mediated by toxic Aβ, but the consequence of TAU being phosphorylated by p38γ to reduce toxicity.

Another important finding was that the γ-secretase inhibitor DAPT seems to increase pTAU levels in all lines. As DAPT prevents cleavage of either CTF C99 or CTF C83, which are the resulting peptides after APP has been cleaved by either β- or α-secretase respectively, it indicates that phosphorylation of TAU can also be regulated with a mechanism that acts independently of Aβ. That hypothesis is supported by the fact that Bace-1 decreased pTAU levels whereas treatment with DAPT did not, although both prevent Aβ-, but only the former prevents CTF C99 generation. The CTF has started to gain more attention (Zhang et al., 2017) and it offers an interesting avenue to follow up. The isogenic AD system could be an excellent tool to further investigate the impact of C99 but also C83, their relationship with TAU and the potential toxic effects.

Finally, it is important to mention that WB analysis and IF are two distinct methods that can be used to characterize the isogenic neuronal cultures. However, while we did obtain similar results or are able to see similar trends via IF and WBs, it is worth mentioning that the results could be different because of the experimental setup. While the WBs show protein quantifications

of all the cells collected from single 24 wells, the measurement via IF is more specialized and defined. It has been reported that filamentous pTau or NFTs accumulate mainly in the neuronal soma. It is possible that after about 50 days in culture during the differentiation protocol neurons build up pTau filaments that is accumulated could deposit in the cytoplasm. We do not expect the β- or γ-secretase inhibitors to have an effect on these deposits after only 3-12 days of treatment and therefore no change by IF is expected. However, the increase in pTau levels induced by the production of Aβ, mainly located in the neuronal projections, could indeed be blocked or impaired by the treatments and this effect detected by WB.

Instead of using the signal derived of all the cells, pTAU intensity was quantified from the soma of CTIP2+ cells.

ELISA results

The performed ELISA experiments were not only a crucial part of the characterization but also a proof-of-principle experiment for the whole purpose of using this isogenic disease model. As I am assuming that mutations in the gene APP can alter Aβ production, which then further downstream might lead to recapitulation of some events of fAD pathology I, I needed to provide proof for the altered APP levels first.

The results exceeded my expectations as higher Aβ40 and Aβ42 levels were confirmed for the AV and SWE lines compared to Wt. The increases were measured in media taken from cortical spheres, dissociated cortical neurons and surprisingly also from iPSCs, pointing out that even very early in development Aβ might start to accumulate. While the fAD mutations increased the levels, the AT line showed decreased levels in all these three different approaches, confirming its potentially protective effect against AD and cognitive decline. These results were accompanied by data that demonstrated that Aβ40 levels increase in a time-dependent manner in AV and SWE, whereas Aβ40 levels for Wt and AT almost remained on a constant very low level. The increase in Aβ over time is based on higher production in the fAD lines due to enhanced β-secretase activity, a feature seen *in vivo* and apparently also recapitulated by our *in vitro* model.

Lastly, I was able to show that the cultures are highly amemnable to treatments with β- and γ-secretase inhibitors, because addition of any of these compounds depleneshed Aβ40 to almost non-detectables levels. However, I also noticed that Aβ40 is much easier to detect than Aβ42, because Aβ40 levels are usually much higher, whereas Aβ42 levels are often close to the

detection range of most commercially availble ELISA sets. I was not surprised about the difficulties I had in measuring Aβ42, as Israel and colleagues already reported that issue using their patient derived iPSCs (2012). The issues can be overcome though by plating cells at higher densities or by simple ordering ELISA kits with a lower detection range.

As the model is isogenic, I can postulate that a high percentage of the results I am generating is very likely based on these SNPs they differ from each other. Still, as I have shown before, I detected differences between lines in their potential to differentiate. I did detect a higher amount of glial cells in both fAD lines compared to Wt, AT and KO, therefore These differences, even though some of them are tiny, might be important because on the one hand it could represent a phenotype, but on the other hand this different composition of cells might influence the results.

To overcome this obstacle I can take advantage of the cortical reporter I introduced into the isogenic lines. Whenever needed, purification of cortical neurons is now achievable via FAC sorting of CTIP2+ green cells. The reporter has been confirmed via IF staining with CTIP2 AB and co-localization of endogeneous and AB signal was higher than 90%.

Organoids results

The first preliminary results generated by confocal imaging of the organoids at day 134 of the differentiation are extremely exciting, even though it was disappointing that I could not detect pTAU in any of the them. As I have been able to detect pTAU via WB (Figures 39 and 40) and also via IF before (Figures 30 and 37), further IHC stainings using higher concentrations of the AB will reveal if the concentration used before was just too little or if I lose the epitode/phospho-site during the sectioning or during the IHC preparation of the samples. However, two points are very exciting and very promising about the results: First, I did see a huge increase in detected Aβ in the AV and SWE lines compared with Wt and AT. Aβ was massively increased not only in the soma but also inside the axon (Figure 58 and 59). The increases inside the neuron can be explained, because in the fAD lines more Aβ is produced by cleavage of β-secretase, which – unlike α-secretase cleavage at the surface – takes place in endosomes, followed by endocytic trafficking of the CTF-99 to lysosomes, multivesicular bodies and mitochondria associated membranes of the ER, where the final cleavage by γ-secretase takes place. Most Aβ peptides are then transported into the lumen, where aggregation into dimer, trimer and oligos takes place. Findings in AD patients as well studies

in mice have shown that intracellular Aβ usually precedes its extracellular deposition into senile plagues or other toxic aggregates (Grundke-Iqbal et al., 1989; Wirths et al., 2001) and recent findings in humans and mice have suggested that these intracellular aggregates contribute to disease progression (LaFerla et al., 2007; Oddo et al., 2003). Even though one study published contradicting results, arguing that intracellular increases of Aβ are correlated with age and can also be observed in healthy people, concluding that its increases will not affect and impair neuronal function (Wegiel et al., 2007). Our findings clearly indicate that intracellular Aβ increases do not correlated with age but are a direct or indirect result of the pathogenic mutations in our fAD lines. As all of our isogenic lines used for the generation of the organoids do have the same passage number and were sectioned on the same day, while having the same genetic background and only differ on the mutation of interest, it allows us to exclude age being a contributing factor in these findings. The results not only highlight the importance of our system being isogenic, but it also proves that it is reliable recapitulating events of AD pathology seen *in vivo*.

The second finding is that I detected diffuse extracellular accumulations of Aβ in the AV and SWE line (Figures 60 and 61). As it has been reported that the AB I used is not only able to detect soluble Aβ but also Aβ plagues (Lasagna-Reeves and Kayed, 2011; Thal et al., 2000) detection of plagues *in vitro* would be groundbreaking as it has never been achieved so far using hES or hiPSCs or any other cell type without overexpressing a combination of different fAD mutations in APP as well as PSEN1. Most transgenic mouse models expressing human mutations found in fAD develop amyloid plagues and Aβ induced synaptic death and cognitive deficits as well, they failed to clearly show Aβ induced formation of NFT followed by neuronal death. Oddo and colleagues showed that only 3xTg mice, carrying mutations in APP, PSEN1 and TAU tend to show both- senile plagues and NFT as well (Oddo et al., 2003). However, the mutation is TAU they introduced was not related to Alzheimer's disease, but one usually found in patients suffering from frontotemporal dementia, where NFT can be found independently of Aβ deposits. In fAD and sAD, TAU does not contain any mutation, but it becomes toxic due to increased phosphorylation through boosted kinase functions.

Choi and colleagues reported robust extracellular deposition of Aβ, including some plagues like structures in combination with deposits of filamentous TAU – no tangles though- using a commercially available and immortalized human neural progenitor cell line in combination with thick-layer dishes (Choi et al., 2014). However, the generated lines were transduced with lentivirus and cells overexpressed at least two different fAD mutations at the same time. It was a good

proof-of-principle experiment which first proved that Aβ is able to form large oligomers and finally plagues like structures *in vitro*, if enough Aβ is produced and it also proved that the thick 3D matrigel prohibits diffusion of soluble Aβ into the surrounding media and therefore accelerates AD pathology. However, formation of plagues was only achieved by overexpressing one mutation in APP in concert with one mutation in PSEN1. While overexpression of genes does not mimic the *in vivo* pathology and the genetic transcriptional and translational context of the cells and therefore might influence the outcome of any experiment drastically, fAD is caused by either mutations in APP or PSEN1, but a combination of 2 mutations in two different genes has not been reported yet. Two other groups have recently reported findings using a combination of 3D cultures and patient derived hiPSCs. While the first group used hiPSCs derived from sporadic AD patients in a 3D spheroid model (Lee et al., 2016), the second group used hiPSCs derived from fAD patients carrying either a mutation in PSEN1 or a duplication of APP (APPDp) and cells were cultured as organoids for a total of 90 (Raja et al., 2016). Both groups reported the incidence of AD pathology, shown by increased Aβ levels and pTAU, however, they failed to show filamentous TAU, NFT or plague like structures. Besides that, both patient derived models were not isogenic as genetically matched control lines were missing. The isogenic model I created overcomes this obstacle by being isogenic. Additionally, I have already been keeping them in culture for 180 days and as I have optimized the conditions, I hope I will be able to keep them in culture for up to a year or maybe even longer, which means I will mature them much longer compared to the reports of Lee and Raja. Much work is still needed, to unravel the identity of the diffuse deposits I detected in the fAD lines. Further immunostainings with at least 2 different Aβ ABs as well as staining with Thioflavin-S and Congo-red, compounds typically used to visualize plagues, are highly needed. However, the detection of extracellular Aβ deposits solely in the lines carrying the fAD mutations has been a huge success either way. In case it turns out that plagues are formed, a groundbreaking step would be reached. It would be the first time that a fAD disease model would recapitulate the disease to such an extent that one of the hallmarks of the disease appears as a clear phenotype. Even if the model fails to show aggregation of filamentous TAU into neurofibrillary tangles downstream of plague formation, the plagues themselves could be of much use. Our 3D organoid differentiation protocol would allow us to produce a great number of organoids at the same time, therefore it could function as a production core for human Aβ plagues. As our lines were derived from human iPSCs and also grown in cultures that mimics the interstitial compartment of the human brain closely, potential plagues would mimic the ones found in human patients and therefore could be used for further studies, drug-screenings and further AB development.

In case it turns out the diffuse deposits are an assembly of Aβ oligomers, it would still be another proof of principle that our model is able to recapitulate fAD up to a certain limit *in vitro* and also very encouraging, because more and more evidence appears that the Aβ oligomers do not only contribute to neural toxicity, but do play a key role in driving fAD pathology (Gandy et al., 2010; Ohshima et al., 2018). Aβ oligomers could explain the lacking correlation of plague burden and AD related manifestations of the disease. On the one hand reports showed that plagues are present even in healthy individual of the elderly and despite significant occurrence no cognitive decline or signs of abnormal neurodegeneration could be detected (Sloane et al., 1997) (Erten-Lyons et al., 2009), but on the other hand that neuronal death in AD patients also occurs in regions where plagues are missing (Erten-Lyons et al., 2009). These result were confirmed by the studies of Lesne and colleagues using a transgenic mouse model, who showed that plagues did not induce memory impairment when Aβ oligomers were absent, but they also showed that reduction of Aβ oligomers over time can lead to increased memory function (Lesne et al., 2008). Taken together these results at least point in the direction that plagues might not be the most toxic form of Aβ, which again, might be interesting for us regarding the results obtained from the current and also upcoming IHC.

Proteomics, InDrop-scRNAseq and Live cell imaging

Proteomic and transcriptional analyses have been successfully performed using the isogenic lines. However, given the amount of data that these experiments generated and given the vast amount of time it takes to go through these immense and valuable data sets for 6 different lines, I was only able to show preliminary data, as the analysis is still ongoing.

The preliminary data from the proteomics already pointed out that several differences in protein expression exist between our lines, and just by going through a few up- and downregulated proteins, I was already able to see interesting differences in pathways involving mitochondria and oxidative stress between protective AT and negative mutation lines. The first impression seems to confirm that the AT line is not only protective against AD by producing fewer total amounts and less aggregation prone Aβ, but also by increasing protein expression like TXNDR2, which actively reduce reactive oxygen levels and therefore do have a protective impact on mitochondria and cell health. However, the upcoming deep analysis will reveal more pathways involved in fAD and hopefully more potential proteins that are up- or down-regulated in mutant lines compared to Wt and AT and therefore do offer insight in fAD pathology.

I performed proteomic analysis from FACS-purified cortical neurons as well as non-purified fac sorted neurons underwent proteomic analysis. However, I will still need to do one more experiment to figure out, if the proteome of the reporter lines used in the first experiments appeared to be homogenous because potential differences were masked as a result of a common stress response to the Fac sorting or because the cell type analyzed simply does not have many of them, I would ideally need to analyze the proteome of purified cortical neurons, that did not undergo Fac sorting. Although that experiment would serve as a perfect control to figure out the procedures' potential impact on the proteome of our hiPSCs, unfortunately it is not doable as there simply is no other way to purify the fluorescent cortical neurons.

Hence, I will use the isogenic lines (non-reporter lines) used for experiment number 2 (non-reporter lines, non-sorted), but this time Fac sort them and perform the proteomic analysis on the whole FAC-sorted population. Differences in expressed proteins compared to the data-set derived from the non-FAC-sorted cells will reveal the impact of the FACS itself and allow further conclusion.

The scRNAseq was originally thought to serve two reasons:

First, as an experiment to find the sub-population within the neuronal cultures in which cells that carry fAD mutation are extremely vulnerable and are more prone to die compared to control or protective line. If that sub-population is found I will create a new targeting vector that targets a gene highly expressed in that sub-population and create reporter lines for that locus like described earlier, which allows purification and then analysis of the proteome with cells of that specific sub-population of all lines, which will hopefully lead to new insights in disease mechanism as well as protection against fAD.

Secondly, the cells were sequenced because I was curious to know how the introduced mutations would impact the transcriptome of our cells. The preliminary data showed that our differentiated neurons cluster into 5 different populations and the most spiking result so far was, that the only protective line in our experimental setup accounted for the majority of cells of one of the clusters. As this model is isogenic it indicates that the positive mutation at position 673 of the APP gene might influence the cells homeostasis, their potential to differentiate into cortical neurons and maybe other variables as well, which are far beyond the already known scope of that line, that so far had been focused on its ability to produce less Aβ over time. However, as the analysis is still ongoing, it is way too early to make conclusions, but the results will hopefully reveal

new, interesting insights in disease mechanism underlying fAD, as this is the first time that scRNAseq using isogenic hiPSCs has been performed.

The live imaging experiment revealed that the protective AT line is more resistant to added stressor compared to the lines carrying the negative mutations, but it also shows better survival over time in untreated conditions. Interestingly I noticed that the effect of better survival became first obvious around 75 to 85 hours after the experiments had started pointing out that differences might be even more obvious, if I am able to extend the time-frame of the survival experiments. However, it was great news to see a difference in survival solely based on the SNPs introduced in APP, because it highlights not only the potential of this fAD model to recapitulate fAD pathology, but it also points out that changes caused by impaired Aβ production impact the cells in many ways as fAD is a very complex, multifaceted disease.

The live imaging experiments will continue and will be of even more value as soon as the data generated from the proteomic and scRNAseq analysis are fully analyzed. In case druggable pathways or gene candidates that might be involved in fAD onset or pathology are identified, either small molecules can be used to specifically target the identified genes or whole libraries can be used for big screens, always accompanied by live cell measurement of survival compared to untreated cells.

While proteomic and scRNAseq analysis might reveal groundbreaking finding, as neither of them have ever been done in an isogenic hiPSCs AD model and I am very exciting about the outcome, I have shown that this isogenic fAD model is it fully capable of recapitulating aspects of fAD like elevated Aβ and pTAU levels *in vitro*. I have also shown that by generating cerebral organoids in 3D culture, I can keep and mature them in culture for more than 180 days, resulting in stronger AD related phenotypes, as aggregated Aβ deposits could be detected within the organoids that had not been seen in cortical spheres so far. Further, I have demonstrated that EBs/ neurons derived from the isogenic lines are highly amenable to treatments with chemical compounds and that they can adapt to live-cell imaging procedures for up to a week so far.

Hence, the model introduced in this study provides an excellent tool to screen for compounds that reverse or inhibit fAD associated phenotypes in a way not possible before.

Summary

In recent years two groundbreaking discoveries were made that allowed researchers to model human diseases *in vitro* like it has not been possible before. The generation of human induced pluripotent stem cells (hiPSCs) (Takahashi and Yamanaka, 2006) provides researchers with the ability to access patient derived cells carrying one or many disease-causing mutations, but also to differentiate the cells into the cell type most affected by the disease, cells that are typically lost at the end stage and therefore hard to study in vivo. The second discovery was the invention of programmable nucleases like the CRISPR-CAS system (Doudna and Charpentier, 2014) that allowed researchers to modify the genome of almost any organism, including hiPSCs, in a very efficient and precise manner. By introducing mutations into the genome or by correcting pathogenic mutations combined with the hiPSCs' potential to differentiate into almost any cell type, new avenues in disease modeling opened up carrying the potential of revolutionizing our understanding of pathologies of many human diseases.

The main goal of this thesis was to create an *in vitro* model for the early-onset, familial form of Alzheimer's disease (fAD) using hiPSCs in concert with genome editing techniques. fAD is caused by mutations in only three genes Presenilin 1, Presenilin 2 and Amyloid precursor protein (APP). Given that most investigations in the Alzheimer´s field have focused on mutations on the first two genes, I decided to create a model targeting the APP gene and specifically on certain fully penetrant mutations that ultimately cause fAD. To avoid genetic variability between different patient derived hiPSC lines, and in order to compare them with the genetically matched healthy controls, I decided to take an isogenic approach. Starting with a control line and using various genome-editing approaches, I generated three lines carrying fAD mutations, one line carrying a mutation that had been associated with protection against AD and cognitive decline and an additional APP KO line. Several clones per line were generated and I confirmed that all lines used in the study carried the right gene modification and were karyotypically normal.

First, I investigated whether the isogenic lines could differentiate into one of the cell types most severely affected by the disease and if I could detect any of the fAD phenotypes observed in vivo, as both points are crucial for a precise disease model *in vitro*. The conducted experiments revealed that the isogenic lines not only efficiently differentiate into cortical neurons, but they also display features of fAD pathology, such as increased Aβ42 and Aβ40 levels as well as high pTAU compared to similar neuronal cultures from the healthy control line. Further characterization of

the isogenic lines revealed that they are highly amenable to treatments with compounds reported to modulate the activity of APP-cleaving enzymes and therefore alter the production of Aβ peptides. Additionally, I discovered that the hiPSC line carrying the protective mutation and the APP KO hiPSC line proliferate faster than the fAD lines, which is an interesting finding that has not been reported yet and that I will follow up in the future.

As AD is a late-onset neurodegenerative disease where aging constitutes the main risk factor, I wondered whether increasing the maturation of differentiated neurons *in vitro*, and hence the possibility of detecting further AD-related phenotypes, could be achieved by maintaining the neurons for longer periods of time in culture. Using a three-dimensional culture method, I have been able to generate cerebral organoids from all the isogenic lines. These are highly complex and organized neuronal structures that include cavities which mimic the interstitial compartment of the human brain. By studying these organoids I have been able to detect dense aggregates of Aβ, indicating that maturation for longer periods of time does indeed correlate with the severity of the disease phenotype that can develop *in vitro*.

Being able to live-track individual neurons and even purify specific subpopulations constitutes a powerful tool necessary to answer certain questions. For that reason, I sub-sequentially targeted all isogenic lines to create highly functional reporter lines expressing the fluorophore mNeonGreen under the control of the CTIP2 promotor, a gene highly expressed in 5th layer cortical neurons. Having these new isogenic lines and using a novel approach of live-cell imaging allowed me to investigate how these mutations in APP influence neuronal survival in a cell-specific and live-longitudinal manner. I was able to detect that the CTIP2 positive neurons carrying the negative fAD mutations are more prone to die, under basal conditions and also in response to stress, and that the ones carrying the positive mutation seem to be protected and survive better than even the healthy control ones. Further studies are required to understand the mechanisms behind this enhanced survival. Finally, in order to investigate the proteomic and transcriptomic differences between the isogenic healthy control and fAD neurons, I subjected them to mass spectrometry and single-cell RNA sequencing analysis, which has not been done before. First preliminary results of the proteomic analysis revealed severe mitochondria dysfunctional network in the fAD cortical neurons and up-regulated pro-survival-related proteins in the cortical neurons carrying the protective mutation, which will be further investigated and analyzed.

Taken together the fAD model that I have generated has been proven to be fully capable of recapitulating major aspects of fAD “in a dish”. Novel biological insights regarding the proliferation and differentiation rate of hiPSCs, the proteome and transcriptome profiles of specific cortical neuronal types carrying fAD mutations, and Aβ extracellular deposition in long-term cultured cerebral organoids have been collected. Being an isogenic model it constitutes an excellent tool not only to study the disease and its underlying biology at a whole new level, but also to screen for compounds aiming at slowing down, reversing or blocking fAD associated phenotypes and to overall study fAD forms in detail not possible before.

In den letzten Jahren wurden zwei bahnbrechende Entdeckungen gemacht, die Wissenschaftler in die Lage versetzen, menschliche Krankheiten *in vitro* zu modellieren, wie es zuvor nicht möglich war. Die Erzeugung von humanen induzierten pluripotenten Stammzellen (hiPSZs) (Takahashi und Yamanaka, 2006) ermöglichte den Forschern den Zugriff auf vom Patienten abgeleitete Zellen, die eine oder viele krankheitsverursachende Mutationen trugen, aber auch die Differenzierung von Zellen in den am stärksten betroffenen Zelltyp der Krankheit, -Zellen, die typischerweise im Endstadium der Krankheit verloren gehen und daher *in vivo* schwer zu untersuchen sind. Die zweite Entdeckung war die Erfindung von programmierbaren Nukleasen wie dem CRISPR-CAS-System (Doudna und Charpentier, 2014), die es Forschern ermöglichen, das Genom fast jedes Organismus, einschließlich der hiPSZs, effizient und sehr genau zu verändern. Durch die Einführung von Mutationen in das Genom oder durch die Korrektur pathogener Mutationen in Kombination mit dem Differenzierungspotenzial von hiPSZs in fast jeden beliebigen Zelltyp, eröffneten sich neue Wege in der Krankheitsmodellierung, die das Potenzial haben, unser detailliertes Verständnis der Pathologien vieler menschlicher Krankheiten zu revolutionieren.

Das Hauptziel dieser Arbeit war die Entwicklung eines *in-vitro* Modells für die familiäre Form der Alzheimer-Krankheit (fAD) unter Verwendung humaner induzierter pluripotenter Stammzellen in Verbindung mit modernen Genome-Editing-Techniken. fAD wird ausschließlich durch Mutationen in den drei Genen Presenilin 1, Presenilin 2 und Amyloid Precursor Protein (APP) verursacht. Da sich die meisten Untersuchungen im Alzheimer-Feld auf Mutationen der

beiden erstgenannten Gene konzentriert haben, entschied ich mich, ein Modell zu erstellen, das sich vollständig auf die in APP vorkommenden und fAD verursachenden Mutationen konzentriert. Um genetische Variabilität zwischen verschiedenen Stammzell-Linien zu vermeiden, die in gängigen, hiPSZ Krankheitsmodellen oftmals vorhanden ist, da dort neben den vom Patienten abgeleiteten Zellen beliebige Zell-Linien als Kontroll-Linien verwendet werden, entschied ich mich für einen isogenen Ansatz. Beginnend mit einer Kontroll-Linie generierte ich mittels Genome-Editing 3 Linien mit fAD Mutationen (fAD Mutanten-Linien), 1 Linie mit einer Mutation, die kürzlich mit protektiven Eigenschaften gegen AD und kognitiven Verfall in Verbindung gebracht wurde, und 1 APP KO-Linie. Alle Linien sind Mycoplasma frei und karyotypisch normal gewesen.

Als Nächstes fragte ich mich, ob die isogenen Linien das Potential besitzen, in einen der von der Krankheit am stärksten betroffenen Zelltyp zu differenzieren und ob *in vivo* existierende fAD-Phänotypen von dem Modell *in vitro* rekapituliert werden können – zwei eminent wichtige Kriterien, die für ein präzises Krankheitsmodell *in vitro* entscheidend sind. Die durchgeführten Experimente zeigten, dass die isogenen Linien nicht nur mit einem hohen Prozentsatz an Zellen in kortikale Neuronen differenzieren, sondern dass sie auch Merkmale der fAD-Pathologie wiedergeben, da erhöhte Amyloid-beta (Aβ) 42 und Amyloid-beta 40 Level, sowie erhöhte Level an phosphoryliertem TAU Protein in den fAD Mutanten-Linien bestätigt wurden. Die weitere Charakterisierung der isogenen Linien zeigte, dass sie die gezielte Behandlung mit chemischen Wirkstoffen sehr gut tolerieren und sie somit das Potential besitzen, modulierbar zu sein durch externe Stimuli. Außerdem konnte ich entdecken, dass sich die protektive Zell-Linie höhere Proliferationsraten aufweist verglichen mit den fAD Mutanten-Linien. Dies ist ein interessanter Fund, der bisher in der fAD Forschung noch nicht berichtet wurde.

Da es sich bei fAD um eine neurodegenerative Erkrankung handelt, deren Pathologie stark mit Alter und Reifung korreliert, fragte ich mich, ob eine Reifung der Zellen *in vitro* über einen längeren Zeitraum zu einem stärkeren fAD-abhängigen Phänotyp führen würde. Mit einer dreidimensionalen Kulturmethode und über einen Zeitraum von 180 Tagen, konnte ich die isogenen Linien in cerebrale Organoids, hochkomplexe neuronale Strukturen, die das interstitielle Kompartiment des menschlichen Gehirns nachahmen. Tatsächlich war ich in der Lage dichte Aβ Aggregate in den fAD Mutanten-Linien zu detektieren, was darauf hinweist, dass eine Reifung der Zellen über längere Zeiträume tatsächlich mit einem ausgeprägteren Phänotyp *in vitro* korreliert.

In der Lage zu sein einzelne Neurone via live-tracking zu beobachten oder auch mit definierten Populationen an differenzierten Zellen arbeiten zu können, ist hilfreich um wichtige Fragestellungen beantworten zu können. Deshalb generierte ich Reporter-Zelllinien, die das Fluorophore mNeonGreen unter der Kontrolle des CTIP2 Promoters exprimieren, ein Marker-Gen für die 5. Ebene des Cortex. Die Reporter-Linien in Kombination mit einer neuen live-cell-imaging Methode, ermöglichten mir zu untersuchen, wie die eingefügten Mutationen in APP die Gesundheit und die Überlebensdauer der Zellen beeinflussen würde. Ich stellte fest, dass die Überlebenskurve der fAD Mutanten-Linien niedriger ist verglichen mit Kontroll- und protektiver Linie und sie außerdem verwundbarer und sensibler auf die Behandlung mit Stressoren reagieren. Schließlich wollte ich die isogenen Linien eingehender untersuchen und habe Proteomik sowie single-cell RNA Sequenzierung von differenzierten Neuronen des Cortex durchgeführt, was bisher noch nie mit isogenen fAD Linien durchgeführt wurde. Erste vorläufige Ergebnisse der Proteom-Analyse ergaben schwerwiegende Defizite im Mitochondrien-Netzwerk in den fAD Mutanten-Linien, die ich tiefergehend analysieren werde.

Zusammenfassend hat sich gezeigt, dass das generierte fAD-Modell in der Lage ist, wichtige Aspekte von fAD „in einer Petri-Schale“ zu rekapitulieren. Dabei wurden neuartige biologische Erkenntnisse über die Proliferation, die Differenzierung, die Langzeit-Kultivierung, sowie über Protein- und RNA Expression in via Genome-Editing generierten fAD Mutanten-Linien gewonnen, die durch Vergleiche der Daten mit Kontroll-Linie, KO- und protektiver Line idealerweise ergänzt werden konnten.

Da das Modell isogen ist, bietet es den Vorteil, dass sämtliche Unterschiede ausschließlich auf die eingefügten Mutationen zurückgeführt werden können. Somit stellt es ein hervorragendes Tool dar, nicht nur um zugrunde liegende Mechanismen von fAD auf einem völlig neuen Level zu untersuchen, sondern auch für das Screening nach Wirkstoffen und Substanzen, die fAD-assozierte Phänotypen umkehren oder hemmen, und somit eine wichtige Etappe auf der lange währenden Suche nach Therapie- oder Heilungsmöglichkeiten dar.

Bibliography

1 Abramov, E., Dolev, I., Fogel, H., Ciccotosto, G.D., Ruff, E., and Slutsky, I. (2009). Amyloid-beta as a positive endogenous regulator of release probability at hippocampal synapses. Nat Neurosci 12, 1567-1576.

2 Akutsu, H., Cowan, C.A., and Melton, D. (2006). Human embryonic stem cells. Methods Enzymol 418, 78-92.

3 Al-Hilaly, Y.K., Williams, T.L., Stewart-Parker, M., Ford, L., Skaria, E., Cole, M., Bucher, W.G., Morris, K.L., Sada, A.A., Thorpe, J.R., *et al.* (2013). A central role for dityrosine crosslinking of Amyloid-beta in Alzheimer's disease. Acta Neuropathol Commun 1, 83.

4 Amadoro, G., Corsetti, V., Florenzano, F., Atlante, A., Ciotti, M.T., Mongiardi, M.P., Bussani, R., Nicolin, V., Nori, S.L., Campanella, M., *et al.* (2014). AD-linked, toxic NH2 human tau affects the quality control of mitochondria in neurons. Neurobiol Dis 62, 489-507.

5 Andersen, J.K. (2004). Oxidative stress in neurodegeneration: cause or consequence? Nat Med 10 Suppl, S18-25.

6 Andreadis, A., Brown, W.M., and Kosik, K.S. (1992). Structure and novel exons of the human tau gene. Biochemistry 31, 10626-10633.

7 Area-Gomez, E., de Groof, A.J., Boldogh, I., Bird, T.D., Gibson, G.E., Koehler, C.M., Yu, W.H., Duff, K.E., Yaffe, M.P., Pon, L.A., *et al.* (2009). Presenilins are enriched in endoplasmic reticulum membranes associated with mitochondria. Am J Pathol 175, 1810-1816.

8 Avilion, A.A., Nicolis, S.K., Pevny, L.H., Perez, L., Vivian, N., and Lovell-Badge, R. (2003). Multipotent cell lineages in early mouse development depend on SOX2 function. Genes Dev 17, 126-140.

9 Babaie, Y., Herwig, R., Greber, B., Brink, T.C., Wruck, W., Groth, D., Lehrach, H., Burdon, T., and Adjaye, J. (2007). Analysis of Oct4-dependent transcriptional networks regulating self-renewal and pluripotency in human embryonic stem cells. Stem Cells 25, 500-510.

10 Banerjee, A., Lang, J.Y., Hung, M.C., Sengupta, K., Banerjee, S.K., Baksi, K., and Banerjee, D.K. (2011). Unfolded protein response is required in nu/nu mice microvasculature for treating breast tumor with tunicamycin. J Biol Chem 286, 29127-29138.

11 Barnes, J., Bartlett, J.W., Wolk, D.A., van der Flier, W.M., and Frost, C. (2018). Disease Course Varies According to Age and Symptom Length in Alzheimer's Disease. J Alzheimers Dis 64, 631-642.

12 Barnham, K.J., Ciccotosto, G.D., Tickler, A.K., Ali, F.E., Smith, D.G., Williamson, N.A., Lam, Y.H., Carrington, D., Tew, D., Kocak, G., *et al.* (2003). Neurotoxic, redox-competent Alzheimer's beta-amyloid is released from lipid membrane by methionine oxidation. J Biol Chem 278, 42959-42965.

13 Barrangou, R., Fremaux, C., Deveau, H., Richards, M., Boyaval, P., Moineau, S., Romero, D.A., and Horvath, P. (2007). CRISPR provides acquired resistance against viruses in prokaryotes. Science 315, 1709-1712.

14 Bartus, R.T., Dean, R.L., 3rd, Beer, B., and Lippa, A.S. (1982). The cholinergic hypothesis of geriatric memory dysfunction. Science 217, 408-414.

15 Bayer, T.A., Jakala, P., Hartmann, T., Havas, L., McLean, C., Culvenor, J.G., Li, Q.X., Masters, C.L., Falkai, P., and Beyreuther, K. (1999). Alpha-synuclein accumulates in Lewy bodies in Parkinson's disease and dementia with Lewy bodies but not in Alzheimer's disease beta-amyloid plaque cores. Neurosci Lett 266, 213-216.

16 Bertram, L., Lange, C., Mullin, K., Parkinson, M., Hsiao, M., Hogan, M.F., Schjeide, B.M., Hooli, B., Divito, J., Ionita, I., *et al.* (2008). Genome-wide association analysis reveals putative Alzheimer's disease susceptibility loci in addition to APOE. Am J Hum Genet 83, 623-632.

17 Beyreuther, K., and Masters, C.L. (1991). Amyloid precursor protein (APP) and beta A4 amyloid in the etiology of Alzheimer's disease: precursor-product relationships in the derangement of neuronal function. Brain Pathol 1, 241-251.

18 Bezprozvanny, I. (2009). Amyloid goes global. Sci Signal 2, pe16.

19 Blessed, G., Tomlinson, B.E., and Roth, M. (1968). The association between quantitative measures of dementia and of senile change in the cerebral grey matter of elderly subjects. Br J Psychiatry 114, 797-811.
20 Boch, J., Scholze, H., Schornack, S., Landgraf, A., Hahn, S., Kay, S., Lahaye, T., Nickstadt, A., and Bonas, U. (2009). Breaking the code of DNA binding specificity of TAL-type III effectors. Science 326, 1509-1512.
21 Botstein, D., and Risch, N. (2003). Discovering genotypes underlying human phenotypes: past successes for mendelian disease, future approaches for complex disease. Nat Genet 33 Suppl, 228-237.
22 Bradshaw, E.M., Chibnik, L.B., Keenan, B.T., Ottoboni, L., Raj, T., Tang, A., Rosenkrantz, L.L., Imboywa, S., Lee, M., Von Korff, A.*, et al.* (2013). CD33 Alzheimer's disease locus: altered monocyte function and amyloid biology. Nat Neurosci 16, 848-850.
23 Brennand, K.J., and Gage, F.H. (2011). Concise review: the promise of human induced pluripotent stem cell-based studies of schizophrenia. Stem Cells 29, 1915-1922.
24 Burridge, P.W., Matsa, E., Shukla, P., Lin, Z.C., Churko, J.M., Ebert, A.D., Lan, F., Diecke, S., Huber, B., Mordwinkin, N.M.*, et al.* (2014). Chemically defined generation of human cardiomyocytes. Nat Methods 11, 855-860.
25 Butler, A., Hoffman, P., Smibert, P., Papalexi, E., and Satija, R. (2018). Integrating single-cell transcriptomic data across different conditions, technologies, and species. Nat Biotechnol 36, 411-420.
26 Caille, I., Allinquant, B., Dupont, E., Bouillot, C., Langer, A., Muller, U., and Prochiantz, A. (2004). Soluble form of amyloid precursor protein regulates proliferation of progenitors in the adult subventricular zone. Development 131, 2173-2181.
27 Camp, J.G., Badsha, F., Florio, M., Kanton, S., Gerber, T., Wilsch-Brauninger, M., Lewitus, E., Sykes, A., Hevers, W., Lancaster, M.*, et al.* (2015). Human cerebral organoids recapitulate gene expression programs of fetal neocortex development. Proc Natl Acad Sci U S A 112, 15672-15677.
28 Capecchi, M.R. (1989). Altering the genome by homologous recombination. Science 244, 1288-1292.
29 Catalano, S.M., Dodson, E.C., Henze, D.A., Joyce, J.G., Krafft, G.A., and Kinney, G.G. (2006). The role of amyloid-beta derived diffusible ligands (ADDLs) in Alzheimer's disease. Curr Top Med Chem 6, 597-608.
30 Chambers, I., Colby, D., Robertson, M., Nichols, J., Lee, S., Tweedie, S., and Smith, A. (2003). Functional expression cloning of Nanog, a pluripotency sustaining factor in embryonic stem cells. Cell 113, 643-655.
31 Chambers, S.M., Fasano, C.A., Papapetrou, E.P., Tomishima, M., Sadelain, M., and Studer, L. (2009). Highly efficient neural conversion of human ES and iPS cells by dual inhibition of SMAD signaling. Nat Biotechnol 27, 275-280.
32 Chasseigneaux, S., Dinc, L., Rose, C., Chabret, C., Coulpier, F., Topilko, P., Mauger, G., and Allinquant, B. (2011). Secreted amyloid precursor protein beta and secreted amyloid precursor protein alpha induce axon outgrowth in vitro through Egr1 signaling pathway. PLoS One 6, e16301.
33 Chen, C.D., Oh, S.Y., Hinman, J.D., and Abraham, C.R. (2006). Visualization of APP dimerization and APP-Notch2 heterodimerization in living cells using bimolecular fluorescence complementation. J Neurochem 97, 30-43.
34 Choi, S.H., Kim, Y.H., Hebisch, M., Sliwinski, C., Lee, S., D'Avanzo, C., Chen, H., Hooli, B., Asselin, C., Muffat, J.*, et al.* (2014). A three-dimensional human neural cell culture model of Alzheimer's disease. Nature 515, 274-278.
35 Cleary, J.P., Walsh, D.M., Hofmeister, J.J., Shankar, G.M., Kuskowski, M.A., Selkoe, D.J., and Ashe, K.H. (2005). Natural oligomers of the amyloid-beta protein specifically disrupt cognitive function. Nat Neurosci 8, 79-84.
36 Cohen, T.J., Guo, J.L., Hurtado, D.E., Kwong, L.K., Mills, I.P., Trojanowski, J.Q., and Lee, V.M. (2011). The acetylation of tau inhibits its function and promotes pathological tau aggregation. Nat Commun 2, 252.

37 Corbett, G.T., Gonzalez, F.J., and Pahan, K. (2015). Activation of peroxisome proliferator-activated receptor alpha stimulates ADAM10-mediated proteolysis of APP. Proc Natl Acad Sci U S A 112, 8445-8450.

38 Cowan, C.A., Klimanskaya, I., McMahon, J., Atienza, J., Witmyer, J., Zucker, J.P., Wang, S., Morton, C.C., McMahon, A.P., Powers, D.*, et al.* (2004). Derivation of embryonic stem-cell lines from human blastocysts. N Engl J Med 350, 1353-1356.

39 Crehan, H., Hardy, J., and Pocock, J. (2013). Blockage of CR1 prevents activation of rodent microglia. Neurobiol Dis 54, 139-149.

40 Daley, G.Q., and Scadden, D.T. (2008). Prospects for stem cell-based therapy. Cell 132, 544-548.

41 Davis, R.L., Weintraub, H., and Lassar, A.B. (1987). Expression of a single transfected cDNA converts fibroblasts to myoblasts. Cell 51, 987-1000.

42 Dawson, G.R., Seabrook, G.R., Zheng, H., Smith, D.W., Graham, S., O'Dowd, G., Bowery, B.J., Boyce, S., Trumbauer, M.E., Chen, H.Y.*, et al.* (1999). Age-related cognitive deficits, impaired long-term potentiation and reduction in synaptic marker density in mice lacking the beta-amyloid precursor protein. Neuroscience 90, 1-13.

43 De Strooper, B., and Karran, E. (2016). The Cellular Phase of Alzheimer's Disease. Cell 164, 603-615.

44 de Wert, G., and Mummery, C. (2003). Human embryonic stem cells: research, ethics and policy. Hum Reprod 18, 672-682.

45 Deane, R., Du Yan, S., Submamaryan, R.K., LaRue, B., Jovanovic, S., Hogg, E., Welch, D., Manness, L., Lin, C., Yu, J.*, et al.* (2003). RAGE mediates amyloid-beta peptide transport across the blood-brain barrier and accumulation in brain. Nat Med 9, 907-913.

46 DeBoer, S.R., Dolios, G., Wang, R., and Sisodia, S.S. (2014). Differential release of beta-amyloid from dendrite- versus axon-targeted APP. J Neurosci 34, 12313-12327.

47 Delvaux, E., Bentley, K., Stubbs, V., Sabbagh, M., and Coleman, P.D. (2013). Differential processing of amyloid precursor protein in brain and in peripheral blood leukocytes. Neurobiol Aging 34, 1680-1686.

48 Demars, M.P., Bartholomew, A., Strakova, Z., and Lazarov, O. (2011). Soluble amyloid precursor protein: a novel proliferation factor of adult progenitor cells of ectodermal and mesodermal origin. Stem Cell Res Ther 2, 36.

49 Demars, M.P., Hollands, C., Zhao Kda, T., and Lazarov, O. (2013). Soluble amyloid precursor protein-alpha rescues age-linked decline in neural progenitor cell proliferation. Neurobiol Aging 34, 2431-2440.

50 Deng, J., Shoemaker, R., Xie, B., Gore, A., LeProust, E.M., Antosiewicz-Bourget, J., Egli, D., Maherali, N., Park, I.H., Yu, J.*, et al.* (2009). Targeted bisulfite sequencing reveals changes in DNA methylation associated with nuclear reprogramming. Nat Biotechnol 27, 353-360.

51 Deng, Y., Wang, Z., Wang, R., Zhang, X., Zhang, S., Wu, Y., Staufenbiel, M., Cai, F., and Song, W. (2013). Amyloid-beta protein (Abeta) Glu11 is the major beta-secretase site of beta-site amyloid-beta precursor protein-cleaving enzyme 1(BACE1), and shifting the cleavage site to Abeta Asp1 contributes to Alzheimer pathogenesis. Eur J Neurosci 37, 1962-1969.

52 Devine, M.J., Ryten, M., Vodicka, P., Thomson, A.J., Burdon, T., Houlden, H., Cavaleri, F., Nagano, M., Drummond, N.J., Taanman, J.W.*, et al.* (2011). Parkinson's disease induced pluripotent stem cells with triplication of the alpha-synuclein locus. Nat Commun 2, 440.

53 Di Fede, G., Catania, M., Morbin, M., Rossi, G., Suardi, S., Mazzoleni, G., Merlin, M., Giovagnoli, A.R., Prioni, S., Erbetta, A.*, et al.* (2009). A recessive mutation in the APP gene with dominant-negative effect on amyloidogenesis. Science 323, 1473-1477.

54 Dimos, J.T., Rodolfa, K.T., Niakan, K.K., Weisenthal, L.M., Mitsumoto, H., Chung, W., Croft, G.F., Saphier, G., Leibel, R., Goland, R.*, et al.* (2008). Induced pluripotent stem cells generated from patients with ALS can be differentiated into motor neurons. Science 321, 1218-1221.

55 Donovan, M.H., Yazdani, U., Norris, R.D., Games, D., German, D.C., and Eisch, A.J. (2006). Decreased adult hippocampal neurogenesis in the PDAPP mouse model of Alzheimer's disease. J Comp Neurol 495, 70-83.

56 Doudna, J.A., and Charpentier, E. (2014). Genome editing. The new frontier of genome engineering with CRISPR-Cas9. Science 346, 1258096.

57 Dulin, F., Leveille, F., Ortega, J.B., Mornon, J.P., Buisson, A., Callebaut, I., and Colloc'h, N. (2008). P3 peptide, a truncated form of A beta devoid of synaptotoxic effect, does not assemble into soluble oligomers. FEBS Lett 582, 1865-1870.

58 Eckert, A., Hauptmann, S., Scherping, I., Meinhardt, J., Rhein, V., Drose, S., Brandt, U., Fandrich, M., Muller, W.E., and Gotz, J. (2008). Oligomeric and fibrillar species of beta-amyloid (A beta 42) both impair mitochondrial function in P301L tau transgenic mice. J Mol Med (Berl) 86, 1255-1267.

59 Eckman, C.B., Mehta, N.D., Crook, R., Perez-tur, J., Prihar, G., Pfeiffer, E., Graff-Radford, N., Hinder, P., Yager, D., Zenk, B., *et al.* (1997). A new pathogenic mutation in the APP gene (I716V) increases the relative proportion of A beta 42(43). Hum Mol Genet 6, 2087-2089.

60 Edbauer, D., Willem, M., Lammich, S., Steiner, H., and Haass, C. (2002). Insulin-degrading enzyme rapidly removes the beta-amyloid precursor protein intracellular domain (AICD). J Biol Chem 277, 13389-13393.

61 Edbauer, D., Winkler, E., Regula, J.T., Pesold, B., Steiner, H., and Haass, C. (2003). Reconstitution of gamma-secretase activity. Nat Cell Biol 5, 486-488.

62 Eisele, Y.S., Fritschi, S.K., Hamaguchi, T., Obermuller, U., Fuger, P., Skodras, A., Schafer, C., Odenthal, J., Heikenwalder, M., Staufenbiel, M., *et al.* (2014). Multiple factors contribute to the peripheral induction of cerebral beta-amyloidosis. J Neurosci 34, 10264-10273.

63 Eisele, Y.S., Obermuller, U., Heilbronner, G., Baumann, F., Kaeser, S.A., Wolburg, H., Walker, L.C., Staufenbiel, M., Heikenwalder, M., and Jucker, M. (2010). Peripherally applied Abeta-containing inoculates induce cerebral beta-amyloidosis. Science 330, 980-982.

64 Erten-Lyons, D., Woltjer, R.L., Dodge, H., Nixon, R., Vorobik, R., Calvert, J.F., Leahy, M., Montine, T., and Kaye, J. (2009). Factors associated with resistance to dementia despite high Alzheimer disease pathology. Neurology 72, 354-360.

65 Esparza, T.J., Zhao, H., Cirrito, J.R., Cairns, N.J., Bateman, R.J., Holtzman, D.M., and Brody, D.L. (2013). Amyloid-beta oligomerization in Alzheimer dementia versus high-pathology controls. Ann Neurol 73, 104-119.

66 Evans, M.J., and Kaufman, M.H. (1981). Establishment in culture of pluripotential cells from mouse embryos. Nature 292, 154-156.

67 Forabosco, P., Ramasamy, A., Trabzuni, D., Walker, R., Smith, C., Bras, J., Levine, A.P., Hardy, J., Pocock, J.M., Guerreiro, R., *et al.* (2013). Insights into TREM2 biology by network analysis of human brain gene expression data. Neurobiol Aging 34, 2699-2714.

68 Freude, K.K., Penjwini, M., Davis, J.L., LaFerla, F.M., and Blurton-Jones, M. (2011). Soluble amyloid precursor protein induces rapid neural differentiation of human embryonic stem cells. J Biol Chem 286, 24264-24274.

69 Freudenberg-Hua, Y., Li, W., and Davies, P. (2018). The Role of Genetics in Advancing Precision Medicine for Alzheimer's Disease-A Narrative Review. Front Med (Lausanne) 5, 108.

70 Friedrich, R.P., Tepper, K., Ronicke, R., Soom, M., Westermann, M., Reymann, K., Kaether, C., and Fandrich, M. (2010). Mechanism of amyloid plaque formation suggests an intracellular basis of Abeta pathogenicity. Proc Natl Acad Sci U S A 107, 1942-1947.

71 Furukawa, K., Sopher, B.L., Rydel, R.E., Begley, J.G., Pham, D.G., Martin, G.M., Fox, M., and Mattson, M.P. (1996). Increased activity-regulating and neuroprotective efficacy of alpha-secretase-derived secreted amyloid precursor protein conferred by a C-terminal heparin-binding domain. J Neurochem 67, 1882-1896.

72 Fusaki, N., Ban, H., Nishiyama, A., Saeki, K., and Hasegawa, M. (2009). Efficient induction of transgene-free human pluripotent stem cells using a vector based on Sendai virus, an RNA virus that does not integrate into the host genome. Proc Jpn Acad Ser B Phys Biol Sci 85, 348-362.

73 Gandy, S., Simon, A.J., Steele, J.W., Lublin, A.L., Lah, J.J., Walker, L.C., Levey, A.I., Krafft, G.A., Levy, E., Checler, F., *et al.* (2010). Days to criterion as an indicator of toxicity associated with human Alzheimer amyloid-beta oligomers. Ann Neurol 68, 220-230.

74 Genomes Project, C., Auton, A., Brooks, L.D., Durbin, R.M., Garrison, E.P., Kang, H.M., Korbel, J.O., Marchini, J.L., McCarthy, S., McVean, G.A., *et al.* (2015). A global reference for human genetic variation. Nature 526, 68-74.

75 Ghiso, J., Calero, M., Matsubara, E., Governale, S., Chuba, J., Beavis, R., Wisniewski, T., and Frangione, B. (1997). Alzheimer's soluble amyloid beta is a normal component of human urine. FEBS Lett 408, 105-108.
76 Glazier, A.M., Nadeau, J.H., and Aitman, T.J. (2002). Finding genes that underlie complex traits. Science 298, 2345-2349.
77 Glenner, G.G., and Wong, C.W. (1984). Alzheimer's disease: initial report of the purification and characterization of a novel cerebrovascular amyloid protein. Biochem Biophys Res Commun 120, 885-890.
78 Goate, A., Chartier-Harlin, M.C., Mullan, M., Brown, J., Crawford, F., Fidani, L., Giuffra, L., Haynes, A., Irving, N., James, L*., et al.* (1991). Segregation of a missense mutation in the amyloid precursor protein gene with familial Alzheimer's disease. Nature 349, 704-706.
79 Goedert, M. (1993). Tau protein and the neurofibrillary pathology of Alzheimer's disease. Trends Neurosci 16, 460-465.
80 Goedert, M., and Jakes, R. (1990). Expression of separate isoforms of human tau protein: correlation with the tau pattern in brain and effects on tubulin polymerization. EMBO J 9, 4225-4230.
81 Goedert, M., and Spillantini, M.G. (2006). A century of Alzheimer's disease. Science 314, 777-781.
82 Goedert, M., Spillantini, M.G., Cairns, N.J., and Crowther, R.A. (1992). Tau proteins of Alzheimer paired helical filaments: abnormal phosphorylation of all six brain isoforms. Neuron 8, 159-168.
83 Goedert, M., Spillantini, M.G., Jakes, R., Rutherford, D., and Crowther, R.A. (1989). Multiple isoforms of human microtubule-associated protein tau: sequences and localization in neurofibrillary tangles of Alzheimer's disease. Neuron 3, 519-526.
84 Goedert, M., Wischik, C.M., Crowther, R.A., Walker, J.E., and Klug, A. (1988). Cloning and sequencing of the cDNA encoding a core protein of the paired helical filament of Alzheimer disease: identification as the microtubule-associated protein tau. Proc Natl Acad Sci U S A 85, 4051-4055.
85 Gomez-Isla, T., Hollister, R., West, H., Mui, S., Growdon, J.H., Petersen, R.C., Parisi, J.E., and Hyman, B.T. (1997). Neuronal loss correlates with but exceeds neurofibrillary tangles in Alzheimer's disease. Ann Neurol 41, 17-24.
86 Gong, C.X., Singh, T.J., Grundke-Iqbal, I., and Iqbal, K. (1993). Phosphoprotein phosphatase activities in Alzheimer disease brain. J Neurochem 61, 921-927.
87 Goodger, Z.V., Rajendran, L., Trutzel, A., Kohli, B.M., Nitsch, R.M., and Konietzko, U. (2009). Nuclear signaling by the APP intracellular domain occurs predominantly through the amyloidogenic processing pathway. J Cell Sci 122, 3703-3714.
88 Greenberg, S.G., Davies, P., Schein, J.D., and Binder, L.I. (1992). Hydrofluoric acid-treated tau PHF proteins display the same biochemical properties as normal tau. J Biol Chem 267, 564-569.
89 Griciuc, A., Serrano-Pozo, A., Parrado, A.R., Lesinski, A.N., Asselin, C.N., Mullin, K., Hooli, B., Choi, S.H., Hyman, B.T., and Tanzi, R.E. (2013). Alzheimer's disease risk gene CD33 inhibits microglial uptake of amyloid beta. Neuron 78, 631-643.
90 Grimm, A., Friedland, K., and Eckert, A. (2016). Mitochondrial dysfunction: the missing link between aging and sporadic Alzheimer's disease. Biogerontology 17, 281-296.
91 Grundke-Iqbal, I., Iqbal, K., George, L., Tung, Y.C., Kim, K.S., and Wisniewski, H.M. (1989). Amyloid protein and neurofibrillary tangles coexist in the same neuron in Alzheimer disease. Proc Natl Acad Sci U S A 86, 2853-2857.
92 Guenther, M.G., Frampton, G.M., Soldner, F., Hockemeyer, D., Mitalipova, M., Jaenisch, R., and Young, R.A. (2010). Chromatin structure and gene expression programs of human embryonic and induced pluripotent stem cells. Cell Stem Cell 7, 249-257.
93 Guerreiro, R., Wojtas, A., Bras, J., Carrasquillo, M., Rogaeva, E., Majounie, E., Cruchaga, C., Sassi, C., Kauwe, J.S., Younkin, S*., et al.* (2013). TREM2 variants in Alzheimer's disease. N Engl J Med 368, 117-127.
94 Gurdon, J.B. (1962). The developmental capacity of nuclei taken from intestinal epithelium cells of feeding tadpoles. J Embryol Exp Morphol 10, 622-640.
95 Haass, C., and Selkoe, D.J. (2007). Soluble protein oligomers in neurodegeneration: lessons from the Alzheimer's amyloid beta-peptide. Nat Rev Mol Cell Biol 8, 101-112.

96 Hacein-Bey-Abina, S., Von Kalle, C., Schmidt, M., McCormack, M.P., Wulffraat, N., Leboulch, P., Lim, A., Osborne, C.S., Pawliuk, R., Morillon, E.*, et al.* (2003). LMO2-associated clonal T cell proliferation in two patients after gene therapy for SCID-X1. Science 302, 415-419.

97 Han, Y.H., Moon, H.J., You, B.R., and Park, W.H. (2009). The effect of MG132, a proteasome inhibitor on HeLa cells in relation to cell growth, reactive oxygen species and GSH. Oncol Rep 22, 215-221.

98 Hanger, D.P., Anderton, B.H., and Noble, W. (2009). Tau phosphorylation: the therapeutic challenge for neurodegenerative disease. Trends Mol Med 15, 112-119.

99 Hanna, J., Wernig, M., Markoulaki, S., Sun, C.W., Meissner, A., Cassady, J.P., Beard, C., Brambrink, T., Wu, L.C., Townes, T.M.*, et al.* (2007). Treatment of sickle cell anemia mouse model with iPS cells generated from autologous skin. Science 318, 1920-1923.

100 Hardy, J., and Allsop, D. (1991). Amyloid deposition as the central event in the aetiology of Alzheimer's disease. Trends Pharmacol Sci 12, 383-388.

101 Hardy, J., and Selkoe, D.J. (2002). The amyloid hypothesis of Alzheimer's disease: progress and problems on the road to therapeutics. Science 297, 353-356.

102 Hardy, J.A., and Higgins, G.A. (1992). Alzheimer's disease: the amyloid cascade hypothesis. Science 256, 184-185.

103 Hatch, R.J., Wei, Y., Xia, D., and Gotz, J. (2017). Hyperphosphorylated tau causes reduced hippocampal CA1 excitability by relocating the axon initial segment. Acta Neuropathol 133, 717-730.

104 Haughey, N.J., Nath, A., Chan, S.L., Borchard, A.C., Rao, M.S., and Mattson, M.P. (2002). Disruption of neurogenesis by amyloid beta-peptide, and perturbed neural progenitor cell homeostasis, in models of Alzheimer's disease. J Neurochem 83, 1509-1524.

105 Heber, S., Herms, J., Gajic, V., Hainfellner, J., Aguzzi, A., Rulicke, T., von Kretzschmar, H., von Koch, C., Sisodia, S., Tremml, P.*, et al.* (2000). Mice with combined gene knock-outs reveal essential and partially redundant functions of amyloid precursor protein family members. J Neurosci 20, 7951-7963.

106 Hebert, L.E., Scherr, P.A., Bienias, J.L., Bennett, D.A., and Evans, D.A. (2003). Alzheimer disease in the US population: prevalence estimates using the 2000 census. Arch Neurol 60, 1119-1122.

107 Heneka, M.T., Carson, M.J., El Khoury, J., Landreth, G.E., Brosseron, F., Feinstein, D.L., Jacobs, A.H., Wyss-Coray, T., Vitorica, J., Ransohoff, R.M.*, et al.* (2015). Neuroinflammation in Alzheimer's disease. Lancet Neurol 14, 388-405.

108 Herms, J., Anliker, B., Heber, S., Ring, S., Fuhrmann, M., Kretzschmar, H., Sisodia, S., and Muller, U. (2004). Cortical dysplasia resembling human type 2 lissencephaly in mice lacking all three APP family members. EMBO J 23, 4106-4115.

109 Ho, A., and Sudhof, T.C. (2004). Binding of F-spondin to amyloid-beta precursor protein: a candidate amyloid-beta precursor protein ligand that modulates amyloid-beta precursor protein cleavage. Proc Natl Acad Sci U S A 101, 2548-2553.

110 Hochedlinger, K., Yamada, Y., Beard, C., and Jaenisch, R. (2005). Ectopic expression of Oct-4 blocks progenitor-cell differentiation and causes dysplasia in epithelial tissues. Cell 121, 465-477.

111 Hockemeyer, D., Wang, H., Kiani, S., Lai, C.S., Gao, Q., Cassady, J.P., Cost, G.J., Zhang, L., Santiago, Y., Miller, J.C.*, et al.* (2011). Genetic engineering of human pluripotent cells using TALE nucleases. Nat Biotechnol 29, 731-734.

112 Hoey, S.E., Williams, R.J., and Perkinton, M.S. (2009). Synaptic NMDA receptor activation stimulates alpha-secretase amyloid precursor protein processing and inhibits amyloid-beta production. J Neurosci 29, 4442-4460.

113 Hollingworth, P., Harold, D., Sims, R., Gerrish, A., Lambert, J.C., Carrasquillo, M.M., Abraham, R., Hamshere, M.L., Pahwa, J.S., Moskvina, V.*, et al.* (2011). Common variants at ABCA7, MS4A6A/MS4A4E, EPHA1, CD33 and CD2AP are associated with Alzheimer's disease. Nat Genet 43, 429-435.

114 Holstege, H., van der Lee, S.J., Hulsman, M., Wong, T.H., van Rooij, J.G., Weiss, M., Louwersheimer, E., Wolters, F.J., Amin, N., Uitterlinden, A.G.*, et al.* (2017). Characterization of pathogenic SORL1 genetic variants for association with Alzheimer's disease: a clinical interpretation strategy. Eur J Hum Genet 25, 973-981.

115 Hoover, B.R., Reed, M.N., Su, J., Penrod, R.D., Kotilinek, L.A., Grant, M.K., Pitstick, R., Carlson, G.A., Lanier, L.M., Yuan, L.L*., et al.* (2010). Tau mislocalization to dendritic spines mediates synaptic dysfunction independently of neurodegeneration. Neuron 68, 1067-1081.

116 Huang, W.J., Zhang, X., and Chen, W.W. (2016). Role of oxidative stress in Alzheimer's disease. Biomed Rep 4, 519-522.

117 Ichida, J.K., Blanchard, J., Lam, K., Son, E.Y., Chung, J.E., Egli, D., Loh, K.M., Carter, A.C., Di Giorgio, F.P., Koszka, K*., et al.* (2009). A small-molecule inhibitor of tgf-Beta signaling replaces sox2 in reprogramming by inducing nanog. Cell Stem Cell 5, 491-503.

118 Irwin, D.J., Cohen, T.J., Grossman, M., Arnold, S.E., Xie, S.X., Lee, V.M., and Trojanowski, J.Q. (2012). Acetylated tau, a novel pathological signature in Alzheimer's disease and other tauopathies. Brain 135, 807-818.

119 Ishida, A., Furukawa, K., Keller, J.N., and Mattson, M.P. (1997). Secreted form of beta-amyloid precursor protein shifts the frequency dependency for induction of LTD, and enhances LTP in hippocampal slices. Neuroreport 8, 2133-2137.

120 Ishino, Y., Shinagawa, H., Makino, K., Amemura, M., and Nakata, A. (1987). Nucleotide sequence of the iap gene, responsible for alkaline phosphatase isozyme conversion in Escherichia coli, and identification of the gene product. J Bacteriol 169, 5429-5433.

121 Israel, M.A., Yuan, S.H., Bardy, C., Reyna, S.M., Mu, Y., Herrera, C., Hefferan, M.P., Van Gorp, S., Nazor, K.L., Boscolo, F.S*., et al.* (2012). Probing sporadic and familial Alzheimer's disease using induced pluripotent stem cells. Nature 482, 216-220.

122 Ittner, A., Chua, S.W., Bertz, J., Volkerling, A., van der Hoven, J., Gladbach, A., Przybyla, M., Bi, M., van Hummel, A., Stevens, C.H*., et al.* (2016). Site-specific phosphorylation of tau inhibits amyloid-beta toxicity in Alzheimer's mice. Science 354, 904-908.

123 Ittner, L.M., Ke, Y.D., Delerue, F., Bi, M., Gladbach, A., van Eersel, J., Wolfing, H., Chieng, B.C., Christie, M.J., Napier, I.A*., et al.* (2010). Dendritic function of tau mediates amyloid-beta toxicity in Alzheimer's disease mouse models. Cell 142, 387-397.

124 Jansen, R., Embden, J.D., Gaastra, W., and Schouls, L.M. (2002). Identification of genes that are associated with DNA repeats in prokaryotes. Mol Microbiol 43, 1565-1575.

125 Jarrett, J.T., Berger, E.P., and Lansbury, P.T., Jr. (1993). The carboxy terminus of the beta amyloid protein is critical for the seeding of amyloid formation: implications for the pathogenesis of Alzheimer's disease. Biochemistry 32, 4693-4697.

126 Jaunmuktane, Z., Mead, S., Ellis, M., Wadsworth, J.D., Nicoll, A.J., Kenny, J., Launchbury, F., Linehan, J., Richard-Loendt, A., Walker, A.S*., et al.* (2015). Evidence for human transmission of amyloid-beta pathology and cerebral amyloid angiopathy. Nature 525, 247-250.

127 Jia, J., Wei, C., Chen, S., Li, F., Tang, Y., Qin, W., Zhao, L., Jin, H., Xu, H., Wang, F*., et al.* (2018). The cost of Alzheimer's disease in China and re-estimation of costs worldwide. Alzheimers Dement 14, 483-491.

128 Jin, K., Galvan, V., Xie, L., Mao, X.O., Gorostiza, O.F., Bredesen, D.E., and Greenberg, D.A. (2004). Enhanced neurogenesis in Alzheimer's disease transgenic (PDGF-APPSw,Ind) mice. Proc Natl Acad Sci U S A 101, 13363-13367.

129 Jones, L., Holmans, P.A., Hamshere, M.L., Harold, D., Moskvina, V., Ivanov, D., Pocklington, A., Abraham, R., Hollingworth, P., Sims, R*., et al.* (2010). Genetic evidence implicates the immune system and cholesterol metabolism in the aetiology of Alzheimer's disease. PLoS One 5, e13950.

130 Jonsson, T., Atwal, J.K., Steinberg, S., Snaedal, J., Jonsson, P.V., Bjornsson, S., Stefansson, H., Sulem, P., Gudbjartsson, D., Maloney, J*., et al.* (2012). A mutation in APP protects against Alzheimer's disease and age-related cognitive decline. Nature 488, 96-99.

131 Jonsson, T., Stefansson, H., Steinberg, S., Jonsdottir, I., Jonsson, P.V., Snaedal, J., Bjornsson, S., Huttenlocher, J., Levey, A.I., Lah, J.J*., et al.* (2013). Variant of TREM2 associated with the risk of Alzheimer's disease. N Engl J Med 368, 107-116.

132 Kamenetz, F., Tomita, T., Hsieh, H., Seabrook, G., Borchelt, D., Iwatsubo, T., Sisodia, S., and Malinow, R. (2003). APP processing and synaptic function. Neuron 37, 925-937.

133 Kanaar, R., Hoeijmakers, J.H., and van Gent, D.C. (1998). Molecular mechanisms of DNA double strand break repair. Trends Cell Biol 8, 483-489.

134 Kandel, E.R., Dudai, Y., and Mayford, M.R. (2014). The molecular and systems biology of memory. Cell 157, 163-186.
135 Kanekiyo, T., and Bu, G. (2014). The low-density lipoprotein receptor-related protein 1 and amyloid-beta clearance in Alzheimer's disease. Front Aging Neurosci 6, 93.
136 Kang, J., Lemaire, H.G., Unterbeck, A., Salbaum, J.M., Masters, C.L., Grzeschik, K.H., Multhaup, G., Beyreuther, K., and Muller-Hill, B. (1987). The precursor of Alzheimer's disease amyloid A4 protein resembles a cell-surface receptor. Nature 325, 733-736.
137 Kang, J., and Muller-Hill, B. (1990). Differential splicing of Alzheimer's disease amyloid A4 precursor RNA in rat tissues: PreA4(695) mRNA is predominantly produced in rat and human brain. Biochem Biophys Res Commun 166, 1192-1200.
138 Karumbayaram, S., Novitch, B.G., Patterson, M., Umbach, J.A., Richter, L., Lindgren, A., Conway, A.E., Clark, A.T., Goldman, S.A., Plath, K.*, et al.* (2009). Directed differentiation of human-induced pluripotent stem cells generates active motor neurons. Stem Cells 27, 806-811.
139 Kayed, R., Head, E., Sarsoza, F., Saing, T., Cotman, C.W., Necula, M., Margol, L., Wu, J., Breydo, L., Thompson, J.L.*, et al.* (2007). Fibril specific, conformation dependent antibodies recognize a generic epitope common to amyloid fibrils and fibrillar oligomers that is absent in prefibrillar oligomers. Mol Neurodegener 2, 18.
140 Kero, M., Paetau, A., Polvikoski, T., Tanskanen, M., Sulkava, R., Jansson, L., Myllykangas, L., and Tienari, P.J. (2013). Amyloid precursor protein (APP) A673T mutation in the elderly Finnish population. Neurobiol Aging 34, 1518 e1511-1513.
141 Kim, D., Kim, C.H., Moon, J.I., Chung, Y.G., Chang, M.Y., Han, B.S., Ko, S., Yang, E., Cha, K.Y., Lanza, R.*, et al.* (2009). Generation of human induced pluripotent stem cells by direct delivery of reprogramming proteins. Cell Stem Cell 4, 472-476.
142 Kim, K., Zhao, R., Doi, A., Ng, K., Unternaehrer, J., Cahan, P., Huo, H., Loh, Y.H., Aryee, M.J., Lensch, M.W.*, et al.* (2011). Donor cell type can influence the epigenome and differentiation potential of human induced pluripotent stem cells. Nat Biotechnol 29, 1117-1119.
143 Kim, T., Vidal, G.S., Djurisic, M., William, C.M., Birnbaum, M.E., Garcia, K.C., Hyman, B.T., and Shatz, C.J. (2013). Human LilrB2 is a beta-amyloid receptor and its murine homolog PirB regulates synaptic plasticity in an Alzheimer's model. Science 341, 1399-1404.
144 Klein, A.M., Kowall, N.W., and Ferrante, R.J. (1999). Neurotoxicity and oxidative damage of beta amyloid 1-42 versus beta amyloid 1-40 in the mouse cerebral cortex. Ann N Y Acad Sci 893, 314-320.
145 Klein, A.M., Mazutis, L., Akartuna, I., Tallapragada, N., Veres, A., Li, V., Peshkin, L., Weitz, D.A., and Kirschner, M.W. (2015). Droplet barcoding for single-cell transcriptomics applied to embryonic stem cells. Cell 161, 1187-1201.
146 Kleinberger, G., Yamanishi, Y., Suarez-Calvet, M., Czirr, E., Lohmann, E., Cuyvers, E., Struyfs, H., Pettkus, N., Wenninger-Weinzierl, A., Mazaheri, F.*, et al.* (2014). TREM2 mutations implicated in neurodegeneration impair cell surface transport and phagocytosis. Sci Transl Med 6, 243ra286.
147 Klug, A., and Rhodes, D. (1987). Zinc fingers: a novel protein fold for nucleic acid recognition. Cold Spring Harb Symp Quant Biol 52, 473-482.
148 Kondo, T., Asai, M., Tsukita, K., Kutoku, Y., Ohsawa, Y., Sunada, Y., Imamura, K., Egawa, N., Yahata, N., Okita, K.*, et al.* (2013). Modeling Alzheimer's disease with iPSCs reveals stress phenotypes associated with intracellular Abeta and differential drug responsiveness. Cell Stem Cell 12, 487-496.
149 Koonin, E.V., Makarova, K.S., and Zhang, F. (2017). Diversity, classification and evolution of CRISPR-Cas systems. Curr Opin Microbiol 37, 67-78.
150 Kristofikova, Z., Ricny, J., Kolarova, M., Vyhnalek, M., Hort, J., Laczo, J., Sirova, J., and Ripova, D. (2014). Interactions between amyloid-beta and tau in cerebrospinal fluid of people with mild cognitive impairment and Alzheimer's disease. J Alzheimers Dis 42 Suppl 3, S91-98.
151 Ksiezak-Reding, H., Morgan, K., Mattiace, L.A., Davies, P., Liu, W.K., Yen, S.H., Weidenheim, K., and Dickson, D.W. (1994). Ultrastructure and biochemical composition of paired helical filaments in corticobasal degeneration. Am J Pathol 145, 1496-1508.
152 Kumar, S., Singh, S., Hinze, D., Josten, M., Sahl, H.G., Siepmann, M., and Walter, J. (2012). Phosphorylation of amyloid-beta peptide at serine 8 attenuates its clearance via insulin-degrading and angiotensin-converting enzymes. J Biol Chem 287, 8641-8651.

153 Kummer, M.P., and Heneka, M.T. (2014). Truncated and modified amyloid-beta species. Alzheimers Res Ther 6, 28.
154 Kummer, M.P., Hermes, M., Delekarte, A., Hammerschmidt, T., Kumar, S., Terwel, D., Walter, J., Pape, H.C., Konig, S., Roeber, S.*, et al.* (2011). Nitration of tyrosine 10 critically enhances amyloid beta aggregation and plaque formation. Neuron 71, 833-844.
155 LaFerla, F.M., Green, K.N., and Oddo, S. (2007). Intracellular amyloid-beta in Alzheimer's disease. Nat Rev Neurosci 8, 499-509.
156 Lambert, J.C., Heath, S., Even, G., Campion, D., Sleegers, K., Hiltunen, M., Combarros, O., Zelenika, D., Bullido, M.J., Tavernier, B.*, et al.* (2009). Genome-wide association study identifies variants at CLU and CR1 associated with Alzheimer's disease. Nat Genet 41, 1094-1099.
157 Lammich, S., Okochi, M., Takeda, M., Kaether, C., Capell, A., Zimmer, A.K., Edbauer, D., Walter, J., Steiner, H., and Haass, C. (2002). Presenilin-dependent intramembrane proteolysis of CD44 leads to the liberation of its intracellular domain and the secretion of an Abeta-like peptide. J Biol Chem 277, 44754-44759.
158 Lancaster, M.A., Renner, M., Martin, C.A., Wenzel, D., Bicknell, L.S., Hurles, M.E., Homfray, T., Penninger, J.M., Jackson, A.P., and Knoblich, J.A. (2013). Cerebral organoids model human brain development and microcephaly. Nature 501, 373-379.
159 Lasagna-Reeves, C.A., Castillo-Carranza, D.L., Sengupta, U., Clos, A.L., Jackson, G.R., and Kayed, R. (2011). Tau oligomers impair memory and induce synaptic and mitochondrial dysfunction in wild-type mice. Mol Neurodegener 6, 39.
160 Lasagna-Reeves, C.A., and Kayed, R. (2011). Astrocytes contain amyloid-beta annular protofibrils in Alzheimer's disease brains. FEBS Lett 585, 3052-3057.
161 Lauritzen, I., Pardossi-Piquard, R., Bourgeois, A., Pagnotta, S., Biferi, M.G., Barkats, M., Lacor, P., Klein, W., Bauer, C., and Checler, F. (2016). Intraneuronal aggregation of the beta-CTF fragment of APP (C99) induces Abeta-independent lysosomal-autophagic pathology. Acta Neuropathol 132, 257-276.
162 Lee, G., Newman, S.T., Gard, D.L., Band, H., and Panchamoorthy, G. (1998). Tau interacts with src-family non-receptor tyrosine kinases. J Cell Sci 111 (Pt 21), 3167-3177.
163 Lee, H.K., Velazquez Sanchez, C., Chen, M., Morin, P.J., Wells, J.M., Hanlon, E.B., and Xia, W. (2016). Three Dimensional Human Neuro-Spheroid Model of Alzheimer's Disease Based on Differentiated Induced Pluripotent Stem Cells. PLoS One 11, e0163072.
164 Lee, J.H., Lau, K.F., Perkinton, M.S., Standen, C.L., Shemilt, S.J., Mercken, L., Cooper, J.D., McLoughlin, D.M., and Miller, C.C. (2003). The neuronal adaptor protein X11alpha reduces Abeta levels in the brains of Alzheimer's APPswe Tg2576 transgenic mice. J Biol Chem 278, 47025-47029.
165 Lesne, S., Koh, M.T., Kotilinek, L., Kayed, R., Glabe, C.G., Yang, A., Gallagher, M., and Ashe, K.H. (2006). A specific amyloid-beta protein assembly in the brain impairs memory. Nature 440, 352-357.
166 Lesne, S., Kotilinek, L., and Ashe, K.H. (2008). Plaque-bearing mice with reduced levels of oligomeric amyloid-beta assemblies have intact memory function. Neuroscience 151, 745-749.
167 Lesne, S.E., Sherman, M.A., Grant, M., Kuskowski, M., Schneider, J.A., Bennett, D.A., and Ashe, K.H. (2013). Brain amyloid-beta oligomers in ageing and Alzheimer's disease. Brain 136, 1383-1398.
168 Li, C., and Gotz, J. (2017). Somatodendritic accumulation of Tau in Alzheimer's disease is promoted by Fyn-mediated local protein translation. EMBO J 36, 3120-3138.
169 Li, S., Hong, S., Shepardson, N.E., Walsh, D.M., Shankar, G.M., and Selkoe, D. (2009). Soluble oligomers of amyloid Beta protein facilitate hippocampal long-term depression by disrupting neuronal glutamate uptake. Neuron 62, 788-801.
170 Li, X., Uemura, K., Hashimoto, T., Nasser-Ghodsi, N., Arimon, M., Lill, C.M., Palazzolo, I., Krainc, D., Hyman, B.T., and Berezovska, O. (2013). Neuronal activity and secreted amyloid beta lead to altered amyloid beta precursor protein and presenilin 1 interactions. Neurobiol Dis 50, 127-134.
171 Liu, Z., Zhu, H., Fang, G.G., Walsh, K., Mwamburi, M., Wolozin, B., Abdul-Hay, S.O., Ikezu, T., Leissring, M.A., and Qiu, W.Q. (2012). Characterization of insulin degrading enzyme and other amyloid-beta degrading proteases in human serum: a role in Alzheimer's disease? J Alzheimers Dis 29, 329-340.
172 Louwersheimer, E., Cohn-Hokke, P.E., Pijnenburg, Y.A., Weiss, M.M., Sistermans, E.A., Rozemuller, A.J., Hulsman, M., van Swieten, J.C., van Duijn, C.M., Barkhof, F.*, et al.* (2017). Rare Genetic Variant in SORL1 May Increase Penetrance of Alzheimer's Disease in a Family with Several Generations of APOE-varepsilon4 Homozygosity. J Alzheimers Dis 56, 63-74.

173 Lu, D.C., Rabizadeh, S., Chandra, S., Shayya, R.F., Ellerby, L.M., Ye, X., Salvesen, G.S., Koo, E.H., and Bredesen, D.E. (2000). A second cytotoxic proteolytic peptide derived from amyloid beta-protein precursor. Nat Med 6, 397-404.

174 Ma, L., Liu, Y., and Zhang, S.C. (2011). Directed differentiation of dopamine neurons from human pluripotent stem cells. Methods Mol Biol 767, 411-418.

175 Mackic, J.B., Stins, M., McComb, J.G., Calero, M., Ghiso, J., Kim, K.S., Yan, S.D., Stern, D., Schmidt, A.M., Frangione, B*., et al.* (1998). Human blood-brain barrier receptors for Alzheimer's amyloid-beta 1- 40. Asymmetrical binding, endocytosis, and transcytosis at the apical side of brain microvascular endothelial cell monolayer. J Clin Invest 102, 734-743.

176 Macosko, E.Z., Basu, A., Satija, R., Nemesh, J., Shekhar, K., Goldman, M., Tirosh, I., Bialas, A.R., Kamitaki, N., Martersteck, E.M*., et al.* (2015). Highly Parallel Genome-wide Expression Profiling of Individual Cells Using Nanoliter Droplets. Cell 161, 1202-1214.

177 Maffioletti, S.M., Gerli, M.F., Ragazzi, M., Dastidar, S., Benedetti, S., Loperfido, M., VandenDriessche, T., Chuah, M.K., and Tedesco, F.S. (2015). Efficient derivation and inducible differentiation of expandable skeletal myogenic cells from human ES and patient-specific iPS cells. Nat Protoc 10, 941-958.

178 Maherali, N., Sridharan, R., Xie, W., Utikal, J., Eminli, S., Arnold, K., Stadtfeld, M., Yachechko, R., Tchieu, J., Jaenisch, R*., et al.* (2007). Directly reprogrammed fibroblasts show global epigenetic remodeling and widespread tissue contribution. Cell Stem Cell 1, 55-70.

179 Makarova, K.S., Haft, D.H., Barrangou, R., Brouns, S.J., Charpentier, E., Horvath, P., Moineau, S., Mojica, F.J., Wolf, Y.I., Yakunin, A.F*., et al.* (2011). Evolution and classification of the CRISPR-Cas systems. Nat Rev Microbiol 9, 467-477.

180 Maloney, J.A., Bainbridge, T., Gustafson, A., Zhang, S., Kyauk, R., Steiner, P., van der Brug, M., Liu, Y., Ernst, J.A., Watts, R.J*., et al.* (2014). Molecular mechanisms of Alzheimer disease protection by the A673T allele of amyloid precursor protein. J Biol Chem 289, 30990-31000.

181 Manczak, M., and Reddy, P.H. (2012). Abnormal interaction of VDAC1 with amyloid beta and phosphorylated tau causes mitochondrial dysfunction in Alzheimer's disease. Hum Mol Genet 21, 5131-5146.

182 Matarin, M., Salih, D.A., Yasvoina, M., Cummings, D.M., Guelfi, S., Liu, W., Nahaboo Solim, M.A., Moens, T.G., Paublete, R.M., Ali, S.S*., et al.* (2015). A genome-wide gene-expression analysis and database in transgenic mice during development of amyloid or tau pathology. Cell Rep 10, 633-644.

183 Matsuda, T., and Cepko, C.L. (2007). Controlled expression of transgenes introduced by in vivo electroporation. Proc Natl Acad Sci U S A 104, 1027-1032.

184 McGeer, P.L., Akiyama, H., Itagaki, S., and McGeer, E.G. (1989). Immune system response in Alzheimer's disease. Can J Neurol Sci 16, 516-527.

185 McLaren, A. (2001). Ethical and social considerations of stem cell research. Nature 414, 129-131.

186 Mehta, P.D., Pirttila, T., Patrick, B.A., Barshatzky, M., and Mehta, S.P. (2001). Amyloid beta protein 1-40 and 1-42 levels in matched cerebrospinal fluid and plasma from patients with Alzheimer disease. Neurosci Lett 304, 102-106.

187 Merino-Serrais, P., Benavides-Piccione, R., Blazquez-Llorca, L., Kastanauskaite, A., Rabano, A., Avila, J., and DeFelipe, J. (2013). The influence of phospho-tau on dendritic spines of cortical pyramidal neurons in patients with Alzheimer's disease. Brain 136, 1913-1928.

188 Miller, J.C., Tan, S., Qiao, G., Barlow, K.A., Wang, J., Xia, D.F., Meng, X., Paschon, D.E., Leung, E., Hinkley, S.J*., et al.* (2011). A TALE nuclease architecture for efficient genome editing. Nat Biotechnol 29, 143-148.

189 Min, S.W., Cho, S.H., Zhou, Y., Schroeder, S., Haroutunian, V., Seeley, W.W., Huang, E.J., Shen, Y., Masliah, E., Mukherjee, C*., et al.* (2010). Acetylation of tau inhibits its degradation and contributes to tauopathy. Neuron 67, 953-966.

190 Mitsui, K., Tokuzawa, Y., Itoh, H., Segawa, K., Murakami, M., Takahashi, K., Maruyama, M., Maeda, M., and Yamanaka, S. (2003). The homeoprotein Nanog is required for maintenance of pluripotency in mouse epiblast and ES cells. Cell 113, 631-642.

191 Mojica, F.J., Diez-Villasenor, C., Garcia-Martinez, J., and Almendros, C. (2009). Short motif sequences determine the targets of the prokaryotic CRISPR defence system. Microbiology 155, 733-740.

192 Mojica, F.J., Diez-Villasenor, C., Soria, E., and Juez, G. (2000). Biological significance of a family of regularly spaced repeats in the genomes of Archaea, Bacteria and mitochondria. Mol Microbiol 36, 244-246.
193 Mok, S.S., Sberna, G., Heffernan, D., Cappai, R., Galatis, D., Clarris, H.J., Sawyer, W.H., Beyreuther, K., Masters, C.L., and Small, D.H. (1997). Expression and analysis of heparin-binding regions of the amyloid precursor protein of Alzheimer's disease. FEBS Lett 415, 303-307.
194 Moore, S., Evans, L.D., Andersson, T., Portelius, E., Smith, J., Dias, T.B., Saurat, N., McGlade, A., Kirwan, P., Blennow, K., *et al.* (2015). APP metabolism regulates tau proteostasis in human cerebral cortex neurons. Cell Rep 11, 689-696.
195 Mullan, M., Crawford, F., Axelman, K., Houlden, H., Lilius, L., Winblad, B., and Lannfelt, L. (1992). A pathogenic mutation for probable Alzheimer's disease in the APP gene at the N-terminus of beta-amyloid. Nat Genet 1, 345-347.
196 Muratore, C.R., Rice, H.C., Srikanth, P., Callahan, D.G., Shin, T., Benjamin, L.N., Walsh, D.M., Selkoe, D.J., and Young-Pearse, T.L. (2014). The familial Alzheimer's disease APPV717I mutation alters APP processing and Tau expression in iPSC-derived neurons. Hum Mol Genet 23, 3523-3536.
197 Nakagawa, M., Koyanagi, M., Tanabe, K., Takahashi, K., Ichisaka, T., Aoi, T., Okita, K., Mochiduki, Y., Takizawa, N., and Yamanaka, S. (2008). Generation of induced pluripotent stem cells without Myc from mouse and human fibroblasts. Nat Biotechnol 26, 101-106.
198 Newman, A.M., and Cooper, J.B. (2010). Lab-specific gene expression signatures in pluripotent stem cells. Cell Stem Cell 7, 258-262.
199 Nichols, J., Zevnik, B., Anastassiadis, K., Niwa, H., Klewe-Nebenius, D., Chambers, I., Scholer, H., and Smith, A. (1998). Formation of pluripotent stem cells in the mammalian embryo depends on the POU transcription factor Oct4. Cell 95, 379-391.
200 Nikolaev, A., McLaughlin, T., O'Leary, D.D., and Tessier-Lavigne, M. (2009). APP binds DR6 to trigger axon pruning and neuron death via distinct caspases. Nature 457, 981-989.
201 Nilsberth, C., Westlind-Danielsson, A., Eckman, C.B., Condron, M.M., Axelman, K., Forsell, C., Stenh, C., Luthman, J., Teplow, D.B., Younkin, S.G., *et al.* (2001). The 'Arctic' APP mutation (E693G) causes Alzheimer's disease by enhanced Abeta protofibril formation. Nat Neurosci 4, 887-893.
202 Nisbet, R.M., Polanco, J.C., Ittner, L.M., and Gotz, J. (2015). Tau aggregation and its interplay with amyloid-beta. Acta Neuropathol 129, 207-220.
203 Nixon, R.A. (2007). Autophagy, amyloidogenesis and Alzheimer disease. J Cell Sci 120, 4081-4091.
204 Nixon, R.A., Cataldo, A.M., and Mathews, P.M. (2000). The endosomal-lysosomal system of neurons in Alzheimer's disease pathogenesis: a review. Neurochem Res 25, 1161-1172.
205 Nussbaum, J.M., Schilling, S., Cynis, H., Silva, A., Swanson, E., Wangsanut, T., Tayler, K., Wiltgen, B., Hatami, A., Ronicke, R., *et al.* (2012). Prion-like behaviour and tau-dependent cytotoxicity of pyroglutamylated amyloid-beta. Nature 485, 651-655.
206 Oddo, S., Caccamo, A., Shepherd, J.D., Murphy, M.P., Golde, T.E., Kayed, R., Metherate, R., Mattson, M.P., Akbari, Y., and LaFerla, F.M. (2003). Triple-transgenic model of Alzheimer's disease with plaques and tangles: intracellular Abeta and synaptic dysfunction. Neuron 39, 409-421.
207 Oeppen, J., and Vaupel, J.W. (2002). Demography. Broken limits to life expectancy. Science 296, 1029-1031.
208 Ohsawa, I., Takamura, C., Morimoto, T., Ishiguro, M., and Kohsaka, S. (1999). Amino-terminal region of secreted form of amyloid precursor protein stimulates proliferation of neural stem cells. Eur J Neurosci 11, 1907-1913.
209 Ohshima, Y., Taguchi, K., Mizuta, I., Tanaka, M., Tomiyama, T., Kametani, F., Yabe-Nishimura, C., Mizuno, T., and Tokuda, T. (2018). Mutations in the beta-amyloid precursor protein in familial Alzheimer's disease increase Abeta oligomer production in cellular models. Heliyon 4, e00511.
210 Okita, K., Matsumura, Y., Sato, Y., Okada, A., Morizane, A., Okamoto, S., Hong, H., Nakagawa, M., Tanabe, K., Tezuka, K., *et al.* (2011). A more efficient method to generate integration-free human iPS cells. Nat Methods 8, 409-412.
211 Pan, X.D., Zhu, Y.G., Lin, N., Zhang, J., Ye, Q.Y., Huang, H.P., and Chen, X.C. (2011). Microglial phagocytosis induced by fibrillar beta-amyloid is attenuated by oligomeric beta-amyloid: implications for Alzheimer's disease. Mol Neurodegener 6, 45.

212 Park, I.H., Zhao, R., West, J.A., Yabuuchi, A., Huo, H., Ince, T.A., Lerou, P.H., Lensch, M.W., and Daley, G.Q. (2008). Reprogramming of human somatic cells to pluripotency with defined factors. Nature 451, 141-146.
213 Patsch, C., Challet-Meylan, L., Thoma, E.C., Urich, E., Heckel, T., O'Sullivan, J.F., Grainger, S.J., Kapp, F.G., Sun, L., Christensen, K*., et al.* (2015). Generation of vascular endothelial and smooth muscle cells from human pluripotent stem cells. Nat Cell Biol 17, 994-1003.
214 Pelech, S.L. (1995). Networking with proline-directed protein kinases implicated in tau phosphorylation. Neurobiol Aging 16, 247-256; discussion 257-261.
215 Perez, M.J., Vergara-Pulgar, K., Jara, C., Cabezas-Opazo, F., and Quintanilla, R.A. (2018). Caspase-Cleaved Tau Impairs Mitochondrial Dynamics in Alzheimer's Disease. Mol Neurobiol 55, 1004-1018.
216 Perez, R.G., Squazzo, S.L., and Koo, E.H. (1996). Enhanced release of amyloid beta-protein from codon 670/671 "Swedish" mutant beta-amyloid precursor protein occurs in both secretory and endocytic pathways. J Biol Chem 271, 9100-9107.
217 Polanco, J.C., Li, C., Bodea, L.G., Martinez-Marmol, R., Meunier, F.A., and Gotz, J. (2018). Amyloid-beta and tau complexity - towards improved biomarkers and targeted therapies. Nat Rev Neurol 14, 22-39.
218 Porteus, M. (2016). Genome Editing: A New Approach to Human Therapeutics. Annu Rev Pharmacol Toxicol 56, 163-190.
219 Porteus, M.H., and Baltimore, D. (2003). Chimeric nucleases stimulate gene targeting in human cells. Science 300, 763.
220 Porteus, M.H., and Carroll, D. (2005). Gene targeting using zinc finger nucleases. Nat Biotechnol 23, 967-973.
221 Puglielli, L., Tanzi, R.E., and Kovacs, D.M. (2003). Alzheimer's disease: the cholesterol connection. Nat Neurosci 6, 345-351.
222 Raghavan, N.S., Brickman, A.M., Andrews, H., Manly, J.J., Schupf, N., Lantigua, R., Wolock, C.J., Kamalakaran, S., Petrovski, S., Tosto, G*., et al.* (2018). Whole-exome sequencing in 20,197 persons for rare variants in Alzheimer's disease. Ann Clin Transl Neurol 5, 832-842.
223 Raja, W.K., Mungenast, A.E., Lin, Y.T., Ko, T., Abdurrob, F., Seo, J., and Tsai, L.H. (2016). Self-Organizing 3D Human Neural Tissue Derived from Induced Pluripotent Stem Cells Recapitulate Alzheimer's Disease Phenotypes. PLoS One 11, e0161969.
224 Rayaprolu, S., Mullen, B., Baker, M., Lynch, T., Finger, E., Seeley, W.W., Hatanpaa, K.J., Lomen-Hoerth, C., Kertesz, A., Bigio, E.H*., et al.* (2013). TREM2 in neurodegeneration: evidence for association of the p.R47H variant with frontotemporal dementia and Parkinson's disease. Mol Neurodegener 8, 19.
225 Reddy, P.H. (2007). Mitochondrial dysfunction in aging and Alzheimer's disease: strategies to protect neurons. Antioxid Redox Signal 9, 1647-1658.
226 Rhein, V., Song, X., Wiesner, A., Ittner, L.M., Baysang, G., Meier, F., Ozmen, L., Bluethmann, H., Drose, S., Brandt, U*., et al.* (2009). Amyloid-beta and tau synergistically impair the oxidative phosphorylation system in triple transgenic Alzheimer's disease mice. Proc Natl Acad Sci U S A 106, 20057-20062.
227 Ritchie, D.L., Adlard, P., Peden, A.H., Lowrie, S., Le Grice, M., Burns, K., Jackson, R.J., Yull, H., Keogh, M.J., Wei, W*., et al.* (2017). Amyloid-beta accumulation in the CNS in human growth hormone recipients in the UK. Acta Neuropathol 134, 221-240.
228 Roche, P.A., and Grodin, M.A. (2000). The ethical challenge of stem cell research. Womens Health Issues 10, 136-139.
229 Rodriguez-Muela, N., Litterman, N.K., Norabuena, E.M., Mull, J.L., Galazo, M.J., Sun, C., Ng, S.Y., Makhortova, N.R., White, A., Lynes, M.M*., et al.* (2017). Single-Cell Analysis of SMN Reveals Its Broader Role in Neuromuscular Disease. Cell Rep 18, 1484-1498.
230 Rohan de Silva, H.A., Jen, A., Wickenden, C., Jen, L.S., Wilkinson, S.L., and Patel, A.J. (1997). Cell-specific expression of beta-amyloid precursor protein isoform mRNAs and proteins in neurons and astrocytes. Brain Res Mol Brain Res 47, 147-156.
231 Roher, A.E., Esh, C.L., Kokjohn, T.A., Castano, E.M., Van Vickle, G.D., Kalback, W.M., Patton, R.L., Luehrs, D.C., Daugs, I.D., Kuo, Y.M*., et al.* (2009). Amyloid beta peptides in human plasma and tissues and their significance for Alzheimer's disease. Alzheimers Dement 5, 18-29.
232 Rouet, P., Smih, F., and Jasin, M. (1994). Introduction of double-strand breaks into the genome of mouse cells by expression of a rare-cutting endonuclease. Mol Cell Biol 14, 8096-8106.

233 Rovelet-Lecrux, A., Hannequin, D., Raux, G., Le Meur, N., Laquerriere, A., Vital, A., Dumanchin, C., Feuillette, S., Brice, A., Vercelletto, M.*, et al.* (2006). APP locus duplication causes autosomal dominant early-onset Alzheimer disease with cerebral amyloid angiopathy. Nat Genet 38, 24-26.

234 Rudin, N., Sugarman, E., and Haber, J.E. (1989). Genetic and physical analysis of double-strand break repair and recombination in Saccharomyces cerevisiae. Genetics 122, 519-534.

235 Sahlin, C., Lord, A., Magnusson, K., Englund, H., Almeida, C.G., Greengard, P., Nyberg, F., Gouras, G.K., Lannfelt, L., and Nilsson, L.N. (2007). The Arctic Alzheimer mutation favors intracellular amyloid-beta production by making amyloid precursor protein less available to alpha-secretase. J Neurochem 101, 854-862.

236 Santacruz, K., Lewis, J., Spires, T., Paulson, J., Kotilinek, L., Ingelsson, M., Guimaraes, A., DeTure, M., Ramsden, M., McGowan, E.*, et al.* (2005). Tau suppression in a neurodegenerative mouse model improves memory function. Science 309, 476-481.

237 Satija, R., Farrell, J.A., Gennert, D., Schier, A.F., and Regev, A. (2015). Spatial reconstruction of single-cell gene expression data. Nat Biotechnol 33, 495-502.

238 Sato, T., Diehl, T.S., Narayanan, S., Funamoto, S., Ihara, Y., De Strooper, B., Steiner, H., Haass, C., and Wolfe, M.S. (2007). Active gamma-secretase complexes contain only one of each component. J Biol Chem 282, 33985-33993.

239 Schinzel, R.T., Ahfeldt, T., Lau, F.H., Lee, Y.K., Cowley, A., Shen, T., Peters, D., Lum, D.H., and Cowan, C.A. (2011). Efficient culturing and genetic manipulation of human pluripotent stem cells. PLoS One 6, e27495.

240 Schneuwly, S., Klemenz, R., and Gehring, W.J. (1987). Redesigning the body plan of Drosophila by ectopic expression of the homoeotic gene Antennapedia. Nature 325, 816-818.

241 Schwank, G., Koo, B.K., Sasselli, V., Dekkers, J.F., Heo, I., Demircan, T., Sasaki, N., Boymans, S., Cuppen, E., van der Ent, C.K.*, et al.* (2013). Functional repair of CFTR by CRISPR/Cas9 in intestinal stem cell organoids of cystic fibrosis patients. Cell Stem Cell 13, 653-658.

242 Scott, K.R., and Barrett, A.M. (2007). Dementia syndromes: evaluation and treatment. Expert Rev Neurother 7, 407-422.

243 Selkoe, D.J. (1991). The molecular pathology of Alzheimer's disease. Neuron 6, 487-498.

244 Selkoe, D.J., and Hardy, J. (2016). The amyloid hypothesis of Alzheimer's disease at 25 years. EMBO Mol Med 8, 595-608.

245 Shacka, J.J., Roth, K.A., and Zhang, J. (2008). The autophagy-lysosomal degradation pathway: role in neurodegenerative disease and therapy. Front Biosci 13, 718-736.

246 Shaner, N.C., Lambert, G.G., Chammas, A., Ni, Y., Cranfill, P.J., Baird, M.A., Sell, B.R., Allen, J.R., Day, R.N., Israelsson, M.*, et al.* (2013). A bright monomeric green fluorescent protein derived from Branchiostoma lanceolatum. Nat Methods 10, 407-409.

247 Shankar, G.M., Li, S., Mehta, T.H., Garcia-Munoz, A., Shepardson, N.E., Smith, I., Brett, F.M., Farrell, M.A., Rowan, M.J., Lemere, C.A.*, et al.* (2008). Amyloid-beta protein dimers isolated directly from Alzheimer's brains impair synaptic plasticity and memory. Nat Med 14, 837-842.

248 Si-Tayeb, K., Noto, F.K., Nagaoka, M., Li, J., Battle, M.A., Duris, C., North, P.E., Dalton, S., and Duncan, S.A. (2010). Highly efficient generation of human hepatocyte-like cells from induced pluripotent stem cells. Hepatology 51, 297-305.

249 Sloane, J.A., Pietropaolo, M.F., Rosene, D.L., Moss, M.B., Peters, A., Kemper, T., and Abraham, C.R. (1997). Lack of correlation between plaque burden and cognition in the aged monkey. Acta Neuropathol 94, 471-478.

250 Slomnicki, L.P., and Lesniak, W. (2008). A putative role of the Amyloid Precursor Protein Intracellular Domain (AICD) in transcription. Acta Neurobiol Exp (Wars) 68, 219-228.

251 Smith, A.G., Heath, J.K., Donaldson, D.D., Wong, G.G., Moreau, J., Stahl, M., and Rogers, D. (1988). Inhibition of pluripotential embryonic stem cell differentiation by purified polypeptides. Nature 336, 688-690.

252 Smithies, O., Gregg, R.G., Boggs, S.S., Koralewski, M.A., and Kucherlapati, R.S. (1985). Insertion of DNA sequences into the human chromosomal beta-globin locus by homologous recombination. Nature 317, 230-234.

253 Soba, P., Eggert, S., Wagner, K., Zentgraf, H., Siehl, K., Kreger, S., Lower, A., Langer, A., Merdes, G., Paro, R*., et al.* (2005). Homo- and heterodimerization of APP family members promotes intercellular adhesion. EMBO J 24, 3624-3634.

254 Sondag, C.M., Dhawan, G., and Combs, C.K. (2009). Beta amyloid oligomers and fibrils stimulate differential activation of primary microglia. J Neuroinflammation 6, 1.

255 Spires-Jones, T.L., and Hyman, B.T. (2014). The intersection of amyloid beta and tau at synapses in Alzheimer's disease. Neuron 82, 756-771.

256 Stadtfeld, M., Nagaya, M., Utikal, J., Weir, G., and Hochedlinger, K. (2008). Induced pluripotent stem cells generated without viral integration. Science 322, 945-949.

257 Stein, S., Ott, M.G., Schultze-Strasser, S., Jauch, A., Burwinkel, B., Kinner, A., Schmidt, M., Kramer, A., Schwable, J., Glimm, H*., et al.* (2010). Genomic instability and myelodysplasia with monosomy 7 consequent to EVI1 activation after gene therapy for chronic granulomatous disease. Nat Med 16, 198-204.

258 Studer, L., Vera, E., and Cornacchia, D. (2015). Programming and Reprogramming Cellular Age in the Era of Induced Pluripotency. Cell Stem Cell 16, 591-600.

259 Suarez-Calvet, M., Kleinberger, G., Araque Caballero, M.A., Brendel, M., Rominger, A., Alcolea, D., Fortea, J., Lleo, A., Blesa, R., Gispert, J.D*., et al.* (2016). sTREM2 cerebrospinal fluid levels are a potential biomarker for microglia activity in early-stage Alzheimer's disease and associate with neuronal injury markers. EMBO Mol Med 8, 466-476.

260 Sultana, R., and Butterfield, D.A. (2010). Role of oxidative stress in the progression of Alzheimer's disease. J Alzheimers Dis 19, 341-353.

261 Takahashi, K., Tanabe, K., Ohnuki, M., Narita, M., Ichisaka, T., Tomoda, K., and Yamanaka, S. (2007). Induction of pluripotent stem cells from adult human fibroblasts by defined factors. Cell 131, 861-872.

262 Takahashi, K., and Yamanaka, S. (2006). Induction of pluripotent stem cells from mouse embryonic and adult fibroblast cultures by defined factors. Cell 126, 663-676.

263 Tanzi, R.E. (2012). The genetics of Alzheimer disease. Cold Spring Harb Perspect Med 2.

264 Thal, D.R., Schultz, C., Dehghani, F., Yamaguchi, H., Braak, H., and Braak, E. (2000). Amyloid beta-protein (Abeta)-containing astrocytes are located preferentially near N-terminal-truncated Abeta deposits in the human entorhinal cortex. Acta Neuropathol 100, 608-617.

265 Thomson, J.A., Itskovitz-Eldor, J., Shapiro, S.S., Waknitz, M.A., Swiergiel, J.J., Marshall, V.S., and Jones, J.M. (1998). Embryonic stem cell lines derived from human blastocysts. Science 282, 1145-1147.

266 Urnov, F.D., Miller, J.C., Lee, Y.L., Beausejour, C.M., Rock, J.M., Augustus, S., Jamieson, A.C., Porteus, M.H., Gregory, P.D., and Holmes, M.C. (2005). Highly efficient endogenous human gene correction using designed zinc-finger nucleases. Nature 435, 646-651.

267 Usenovic, M., Niroomand, S., Drolet, R.E., Yao, L., Gaspar, R.C., Hatcher, N.G., Schachter, J., Renger, J.J., and Parmentier-Batteur, S. (2015). Internalized Tau Oligomers Cause Neurodegeneration by Inducing Accumulation of Pathogenic Tau in Human Neurons Derived from Induced Pluripotent Stem Cells. J Neurosci 35, 14234-14250.

268 Van Nostrand, W.E., Melchor, J.P., Cho, H.S., Greenberg, S.M., and Rebeck, G.W. (2001). Pathogenic effects of D23N Iowa mutant amyloid beta -protein. J Biol Chem 276, 32860-32866.

269 Venugopal, C., Pappolla, M.A., and Sambamurti, K. (2007). Insulysin cleaves the APP cytoplasmic fragment at multiple sites. Neurochem Res 32, 2225-2234.

270 Vogelsberg-Ragaglia, V., Schuck, T., Trojanowski, J.Q., and Lee, V.M. (2001). PP2A mRNA expression is quantitatively decreased in Alzheimer's disease hippocampus. Exp Neurol 168, 402-412.

271 von Bergen, M., Barghorn, S., Biernat, J., Mandelkow, E.M., and Mandelkow, E. (2005). Tau aggregation is driven by a transition from random coil to beta sheet structure. Biochim Biophys Acta 1739, 158-166.

272 von Rotz, R.C., Kohli, B.M., Bosset, J., Meier, M., Suzuki, T., Nitsch, R.M., and Konietzko, U. (2004). The APP intracellular domain forms nuclear multiprotein complexes and regulates the transcription of its own precursor. J Cell Sci 117, 4435-4448.

273 Vossel, K.A., Xu, J.C., Fomenko, V., Miyamoto, T., Suberbielle, E., Knox, J.A., Ho, K., Kim, D.H., Yu, G.Q., and Mucke, L. (2015). Tau reduction prevents Abeta-induced axonal transport deficits by blocking activation of GSK3beta. J Cell Biol 209, 419-433.

274 Wang, Y., Cella, M., Mallinson, K., Ulrich, J.D., Young, K.L., Robinette, M.L., Gilfillan, S., Krishnan, G.M., Sudhakar, S., Zinselmeyer, B.H., *et al.* (2015). TREM2 lipid sensing sustains the microglial response in an Alzheimer's disease model. Cell 160, 1061-1071.

275 Wang, Y., and Ha, Y. (2004). The X-ray structure of an antiparallel dimer of the human amyloid precursor protein E2 domain. Mol Cell 15, 343-353.

276 Warren, L., Manos, P.D., Ahfeldt, T., Loh, Y.H., Li, H., Lau, F., Ebina, W., Mandal, P.K., Smith, Z.D., Meissner, A., *et al.* (2010). Highly efficient reprogramming to pluripotency and directed differentiation of human cells with synthetic modified mRNA. Cell Stem Cell 7, 618-630.

277 Wegiel, J., Kuchna, I., Nowicki, K., Frackowiak, J., Mazur-Kolecka, B., Imaki, H., Wegiel, J., Mehta, P.D., Silverman, W.P., Reisberg, B., *et al.* (2007). Intraneuronal Abeta immunoreactivity is not a predictor of brain amyloidosis-beta or neurofibrillary degeneration. Acta Neuropathol 113, 389-402.

278 Wegmann, S., Medalsy, I.D., Mandelkow, E., and Muller, D.J. (2013). The fuzzy coat of pathological human Tau fibrils is a two-layered polyelectrolyte brush. Proc Natl Acad Sci U S A 110, E313-321.

279 Wei, W., Norton, D.D., Wang, X., and Kusiak, J.W. (2002). Abeta 17-42 in Alzheimer's disease activates JNK and caspase-8 leading to neuronal apoptosis. Brain 125, 2036-2043.

280 Wernig, M., Meissner, A., Foreman, R., Brambrink, T., Ku, M., Hochedlinger, K., Bernstein, B.E., and Jaenisch, R. (2007). In vitro reprogramming of fibroblasts into a pluripotent ES-cell-like state. Nature 448, 318-324.

281 Wilmut, I., Schnieke, A.E., McWhir, J., Kind, A.J., and Campbell, K.H. (1997). Viable offspring derived from fetal and adult mammalian cells. Nature 385, 810-813.

282 Wirths, O., Multhaup, G., Czech, C., Blanchard, V., Moussaoui, S., Tremp, G., Pradier, L., Beyreuther, K., and Bayer, T.A. (2001). Intraneuronal Abeta accumulation precedes plaque formation in beta-amyloid precursor protein and presenilin-1 double-transgenic mice. Neurosci Lett 306, 116-120.

283 Wischik, C.M., Novak, M., Thogersen, H.C., Edwards, P.C., Runswick, M.J., Jakes, R., Walker, J.E., Milstein, C., Roth, M., and Klug, A. (1988). Isolation of a fragment of tau derived from the core of the paired helical filament of Alzheimer disease. Proc Natl Acad Sci U S A 85, 4506-4510.

284 Wisniewski, T., Ghiso, J., and Frangione, B. (1991). Peptides homologous to the amyloid protein of Alzheimer's disease containing a glutamine for glutamic acid substitution have accelerated amyloid fibril formation. Biochem Biophys Res Commun 179, 1247-1254.

285 Wunderlich, P., Glebov, K., Kemmerling, N., Tien, N.T., Neumann, H., and Walter, J. (2013). Sequential proteolytic processing of the triggering receptor expressed on myeloid cells-2 (TREM2) protein by ectodomain shedding and gamma-secretase-dependent intramembranous cleavage. J Biol Chem 288, 33027-33036.

286 Xia, D., Li, C., and Gotz, J. (2015). Pseudophosphorylation of Tau at distinct epitopes or the presence of the P301L mutation targets the microtubule-associated protein Tau to dendritic spines. Biochim Biophys Acta 1852, 913-924.

287 Xiang, Y., Bu, X.L., Liu, Y.H., Zhu, C., Shen, L.L., Jiao, S.S., Zhu, X.Y., Giunta, B., Tan, J., Song, W.H., *et al.* (2015). Physiological amyloid-beta clearance in the periphery and its therapeutic potential for Alzheimer's disease. Acta Neuropathol 130, 487-499.

288 Yamazaki, T., Koo, E.H., and Selkoe, D.J. (1997). Cell surface amyloid beta-protein precursor colocalizes with beta 1 integrins at substrate contact sites in neural cells. J Neurosci 17, 1004-1010.

289 Yang, T., Li, S., Xu, H., Walsh, D.M., and Selkoe, D.J. (2017). Large Soluble Oligomers of Amyloid beta-Protein from Alzheimer Brain Are Far Less Neuroactive Than the Smaller Oligomers to Which They Dissociate. J Neurosci 37, 152-163.

290 Young, J.E., Boulanger-Weill, J., Williams, D.A., Woodruff, G., Buen, F., Revilla, A.C., Herrera, C., Israel, M.A., Yuan, S.H., Edland, S.D., *et al.* (2015). Elucidating molecular phenotypes caused by the SORL1 Alzheimer's disease genetic risk factor using human induced pluripotent stem cells. Cell Stem Cell 16, 373-385.

291 Yu, J., Vodyanik, M.A., Smuga-Otto, K., Antosiewicz-Bourget, J., Frane, J.L., Tian, S., Nie, J., Jonsdottir, G.A., Ruotti, V., Stewart, R., *et al.* (2007). Induced pluripotent stem cell lines derived from human somatic cells. Science 318, 1917-1920.

292 Zempel, H., Luedtke, J., Kumar, Y., Biernat, J., Dawson, H., Mandelkow, E., and Mandelkow, E.M. (2013). Amyloid-beta oligomers induce synaptic damage via Tau-dependent microtubule severing by TTLL6 and spastin. EMBO J 32, 2920-2937.

293 Zhang, D., Jiang, W., Liu, M., Sui, X., Yin, X., Chen, S., Shi, Y., and Deng, H. (2009). Highly efficient differentiation of human ES cells and iPS cells into mature pancreatic insulin-producing cells. Cell Res 19, 429-438.

294 Zhang, F., Wen, Y., and Guo, X. (2014). CRISPR/Cas9 for genome editing: progress, implications and challenges. Hum Mol Genet 23, R40-46.

295 Zhang, S., Wang, Z., Cai, F., Zhang, M., Wu, Y., Zhang, J., and Song, W. (2017). BACE1 Cleavage Site Selection Critical for Amyloidogenesis and Alzheimer's Pathogenesis. J Neurosci 37, 6915-6925.

296 Zhang, Y., McLaughlin, R., Goodyer, C., and LeBlanc, A. (2002). Selective cytotoxicity of intracellular amyloid beta peptide1-42 through p53 and Bax in cultured primary human neurons. J Cell Biol 156, 519-529.

297 Zhao, P., Zhang, Z., Ke, H., Yue, Y., and Xue, D. (2014). Oligonucleotide-based targeted gene editing in C. elegans via the CRISPR/Cas9 system. Cell Res 24, 247-250.

298 Zheng, H., Jiang, M., Trumbauer, M.E., Sirinathsinghji, D.J., Hopkins, R., Smith, D.W., Heavens, R.P., Dawson, G.R., Boyce, S., Conner, M.W*., et al.* (1995). beta-Amyloid precursor protein-deficient mice show reactive gliosis and decreased locomotor activity. Cell 81, 525-531.

299 Zheng, H., and Koo, E.H. (2006). The amyloid precursor protein: beyond amyloid. Mol Neurodegener 1, 5.

300 Zheng, W.H., Bastianetto, S., Mennicken, F., Ma, W., and Kar, S. (2002). Amyloid beta peptide induces tau phosphorylation and loss of cholinergic neurons in rat primary septal cultures. Neuroscience 115, 201-211.

301 Zilionis, R., Nainys, J., Veres, A., Savova, V., Zemmour, D., Klein, A.M., and Mazutis, L. (2017). Single-cell barcoding and sequencing using droplet microfluidics. Nat Protoc 12, 44-73.

Global Health Estimates 2016: Disease burden by Cause, Age, Sex, by Country and by Region, 2000-2016. Geneva, World Health Organization, 2018 (http://www.who.int/healthinfo/global_burden_disease/estimates/en/index1.html)